UNIVERSITÀ DEGLI STUDI DI PALERMO

Corso di Dottorato di Ricerca in
"Energia e Tecnologie dell'Informazione - curriculum Fisica Tecnica e Ingegneria Nucleare"
Dipartimento di Energia, ingegneria dell'Informazione e modelli Matematici
Settore Scientifico Disciplinare ING-IND/19

INTEGRAL APPROACH TO THE SAFETY DESIGN OF THE EU-DEMO HELIUM-COOLED PEBBLE BEDS WITH REFERENCE TO THE ASSOCIATED RELEVANT SYSTEMS

IL DOTTORE
SALVATORE D'AMICO

IL COORDINATORE
PROF. MAURIZIO CELLURA

IL TUTOR
PROF. PIETRO ALESSANDRO DI MAIO

CICLO XXXII
ANNO CONSEGUIMENTO TITOLO 2020

Contents

List of Acronyms

ACPs	Activated Corrosion Products
ASDEX	Axially Symmetric Divertor EXperiment
BB	Breeding Blanket
BD	Burst Disk
BL	Bleed Line
BoP	Balance of Plant
BP	Backplate
BSS	Back Supporting Structure
BU	Breeder Unit
BV	Bleed Valve
BWR	Boiling Water Reactor
BZ	Breeder Zone
CATHARE	Code for Analysis of THermalhydraulics under Accident of Reactor and safety Evaluation
CEA	Atomic Energy and Alternative Energies Commission
CFD	Computational Fluid Dynamics
COB	Central Outboard Blanket
CP	Cooling Plates
DBTT	Ductile-Brittle Transition Temperature
DCLL	Dual Coolant Lead Lithium
DEG	Double-Ended Guillotine
DEMO	Demostration
Div	Divertor
dpa	displacement per atom
DSA	Deterministic Safety Analysis
EDF	Electricité de France
ERCOFTAC	European Research Community On Flow, Turbulence and Combustion
ESS	Energy Storage System
EU	European Union
EV	Expansion Volume
EVC	Ex-Vessel Components
FDM	Finite Difference Method
FEM	Finite Element Method
FFMEA	Functional Failure Modes and Effects Analysis
FP	Feeding Pipe
FPP	Fusion Power Plant
FVM	Finite Volume Method
FW	First Wall
GCR	Gas Cooled Reactor

GRICAMAN	GRId CAp MANifolds
HCPB	Helium Cooled Pebble Beds
HCLL	Helium Cooled Lithium Lead
HEBLO	HElium Blanket LOop
H&CD	Heating and Current Drive
HELOKA	HElium LOop KArlsruhe
HETRA	HEat TRAnsfer
HL	Hot Leg
HTC	Heat Transfer Coefficient
HX	Heat eXchanger
IRSN	Institut de Radioprotection et de Sûreté Nucléaire
IB	Inboard Blanket
IC	Isolation Condenser
ICE	Ingress of Coolant Event Ingress of Coolant Event
I&C	Instrumentation and Control
IE	Initiating Event
IHTS	Intermediate Heat Transfer System
IHX	Intermediate Heat eXchanger
INR	Institute of Neutron Physics and Reactor Technique
IVC	In-Vessel Components
JET	Joint European Torus
JT-60	Japan Torus-60
KALOS	KArlsruhe Lithium OrthoSilicate
L/RIB	Left/Right Inboard Blanket
L/ROB	Left/Right Outboard Blanket
LOCA	Loss Of Coolant Accident
MMS	Multi Module Segment
NET	Next European Torus
NPP	Nuclear Power Plant
OB	Outboard Blanket
PCD	Pre-Conceptual Design
PCS	Power Conversion System
PFC	Plasma Facing Component
PFD	Process Flow Diagram
PHTS	Primary Heat Transfer System
PI	Proportional-Integral
PIE	Postulated Initiating Event
PPCS	Power Plant Conceptual Studies

PREMUX	PRE-test Mock-Up eXperiment
PSA	Probabilistic Safety Analysis
PWR	Pressurized Water Reactor
RAMI	Reliability/Maintainability/Availability/Inspectability
RANS	Reynolds Averaged Navier-Stokes
RELAP	Reactor Excursion and Leak Analysis Program
RL	Relief Line
RM	Remote Maintenance
S&E	Safety and Environmental
SMS	Single Module Segment
SST	Shear Stress Transport
ST	Suppression Tank
T	Tritium
TBM	Test Blanket Module
TBR	Tritium Breeding Ratio
TCR	Tokamak Cooling Room
TRACE	TRAC/RELAP Advanced Computational Engine
US	United States
VV	Vacuum Vessel
VVPSS	Vacuum Vessel Pressure Suppression System
WCLL	Water Cooled Lithium-Lead
WPBB	Work Package Breeding Blanket
WPSAE	Work Package Safety and Environment

List of Symbols

Latin Symbols

Symbol	Unit	Description
a	[kg^{-1} m^{-1}]	Coefficient of pressure drop characteristic curve
a_1	[-]	constant in the SST limiter
B		Constant of the logarithmic law on a rough surface
b	[-]	Coefficient of pressure drop characteristic curve
C_f	[-]	Skin friction coefficient
d**S**	[cm^2]	Elementary surface vector
$DISS_k$	[W/m^3]	Phase k energy dissipation function
D_h	[m]	Hydraulic Diameter
d_0	[-]	length scale in Knopp et al. model
E_{fus}	[MeV]	Fusion reaction energy yield
E_i	[J/m^3s^{-1}]	Rate of energy transfer per unit volume across phase interfaces
E_k	[J]	Kinetic energy
F_1, F_2	[-]	Functions of the BSL and SST models
F_3	[-]	Function in the Hellsten and Laine correction
G_i	[kg s^{-1}]	Inlet mass flow rate
G_{nom}	[kg s^{-1}]	Nominal mass flow rate
K		Resistance loss coefficient
k_s	[µm]	Sand grain roughness height
k_S, k_R	[-]	Bounds of the transition regime
m	[kg]	Mass
M_{V_t}	[kg]	System total mass contained in the volume V_t
p	[Pa]	Fluid pressure
p^{in}	[Pa]	Inlet fluid pressure
p_i^{out}	[Pa]	Outlet fluid pressure
P_{fus}	[W]	Fusion power

Symbol	Unit	Description
q''	[W m^{-2}]	Heat flux
q'''_g	[W m^{-3}]	Volumetric density or heat power or power density generated within the body
Q	[-]	Plasma fusion gain
Q	[J]	Heat supplied to the system
$\mathbf{r}$	[m]	Position vector
S	[m^2]	Surface area
t	[s]	Time
T^{in}	[K]	Inlet fluid temperature
TBR	[-]	Tritium Breeding Ratio
$\mathbf{u_f}$	[m s^{-1}]	Vectorial fluid velocity
u_i	[m s^{-1}]	Flow velocity along one dimension
u_τ	[m s^{-1}]	Friction velocity
U	[J]	Internal system energy
y	[m]	Poloidal coordinate in the global coordinate system
y^+	[-]	Non-dimensional wall distance
z	[m]	Toroidal coordinate in the global coordinate system

Greek Symbols

Symbol	Unit	Description
α	[-]	Void fraction
β	[-]	Pressure gradient coefficient
β, β^*, γ	[-]	Constant of the k-ω model
Δp	[Pa]	Pressure drop
Δu^+	[-]	Shift of the logarithmic region due to wall roughness
δ	[m]	Boundary layer thickness
ε	[m^2 s^{-3}]	Turbulent kinetic energy dissipation rate
k	[m^2 s^{-2}]	Turbulent kinetic energy
λ	[W m^{-1} K^{-1}]	Thermal conductivity

Symbol	Unit	Description
μ_f	[Pa s^{-1}]	Fluid dynamic viscosity
ν_f	[m^2 s^{-1}]	Fluid kinematic viscosity
ρ_a	[kg m^{-3}]	Noncondensable gas density
ρ_b	[kg m^{-3}]	Spatial boron (solute) density
ρ_g	[kg m^{-3}]	Gas density
ρ_l	[kg m^{-3}]	Liquid density
ρ_k	[kg m^{-3}]	Phase k density
ρ	[kg m^{-3}]	Fluid density
σ, σ_κ, σ_ω	[-]	
τ_w	[Pa]	Wall friction
Ω	[-]	Vorticity or mean strain rate norm in the SST limiter
ω	[1/s]	Specific dissipation rate

Symbols

Symbol	Unit	Description
$_e$	[-]	Value at the outer edge of the boundary layer
$_w$	[-]	Wall value
$^+$	[-]	Value in wall units

1 Introduction

As reported in the World Population Prospects realised in 2019 by the United Nation Department of Economic and Social Affairs, more than 10 billion people are forecast to inhabit the Earth in 2100 [1]. The energy supply necessary to sustain such a growth is therefore a key issue for the future of mankind over the next decades.

According to the New Policies Scenario revealed by the U.S. Energy Information Administration in the International Energy Outlook edited in 2018 [2], it is expected a growth of the primary energy demand from 2017 to 2040 by 27 %; with the liquid fuels and natural gas demand rising by 10 and 43 % respectively, whereas the coal demand envisaged to remain close the current level, about 44 PWh. Considering that such a growth is led by developing economies - mainly China and India - which fulfil their demand by adopting high greenhouse gas emissions energy sources [3], the endowment of decarbonized energy technologies, along with the enhancement of current renewable energy sources, surely plays a pivotal role.

The above-mentioned context acquires a noteworthy importance taking into account the long-term goal provided by the Paris Agreement to keep the increase in global average temperature to well below 2 K above pre-industrial levels [4]. Obtaining such an ambitious target relies on several different considerations, mainly related to the world population growth, the development of global economy and the evolution of the living standards.

Within this framework, international policies have been already fielded in order to realize a competitive and low or null-carbon energy system appropriate for sustaining the energy demand. Indeed, several free-emission energy technologies have been investigated and among them, the thermonuclear fusion has been the object of many research activities carried out worldwide over the last decades. Demonstrating the effectiveness as possible future energy source of nuclear fusion has been the main ambition of the scientific community together with that of providing its feasibility at an industrial level. Moreover, fusion energy has intrinsic safety features which encourage its large-scale exploitation making it extremely attractive for the public. In fact, considering the ambitious goals of the European Union (EU) to obtain a greenhouse gas emission curtail to 80-95 % below 1990 levels by 2050, it becomes clear how nuclear energy is a crucial decarbonisation option and, on a 2050 perspective, it will become clearer which role fusion power will be able to play[5, 6].

Bearing in mind the importance of nuclear fusion energy role, several research facilities have been developed over the last decades, including JET [7] in United Kingdom and ASDEX Upgrade [8] in Germany, aimed at investigating the plasma physics fundamentals, such as plasma confinement, heating and stability.

At the next stage towards consolidating the fusion energy fundamentals and the electricity production from fusion energy there is the operation of a fusion machine, based on a self-sustained burning plasma. The ITER project [9], being developed within an international consortium of partners, has been designed to cope with such a delicate objective. The ITER fusion reactor, under construction in southern France, is essentially devoted to study the physics aspects of plasmas for fusion power and some of the technological challenges envisaged for the realization of a fusion power plant.

Nowadays, EU has a leading position in fusion research and development with a view to becoming a key player in the fusion market. In order to move towards the advancement of nuclear fusion, it has been identified a long-term strategy within the framework of the “European Research Roadmap to the realisation of fusion energy”. The scenario pictured in this roadmap foresees several steps to achieve this goal, the main of which are (i) the demonstration of large-scale fusion power by adopting ITER and (ii) delivering electricity to the grid via a DEMOnstration fusion power plant (DEMO), being the last step between ITER and a commercial fusion power plant [10]. In this regard, a major goal of the DEMO reactor is the

implementation, in a coherent architecture, of the above-mentioned fusion intrinsic safety features in order to ensure inherent passive resistance to any incidents and to avoid the need of evacuation in the worst incident case. The experience of the ITER licensing process has highlighted that the safety of the DEMO reactor must be assured by passive systems and the defence in depth approach, emphasising the confinement objective of the vacuum vessel, the expansion volumes and the related system to retain the directly mobilisable inventories.

With a view to satisfy such a top-level requirement, an integral approach to perform realistic assessment of the DEMO reactor system thermal-hydraulic performances under steady state, operational and accidental transient conditions, is proposed and critically discussed in this dissertation.

The experience of the ITER licensing process has highlighted that the safety of the DEMO reactor must be assured by passive systems and the defence in depth approach, emphasising the confinement objective of the vacuum vessel, the expansion volumes and the related system to retain the directly mobilisable inventories.

Within this framework, the main goal of the research activity carried out during the PhD course in "Energia e Tecnologie dell'Informazione - curriculum fisica tecnica e ingegneria nucleare (XXXII ciclo)" ("Energy and Information Technologies - nuclear engineering and applied physics curriculum, 32nd cycle") has been selecting the most representative and critical accidental scenarios in order to evaluate their potential consequences in terms of plant failure proposing design variations of components aimed to improve the overall plant safety and reliability performances.

1.1 Notes on Fusion Energy

Nuclear fusion is an exergonic process whereby two light nuclei combine to form a heavier and one, releasing energetic reaction products. Indeed, the mass difference (Δm) appears as energy (E) according to Einstein's law $E = (\Delta m) \cdot c^2$, where c denotes the speed of light. The resultant nucleus is more stable compared to the reacting nuclei due to the increased binding energy per nucleon. The binding energy curve is obtained by dividing the total nuclear binding energy by the number of nucleons, see Figure 1-1. The fact that there is a peak in the binding energy curve in the region of stability near iron means that either the breakup of heavier nuclei (fission) or the combining of lighter nuclei (fusion) will yield nuclei which are more tightly bound (less energy per nucleon) [11].

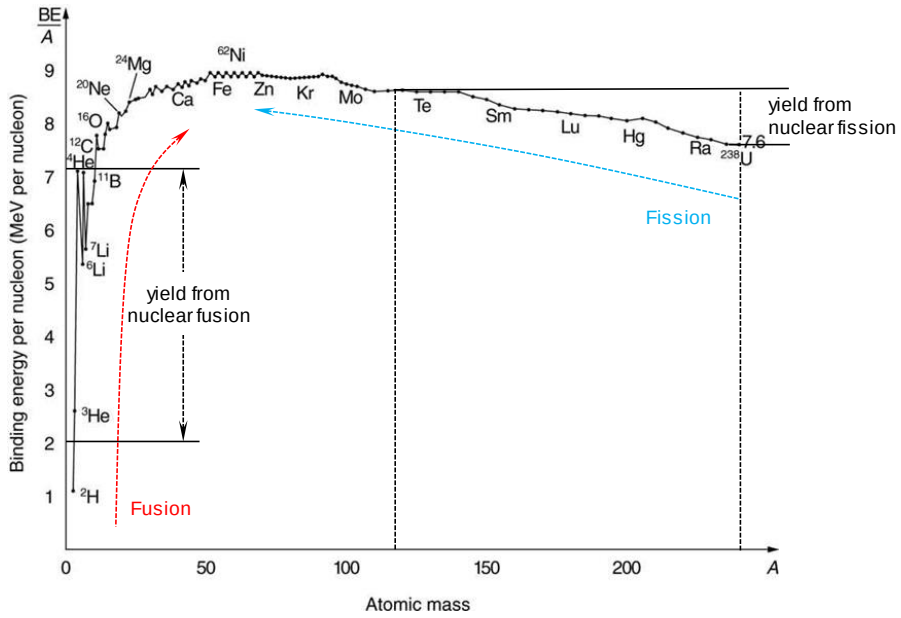

Figure 1-1: Bounding Energy (BE) per Nucleon. Light nuclei fusing in medium-mass ones are destroying mass releasing energy, in fact the BE/A is greater for the product nuclei [12].

The most important application of man-made plasmas is in the control of thermonuclear fusion reactions, which holds a vast potential for the generation of power. The basic problem in achieving controlled fusion is to generate a plasma at very high temperatures (with thermal energies at least in the 10 keV range) and hold its particles together long enough for a substantial number of fusion reactions to take place. The need for high temperatures comes from the fact that, in order to undergo fusion, the positively charged nuclei must come very close together (within a distance of the order of 10^{-14} m), which requires sufficient kinetic energy to overcome the electrostatic coulomb repulsion [13]. Therefore, a in order to bring these nuclei together sufficiently close so as to overcome the electrostatic repulsion and allow the strong interaction to take place, two light nuclei like hydrogen would require prohibitively high energies to be produced in a device.

However, thanks to the existence of the so called quantum tunnelling effect thermonuclear reactions can occur at much lower energies. This effect predicts that it exists a non-zero probability of a particle travelling through a barrier such as the one produced by the Coulomb forces. This probability becomes significant enough at high energies. The occurrence probability, i.e. the cross section σ, of the principal nuclear fusion reactions for different particles energies is shown in Figure 1-2.

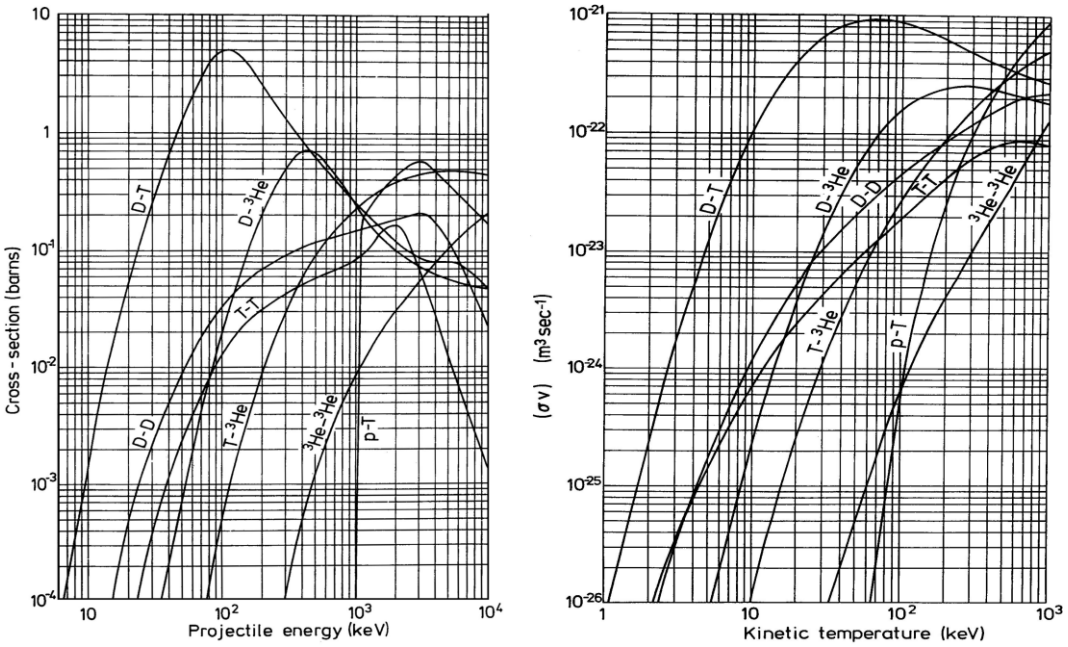

Figure 1-2: Main thermonuclear fusion reactions. Left (a): cross section as a function of the incident nucleus energy. Right (b): fusion reactivity in terms of the average of the fusion cross-section σ over the relative velocities v as function of the plasma temperature [14].

Amongst the possible fusion reactions, the principal are those involving isotopes of hydrogen, namely deuterium (D) and tritium (T) as follows:

$$ {}_1^2\mathrm{D} + {}_1^2\mathrm{D} \rightarrow {}_2^3\mathrm{He} + {}_0^1\mathrm{n} \qquad (Q_{DD} = 3.27\mathrm{MeV}), \qquad (1.1) $$

$$ {}_1^2\mathrm{D} + {}_1^2\mathrm{D} \rightarrow {}_2^3\mathrm{He} + {}_1^1\mathrm{p} \qquad (Q_{DD} = 4.03\mathrm{MeV}). \qquad (1.2) $$

$$ {}_1^2\mathrm{D} + {}_1^3\mathrm{T} \rightarrow {}_2^4\mathrm{He} + {}_0^1\mathrm{n} \qquad (Q_{DT} = 17.58\mathrm{MeV}). \qquad (1.3) $$

$$ {}_1^2\mathrm{D} + {}_2^3\mathrm{He} \rightarrow {}_2^4\mathrm{He} + {}_1^1\mathrm{p} \qquad (Q_{DHe} = 18.34\mathrm{MeV}). \qquad (1.4) $$

The reaction between D and T reported in 1.3 seems to be the most promising since it has a greater cross section at feasible plasma temperatures (thermal energies in the 10 keV range), Figure **1-2**, compared to the

others reported. The products of the D-T reaction are the alpha particle ${}_2^4\mathrm{He}$ and a neutron ${}_0^1\mathrm{n}$ which are sharing the released energy in an inversely proportional fashion with respect to their mass [13].

While the world's oceans as well as water lakes and rivers contain a copious supply of deuterium (0.0153 at.% in sea-water [15]), tritium is rare: it is a radioactive beta emitter with a half-life of 12.3 years, with the total steady state atmospheric and oceanic quantity of tritium produced by cosmic radiation estimated to be on the order of 50 kg. The main source of tritium is foreseen to be its breeding by capture fusion neutrons in the lithium contained in the Breeding Blanket (BB) surrounding the fusion core. The most relevant reactions in ${}_3^6\mathrm{Li}$ and ${}_3^7\mathrm{Li}$ are:

$$ {}_0^1\mathrm{n} + {}_3^6\mathrm{Li} \rightarrow {}_1^3\mathrm{T} + {}_2^4\mathrm{He} \qquad (Q_{nLi} = 4.78\mathrm{MeV}), \tag{1.5} $$

$$ {}_0^1\mathrm{n} + {}_3^7\mathrm{Li} \rightarrow {}_1^3\mathrm{T} + {}_2^4\mathrm{He} + {}_0^1\mathrm{n}' \qquad (Q_{nLi} = -2.47\mathrm{MeV}). \tag{1.6} $$

Reaction 1.6 is particularly interesting because the inelastically scattered neutron appearing at lower energy can continue to breed more tritium. Thus, in principle, it could be possible in such a system to produce more than one triton per neutron born in the D-T reaction. Indeed, the current reactor concepts adopting the D-T reaction generally assume a lithium-based blanket along with a neutron multiplier (Beryllium or Lead) to increase the neutron population by means of (n, 2n) reactions to compensate the parasitic losses [11]. In a thermonuclear reactor, the energy rate associated with the alpha particles produced during the D-T fusion reaction must be sufficient to maintain the energy of the reagents in the plasma, which is affected mainly of by radiation (bremsstrahlung, synchrotron and line radiation) and diffusion (plasma heat conduction) losses. This self-sustained energy state is defined burning plasma, while the moment when the burn takes place is known as plasma ignition. The fusion energy gain factor Q_g is then defined as the ratio between the nuclear fusion power P_{fu} and the total plasma heat P_h needed to sustain the thermonuclear fusion reactions:

$$ Q_g = \frac{P_{fu}}{P_h} \tag{1.7} $$

The fusion breakeven is referred to $Q_g = 1$. However, values of Q_g ~20 would be required to keep a thermonuclear fusion reactor controllable [16]. A general condition to achieve a burning plasma in a thermonuclear reactor is given by the so-called triple product $n\tau_E T$, which derives from the well-known Lawson criterion [17].

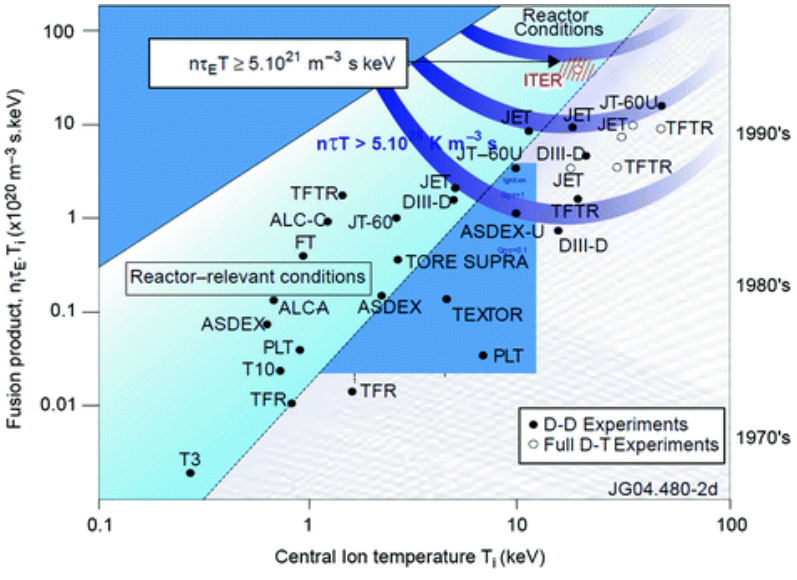

Figure 1-3: Triple product as a function of ion temperature for different tokamak experiment [15].

In the triple-product, the condition of burning plasma is achieved when the product defined by the plasma temperature T (kinetic energy of the reagents), the confinement time τ_E (time required to maintain the plasma above the ignition temperature) and the ion density n of the plasma is higher than a certain value, which depends on the reaction type. In the case of the D-T reaction, the triple product $n\tau_E T$ has a minimum of $2.9 \cdot 10^{28}$ sK/m^3 at 13 keV, see Figure 1-3, representing a temperature of ~150 million K [18].

In order to withstand such temperatures in a specified reactor domain for a sufficiently long time and since there are no materials able to remain in a solid state under these conditions, several confinement methods have been identified. Amongst them the two most investigated are the magnetic confinement and the inertial one. In the inertial confinement the reagents are in a pellet-like containment which is usually heated up by means of lasers until it implodes. The scientific and technological level of maturity of such a confinement is still at early stage and does not permit yet to suggest any particular approach for a demonstration reactor [19]. The magnetic confinement has a broader scientific and technological background, supported already with several devices aimed at demonstrating its technical feasibility. It is based on the fact that the particles forming the plasma are ionized and moving in a magnetic field they experience a Lorentz force which is perpendicular to both the their direction motion and to the magnetic field direction. This force does not affect the component of particles motion in the magnetic field direction, but it causes acceleration at right angles to the particle direction in the plane perpendicular to the magnetic field direction, producing a circular particle motion in that plane. Thus, a particle in a magnetic field moves along the field and spiral about it. The magnetic field lines may be configured to remain completely within a confinement chamber by the proper choice of position and currents in a set of magnetic coils. The simplest such configuration is the torus where two concepts have been investigated: tokamak [20] and stellarator [21]; see Figure 1-4.

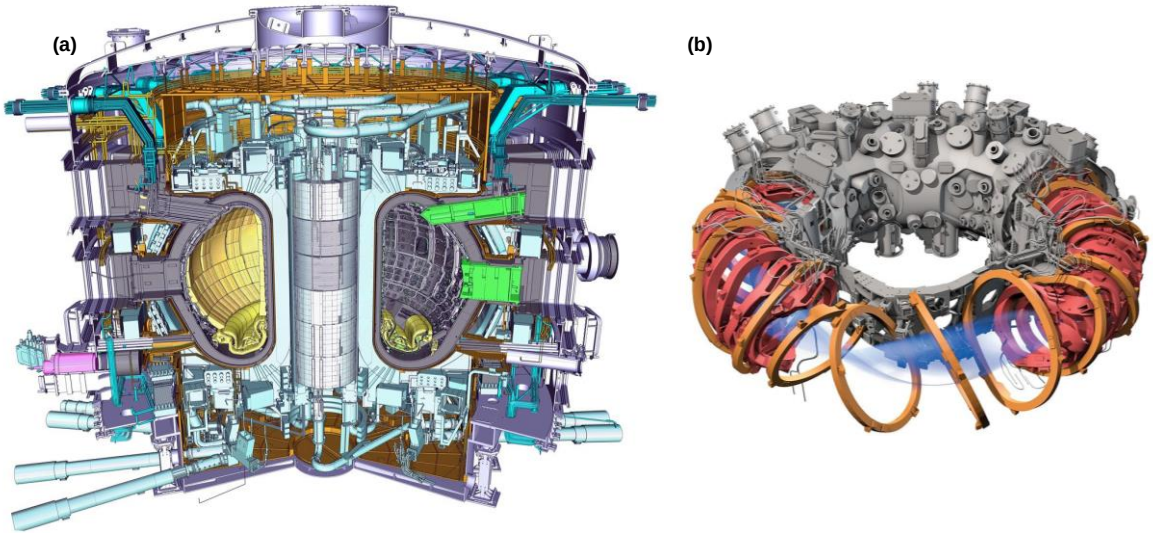

Figure 1-4: Conceptual design of fusion reactor based on magnetic confinement: (a) tokamak and (b) stellarator.

Most of the fusion reactors already developed are based mainly on the tokamak concept (JET in Europe, DIII-D in USA and JT-60 in Japan). The same configuration will be adopted for the next fusion machines (ITER and DEMO). The dissertetion herewith discussed will focus on the tokamak fusion reactor and, more specifically, to the European DEMO reactor.

1.2 The DEMOnstration Fusion Power Plant

The EUROfusion Consortium, on behalf of the European Commission, has issued a Roadmap to fusion

electricity by 2051. According to the strategy proposed DEMO will be the single step between ITER and a commercial fusion power featuring all the key systems and components and thus, proving the credibility of nuclear fusion as a reliable energy source [10, 22, 23]. For this reason, taking advantage of the progresses potentially demonstrated by ITER, DEMO shall be properly designed. The design process is divided in few different phases, following the definition of the objectives which are directly related to the performances and to the requirements expected by the DEMO machine. Moreover, certain targets have been defined in the Roadmap, which will have to rely on consolidated technical solutions and proofed materials under high level neutron fluence, possibly extrapolated from the ITER exploitation [10].

The general goals of DEMO, depicted in Figure 1-5, are [23-25]:

- to demonstrate power extraction at high temperature delivering a net electrical output to the grid (~300-500 MWe);
- to demonstrate a tritium self-sufficiency and a closed tritium fuel cycle producing more tritium than the one consumed (e.g. the number of tritium atoms produced per fusion neutron also known as tritium breeding ratio (TBR) has to be greater than 1 with a foreseen design value of 1.05);
- to demonstrate attractive safety and low environmental impact minimising the worker exposure and the radioactive wastes with no need of long-term storage;
- to demonstrate acceptable Reliability/Maintainability/Availability/Inspectability (RAMI) using remote maintenance and minimising the number of unscheduled shutdown.

Amongst these top-level functions there are several technology and integration problems which present a very strong interdependencies and they should be addressed in a holistic manner since the early stage of the DEMO design. Some of them are related to the design of the first-wall (FW), the selection of the BB concept and its related balance-of-plant (BoP) systems, the configuration of the divertor, the suitable remote maintenance (RM) scheme and the heating and current drive (H&CD) technologies to be employed according to an adoptable plasma scenario [10, 22].

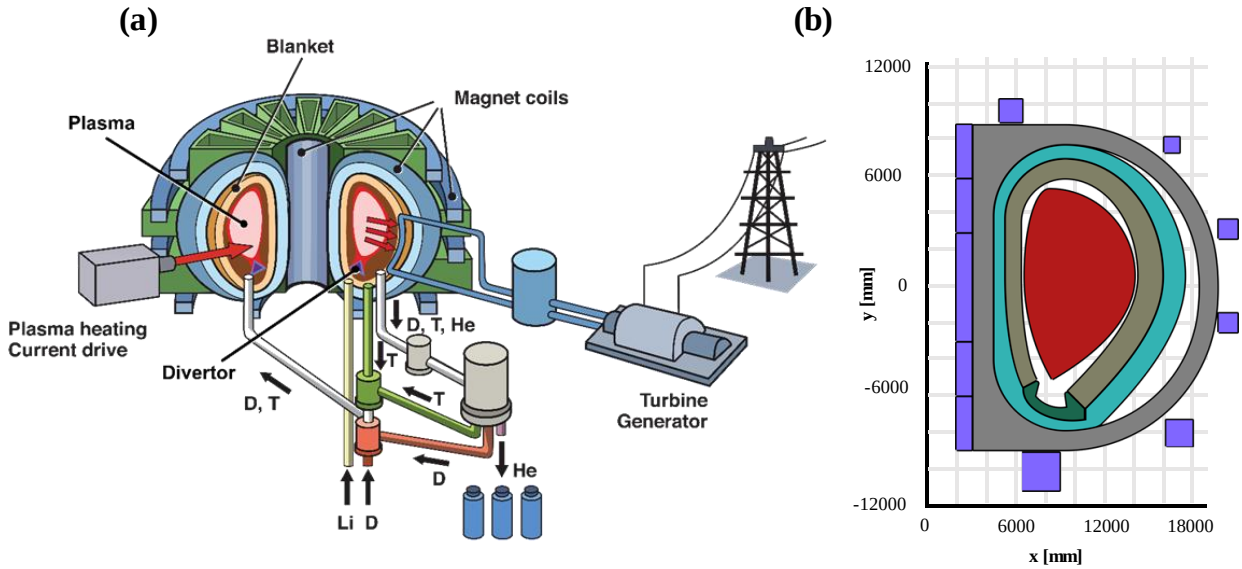

Figure 1-5: Conceptual representation of DEMO with its main systems (a) and section of the reactor core (b).

Indeed, the technical features of the DEMO plant design solution depends upon the performance requirements and technological assumptions. The task of choosing an appropriate set of design parameters and engineering technologies involves trade-offs between the attractiveness and technical risk associated with the various design options.

The configuration adopted as reference for the research activities herewith described is the EU-DEMO

baseline 2017 [26], with a fusion power of 1998 MW. According to this baseline, the DEMO reactor consists of 16 identical sectors of 22.5° in the toroidal direction (φ) subdivided conforming to the coils number. Each sector includes 5 BB segments: 2 for the inboard (IB) and 3 for the outboard (OB).The systems composing a typical DEMO sector are depicted in Figure 1-6 [24]:

- the BB surrounding the plasma and which removes the thermal power released by neutrons and alpha-particles, produces tritium and shields the Vacuum Vessel (VV) and coils;
- the divertor, a high heat flux component which collects the particles and energy exhausted by the plasma. Its magnetic and geometrical topology is chosen in order to intersect the divertor within the last closed flux surface;
- the thermal shield which shields the cryogenic magnet system from the radiation coming from the VV. It is practically a shell-like structure which encloses the VV and its openings (ports);
- the upper, lower and equatorial ports which provide, iter alia, the access to the In-Vessel components such as the BB segments and the divertor;
- the VV providing the primary vacuum and which shields the magnet system from the neutrons. It is a torus-shaped double-walled pressure vessel composed by three different layers;
- the central solenoid, poloidal and toroidal field coils which provide the magnetic field required to confine the plasma and to define its poloidal structure;
- the cryostat which acts as a barrier in order to isolate the magnets system from the surrounding environment.
- the bioshield, a 2 m thick shield made of borated concrete which reduces the neutron and gamma fluence coming from the plasma chamber to sufficiently low levels suitable for worker access [27].

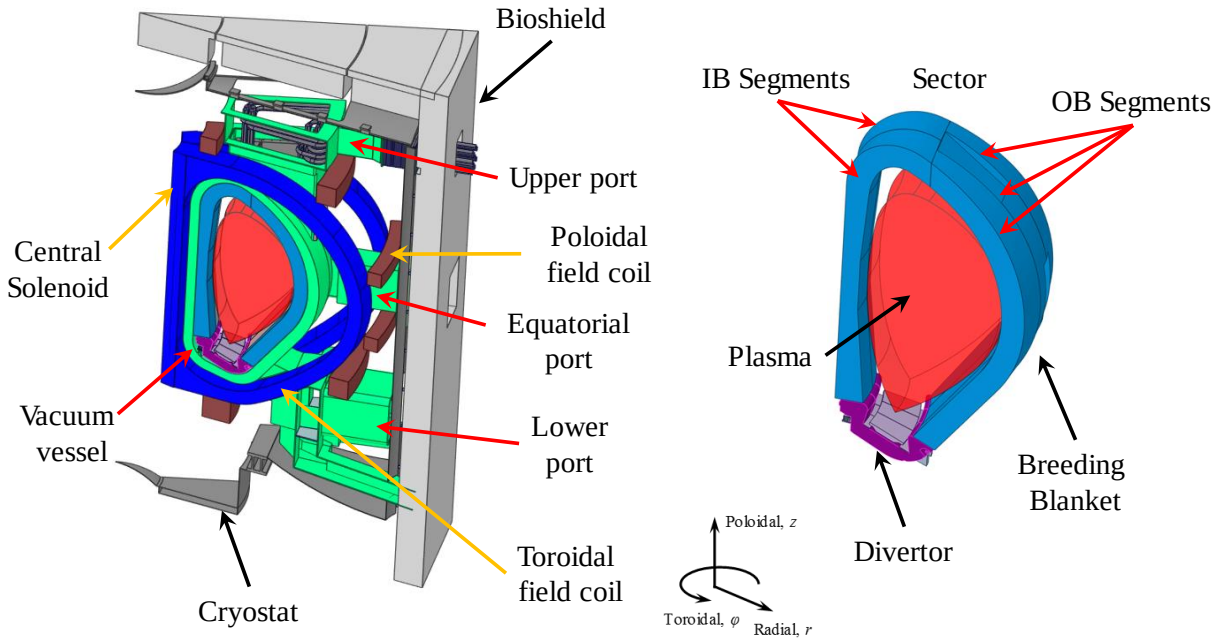

Figure 1-6: DEMO Baseline 2017 configuration with details of the main components

The EU-DEMO baseline 2017 is based on a single-null divertor configuration where the plasma facing components are covered with tungsten similarly to the FW. Moreover, the analysed baseline includes also the adoption of limiters as FW protection strategy against some plasma transients which can damage its integrity. As concerns the structural material to be used for the BB, it is currently planned to adopt the 9Cr-1WVTa Reduced Activation Ferritic-Martensitic steel (Eurofer 97) with a 20 dpa damage limit and conservative design margins [22, 28]. Instead, for the VV the AISI ITER-grade 316 has been selected. The VV represents the first confinement barrier and it plays a pivotal role in the safety design of the DEMO

reactor considering the paramount goal to ensure the inherent passive resistance to any incidents and to avoid the need of evacuation in the worst incident case.

Lastly, concerning the pulsed operation of DEMO, which represents a significant challenge to the design of its heat transfer and conversion system, it has been foreseen to have a plasma pulse of 2 hours with a dwell time of 10 minutes.

1.3 The EU-DEMO Helium-Cooled Pebble Beds Fusion Reactor and its Relevant Systems: a short introduction

As a key part of the Roadmap to Fusion Electricity in Europe [10], the EU is conducting since 2014 the so-called Pre-Conceptual Design (PCD) phase to lay the technical foundation for the EU DEMO fusion reactor [28]. The goal of the PCD is to explore different possible design options until its conclusion in 2020 when the most promising solutions will be adopted for the successive steps of the Roadmap. Indeed, concerning the BB, four blanket concepts were originally considered in the PCD phase covering all the possible technologies that are believed encouraging for DEMO. These included the two helium-cooled concepts (Helium Cooled Lithium Lead – HCLL, - which uses molten lithium lead as breeder/neutron multiplier and Helium-Cooled Pebble Beds – HCPB, which adopts solid ceramic breeder/neutron multiplier), the Water-Cooled Lithium-Lead (WCLL) conceived with molten lithium lead as breeder/neutron multiplier and, lastly, the Dual-Coolant Lithium-Lead (DCLL) using helium and liquid breeder/neutron multiplier which also serves as coolant.

Nonetheless, the recognition of the integration aspects' importance, especially those related to the choice of the breeding blanket coolant, which affect the whole DEMO plant [23], have motivated a critical re-evaluation of the technical choices for the DEMO BB focusing on the two concepts: namely the HCPB and WCLL. These concepts allow to investigate a broad range of breeder and multiplier materials as well as to cover the cooling solutions. In this dissertation, for the sake of brevity, we will focus on the HCPB concept that is hereafter described in detail.

In this regards, the HCPB concept has been investigated in all major past EU studies, since the NET Program during 1990-1999 [29], to the Power Plant Conceptual Studies (PPCS) during 2000-2004 [5] and the DEMO studies in 2005-2007 [30]. Several design iterations have thus been considered to get closer to a workable solution. The current HCPB BB design is based on a Single Module Segment (SMS) configuration which is shown in Figure 1-7. It offers a better structural integrity respect to the Multi Module Segment (MMS) previously studied [31].

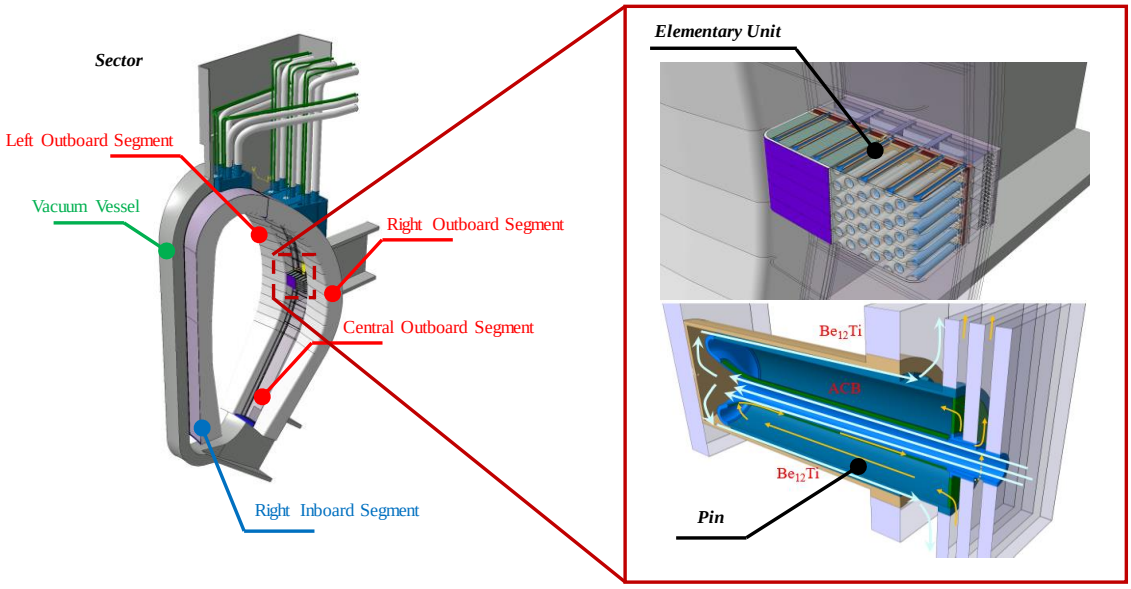

Figure 1-7: HCPB DEMO Single Module Segment configuration

The main innovative feature of such a configuration is the breeding zone architecture which resembles the fission structure being based on a fuel-pins arrangement [31]. Further information about the HCPB-BB and its associate relevant systems, being studied in this dissertation, will be provided in the following paragraphs.

1.3.1 The Solid Breeding Blanket Solution

The enhanced HCPB architecture proposed for the DEMO baseline 2017 is based on an arrangement of the so-called fuel-breeder pins, where there are two concentric tubes, forming the inner and outer cladding, filled with an advanced pebble bed of a solid solution of Li_4SiO_4 and Li_2TiO_3 called KArlsruhe Lithium OrthoSilicate (KALOS). The claddings are joined at the front of the pin (near the plasma side) by a reversed funnel giving a pen-like shape to this section. The fuel-breeder pins are inserted inside a pressure tube, which joins the FW with the BZ backplate and acts as structural elements against a pressurization during an accidental coolant ingress inside the BZ. The FW is a 20 mm-thick U-shaped and actively cooled plate facing the plasma, which incorporates a 2 mm thick W armor as sacrificial layer against plasma erosion from fast particles. The $Be_{12}Ti$ (Beryllide) has been adopted as neutron multiplier due to its positive neutronic and safety characteristics. The Beryllide is in form of hexagonal prismatic blocks with a central bore where the pins are located, see Figure 1-8. The tritium produced in both KALOS and $Be_{12}Ti$ is extracted and transported out of each segment using helium as purge gas with an addition of 0.1%wt. H_2 and at an operative pressure of 0.2 MPa. The purge gas enters firstly to the $Be_{12}Ti$ prismatic blocks and sweeps them from the top down, while in a second step, it enters into the pins (all connected in parallel), flushing the KALOS beds from the BZ backplate to their front to be then collected towards the outlet manifold.

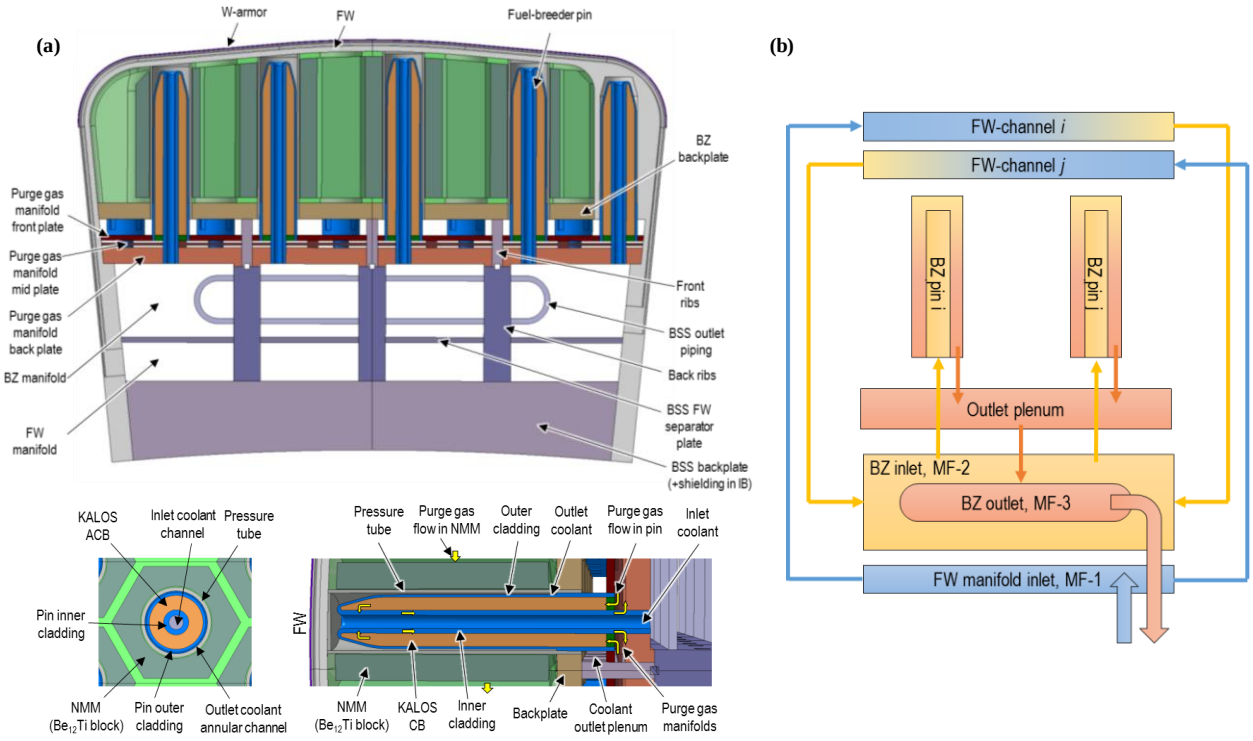

Figure 1-8: Reference HCPB BB design (a) and schematic flow path (b).

Helium gas is used as coolant due to its neutronic and chemical inertness, providing an excellent neutron economy and a very good compatibility with the involved materials. It enters at 573.15 K and with an operating pressure of 8 MPa. It first flows from the FW inlet manifold (MF-1) to the FW cooling channels,

which are cooled in a counter flow arrangement to homogenize the temperature distribution. The coolant is then collected into the BZ inlet manifold (MF-2), where is distributed into the fuel pins. The coolant is then collected from the pins in the outlet plenum and redirected to the BZ outlet (MF-3), which is the outlet piping, at approximately 793.15 K [32-34].

1.3.2 The Balance of Plant Design Reference

As stated before, one of the main goal of the DEMO reactor is to produce several hundred MW of electricity in a safe and reliable way. To that end, the reactor design is strongly oriented to the Balance of Plant (BoP) which includes several systems working together to guarantee its efficient operation.

The system at the heart of the BoP is generally the Power Conversion System (PCS), to which the thermal power is delivered by the Primary Heat Transfer System (PHTS) in order to be converted in mechanical and then into electrical power respectively by means of the turbine and the alternator.

The BB-PHTS may be considered the core of the BoP considering that extracts the 80% of the total power generated in DEMO while the other 20% is released in the Divertor (Div) and Vacuum Vessel (VV) PHTSs [35, 36].

Furthermore, with the aim of softening the potential negative impact of plasma pulsing on the PCS equipment (especially the turbine), a configuration which foresees the use of an Intermediate Heat Transfer System (IHTS), equipped with an Energy Storage System (ESS), has been investigated for the BoP of DEMO. According to this configuration, during the pulsed operation the ESS collects a portion of the thermal energy transferred by the blanket in order to give it to the PCS during the dwell time; this device should therefore limit sharp changes in turbine load allowing pseudo steady-state working conditions both during pulse and dwell time, see Figure 1-9 [37, 38].

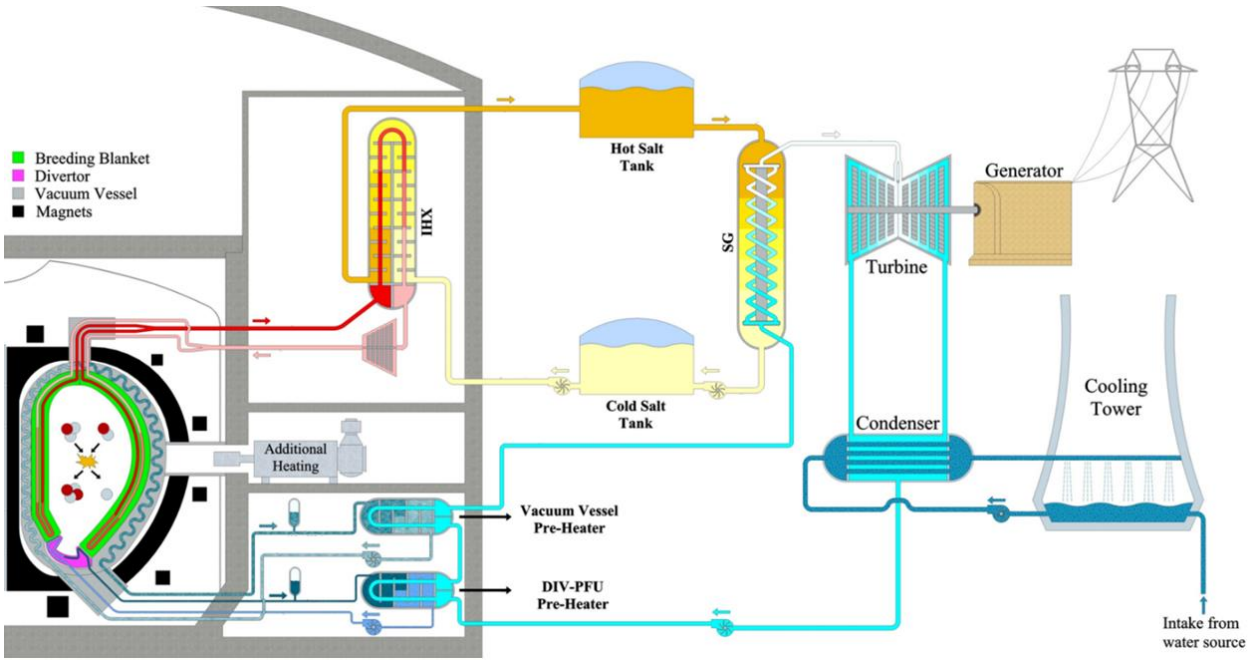

Figure 1-9: HCPB BoP conceptual scheme [35].

The ESS of the DEMO is an industrial 2-tanks design commonly used in concentrated solar power plants which uses HITEC molten salt [39] as heat transfer fluid because of its good thermal stability within the range of DEMO operative temperatures and its relatively low freezing point. This gives more margins to withstand normal and off-normal transients. The adoption of an ESS, where part of the thermal energy is accumulated as sensible heat, allows to operate the turbine at almost continuous load equal to about the 81% of the blanket power. However, since the energies of divertor and VV are not stored, the feed-water heat-up strategy foresees variable steam extractions from turbine and by-pass lines for divertor and VV heat

exchangers. This allows continuous plant operations and flexibility in the range of turbine power scale of ±20% limiting, at the same time, thermal transients inside the PCS caused by the DEMO pulsed operations.

The preliminary conceptual design of PCS for DEMO envisages a classical superheated steam Rankine cycle operating at about 58 bar with superheated steam at 718.15 K. It is equipped with steam generator, reheater - in between high and low pressure turbine stages heated by using a stream of hot molten salt -, deaerator, condenser and feed-water pre-heaters. The pre-heaters are of condensing type or single phase fluid in both tube and shell side. In particular, the latter are represented by the heat exchangers of divertor and VV PHTSs which are integrated in PCS as additional (low temperature) heat sources to improve system efficiency [40-42].

1.3.3 The Vacum Vessel and the Related Safety Systems

The DEMO VV, reported in Figure 1-10, has to fulfil several requirements, due to its design and constructional concept as well. It represents the first confinement barrier of the nuclear facility DEMO. It has also to be hermetically sealed maintaining high vacuum environment and it has to shield the superconducting magnets as well as the maintenance areas and the environment against neutron radiation. In addition, using tritium as fuel for the nuclear fusion reactions, it requires additional safety and material compatibility considerations [43].

The intended design of the DEMO VV is based on the concept chosen for the ITER VV. Presently it is foreseen to build the VV assembly with all the attached ports in stainless steel 316 L(N) which is already included in several nuclear code frameworks, e.g. RCC-MR Edition 2015. The VV is planned to be constructed as a double shell structure. A sufficient quantity of ribs for reinforcement are foreseen between the inner and outer shells. The properly dimensioned interspace is planned to be filled ≈55 Vol. % by steel plates and cooled by liquid water for neutron and radiation shielding. The VV is obliged to safely withstand any anticipated loading conditions, including earthquake, gravity, coolant pressure, and any combinations thereof [44].

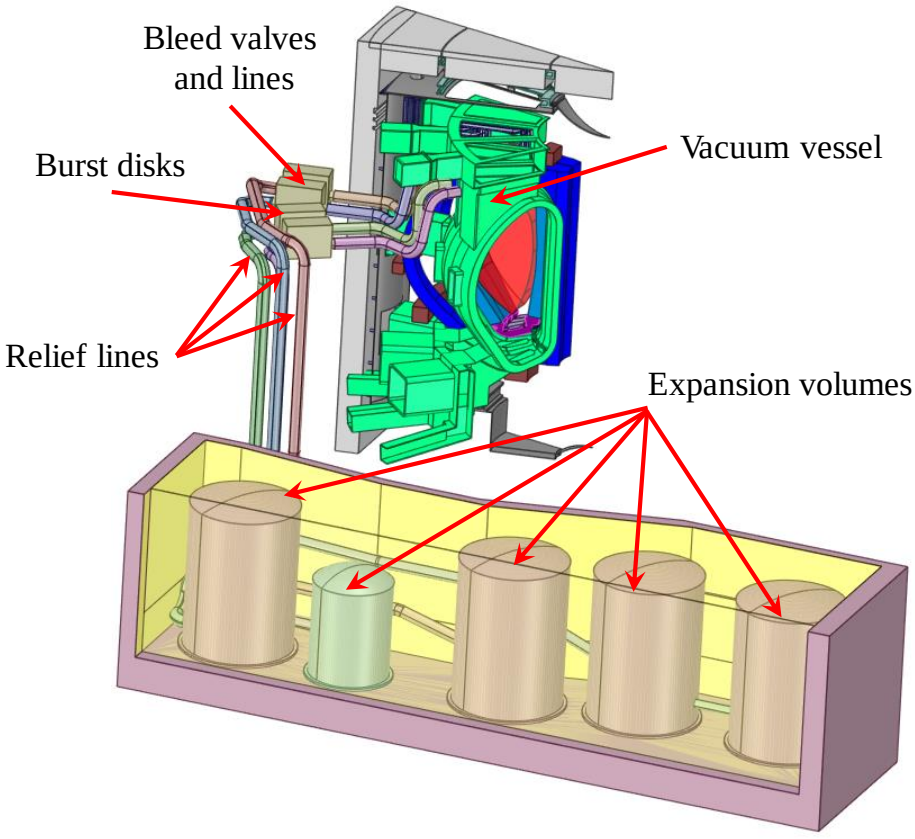

Figure 1-10: VVPSS layout.

The neutron heat received by the vessel is removed by water serving also as moderator to enhance its shielding capability. In order to avoid regular vessel baking cycles at 473.15 K and to reduce thermal expansion relative to the in-vessel components (IVCs), for the DEMO VV has been proposed to be cooled with water at 473.15 K and 3.15 MPa [22]. Currently, there are some studies to assess the possibility to maintain the VV temperature to ~ 313.15 K [44].

Moreover, since the licensing case will make maximum use of 'passive safety', so that the rupture of an in-vessel component such as a blanket will be managed mainly by passive devices (such as bursting discs and connected expansion vessels) to ensure the integrity of the primary confinement boundary [22].

According to the selected reference accident scenarios for DEMO reported in [45], one of the design basis accidents (DBAs) is the in-vessel Loss of coolant accident (in-vessel LOCA) due to a double ended guillotine break in the feeding pipes located inside the VV upper port which may determine a failure of the FW as well. Since the VV operates at very low pressure, any coolant release inside the VV (Ingress of Coolant Event – ICE) involves a pressure increase which should be kept below the design value (0.2 MPa as in ITER). To that end, it is foreseen to connect the VV to a Pressure Suppression System (VVPSS) by means of Burst Disks (BDs) which passively open when the differential pressure between the components reaches a certain value (0.15 MPa) allowing to withstand the overpressurizzation. Moreover, to avoid the rupture of the BDs for small leakages, the connection lines host Bleed Valves (BVs) which practically act as bypass of the BDs and they open at lower pressure setpoint (0.09 MPa).

1.4 Applications of Thermal-Hydraulic System Codes to EU-DEMO Helium-Cooled Pebble Beds Design and Accident Analyses

Thermal-hydraulics in fusion nuclear reactors is a very wide-ranging subject and includes diverse topics as: gravity-dominated stratified flow in pipes with a free surface including hydraulic jumps, momentum-driven critical flow through passages and restrictions, fluid-structure interactions (e.g. fluid jet impingement on structures), flow boiling and condensation, flow and heat transfer regimes, energy transfer to fluids and structures from nuclear sources, and a multitude of other phenomena. The study of these topics may range from one-dimensional to three-dimensional flow fields that interact with structures. Furthermore, for many of the scenarios which must be considered in nuclear reactors, important variables and phenomena change as a function of time.

Thermal-hydraulic analyses are governed not only by their boundary and initial conditions, but also by limiting values of important figures-of-merit which define maximum or minimum acceptable limits stemming from design/operational or safety requirements. Therefore the thermal-hydraulic analysis objectives may often be separated into two broad categories:

- Design: limits defined to ensure the plant design is robust and thus can operate economically with minimal shutdowns and operational costs and
- Safety: limits defined by law or regulatory rules which are specified to protect public health or living standards.

Thermal-hydraulic design analyses focus on creating nuclear systems and components which are robust and reliable, have a long and trouble-free lifetime, are efficient and economical to operate, do not tend to stray into unwanted transient scenarios leading to shutdowns that challenge equipment design limits, and are easy to inspect and maintain.

Since design analyses generally deal with normal steady state conditions and with the operational transients, such analyses are generally focused on non-safety grade equipment performance and phenomena that are known to affect plant efficiency, reliability, and long-term operations.

These thermal-hydraulic analyses rely on numerical analysis tools (sometimes used also for safety

analyses) such as: system analysis codes, fuel behaviour codes and containment performance evaluation tools, computational fluid dynamics (CFD), heat transfer numerical codes and many specialized thermal-hydraulic tools tuned for analysing specialized operational conditions.

On the other hand, thermal-hydraulic safety analyses focus on ensuring the fusion nuclear systems and components always operate with operational margins. This allows to apply the 'defence-in-depth' approach required by the regulatory agencies. The principle of defence-in-depth requires three levels of protection of public health and safety, as follows:

- Nuclear facilities are designed to not fail for the range of normal and abnormal conditions they might reasonably experience during their operating life, including extreme natural phenomena and man-made hazards;
- Redundant and diverse support systems are provided to detect initiating events or incipient failures and shut the reactor down before damage can occur following events within the design basis;
- Redundant and diverse emergency systems, including emergency cooling and containment systems, are provided to limit the release of radioactivity to the environment and thereby mitigate accident consequences if the first two levels of defence fail.

Since thermal-hydraulic safety analysis generally are used to assess the margin between calculated key figures-of-merit and their limits imposed by national law, the analysis tools have to a very rigorous protocol which is closely examined and monitored by the licensing authorities. Thermal-hydraulic tools used for safety analyses are created to study the behaviour of the nuclear system under very adverse transient conditions which may lead to radioactive products release.

Whether for the purposes of designing a nuclear system or demonstrating its safety, the investigation approach comply with the following steps:

- Identifying the nuclear reactor operational and accident envelopes,
- Isolating the key phenomena in each of the plant scenarios that comprise the operational conditions leading to an accidental scenario,
- Developing numerical models that accurately reproduce the behaviour of the key phenomena for the scenarios of interest,
- Assessing the numeric models to demonstrate their adequacy for the given scenarios calculating the nuclear reactor behaviour in a manner which can be trusted by the plant designers and regulatory authorities,
- Performing the calculations showing that the nuclear reactor meets the necessary design and licensing requirements.

Achieving the above mentioned goals, the thermal-hydraulic design is validated both from a design and safety point of view [46].

1.5 Motivation and goal of the Thesis

A complete investigation of the DEMO fusion reactor performances, under both steady state, operational and accidental transient conditions, is currently being promoted and supported within the EUROfusion action, paying attention to the Safety and Environmental (S&E) aspects which are, from the very beginning of conceptual design, the heart of the DEMO project. The favourable characteristics of fusion power in terms of low accident potential, good operational safety and minimal environmental impact provide a potential for excellent S&E performance. But to fully realise this potential the design has to incorporate safety provisions to minimize hazards and ameliorate the consequences of any abnormal operation or system failure.

Therefore, in view of the final development of DEMO fusion reactor it has to be considered as pivotal its ability to meet the safety objectives both for the equipment and the external environment. This ability

has to be proved by safety analysis that is a well-known and acknowledged tool for assessing the safety level of nuclear power plants.

The PhD research project finds its place within the framework of the Work Package Safety and Environment (WPSAE) of EUROfusion action, being mainly focussed on the theoretical-numerical investigation of the safety performances of the HCPB DEMO reactor system. In particular, the main objective of the research project has been to perform a realistic assessment of the DEMO reactor system thermal-hydraulic performances under steady state, operational and accidental transient conditions, selecting the most representative and critical accidental scenarios and evaluating their potential consequences in terms of plant failure providing proper feedback to designers for their mitigation.

Therefore, in order to have a realistic assessment of the DEMO reactor system thermal-hydraulic performances, the definition of an indirect coupling procedure of both 1D and 3D codes has been pursued. It integrates the system code aptitude to synthetically simulate the thermal-hydraulic performances of wide and complex energy transfer systems in presence of multi-components two-phase flows, with the highly realistic predictive potential guaranteed by 3D CFD codes in the assessment of the thermo-fluid dynamic behaviour of coolant flowing through newly conceived and deeply 3D circuits.

1.6 Organization of the Chapters

This thesis consists of five main chapters, as briefly described hereafter.

In Chapter 2, the theoretical background behind the integration methodology is described with particular focus to the basic laws at the heart of both 3-D and 1-D approaches.

The validation of the methodology adopted in analysing the DEMO thermal-hydraulic behaviour is reported in Chapter 3.

In Chapter 4, the thermal-hydraulic behaviour assessment of the DEMO reactor under normal operational conditions by using the developed methodology is reported. Particular efforts have been spent to identify a suitable strategy to assure the requirement of maintaining the blanket inlet temperature to about 573.15 K.

In Chapter 5, it has been assessed the reactor behaviour under the identified representative accidental scenarios to evaluate their consequences and suggesting a possible design modification to ameliorate its safety performances.

Finally, the main conclusions and outlooks for the future activities are summarised in Chapter 6. Additional details and information are reported in the Appendix.

2 Theoretical and Conceptual Framework for the Nuclear Fusion Thermal-Hydraulics Modeling

In this chapter, a brief overview of the main mathematical models adopted by both CFD and system codes is given. Attention has been paid to their numerical implementation for the purpose of clarifying the basis of the employed procedure. Indeed, due to the extreme complexity of the flow domain in DEMO, the research activity has been carried out following a theoretical-computational approach based on the finite volume method. In this regards, a suitable release of ANSYS CFX code and the RELAP5-3D thermal-hydraulic system code have been properly integrated, with the aim of adequately predicting the thermal-hydraulic phenomena occurring in the reactor.

2.1 Computational Fluid Dynamic Codes for Nuclear Energy Applications

Designing a safer and efficient nuclear reactor, whether it is a fission or fusion nuclear reactor, certainly involves many challenges considering their complex thermal-hydraulic behaviour which includes numerous deeply 3D components. The main objective of thermal-hydraulic analysis of reactors is to figure out whether the coolant could take properly away the heat under steady and transient conditions ensuring the integrity of the components. Some studies can be aimed just at optimizing the thermal-hydraulic behaviour of its components as well.

In the past years, several system codes (RELAP5, TRACE, CATHARE and etc.) had been developed for the analysis of integral thermal-hydraulic feature; they are generally based, as will be highlighted in §2.2, on a lumped and one dimensional model or simplified pseudo-multi-dimensional model [47-49]. These system codes allow the evaluation of thermal-hydraulic features in one-dimensional or simplified pseudo-multi-dimension taking also the influence of the geometrical parameters into consideration. However, the codes mentioned above do not have the capability to obtain a comprehensive and systematic overview of 3D parameters in nuclear reactor.

Nevertheless, considering their numerical limitation, in nuclear thermal fluid problems 3D CFD codes were developed mainly for the quantification of parametric study [46]. Indeed, it is only in recent years that a rigorous research related to the validations of CFD had been pursued by comparing representative benchmarks and utilizing some specially developed guidelines, which has also promoted a wider application of CFD codes in the field of nuclear engineering [50]. In fact, the bibliographic research done has shown that just specific 3D thermal-hydraulic features and in some key equipment, namely the reactor pressure vessel and steam generator, have been analysed by means of CFD codes [51{Cong, 2014 #109, 52-55]. In particular, the flow field in downcomer, lower plenum and in the reactor core were thoroughly analysed with the application of several CFD codes (ANSYS FLUENT, CFX, STAR-CD, etc.); although mention should be made of some attempts to study the whole primary circuit of a fission nuclear reactor which encourage their application to broader problems even if within certain constrains [56]. Thus, given the complexity of nuclear reactor geometries and constraint of computer's capacity, it would be difficult to perform 3D simulation based on microscopic mesh. Since billions of grids are required in the microscopic mesh to model all the reactor components, the approach would consume considerable computing resource and time.

Hence, considering also the need to obtain a realistic prediction of the thermal-hydraulic behaviour of the DEMO reactor and its relevant systems, an integrated procedure considering both ANSYS CFX and RELAP5-3D system code aptitudes has been developed. The integral approach methodology is explained in §2.3 immediately after a general overview of the fundamental equations underlying the procedure.

2.1.1 Computational Fluid Dynamics: Fundamental Physical Laws

The development of an analytical description of fluid flow is based upon the expression of the physical

laws related to fluid flow in a suitable mathematical form. The dynamic behaviour of a fluid from a macroscopic point of view is described by Navier-Stokes equations complemented by a set of boundary and initial conditions or by the state equation in case of gas mixture. There are three fundamental physical laws that, with the exception of relativistic and nuclear phenomena, apply to each and every flow independently of the nature of the fluid under consideration. These laws are the principle of mass conservation (continuity equation), the second principle of dynamics (balance of momentum) and first principle of thermodynamics (energy conservation). In a Lagrangian framework, suitable for deriving conservation laws, consider the fluid control volume V_T enclosed by a surface St and located in a fluid flow field as depicted in Figure 2-1.

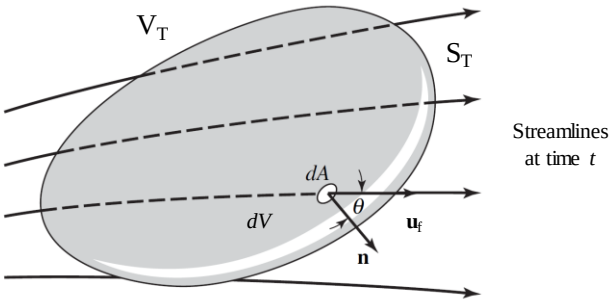

Figure 2-1: Fluid flow through a control volume V_T.

The three fundamental laws previously disclosed are:

- The law of conservation of mass: $\iint_{S_T} \rho(\mathbf{u}_f \cdot \mathbf{n})dS + \frac{\partial}{\partial t}\iiint_{V_T} \rho dV = 0$,
- The Newton's second law of motion: $\sum \mathbf{F} = \iint_{S_T} \mathbf{u}_f \rho(\mathbf{u}_f \cdot \mathbf{n})dS + \frac{\partial}{\partial t}\iiint_{V_T} \rho \mathbf{u}_f dV$,
- The first law of thermodynamics: $\frac{\delta Q}{dt} - \frac{\delta W}{dt} = \iint_{S_T} e\rho(\mathbf{u}_f \cdot \mathbf{n})dS + \frac{\partial}{\partial t}\iiint_{V_T} e\rho dV$,

where ρ is the density of the fluid contained in the volume V_T at time t, $\Sigma\mathbf{F}$ is the result of external forces acting on the system, Q is the heat supplied to the system and W is the work performed by the system. In the case of a system consisting of a fluid in motion, the total energy E represents the sum of the potential energy U and kinetic energy K. If it is indicated with u_f the fluid velocity, with e its specific energy and with e_{tot} the total specific energy, sum of the two contributions:

$$\mathbf{e}_{tot} = \mathbf{e} + \frac{|\mathbf{u}_f|^2}{2} \tag{2.1}$$

Hence, they can be re-arranged [57] in:

$$\frac{\partial}{\partial t}\iiint_{V_T} \rho dV = \iiint_{V_T} \left[\frac{\partial \rho}{\partial t} + \nabla \cdot (\rho \mathbf{u}_f)\right] dV = 0 \tag{2.2}$$

$$\frac{\partial}{\partial t}\iiint_{V_T} \rho \mathbf{u}_f dV = \iiint_{V_T} \left[\frac{\partial \rho \mathbf{u}_f}{\partial t} + \nabla \cdot (\rho \mathbf{u}_f \times \mathbf{u}_f)\right] dV = \sum \mathbf{F} \tag{2.3}$$

$$\frac{\partial}{\partial t}\iiint_{V_T} \rho e_{tot} dV = \iiint_{V_T} \left[\frac{\partial \rho e_{tot}}{\partial t} + \nabla \cdot (\rho e_{tot} \mathbf{u}_f)\right] dV = \frac{\delta Q}{dt} - \frac{\delta W}{dt} \tag{2.4}$$

The (2.2) practically states that:

$$\frac{\partial \rho}{\partial t} + \nabla \cdot (\rho \mathbf{u}_f) = 0 \tag{2.5}$$

which is the differential form of the equation of conservation of mass. As regards the Newton's second law (2.3), the sum of the forces $\Sigma\mathbf{F}$ acting on the volume is due both to the volume and surface forces. The latter is the result of the integral of the stresses on the surface S_t. Considering the generic i-th component of $\Sigma\mathbf{F}$, it is possible to write:

$$F_i = \iiint_{V_T} \rho g_i dV + \iint_{S_T} \sigma_{ij}^f n_j dS \tag{2.6}$$

where g_i is a volumetric force per unit mass in the direction x_i, namely an acceleration, and σ_{ij}^f is the fluid stress tensor. The stress tensor is composed of two terms: the static one ($-p\delta_{ij}$) due to normal stresses with the same intensity in the three directions (i.e. pressure), and the dynamic (τ_{ij}) due to the fluid motion. For a Newtonian fluid, the dynamic term (τ_{ij}) is expressed through the (2.7) [58]:

$$\tau_{ij} = \mu_f \left(\frac{\partial u_i}{\partial x_j} + \frac{\partial u_j}{\partial x_i} - \frac{2}{3} \frac{\partial u_S}{\partial x_S} \delta_{ij} \right) \tag{2.7}$$

where μ_f is the fluid viscosity and δ_{ij} is the Kronecker delta. Therefore the fluid stress tensor σ_{ij}^f is defined as follows:

$$\sigma_{ij}^f = -p\delta_{ij} + \mu_f \left(\frac{\partial u_i}{\partial x_j} + \frac{\partial u_j}{\partial x_i} - \frac{2}{3} \frac{\partial u_S}{\partial x_S} \delta_{ij} \right) \tag{2.8}$$

Applying to the (2.6)(2.6) the theorem of divergence and substituting the definition of stress tensor (2.8) as well as the (2.7), it is possible to write

$$F_i = \iiint_{V_T} \left\{ \rho g_i - \frac{\partial p}{\partial x_i} + \frac{\partial}{\partial x_j} \left[\mu_f \left(\frac{\partial u_i}{\partial x_j} + \frac{\partial u_j}{\partial x_i} - \frac{2}{3} \frac{\partial u_S}{\partial x_S} \delta_{ij} \right) \right] \right\} dV \tag{2.9}$$

Substituting the expression (2.9) in (2.3) and considering that it has to be satisfied for any volume V_t, the momentum equations, or Navier-Stokes equations, can be written as follows:

$$\frac{\partial \rho u_i}{\partial t} + \frac{\partial \rho u_i u_j}{\partial x_j} = \rho g_i - \frac{\partial p}{\partial x_i} + \frac{\partial}{\partial x_j} \left(\mu_f \left(\frac{\partial u_i}{\partial x_j} + \frac{\partial u_j}{\partial x_i} - \frac{2}{3} \frac{\partial u_S}{\partial x_S} \delta_{ij} \right) \right) \tag{2.10}$$

Concerning the energy equation (2.4), two contributions have to be taken into account: the volumetric heating, which for the systems we are considering is due to the adsorption/emission of radiation and the heat transfer across the volume surface S_t generated by a temperature gradient. With regards to the first term and considering that the mass of the moving fluid element is ρdV, the heating power associate with the fluid volume is $\rho \dot{q} dV$, where $\dot{q}$ is the specific heating power, so that the product $\rho \dot{q}$ is the volumetric density of heating power q_g'''. Concerning the second contribution and with respect to an isotropic fluid, the heat flux $\mathbf{q}''$ can be expressed according to the Fourier's law: $\mathbf{q}'' = -\lambda \nabla T$ where λ is the thermal conductivity and ∇T the temperature gradient. Therefore, the incoming thermal power through the surface S_t can be written as:

$$\frac{\delta Q}{dt} = \iiint_{V_T} q''' dV + \iint_{S_T} \lambda \nabla T \cdot \mathbf{n} dS = \iiint_{V_T} q''' dV + \iint_{S_T} \lambda \frac{\partial T}{\partial x_j} n_j dS \,. \tag{2.11}$$

Regarding the work done by the control volume V_t, it is possible to write:

$$\frac{\delta W}{dt} = -\iiint_{V_T} \rho g_i u_i dV - \iint_{S_T} \sigma_{ij} n_j u_i dS\,, \tag{2.12}$$

where the first term on the right side is the volumetric forces while the second term the surface ones.

Using the divergence theorem for the (2.11) and (2.12), substituting the (2.8), (2.11) and (2.12) in (2.4) and remembering the expression must be verified for any V_t, the first principle of Thermodynamics for a fluid in motion written in a differential form becomes:

$$\left[\frac{\partial \rho e_{tot}}{\partial t} + \frac{\partial \rho e_{tot} u_j}{\partial x_j}\right] = q''' + \frac{\partial}{\partial x_j}\left(\lambda \frac{\partial T}{\partial x_j}\right) + \frac{\partial}{\partial x_j}\left(u_i \mu_f \left(\frac{\partial u_i}{\partial x_j} + \frac{\partial u_j}{\partial x_i} - \frac{2}{3}\frac{\partial u_S}{\partial x_S}\delta_{ij}\right)\right) + \rho g_i u_i \tag{2.13}$$

The expression (2.5), (2.10) and (2.13) represents respectively the conservation equations of mass, momentum and energy transfer. Since they can be analytically solved only in a limited range of simple cases, they are generally discretized and solved numerically.

Additionally, the CFD codes allow to solve other equations in order to describe other processes (i.e. combustion or diffusion of scalar quantities) as well as to use approximating models, such as the ones devoted to describe turbulence phenomena.

The general form of the transport equation for an additional scalable variable Φ is:

$$\frac{\partial(\rho\Phi)}{\partial t} + \frac{\partial(\rho u_i \Phi)}{\partial x_i} = \frac{\partial}{\partial x_i}\Gamma\frac{\partial \Phi}{\partial x_i} + S_\Phi \tag{2.14}$$

where Γ is the diffusivity and SΦ the variable source.

The transport equations must be coupled with constitutive equations of state for density and for enthalpy, so to form a closed system. State equations are characterised by the general form:

$$\rho = \rho(p,T) \quad \text{and} \quad c_p = c_p(p,T) \tag{2.15}$$

Basically, the form of the state equations depend on the fluid type. For example, for incompressible fluids, density is constant and cp is at most a function of temperature: $\rho = \rho_{const}$ and $c_p = c_p(T)$. For an ideal gas, as can be considered the helium coolant at the operative conditions in our DEMO system, c_p is at most a function of temperature and density is calculated from the ideal gas law:

$$\rho = \frac{w\, p_{abs}}{R_0 T} \tag{2.16}$$

where w is the molecular weight, p_{abs} is the absolute pressure and R_0 is the universal gas constant.

2.1.2 Methodological Apsects – Adopted Turbolence Model

Turbulent flows behaviour might be directly described by the conservation equations. Nevertheless, since they are characterised by many length and time scales phenomena, prohibitively fine meshes should be set-up in order to describe them effectively.

Consequently, statistical turbulence models have been developed. In these models, each variable describing a turbulent flow is considered as the sum of a fluctuating component and an average (smoothly varying) component. For example, velocity along the i-th direction may be decomposed as follows:

$$u_i = \bar{u}_i + u'_i \tag{2.17}$$

into a time varying component (u'_i) and an average component ($\bar{u}_i$). The latter is obtained as:

$$\bar{u}_i = \frac{1}{\Delta t}\int_t^{t+\Delta t} u_i\, dt \tag{2.18}$$

where Δt is a time scale that is large if compared to turbulent fluctuations, but small if compared to the

analysed transient time scale.

Introducing this division in averaged and fluctuating quantities inside the original Navier-Stokes equations in equation (2.10) and time averaging these equations, the Reynolds Averaged Navier-Stokes (RANS) equations are obtained:

$$\frac{\partial\left(\rho\bar{u}_i\right)}{\partial t}+\frac{\partial\left(\rho\bar{u}_i\bar{u}_j\right)}{\partial x_j}=-\frac{\partial\bar{p}}{\partial x_i}+\frac{\partial}{\partial x_j}\left[\mu\left(\frac{\partial\bar{u}_i}{\partial x_j}+\frac{\partial\bar{u}_j}{\partial x_i}\right)\right]-\frac{\partial\left(\rho\overline{u'_i u'_j}\right)}{\partial x_j}+\rho g_i \tag{2.19}$$

Once deriving the RANS equations, their system needs to be closed, since Reynolds stresses, defined as $-\rho\overline{u'_i u'_j}$, have introduced new variables.

The closure relations used to evaluate the additional Reynolds stresses define the type of turbulence model. Specifically, RANS turbulence models can be broadly divided into two classes: eddy viscosity models, briefly described in the following, and Reynolds stress models, not addressed in this dissertation foe the sake of brevity.

The eddy viscosity turbulence models are based on the assumption that in a turbulent flow small eddies are continuously forming and dissipating and that Reynolds stresses can be considered proportional to mean velocity gradients. The following equation illustrates the "eddy viscosity hypothesis", highlighting the relationship between Reynolds stresses and mean velocity gradients as well as μ_t, which represents the turbulent viscosity (also called eddy viscosity):

$$-\rho\overline{u'_i u'_j}=-\frac{2}{3}\rho k\delta_{ij}+\mu_t\left[\left(\frac{\partial\overline{u_i}}{\partial x_j}+\frac{\partial\overline{u_j}}{\partial x_i}\right)-\frac{2}{3}\delta_{ij}\frac{\partial\overline{u_k}}{\partial x_k}\right] \tag{2.20}$$

where k is the turbulent kinetic energy, defined as:

$$k=\frac{1}{2}\overline{u'^2_i} \tag{2.21}$$

Substituting equation (2.20) into the RANS equations of equation (2.19), they become:

$$\frac{\partial\left(\rho\bar{u}_i\right)}{\partial t}+\frac{\partial\left(\rho\bar{u}_i\bar{u}_j\right)}{\partial x_j}=-\frac{\partial p}{\partial x_i}+\frac{\partial}{\partial x_j}\left[\left(\mu+\mu_t\right)\left(\frac{\partial\bar{u}_i}{\partial x_j}+\frac{\partial\bar{u}_j}{\partial x_i}\right)\right]+\rho g_i \tag{2.22}$$

where:

$$p=\bar{p}+\frac{2}{3}\rho k+\frac{2}{3}\left(\mu+\mu_t\right)\frac{\partial\overline{u_k}}{\partial x_k} \tag{2.23}$$

Likewise, the Reynolds averaged energy equation and the generic Reynolds averaged transport equation may be expressed respectively as:

$$\frac{\partial\left(\rho\, c_p\,\bar{T}\right)}{\partial t}+\frac{\partial\left(\rho\,\bar{u}_i\, c_p\,\bar{T}\right)}{\partial x_i}=\frac{\partial}{\partial x_i}\left[\left(\lambda+c_p\frac{\mu_t}{\sigma_t}\right)\frac{\partial\bar{T}}{\partial x_i}\right]+\bar{q}''' \tag{2.24}$$

$$\frac{\partial\left(\rho\bar{\Phi}\right)}{\partial t}+\frac{\partial\left(\rho\overline{u_i}\overline{\Phi}\right)}{\partial x_i}=\frac{\partial}{\partial x_i}\left[\left(\Gamma+\frac{\mu_t}{\sigma_t}\right)\frac{\partial\bar{\Phi}}{\partial x_i}\right]+S_\Phi \tag{2.25}$$

where σ_t is the Prandtl turbulent number. In their turn, the eddy viscosity models can be distinguished by the way eddy viscosity (μ_t) is derived. Among them, the two-equation turbulence models are widely used, since they offer a good compromise between numerical effort and computational accuracy.

In particular, the k-ε and the k-ω two-equation models define the turbulent viscosity as the product of a

turbulent velocity and turbulent length scale. In two-equation models, the turbulence velocity scale is computed from the turbulent kinetic energy, which is provided from the solution of its transport equation. The turbulent length scale is estimated from two properties of the turbulence field. The k-ε model introduces two new variables into the system of equations. The turbulence kinetic energy, k, it is defined as the variance of the fluctuations in velocity, as shown in equation (2.21), and it has the dimensions of ($L^2\ T^{-2}$). Whilst, ε is the rate at which the velocity fluctuations dissipate (the turbulence eddy dissipation) and has dimensions of k per unit time ($L^2\ T^{-3}$).

An alternative to the ε-equation is the ω-equation as developed by Wilcox [59]. The ω-equation has significant advantages near the surface and accurately predicts the turbulent length scale in adverse pressure gradient flows, leading to improved wall shear stress and heat transfer predictions. Furthermore, the model has a very simple low-Re formulation, which does not require additional non-linear wall damping terms like it is the case for low-Reynolds (low-Re) k-ε models. However, the main deficiency of the standard k-ω model is the strong sensitivity of the solution to free stream values for ω outside the boundary layer. In order to avoid this problem, an optimally formulated two-equation model, the Shear-Stress-Transport (SST) model has been proposed by Menter [60] and it is extensively used in a wide range of applications, such as the design of the DEMO BB [61]. The SST model combines the k-ω model near the wall and the k-ε model away from the wall as a unified two-equation turbulence model. The SST model has been proposed in [60] has been adopted for the analysis reported in this dissertation.

In combination with the SST model, ANSYS CFX offers also an improved near wall treatment, which gradually switches from a classical low-Re formulation on fine grids to a log-wall function formulation on coarser meshes. This automatic switch of the wall function formulation reduces the stringent grid resolution requirements of the standard low-Re number turbulence models: this is essential for a successful application of the method to the complex flows considered in this work, where a fine near wall grid can usually not be ensured for all walls in the domain. Another important element which needs to be considered is the heat transfer predictions is the transition from laminar to turbulent flow. Indeed, the transition process can have an important effect on the wall temperature distribution of components where low-Re numbers are observed. Usually, the simulations are carried out as "fully turbulent", but there can be a substantial portion of laminar flow with significantly lower heat transfer rates. However, the SST turbulence in its original formulation [62], gives more accurate predictions being also less sensitive to grid variations in the assessment test performed. To recap, the SST model combines the advantages of the k-ε and k-ω models achieving an optimal model formulation for a wide range of applications. To that end, a blending function F_1 has been introduced which is equal to one near the solid surface and equal to zero for the flow domain away from the wall. So, it activates the k-ω model in the near wall region and the k-ε model for the rest of the flow.

This approach allows to use the attractive near-wall performance of the k-ω model without the potential errors resulting from the free stream sensitivity of the model. In addition, the SST model also features a modification of the definition of the eddy viscosity via the Prandtl-Kolmogorov relation, which can be interpreted as a variable c_μ, while c_μ in the k-ε model is constant. This modification is required to accurately capture the onset of separation under pressure gradients. The modelled equations for the turbulent kinetic energy k and the turbulence frequency ω are as follows:

$$\frac{\partial(\rho k)}{\partial t}+\frac{\partial\left(\rho\overline{u_i}k\right)}{\partial x_i}=\frac{\partial}{\partial x_i}\left[\left(\mu+\frac{\mu_t}{\sigma_k}\right)\frac{\partial k}{\partial x_i}\right]+\tilde{P}_k-\beta^*\rho\omega k \tag{2.26}$$

$$\frac{\partial(\rho\omega)}{\partial t}+\frac{\partial\left(\rho\overline{u_i}\omega\right)}{\partial x_i}=\frac{\partial}{\partial x_i}\left[\left(\mu+\frac{\mu_t}{\sigma_\omega}\right)\frac{\partial\omega}{\partial x_i}\right]+\frac{\alpha}{\nu_t}P_k-\beta\rho\omega^2+2(1-F_1)\rho\sigma_\omega\frac{1}{\omega}\frac{\partial k}{\partial x_i}\frac{\partial\omega}{\partial x_i} \tag{2.27}$$

where the blending function F_1 is calculated from:

$$F_1 = \tanh(\arg_1^4) \tag{2.28}$$

$$\arg_1 = \min(\max(\frac{\sqrt{k}}{\beta^* \omega y}; \frac{500\upsilon}{y^2 \omega}); \frac{4\rho\sigma_{\omega 2} k}{CD_{k\omega} y^2}) \tag{2.29}$$

$$CD_{k\omega} = \max(2\rho\sigma_{\omega 2} \frac{1}{\omega} \frac{\partial k}{\partial x_i} \frac{\partial \omega}{\partial x_i}); 1.0e-10) \tag{2.30}$$

The turbulent viscosity is then calculated as:

$$\mu_t = \min(\frac{\rho k}{\omega}; \frac{a_1 \rho k}{SF_2}) \tag{2.31}$$

with the constant $a_1 = 0.31$ and the blending function F_2 obtained from:

$$F_2 = \tanh(\arg_2^2) \tag{2.32}$$

$$\arg_2 = \max(2\frac{\sqrt{k}}{\beta^* \omega y}; \frac{500\upsilon}{y^2 \omega}) \tag{2.33}$$

The other coefficients and further information about the blending functions can be found in [60, 63].

The SST turbulence model requires an algebraic formulation for the treatment of the energy equation near the wall linking temperature and heat flux. The formulation used is:

$$\Theta^+ = \Pr y^+ e^{-\Gamma} + [2.12 \ln(1 + y^+) + \beta(\Pr)] e^{-1/\Gamma} \tag{2.34}$$

where:

$$\beta(\Pr) = (3.85 \Pr^{1/3} - 1.3)^2 + 2.12 \ln(\Pr) \text{ and } \Gamma = \frac{0.01(\Pr y^+)^4}{1 + 5 \Pr^3 y^+} \tag{2.35}$$

The non-dimensional temperature is defined as:

$$\Theta^+ = \frac{T_w - T}{T_\tau} \text{ with } T_\tau = \frac{q_w}{\rho c_p u_\tau} \tag{2.36}$$

Regarding the near wall treatment, in the SST model the near wall boundary condition exploits the simple and robust near wall formulation of the k-ω model and switches automatically from a low-Reynolds number formulation to a wall function treatment based on the grid density [64]. A blending function depending on y^+ is used. The solutions for ω in the linear and the logarithmic near-wall region are:

$$\omega_{Vis} = \frac{6\nu}{0.075 y^2} \text{ and } \omega_{log} = \frac{u_\tau}{0.3\kappa y} \tag{2.37}$$

They can be re-formulated in terms of y+ and a smooth blending can be performed:

$$\omega_1(y^+) = \sqrt{\omega_{Vis}^2(y^+) + \omega_{log}^2(y^+)} \tag{2.38}$$

A similar formulation is used for the velocity profile near the wall:

$$u_\tau^{Vis} = \frac{u_1}{y^+} \text{ and } u_\tau^{log} = \frac{u_1}{\frac{1}{\kappa} \ln(y^+) + C} \tag{2.39}$$

with

$$u_\tau = \sqrt[4]{(u_\tau^{Vis})^4 + (u_\tau^{log})^4} \tag{2.40}$$

This formulation gives the relation between the velocity near the wall and the wall shear stress.

Notwithstanding most fluid mechanics application deals with smooth surfaces, wall roughness can be encountered in a wide variety of situations. For example, it has been foreseen to equip the HCPB DEMO FW with ribs or by using surface with a properly augmented roughness (300 μm at special places) aimed at ameliorating the heat transfer capability of such a component [32]. Thus, to better predict the fluid flow behaviour over a rough surface it becomes pivotal to adopt a turbulence model with a suitable near wall treatment. The engineering approach adopted in predicting the flow where rough surfaces are involved is the so-called equivalent sand grain approach. It consists of two parts: on the one hand, some correlations are used to characterize the surface by the sand grain height. On the other hand, this sand grain roughness height is introduced as a new parameter in the turbulence model to enhance turbulence in the wall region, increase the momentum transport toward the wall and reproduce the drag increase. Three different roughness regimes have been identified: (i) the 'aerodynamically smooth' regime where the roughness elements are embedded in the viscous sublayer, so that the friction drag is not modified; (ii) the 'fully rough' regime where the friction drag significantly increases. This roughness effect is independent of the Reynolds number, namely is no longer a viscous effect. The drag increase is only due to pressure forces on the roughness elements. And then, there is the 'transition' regime in between the first two, where both viscous and pressure forces on the roughness elements contribute to the drag.

A key parameter to characterize the roughness effects is the non-dimensional roughness height:

$$k_s^+ = \frac{k_s u_\tau}{\mu} \tag{2.41}$$

where k_s is the roughness element height or the equivalent sand grain, $u_\tau = \sqrt{(\tau_w/\rho)}$ the friction velocity based upon the wall shear stress and density and μ the viscosity. It must be noted that the equivalent sand grain roughness is a concept relating any rough surface to the sand grain size which yields the same drag increase in the fully rough regime.

Near the wall, the flow is highly perturbed by the presence of the roughness elements so that three to five roughness heights above the surface is needed to retrieve a flow, which is locally homogeneous in planes parallel to a reference surface and no longer depends upon the location of the roughness elements. This region, strongly affected by the exact location of the roughness elements is called the roughness sublayer. Above it, the main flow characteristics are similar to those over a smooth surface, once scaled by the increased friction level. Practically, above the roughness sublayer the logarithmic law is preserved but shifted, as can be derived from the following law:

$$u^+ = \frac{1}{\kappa}\ln y^+ + C - \Delta u^+ \quad \text{with} \quad u^+ = \frac{u}{u_\tau} \quad \text{and} \quad y^+ = \frac{y u_\tau}{\mu} \tag{2.42}$$

There are several relations to evaluate this velocity shift Δu^+ [60]. It is common practice to correct the turbulence models to account for the wall roughness modifying only the specific dissipation. The correction in the SST turbulence model is based on the consideration that a shift Δu^+ of the velocity profile can be obtained by imposing as wall conditions for the flow over a rough surface the solution given by the model over a smooth surface at a distance from the wall where the velocity is equal to the desired velocity shift Δu^+. Essentially, the correction resort to the following statements:

$$k_w^+ = \max(0; k_0^+) \tag{2.43}$$

$$k_0^+ = \frac{1}{\sqrt{\beta^*}} \tanh\left[\left(\frac{\ln \frac{k_s^+}{30}}{\ln 10} + 1 - \tanh \frac{k_s^+}{125}\right) \tanh \frac{k_s^+}{125}\right] \tag{2.44}$$

$$\omega_w^+ = \frac{300}{k_s^{+2}} \left(\tanh \frac{15}{4k_s^+}\right)^{-1} + \frac{191}{k_s^+} \left(1 - \exp\left(-\frac{k_s^+}{250}\right)\right) \tag{2.45}$$

The suggested correction of the SST turbulence model can be adopted in ANSYS CFX by properly selecting some 'beta functions' which allows to activate the so-called 'blended near wall treatment' ensuring to capture the coupled effects of both wall roughness and pressure gradients {ANSYS, 2017 #127}.

2.1.3 Computational Fluid Dynamic Model Set-Up

The Navier-Stokes differential equations system is a set of balance equations describing fluid flows and the associate phenomena which cannot be analytically solved except in special conditions [65].

For practical cases, the system can be numerically solved by using a proper discretisation method for approximating the differential equations with algebraic. In fluid mechanics, the branch that uses numerical analysis to solve problems involving fluid flows is called CFD and its methodological procedure consists of defining the following models [66]:

- Physical model. According to the target application, in a numerical simulation, it has been selected the appropriate model able to approximate the real phenomena physics. They usually include approximation of the conservation laws found in § 2.1.1.
- Mathematical model. The differential equation should be approximate by a system of algebraic equations for a set of variables in some discrete spatial locations and time. Several methods are used for the discretisation, among which the most widely used are: (i) the class of the Finite Difference Methods (FDM) where the differential balance equations are approximated by finite differences; (ii) that of Finite Volume Methods (FVM) which use the integral form of conservation equations that are solved for a discrete number of finite or control volumes, and then (iii) the class of Finite Element Methods (FEM) which is very similar to the FVM one, except that the equations are multiplied by a weight function before to be integrated over the domain.
- Discretization model. The discrete locations at which the variables are to be calculated are defined by the numerical grid which is essentially a discrete representation of the geometric domain on which the problem has to be solved. It divides the solution domain into a finite number of subdomains (elements, control volumes, etc.). The grid can be structured, unstructured or block-structured. The structured mesh consists in families of grid lines that do not cross each other allowing a consecutively numbering. The position of any grid point (or control volume) within the domain is uniquely identified by a set of two (in 2D) or three (in 3D) indexes, e.g., (i, j, k). The unstructured mesh is the most flexible type of grid that can be adapted to complex geometries. In principle, such grids could be used with any discretization scheme, but they are best adapted to the finite volume and finite element approaches. The elements or control volumes may have any shape and there is no restriction on the number of neighbour elements or nodes. In the block-structured mesh, there are two (or more) level of subdivision of solution domain that can be irregular (unstructured) and regular (structured).
- Solution method. The selection of the solution method depends on the problem and of the discretisation model selected as well as on the grid. Usually, the solution methods use successive linearization scheme of the equations and, then, the resulting linear system is solved by iterative

techniques.

Usually, the CFD analyses are aimed at assessing the temperature, velocity and pressure fields in the domain considered. For this reason, these analyses are extensively used to assess the DEMO design and nowadays to improve the reliability of safety analyses performed by the proposed integral approach.

ANSYS CFX uses an element-based finite volume method where the spatial domain is meshed to obtain finite volumes in which relevant quantities such as mass, momentum, and energy are estimated. The conservation equations ((2.5) (2.10) (2.13)), used in ANSYS CFX, are discretised over the volumes and surfaces elements as described in [67]. The set-up of the finite volume models developed for the components analysed during the research activity have been carried out trying to comply with the ERCOFTAC Best Practice Guidelines [68]. In particular, the finite volume model set-up has been articulated in the following steps:

- flow domain discretization;
- constitutive model definition;
- loads and boundary conditions definition;
- turbulence model definition.

The flow domain discretization has been carried out importing or in certain cases drawing, by means of the ANSYS Design Modeler or SpaceClaim tools, the CAD file modelling the coolant flow domain of the component to be analysed. Then, since calculation time strongly depends on the mesh density and topology and, on the other hand, a poor mesh may result in un-realistic predictions, a sensitivity analysis has been carried out in order to select a mesh fine enough to give stable predictions with a further increase of its density, without inducing too long calculation times (all simulations have been carried out on a series of at least three grids to test grid independence).

In particular, a special attention has been given to the inflation layer adoption in the discretization of the near wall flow domain region when assessing the mesh configuration to be implemented for the calculation, since it plays a pivotal role in obtaining realistic numerical predictions under grid independency conditions. With regards to the pressure drops assessment in a relevant FW channel of an IB segment, in the following is reported the rationale behind the selected number of inflation layers. In this case, to discretize the FW channel which geometrical data are reported in Table 2-1, five different configurations have been tested. Starting from a grid with the thickness of first inflation layer set to 50 μm, finer grids have been gradually made, up to reaching a first layer thickness of 2 μm. This choice has been followed in order to obtain data both from calculation grids whose first layer has fallen within the radial zone enclosed by the wall asperities, as well as from those coarser meshes in which the code would have adopted automatic wall functions to grab the flow behaviour in the wall region ($\varepsilon = 11.35$ μm). Moreover, depending on the considered first layer height, the total number of layers and their growth rates have been suitably imposed to avoid a sharp transition between the last inflation layer and the element size characterizing the core of the calculation grid. Table 2-2 summarize the parameters used for this preliminary set of analyses, while some details of the grids investigated are reported in Figure 2-2.

Table 2-1: Main characteristic of the investigate FW channel

Item	Unit	Value
D_H	[m]	1.105E-02
L_{Tot}	[m]	3.039E+00
Mass flow rate	[kg/s]	2.500E-02
Velocity	[m/s]	3.657E+01
Reynolds	[-]	8.107E+04
Wall roughness ε	[μm]	1.135E+01
Δp_{Design}	[kPa]	4.181E+01

Table 2-2: Main parameters investigated

Case	First layer thickness [μm]	Number of layers [-]	Growth rate [-]
1	2	32	1.20
2	10	28	1.33
3	20	22	1.33
4	30	18	1.41
5	50	10	1.41

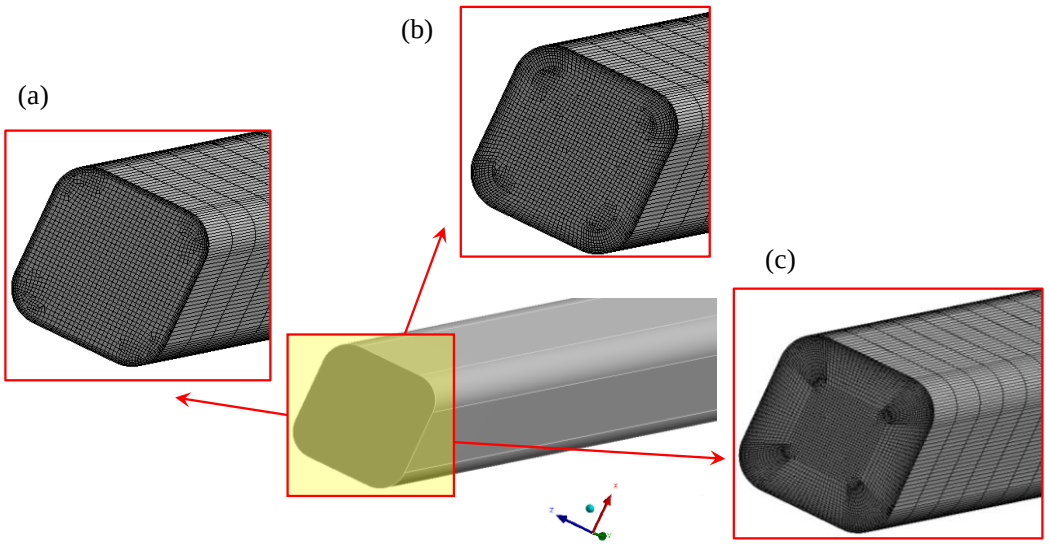

Figure 2-2: Detail of the investigated grid: (a) 10 inflation layers, (b) 20 inflation layers, (c) 30 inflation layers.

As shown in Figure 2-3 the evaluated pressure drops tend to stabilize around a values of 39.8 kPa, where the first 3 cases with a first layer height of 2, 10 and 20 microns, respectively, feel relative maximum variations below 1 %, being the case 4 and 5 almost identical.

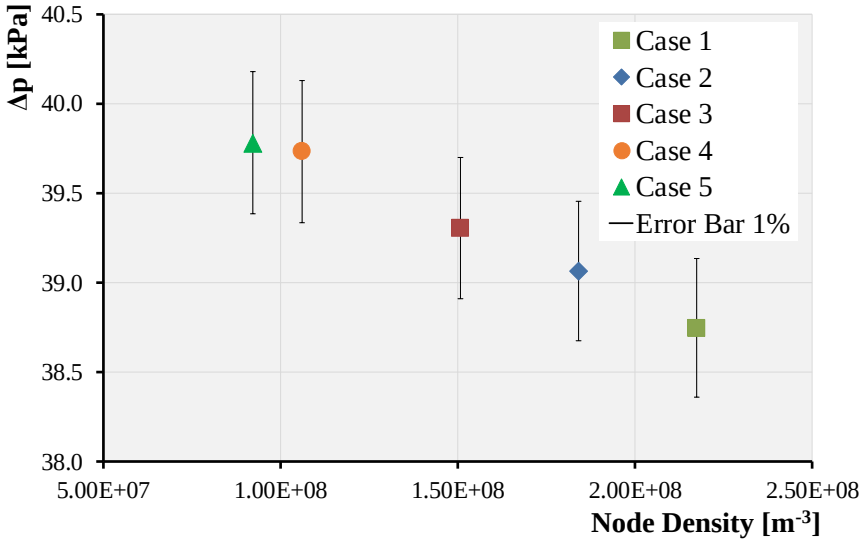

Figure 2-3: Total pressure drop prediction.

Therefore, in view of these results, to minimize the number of nodes (and elements) in the calculation

grid while keeping characteristic sizes that might have ensure both grid independency and accuracy, the mesh parameters pertaining to the Case 5 have appeared a good trade-off choice to which we can refer to analyse similar components.

Furthermore, another parameter which has been continuously checked during the post-processing phase in order to assure a good near wall resolution is the dimensionless wall scale. In fact, to take advantage of the reduction in errors offered by the automatic switch to a low-Re near wall formulation when adopting a turbulence model based on the omega-equation, such as the SST model, it is recommended to use $y^+ <1$ or at least $y^+ < 2$, which is really difficult to achieve dealing with complex geometries. For example, Figure 2-4 shows the y^+ contour map obtained for the whole simplified COB segment described in §4.2; in this case the condition to have a dimensionless wall scale below 2 was satisfied for just the ~70% of the wall surface.

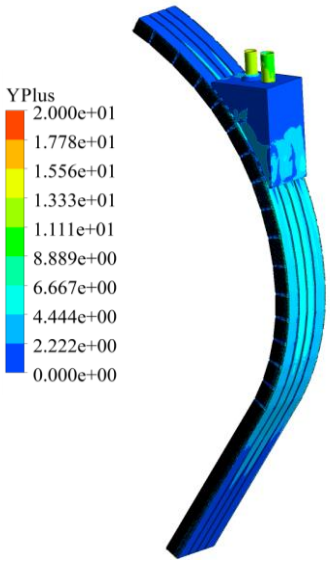

Figure 2-4: y^+ contour plot for the COB segment model.

In addition, a sensitivity analysis concerning the node density has been generally performed by varying the body sizing adopted in generating the grid, for example Figure 2-5 shows the one made for the COB segment. Typically, a good compromise between results accuracy and calculation time is obtained generating meshes with a node density ranging between 10^6 and 10^8 node/m³.

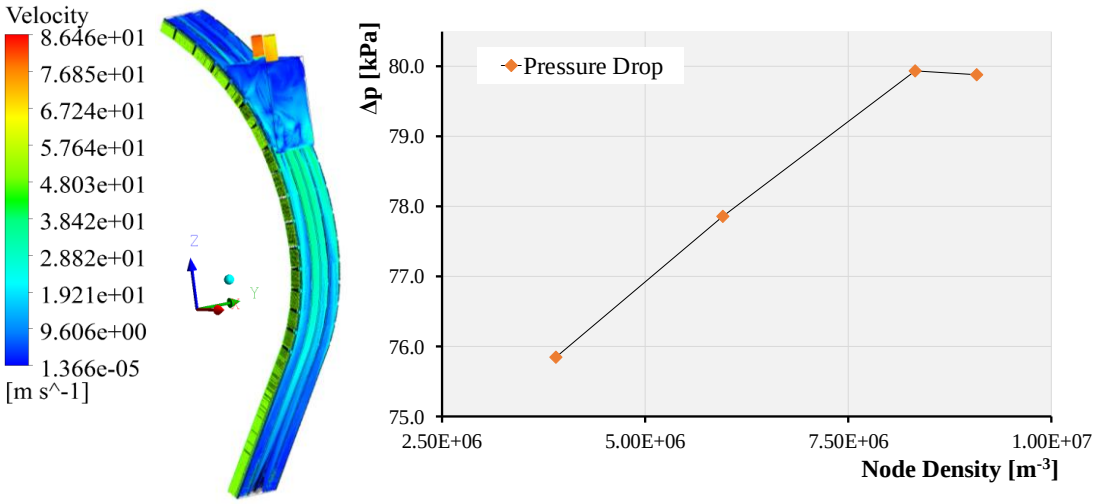

Figure 2-5: Pressure drop prediction for the COB segment.

Concerning the constitutive model definition, all the helium thermofluid-dynamic properties have been adopted according to the data provided by the US National Institute of Standards and Technology (NIST) and reported in [34].

As to the loads and Boundary Conditions (BCs) definition, at the circuit inlet section the total pressure value has been generally imposed. In particular, ANSYS CFX solves the CFD equations in terms of relative pressure and the absolute pressure is simply calculated as the sum of the relative and the reference pressures. A common practice has been to set the reference pressure to a value close to the average absolute pressure in the whole circuit, in order to reduce round-off errors and pressure wiggles. Furthermore, at the outlet section the target mass flow rate has been typically imposed. The interface between the coolant and the circuit steel walls has been modelled by means of a no-slip condition. Concerning turbulence treatment, the SST model has been adopted as already disclosed in §2.1.2 because of its good capabilities in terms of accuracy and robustness when applied to complex geometries. Once set-up the finite volume model, the analysis settings are properly defined. In particular, steady-state analyses have been carried out adopting the ANSYS CFX "false transient" algorithm to speed-up convergence of numerical simulations. Initial values can be set automatically if a good initial guess is not known or is not required. Although accurate initial values may not always be available, a good approximation can speed up a steady-state simulation, reducing the chance that its solution fails to converge due to diverging residuals. The more complicated are simulation and models adopted, the more pivotal is to start the solution process with sensible initial values. For this reason, it has been decided to get an initial solution with a less accurate numerical scheme and signally the "upwind" one, properly tuning the maximum time-scale parameter. It has then been implemented as initial condition into a further CFD analysis, to be carried out with the more accurate "high resolution" advection numerical scheme, in order to obtain the more reliable final thermofluid-dynamic solution.

2.2 Thermal-Hydraulic System Codes for Nuclear Energy Applications

As mentioned earlier, nuclear reactors are quite complex systems requiring detailed analysis to evaluate their performances during both normal operations as well as accident and transient conditions. Since 1960's, the computer codes used to analyse these complex reactor systems are called "system codes" [69]. System codes have been adopted for both the design and safety analyses of such systems due to their potential to model reactor components such as pipes, pressurizers, valves and pumps. These hydrodynamic models have frequently been extended to include the capability to model multiple phase flows and the interaction between coolant phases in order to capture heat transfer properties and mass exchange between the phases. Components modelling heat transfer through materials, as well as nuclear heat generation and basic control elements are also part of system code analyses that can be used to implement reactor control systems. In the following paragraphs a brief overview of system codes fundamentals shared among those embraced by the involved scientific community (RELAP5, TRACE and CATHARE) will be provided [46, 70], even if more focused on the RELAP5-3D one, since it was adopted for the integral procedure reported in this dissertation.

2.2.1 The Structure of Thermal-Hydraulic System Codes

The thermal-hydraulic system codes have played and will play a pivotal role for investigating thermal-hydraulics of complex systems in various situations and particularly in safety analysis. They have integrated the available knowledge gained during decades analysing a large number of experiments. The system codes include thermal-hydraulic balance equations, models for conduction, radiation, neutron physics, fuel thermo-mechanics, chemical reactions, instrumentation and control (I&C) systems and most of them encompass a graphical interface to speed-up the nodalization procedure. They are used to simulate reactor thermal-hydraulics in normal operation and during design basis accidents demonstrating good capabilities

in predicting, with sufficient confidence, many of the accidental transients considered.

Indeed, nuclear reactor safety technology is based on deterministic safety analysis (DSA) and probabilistic safety analysis (PSA). In order to perform DSA, fully qualified computational tools are needed and, among them, the system codes have played a prominent part since their ability to model the whole reactor system with all the interactions between circuits and components. To some extent the thermal-hydraulic system codes are multiphysics simulation tools since they are including different physics modules, such as:

- thermal-hydraulics, conduction and radiation heat transfer modules;
- compressor, pump and turbine models;
- special system component models (pressurizer, accumulator, etc.);
- regulations, control and protection systems.

Depending on the reactor component and on the situation of interest, phenomena may be treated with more or less space resolution. Indeed, the system codes have usually three different level of spatial discretization: (i) 0D models or lumped parameter models which may be used to model components where velocities are low; (ii) 1D models for flow in components which have a privileged flow direction; (iii) 2D or pseudo-3D models for components with a fully 3D velocity field. As concerns the numerical solution methods in system codes, they consist in variants of FVM and FDM based on the Implicit Continuous-fluid Eulerian techniques. Although all system codes are quite similar in the space discretization schemes, they differ greatly depending on the time discretization method adopted, which may be semi-implicit or fully implicit. To ensure the stability of semi-implicit schemes the material Courant condition on the time step has to be respected, whilst implicit methods may use very large steps without any limitation. This is very convenient for stationary initial state or even for very slow transients. Among the most used system codes, the CATHARE code has selected a fully implicit scheme, at least for 0D and 1D components [46, 48].

2.2.2 Theory and Implementation of Thermal-hydraulic System Codes - Balance and Constitutive Equations

As concerns the conservation equations for mass, momentum and energy, they are consistently implemented in all the system codes. The balance equations are written for each phase and, when they are written for the vapour and liquid phases they are referred to as the well-known six-equation model. In this model the mass conservation equation for 1D components becomes:

$$\frac{\partial}{\partial t}\left(\alpha_k \rho_k\right) + \frac{1}{S}\frac{\partial}{\partial x}\left(S \alpha_k \rho_k u_k\right) = \Gamma_K \tag{2.46}$$

where the subscript k indicates the phase, either vapour (g) or liquid (f). The first term on the left hand side of Eq. (2.46) is the time rate of mass change for the phase k, while the second term is the change in mass of phase k due to the mass entering or leaving the control volume. The Γ_k is the volumetric mass exchange rate of phase k. The mass conservation equation formulation does not consider mass sources or sinks thus the mass lost from one phase must be acquired by the other one ($\Gamma_f = -\Gamma_g$). It has been written in "area-average" notation, since RELAP5-3D assumes that the total mass transfer can be partitioned into contributions from mass transfer at the vapor/liquid interface near the wall (Γw) and interfacial mass transfer in the bulk fluid (Γig).

The 1D momentum equation is:

$$\begin{aligned} \alpha_k \rho_k S \frac{\partial u_k}{\partial t} + \frac{1}{2}\alpha_k \rho_k S \frac{\partial u_k^2}{\partial x} = \quad & -\alpha_k S \frac{\partial p}{\partial x} + \alpha_k \rho_k B_x S - \left(\alpha_k \rho_k S\right) FW_k u_k + \\ & + \Gamma_k S\left(u_{kl} - u_k\right) - \left(\alpha_k \rho_k S\right) FI_k \left(u_k - u_r\right) + \\ & - C \alpha_k \alpha_r \rho_m S \left[\frac{\partial\left(u_k - u_r\right)}{\partial t} + u_r \frac{\partial u_k}{\partial x} - u_k \frac{\partial u_r}{\partial x} \right] \end{aligned} \tag{2.47}$$

which is written in terms of momentum per unit volume using the velocity variables u_g and u_f. The spatial variation of the momentum terms is expressed in terms of u_f^2 and u_g^2. As arranged, the momentum conservation can be easily reduced to the Bernoulli equation in case of steady, incompressible, and frictionless flow. It is important to observe that the momentum equation has a reduced effect on the solution when compared to the mass and energy equations. Indeed, the system flows are mainly dominated by large sources and sinks of momentum (i.e. compressor, abrupt area changes, etc.). Moreover, such a formulation assumes that the phasic pressures are equal and that the interfacial pressure is the same as the phasic pressures (except in special cases, namely for stratified flows). As concerns phasic viscous stresses, they are considered only at the interface. The implemented interface force terms include both the viscous and pressure stresses.

With regard to the 1D component energy conservation equation, it becomes:

$$\frac{\partial(\alpha_k\rho_k U_K)}{\partial t}+\frac{1}{S}\frac{\partial(S\alpha_k\rho_k U_K u_k)}{\partial x}= -p\frac{\partial\alpha_k}{\partial t}-\frac{p}{S}\frac{\partial(S\alpha_k u_k)}{\partial x}+Q_{wk}+ +Q_{ik}+\Gamma_{ig}h_k^*+\Gamma_w h_k^{'}+DISS_k \tag{2.48}$$

In the RELAP5 series of codes, the energy conservation model implemented simplifies the calculation by neglecting Reynolds heat flux, interfacial energy storage and internal phasic heat transfer. The conservation equations are written for the liquid and vapour phases only. Indeed, the conservation equations model the exchange of mass, energy, and momentum between the phases, but do not explicitly model the entrained droplets or vapour bubbles, which are captured by a change in the void fraction reported for the control volume in question.

Moreover, the RELAP5-3D code includes also a multidimensional component that was developed to better model the multi-dimensional features in reactor systems, such as core, downcomer regions and the steam generator components. The multidimensional component can model one, two or three dimensional arrays of volumes with internal junctions to connect the volumes. The mass, momentum, and energy equations are documented in the RELAP5-3D manual [47, 71]. Mass conservation in the multidimensional component is computed as shown in Eq. (2.49) for the k phase:

$$V\left(\rho\frac{\partial\alpha_k}{\partial t}+\alpha_k\frac{\partial\rho}{\partial t}\right)+\sum_i S_i\alpha_i\rho_i u_{in}=V\Gamma \tag{2.49}$$

where α_i and α_k are defined as:

$$\alpha_i=\frac{S_{ki}}{S_i}\quad\text{and}\quad\alpha_k=\frac{V_k}{V} \tag{2.50}$$

Whilst, the conservation of momentum is computed as reported in Eq. (2.51)

$$\rho_k\left(\frac{\partial u_k}{\partial t}+u_k\nabla\cdot u_k\right)=-\nabla p+\sigma+\rho_k f \tag{2.51}$$

Finally, the internal energy conservation is evaluated as:

$$V\left(\rho U\frac{\partial\alpha_k}{\partial t}+\alpha_k U\frac{\partial\rho}{\partial t}+\alpha_k\rho\frac{\partial U}{\partial t}\right)+\sum_i S_i\alpha_i\rho_i U_i u_{in}= -\iint_{S_c}\mathbf{q}\cdot\mathbf{n}dS+Q_i V+h_i\Gamma V+D_s V -p\left[\frac{\partial\alpha_k V}{\partial t}+\sum_i S_i\alpha_i u_{in}\right]+RV \tag{2.52}$$

However, the reactor systems are not always limited to just two phases. Indeed, very often there are solutes dissolved into the coolant as well as noncondensable gasses as part of the vapour phase or in solution with the liquid phase. The effects of these added phases on the flow field are modelled by the system codes with some simplifying assumptions. For example, RELAP5-3D assumes that:

- the noncondensable gas or the solute are at the same temperature and pressure as their surroundings;
- the solute or noncondensable gasses do not affect the properties of the liquid or vapour;
- the solute or gas moves at exactly the same velocity as the fluid.

These assumptions simplify the modelling of the additional phases to a single mass conservation equation for each phase. As long as the assumptions can be considered valid, it is not necessary to add energy and momentum conservation equations to track the dissolved solute and gasses. In fact, RELAP5-3D solves two mass conservation equations. One (Eq. (2.53)) is used to track the mass of dissolved solute in the liquid coolant, and the other (Eq. (2.55)) is used to track noncondensable gases in the vapour phase. If more than one type of noncondensable gas is present, Eq. (2.55) can be modified to include an additional term, X_{ni} in each parenthetical term. X_{ni} is the noncondensable gas phase for the i-th noncondensable species. In this way, the code can account for more than one noncondensable gas in the model.

$$\frac{\partial \rho_b}{\partial t} + \frac{1}{S}\frac{\partial}{\partial x}\left(S\rho_b u_f\right) = 0 \tag{2.53}$$

$$\rho_b = \alpha_f \rho_l C_b = \rho_m \left(1 - X\right) C_b \tag{2.54}$$

$$\frac{\partial}{\partial t}\left(\alpha_g \rho_g X_n\right) + \frac{1}{S}\frac{\partial}{\partial x}\left(S\alpha_g \rho_g X_n u_g\right) = 0 \tag{2.55}$$

$$X_n = \frac{M_n}{M_n + M_s} \tag{2.56}$$

Although the assumptions of the noncondensable gas conditions do not require a completely separate energy conservation equation for the gas, the liquid energy equation must still be modified when noncondensable gasses are modelled. The sensible heat transfer rate per unit volume (Q_{gf}) is subtracted from the energy balance for the vapour phase and added to the liquid energy balance equation. This sensible heat transfer rate is the heat transfer at the noncondensable gas-liquid interface. This term must be included due to the fact that the interfacial terms use a saturation temperature that is based on the bulk vapour partial pressure instead of the saturation temperature based on the local vapour partial pressure. The sensible heat transfer rate is computed as shown in Eq. (2.57).

$$Q_{fg} = \left(\frac{p - p_s}{p}\right) h_{fg}\left(T_g - T_f\right) + \frac{p_n}{p} h_{fg}\left(T_g - T_f\right) \tag{2.57}$$

The interfacial heat transfer and mass transfer terms (Q_{ig} and Γ_g) also change slightly when noncondensable gasses are present. The RELAP5-3D includes a third additional mass balance equation to track radionuclides; their modelling assumes:

- that the fluid properties (liquid or vapour/gas) are not affected by the presence of the radionuclides,
- energy absorbed by the fluid from decay of the radionuclides is negligible,
- radionuclides are well-mixed with the transporting phase, implying that they are transferred at the phase velocity.

As with the noncondensable gasses, these assumptions reduce the required conservation equations. Mass conservation for the radionuclides is the only required continuity equation. The mass conservation equation for the radionuclide specie is:

$$\frac{\partial C}{\partial t} + \frac{1}{S}\frac{\partial}{\partial x}\left(CSu\right) = S_o \tag{2.58}$$

where the density number C can be converted to the mass density by using the following expression:

$$\rho = \frac{CM_w}{N_A} \tag{2.59}$$

As stated before, the balance equations are very often simplified by averaging over volume and time. Thus, closure relations have to be used in order to compensate for the lost information during the averaging process, allowing also to make a solvable set of equations. There are many closure relationships available for each flow regime modelled by the codes. Many of the differences between the system codes result just from the selection and application of such closure relationships, since they severely affect the solution methods. Indeed, some closure relationships require re-meshing of regions in the model and this operation can change the solution time, as well as the accuracy and stability of the solution.

Closure relationships compute heat transfer rates between phases, heat transfer coefficients between phases and the walls, the viscous shear in the flow, mass exchange among fields at the phase boundaries, momentum exchange at the phase interfaces, drag forces at the solid boundaries, turbulence terms in the continuous fields, droplet entrainment and de-entrainment and other similar information.

The applicability of system codes in analysing the next generation power plants, such as fusion reactors, passes through the validity range of their implemented models, with a special focus to the closure relationships concerning [72]:

- interfacial drag;
- interfacial heat transfer;
- wall-to-fluid heat transfer;
- critical heat flux closure models;
- reflood modelling;
- wall-to-wall radiation.

A complete characterization of the closure relations, even just for RELAP5-3D would require much more explanation than is possible in this dissertation. Moreover, an exhaustive explanation of them, like that for the balance equations listed before, is available within the user manual for each system code. Indeed, the main objective of this paragraph was just to underline the balance equations modelling approach adopted by the system codes highlighting their simplifications.

2.2.3 The Nodalization Modelling Method

System codes model the thermal-hydraulic physical system and other related coupled systems, which can be either the cooling circuits of a nuclear reactor or the circuits of a test facility, that have to be simulated by solving a proper set of equations. The fluid domain is split into a number of meshes or 'control volumes' where the balance equations listed in §2.2.2 are solved. This determines a discretized set of equations where physical parameters such as pressures, temperatures, and velocities are calculated in a set of nodes. Mathematically speaking, the simplification reduces the state space of the system to a finite dimension, and the partial differential equations of the continuous (infinite-dimensional) time and space model of the physical system into ordinary differential equations with a finite number of parameters. This process is often called 'the nodalization' and includes many choices which have an important influence on the quality of predictions, such as:

- modelling some component of the reactor fluid domain by either 0-D, 1-D, 2-D, or 3-D models;
- choosing the number and type of meshes (or control volumes) in each component;
- choosing to model heat transfers in solid structures by either 1-D, 2-D, or 3-D models and the mesh size for heat conduction;
- choosing between several options for modelling compressors, pumps, turbines, valves, safety valves, check valves, flow limiters and so on;
- modelling some special systems such as separators and dryers in steam generators;

- modelling instrumentation and control with possible regulations;
- choosing the pressure loss coefficients in all component of the circuits;
- choosing to activate some special model options in specific components;
- choosing the heat losses modelling;
- choosing the break flow model with possible multipliers;
- modelling of the heat exchangers and choosing the proper mesh size for fluid and solid walls;
- using additional transport equations for noncondensable gases;
- using additional transport equations for radioactive elements;
- coupling to other possible calculation (i.e. containment, source term, etc.).

Such choices are necessary for building the so-called 'input deck' for a thermal-hydraulic system code calculation. In addition to the nodalization, information is necessary to define the process to obtain an initial state - which is often a stationary and reference state - and the scenario of the transient with all necessary boundary conditions all along the transient (break opening, automatic safety system actuations, operator actions, etc.). The time step management is also part of an input deck and it is an important choice of the user which may affect the calculation accuracy.

As concerns RELAP5-3D, the two-fluid equations of motion (described in §2.2.2) are solved numerically using a semi-implicit finite-difference technique. The code solves eight field equations [71]. The primary dependent variables are pressure, phasic specific internal energies, vapour volume fraction, phasic velocities, non-condensable quality, and boron density. The independent variables are time and distance. The secondary dependent variables used in the equations are phasic densities, phasic temperatures, saturation temperature and noncondensable mass fraction in noncondensable gas phase for the i-th noncondensable species. Fluid properties are calculated from thermodynamic tables that tabulate saturation properties as a function of temperature, saturation properties as a function of pressure and single-phase properties as a function of pressure and temperature. The properties and derivatives in the tables are saturation pressure, saturation temperature, specific volume, specific internal energy and three derivatives (i.e. the isobaric thermal expansion coefficient, the isothermal compressibility, and the specific heat at constant pressure) [47].

2.3 Description of the Integral Approach Methodology

As already disclosed in §1.3, due to the extreme complexity of the HCPB DEMO reactor systems, any possibility of adopting a theoretical-analytical methodology is definitely excluded. Hence, the research activity has been carried out following a theoretical-computational approach based on the Finite Volume Method and adopting suitable releases of both RELAP5-3D (version 4.4.2) and ANSYS CFX (version 19.1). These two tools have been properly integrated in order to achieve a more detailed and realistic simulation of the HCPB DEMO plant thermal-hydraulics with respect to the state of the art. This integral approach has allowed to take advantage of the best characteristics of both the computational tools.

In fact system codes, and RELAP5-3D in particular, are traditionally used since 60's as a powerful computational tools for the simulation of the steady state and transient thermal-hydraulic behaviour of industrial plants (nuclear power plants, chemical plants, etc.) where single component, two-phase flows allow energy transfer and conversion. They theoretically rely on the solution of one-dimensional forms of the conservation equations for mass, momentum and energy, properly integrated with a set of constitutive and closure equations. These are intended to model fluid thermo-dynamic behaviour, distributed and concentrated hydraulic resistances according to flow pattern as well as specific thermo-fluid dynamic phenomena such as choking flow, counter-current flow limit and similar. Therefore, they result deeply based on empirical correlations that, after decades of refinement, are suitable of realistic predictions as to networks of pipes, vessel, compressors and heat exchangers. Anyway, these correlations might limit their

predictive potential whether applied to newly conceived, complex and deeply 3-D circuits such those of a fusion reactor cooling system, as it has been described in §2.2. On the other hand ANSYS CFX simulates, in a fully 3-D approach, the thermo-fluid dynamic behaviour of fluid flows, taking into account passive scalars (temperature, enthalpy, concentration, etc.) convective/diffusive transport phenomena and including other related physical processes. In particular, with reference to §2.1, it numerically solves the thermo-fluid dynamic equations governing the fluid flow over the region of interest with the prescribed boundary conditions. Then, ANSYS CFX is suitable to realistically predict the thermo-fluid dynamic behaviour of single-phase, single-component flows both in laminar, transition and fully turbulent regimes, while showing still unsolved issues and criticalities whether applied to the simulation of two-phase flows [67]. The recent progress in the implemented meshing algorithms, particularly those oriented to free-meshing applications suitable for the discretization of complex 3-D flow domains, the wide library of qualified turbulence models implemented and validated, the complete assessment of the 'near wall treatment' explained in §2.1.2, the robustness of the numerical techniques adopted and the flexibility in convergence control settings as well as the high level of post-processing capabilities have contributed to boost the adoption of ANSYS CFX for the numerical assessment of the steady state thermal-hydraulic behaviour of single-phase flows taking place in circumscribed regions of fusion reactor components.

Therefore, in order to have a realistic assessment of the HCPB DEMO reactor system thermal-hydraulic performances under both steady state, operational and accidental transient conditions, the definition of an indirect coupling procedure of both 1-D and 3-D codes has been pursued. In this way, the integration of the system code aptitude to synthetically simulate the thermal-hydraulic performances of wide and complex energy transfer systems with the highly realistic predictive potential guaranteed by the 3-D CFD code in the thermo-fluid dynamic assessment of fluids flowing through deeply 3-D circuits has been performed.

In particular, with reference to those components where deeply 3-D thermo-fluid-dynamic phenomena take place (e.g. HCPB DEMO BB), a detailed parametric analyses have been performed by means of ANSYS CFX aiming at assessing the hydraulic characteristic function of the component, giving the functional dependence of its total pressure drop on the corresponding mass flow rate under steady state conditions. Once obtained, this function has been adopted to derive the dependence on mass flow rate of the effective concentrated hydraulic loss coefficients of each sub-component (e.g. FW channels, pins, etc.) which have been given in input to RELAP5-3D in order to let it simulate realistically the whole circuit with a lumped parameter approach [73]. More precisely, the procedure has been implemented by means of the following steps:

1. investigation of the characteristic function $\Delta p(G)$ of the HCPB DEMO BB segment' components, which expresses the functional dependence of the pressure drop across the segment, Δp, from the mass flow rate G that across it;
2. analysis of mass flow rate distribution and pressure drops across the whole segment, using a porous media model for simulating each sub-component in which the hydraulic characteristic function has been applied [55, 74], in order to derive its effective concentrated hydraulic loss coefficients;
3. once derived the dependence on mass flow rate of such loss coefficients, it will be given as input to the RELAP5-3D code in order to let it simulate realistically the segment.

Regarding the first step, the following methodology has been adopted:

1. the thermodynamic conditions of the coolant along the sub-components p^{in} and T^{in} are set (the T^{in} used in this analysis corresponds to the mean of the HCPB operational temperatures, namely 683.15 K);
2. a series of outlet mass flow rates is defined, G_i with $i = 1...N$;

3. the outlet pressure p_i^{out} , is determined by means of suitable computational analyses: $\Delta p_i = p^{in} - p_i^{out} \ \forall \ i = 1...N$;
4. the characteristic function Δp(G) is deduced, by means of the numerical interpolation of the obtained N pairs $(G_i, \Delta p_i)$;
5. the characteristic function of the resistance loss coefficient K(u) is deduced, by means of numerical interpolation of the obtained N pairs (ui, Ki).

The characteristic curves are interpolated by means of the following functional expression:

$$\Delta p(G) = aG^b \tag{2.60}$$

where a and b are coefficients determined according to the fourth step. Hence, the linear resistance loss coefficient is obtained as follows:

$$\frac{K}{L} = \frac{2\rho S^2 a G^{b-2}}{L} \tag{2.61}$$

where ρ is the fluid density, S is the area on which the variables are evaluated and L is the length of circuit on which the thermal-hydraulic characteristic is evaluated. Such coefficient can be easily rearranged in the following form:

$$\frac{K}{L} = \alpha u^{\beta} \tag{2.62}$$

where α and β are coefficients determined according to the fifth step and equal to:

$$\alpha = \frac{2a\rho^{b-1}S^b}{L} \ \text{ and } \ \beta = 2 - b \tag{2.63}$$

In order to perform the first step for the determination of the thermal-hydraulic characteristics, suitable models for the HCPB DEMO BB segment sub-components have been set up and will be described in chapter 4.24.

3 Validation of the Thermal-Hydraulic Modeling Approach Adopted for the EU-DEMO HCPB Reactor Simulation

3.1 Introduction

The validation procedure of the proposed integral approach to the safety design of the EU-DEMO HCPB reactor, already illustrated in §2.3, is reported in this chapter. In particular, the proposed thermal-hydraulic modelling strategy has been validated by means of both an experimental test, performed on the HEat TRAnsfer (HETRA) test facility [75], and a code-to-code benchmark which has involved the CATHARE system code. The latter code was already validated and extensively used in the framework of nuclear fission reactors, in order to assess Gas Cooled Reactors (GCRs) [76, 77]. Indeed, the validation through the HETRA facility experimental campaign has allowed verifying the suitability of the adopted thermal-hydraulic modelling methodology to the DEMO thermal-hydraulic simulations. In fact, this activity has allowed to choose the proper boundary conditions and the heat structures modelling approach in order to reproduce the temperature distribution in the structural material.

Furthermore, the benchmark of the proposed integral approach with the extensively validated CATHARE system code has allowed testing its prediction capability for the simulation of a fusion gas-cooled system. The validation procedure is widely described in the following.

3.2 Validation through the experimental campaign carried out on the HETRA facility

In order to perform the validation of the proposed integral approach through suitable experimental data, some of the experiments carried out at the Institute of Neutron Physics and Reactor Technique (INR) of the Karlsruhe Institute of Technology (KIT) were preliminary explored. In particular, those experimental campaigns concerning the ITER HCPB Test Blanket Module (TBM) have been considered. Indeed, the HCPB TBM has been developed as one of the two blanket concepts chosen in the frame of the European Blanket Programme to be tested in ITER, as a DEMO relevant blanket [28]. In this regard, the considered experiments were conceived in support of the HCPB TBM design, being aimed at both validating the adopted models and verifying the findings of preliminary calculations.

For the purposes of the research work reported in this dissertation, three main experiments have been taken into account:

- GRICAMAN, a test facility developed to mainly verify whether the mass flow distribution along the cooling channels corresponds to the design one, see Figure 3-1. The facility has been designed to operate in flow similarity conditions, thus the helium-coolant at 8 MPa and an average temperature of 643.15 K has been substituted with air at 0.3 MPa and 298.15 K [78, 79];
- PREMUX, depicted in Figure 3-2, conceived to serve as a proof-of-concept test for a new heater system to be integrated in an out-of-pile testing of a functional mock-up of a HCPB TBM breeder unit and to validate the thermal and thermo-mechanical models adopted [80];
- HETRA, a FW mock-up developed to assess the design strategy based on simplified evaluations and models [75, 81].

Among them, the latter has been selected both for the data availability and for its relevance with respect to DEMO cooling conditions. Hence, a direct connection among HETRA facility and DEMO HCPB reactor can be established by means of the ITER HCPB TBM and, as a consequence, the performed validation procedure performed on HETRA experimental results can be considered as DEMO-relevant.

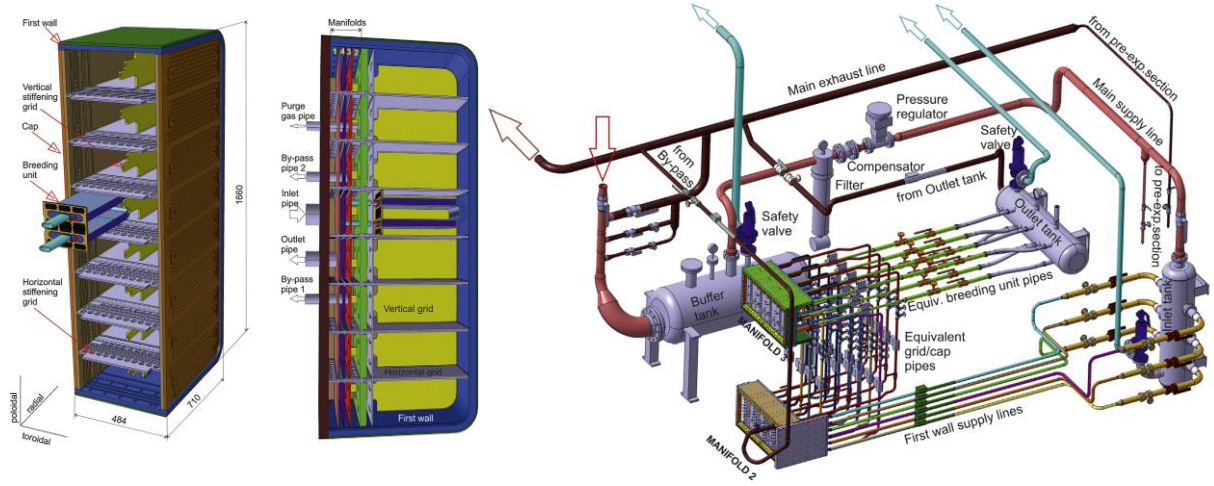

Figure 3-1: (a) HCPB TBM Version 2.1 used as reference for designing the (b) GRICAMAN facility [78].

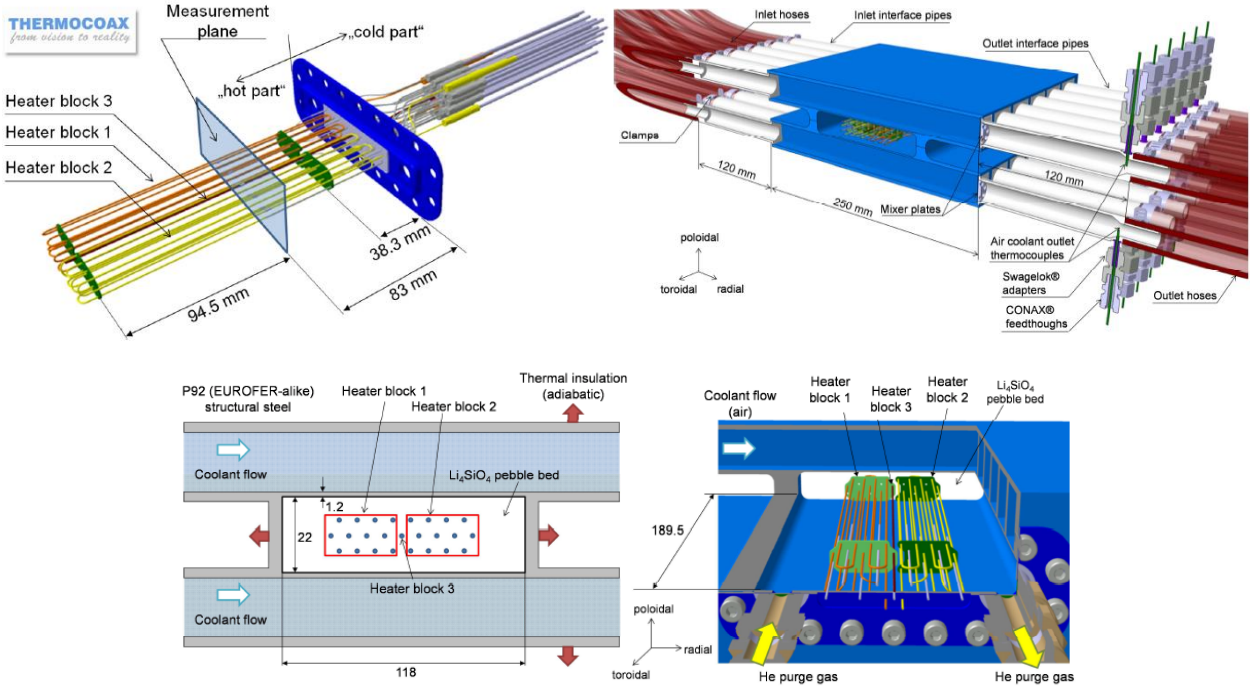

Figure 3-2: PREMUX test section [80].

3.2.1 The HETRA Facility: a Mock-Up of the HCPB Test Blanket Module First Wall

The HETRA test section has been designed to represent a suitable mock-up for the HCPB TBM first wall. In particular, the facility reproduces the horizontally oriented version of the HCPB TBM, the so-called version 1.1, before it was updated to a vertically oriented layout.

However, regardless of the version, the HCPB TBM, as well as the DEMO reactor, is endowed with a U-shaped FW adopting the reduced-activation ferritic-martensitic Eurofer steel as structural material. This design choice implies a requirement on the maximum allowable temperature within the FW structure. Indeed, for safety reasons, the Eurofer maximum temperature has to be maintained safely below the 823.15 K [24, 74]. Above this limit temperature, some Eurofer thermomechanical properties dramatically decrease, significantly increasing the risk of the insurgence of the incipient structural crisis condition. Therefore, in order keep the FW temperature well below the 823.15 K, in both HCPB TBM and DEMO, the helium-coolant enters the FW cooling channels with a temperature of 573.15 K and a pressure equal to 8 MPa.

As matter of fact, the FW is a peculiar component which undergoes an extreme asymmetric heat load combination heavily affecting the temperature distributions within the structural material. Thus, in view of satisfying the requirement on the Eurofer maximum allowable temperature, it had to be considered pivotal to demonstrate the capability to meet such a prescription already in the early design stages. To this end, the proper cooling approach has to be selected. In this regard, some preliminary analyses revealed that the asymmetrical heating affects the heat transfer phenomenology so that the FW could not be cooled in a reliable manner with the originally planned hydraulically smooth channels. Then, these preliminary outcomes led to shift the focus towards the possibility to adopt heat transfer improvements, such as an augmented surface roughness of 20 μm, which has proven to be satisfactory at first glance.

Therefore, the intention to empirically prove the outcomes of such preliminary numerical investigations was the main reason which leads to design, manufacture and to operate the HETRA facility.

The HETRA test section, as shown in Figure 3-3, involves only one of the three serially connected U-passes that were foreseen for the HCPB TBM version 1.1, as they exhibit a similar thermal-hydraulic behaviour. Moreover, compared to the original HCPB TBM, HETRA is heated only on the side representing the plasma face side although, in reality, the FW is also heated from the back side by the breeding zone. Anyway such heating power is several times lower compared to that on the plasma side, so it can be neglected [81].

Hence, the main component of the test section is a U-shaped channel which consists of a heated section made of Eurofer, reproducing the same geometrical characteristics of the HCPB TBM FW, and two side channels, designed to provide the relevant flow conditions occurring at the inlet and outlet of the heated test section. In order to avoid any flow disturbances where the heated section is connected to the side channels, the flanges cross section was maintained the same as the channel one.

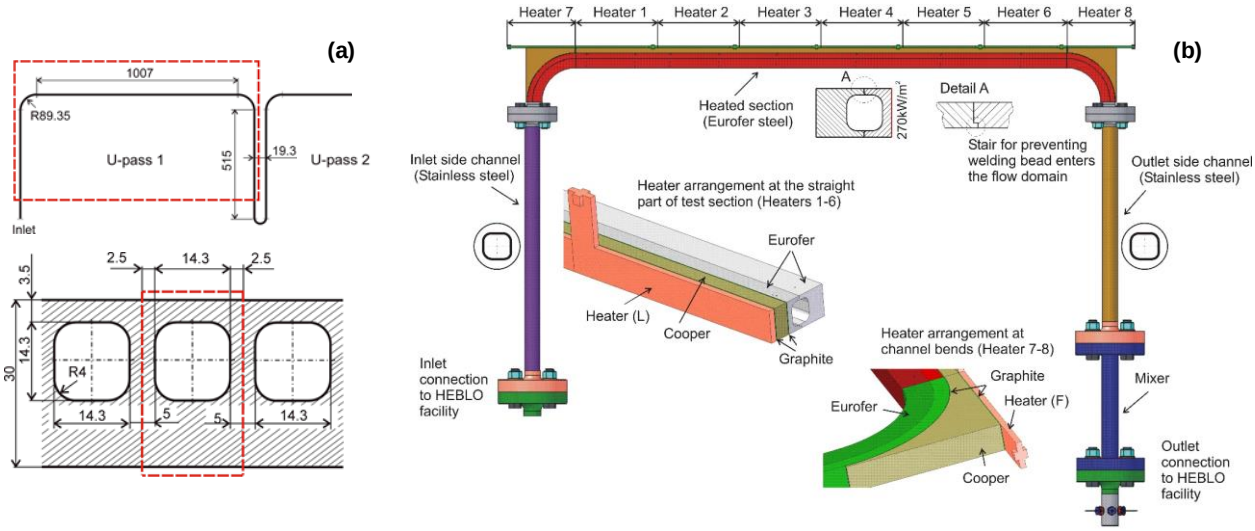

Figure 3-3: In the red frame the channel used as basis for the definition of HETRA investigation domain (a) and the HETRA CAD design model (b) [82].

In the framework of HETRA experimental campaign, two heated sections have been foreseen: a section with hydraulically smooth walls and another one with hydraulically rough surfaces.

The heat flux on the FW plasma facing side of HETRA test section has been simulated by using a set of 8 different heaters able to provide the TBM relevant heat flux of 270 kW/m².

In order to ensure a uniform heat flux and with a view to diminish the effects of a possible imperfect thermal contact, the gap between the heaters and the channel wall has been bridged with two thin graphite sheets (see detail in Figure 3-3 (b)) of 0.5 mm thick, while in between the two graphite sheets three distinct cooper parts have been placed: a 10 mm thick slab above the straight part of the heated section and two side

parts designed to fit the channel bends. The outlet side channel has been equipped with a mixer to precisely avoid an incorrect determination of fluid bulk temperature due to the expected asymmetrical heating. In fact, the helium outlet temperature has been measured directly downstream it.

The HETRA test section has been supplied with helium at the HCPB TBM relevant conditions by exploiting the HElium Blanket LOop (HEBLO), already existing at the INR, which was able to provide coolant at 8 MPa and 573.15 K as it was for the small-scale blanket test section reported in [83].

As concerns the thermal insulation of the facility, it was originally planned to use a vacuum tube, which is a vessel of stainless steel with an outer diameter of 220 mm and 3 mm thick equipped with two harmonica type bellows to withstand thermal expansions, directly welded to the inlet and outlet side channels. Its blind side flanges host the needed openings for the thermocouples threads and the electrical supplier for the heaters as well, as shown in Figure 3-4. The vacuum that has been obtained by using a turbo-molecular pump was in the range of 0.3 - 0.04 Pa, capable of avoiding the onset of heat convection. Moreover, to further decrease heat losses due to the thermal radiation, a mirror barrier has been inserted into the vacuum tube. However, this thermal insulation arrangement has been used to perform only the measuring series on the smooth channel. Indeed, while performing the high temperature measuring tests, some electrical insulation problems were observed. These have led to switch to mineral wool insulation type.

Since the main purpose of the experimental investigations performed with HETRA test section has been to provide a suitable data set for the verification of corresponding computational models, special attention has been given to put in place the appropriate measuring scheme for the Eurofer temperature and coolant pressure drops. In fact, they have been considered the most important parameters to focus on.

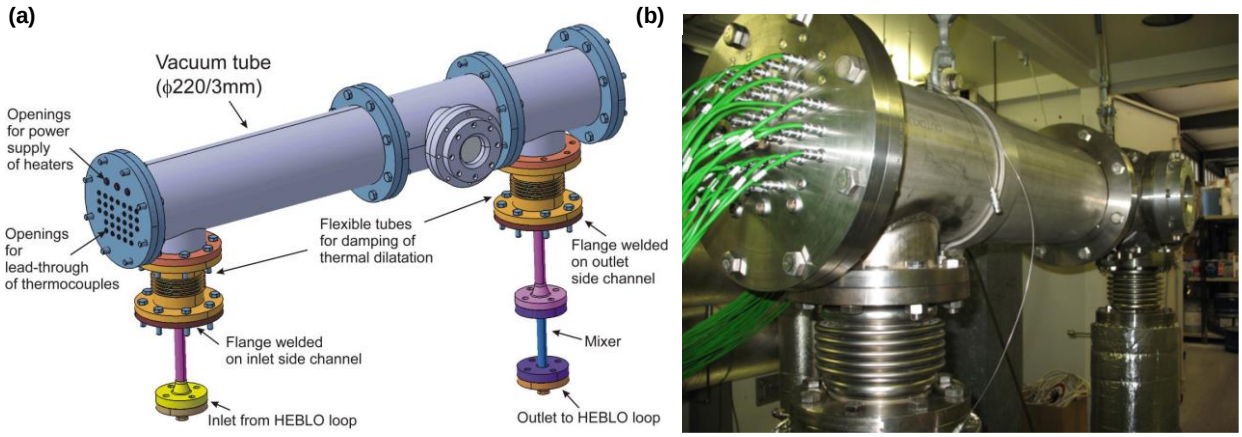

Figure 3-4: HETRA test section with vacuum vessel as thermal insulation [75]: general overview (a) and real aspect (b).

Nevertheless, some further measurements have been foreseen just for the purpose of controlling and regulating. Indeed, they are: measurements of heater temperature, measurements of coolant parameters (such as: mass flow rate, inlet and outlet temperature and absolute temperature) as well as measurements of the electrical current and voltage to determine the power supplied.

A detailed layout of the measuring scheme adopted is presented in Figure 3-5. In particular, as regards the Eurofer temperature, it was foreseen to determine its distribution through 60 measuring points (thermocouples) grouped into 6 identical sets called ‘measuring planes’. Hence, there are 10 different measuring positions for each measuring plane and, as can be derived from the detail in Figure 3-5 showing the thermocouples positions, 5 of them are placed exactly in the cross-section centreline. The latter have been considered for the development of the work reported in this dissertation as they have been identified as the most significative.

The inlet helium temperature is measured before entering to HETRA test section in correspondence of

HEBLO connection pipeline (measuring position T_{F1} in Figure 3-5), just downstream the orifice plate used to measure the mass flow rate. Instead, the outlet temperature is determined through the two measurement positions T_{F2} and T_{F3} reported in Figure 3-5.

As far as the determination of pressure drops within the HETRA test section is concerned, it has been foreseen to adopt pressure taps both at the inlet and at the outlet of the two side channels (see measuring locations P_2 and P_3 in Figure 3-5) paying special attention to place such taps where could not there be flow disturbances.

For the sake of completeness, Table 3-1 is summarising the thermal physical properties of the main materials involved at 573.15 K, while their dependence on temperature is described in [84, 85] and it is not here reported for sake of brevity.

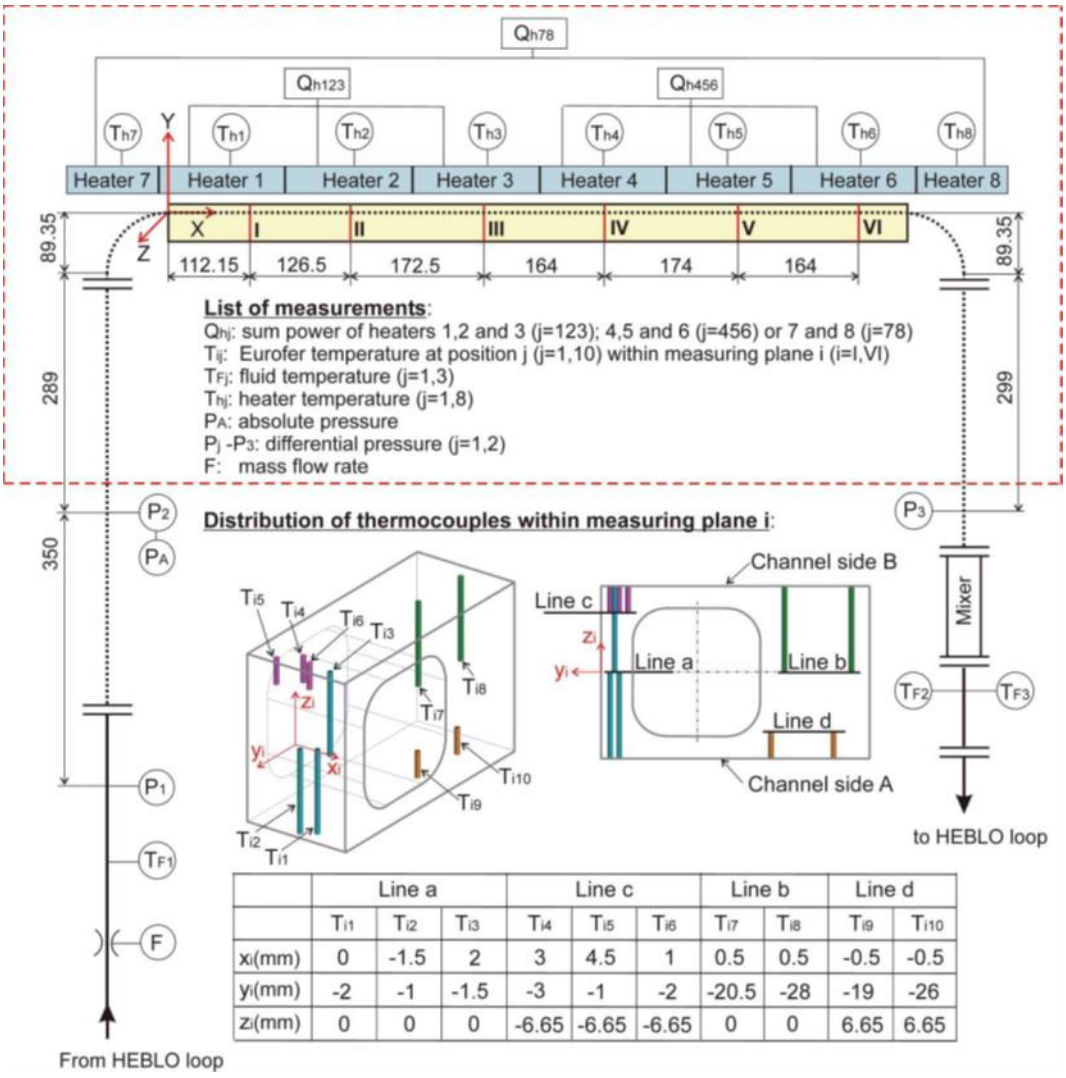

	Line a			Line c			Line b		Line d	
	T_{i1}	T_{i2}	T_{i3}	T_{i4}	T_{i5}	T_{i6}	T_{i7}	T_{i8}	T_{i9}	T_{i10}
x_i(mm)	0	-1.5	2	3	4.5	1	0.5	0.5	-0.5	-0.5
y_i(mm)	-2	-1	-1.5	-3	-1	-2	-20.5	-28	-19	-26
z_i(mm)	0	0	0	-6.65	-6.65	-6.65	0	0	6.65	6.65

Figure 3-5: Flow diagram and measuring scheme of HETRA test section [82].

Table 3-1: Thermal physical properties of HETRA materials

Material	Density [kg/m³]	Thermal Conductivity [W/m·K]	Specific heat [J/kg·K]
Eurofer	7685	33.2	527
Copper	8933	401	385
AISI 316 SS	8238	13.4	468
Graphite	2210	$\lambda_{/\!/}$ 1950 - $\lambda_{\perp}$ 5.7	709

The experimental campaign conducted on HETRA has involved a set of 6 measuring series (from M1 to M6, identified by means of specific labels), reported in Table 3-2, which have been defined by varying three main parameters:

- the surface roughness of the heated section, considering a smooth channel with an average R_z = 0.5 μm and a rough one with $R_z \approx 20$ μm. In the identification labels, they have been denoted with 'S' for the smooth and 'R' for the rough channel;
- the inlet temperature of the helium coolant ($T_{He,i}$). Two values have been considered: 323.15 K (50 °C) and 573.15 K (300 °C) which have been identified, in the experiment labels, as 'THe50' and 'THe300', respectively;
- the heater power (Q_H). With regards to the notation adopted for the series identification labels, 'L' stands for the German word for power (Leistung) while 2x has been used to indicate that the heaters are powered by 2 electrical sources. Table 3-2 is reporting also the power effectively transferred to the helium coolant (Q_{He}), in order to have an idea about the heat losses (Q_L), calculated by an energy balance once measured the helium inlet and outlet temperature.

Table 3-2: HETRA facility test matrix

Measuring series		m_{He}	$T_{He,i}$	Q_H	Q_{He}	Q_L
Nr.	Name	[g/s]	[K]	[W]	[W]	[%]
Hydraulically smooth channel						
M1	STHe50L2x2600	80	323.15	2x2600		
M2	STHe300L2x2290	80	573.15	2x2600	2x2290	11.9
Hydraulically rough channel						
M3	RTHe50L2x2600	80	323.15	2x2600		
M4	RTHe300L2x2444	80	573.15	2x2600	2x2444	6
M5	RTHe300L2x1984	80	573.15	2x2100	2x1984	5.5
M6	RTHe300L2x1504	80	573.15	2x1600	2x1504	6

Considering the data availability, the adopted test for the validation activity has been that identified as M2-STHe300L2x2290. As it is pointed out in Table 3-2, such a test is characterized for having observed the greater heat power losses.

It has to be considered that the amount and the spatial distribution of the thermal power losses strongly influence the temperature distribution within the Eurofer structure. As the spatial distribution of the lost thermal power is not known from the measurements, two limit cases have been identified, as diffusely explained in the following. In the first case, the Q_H power is assumed to be totally transferred to the structure, practically assuming that no heat power loss arise, whereas in the second case the Q_{He} power has been uniformly imposed to the FW plasma face. Then, the temperatures obtained from the experimental campaigns have to be in between the numerically predicted temperature values.

3.2.2 The HETRA Computational Fluid Flow and Heat Transfer Models

A computational model of the HETRA test section has been developed for the RELAP5-3D system code in order to assess the code capability to predict the heat transfer phenomena and consequently to reproduce the temperature distribution experimentally observed. In this way, the followed modelling approach would be validated against experimental results.

The computational domain which has been used for modelling of HETRA test section is presented in Figure 3-6. It involves all the main components of the test section presented in Figure 3-3, except the heater which have been simulated imposing an average heat flux on the external surface of the heated section.

The model developed consists of 19 thermal-hydraulic components, being 5 PIPEs, 6 SINGLE JUNCTIONs, 2 TIME DEPENDENT VOLUMEs, 1 TIME DEPENDENT JUNCTION and 6 HEAT

STRUCTUREs. In addition, 3 CONTROL BLOCKs, 247 SIGNAL VARIABLEs and 2 TABLEs complete the model. The fluid conditions at the inlet are set through a TIME DEPENDENT VOLUME, while the mass flow rate is set at the outlet through a TIME DEPENDENT JUNCTION.

In order to better reproduce the hydraulic performance of the analysed system, the procedure described in §2.3 has been implemented to obtain the resistance loss coefficient reported in Equation (2.62) which has been provided as input to the RELAP5-3D model.

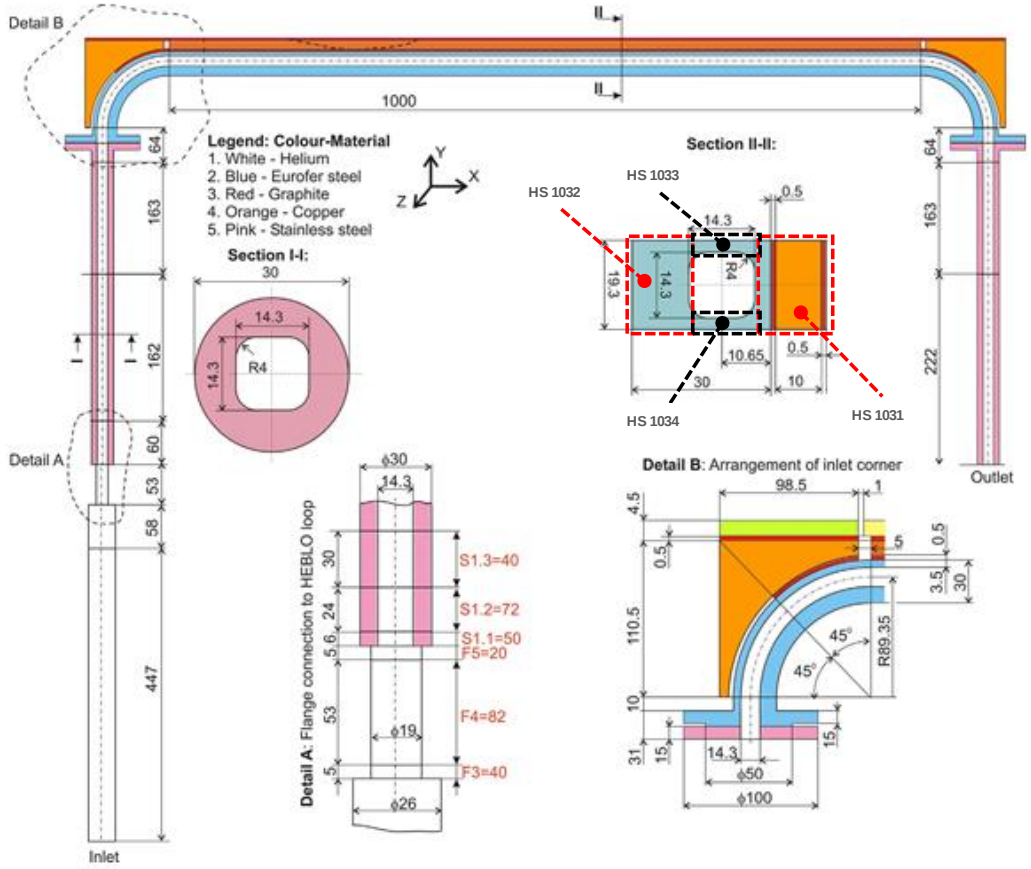

Figure 3-6: Main geometrical parameters of HETRA test section.

Figure 3-8 is showing the good agreement between the experimental hydraulic characteristic obtained at 293.15 K in comparison with the calculated ones. Indeed, the discrepancy between the pressure drop predicted by RELAP5-3D at the nominal mass flow rate value of 0.08 kg/s and the experimental measure is about 0.63%. The main assumptions and boundary conditions adopted for the HETRA model are reported in Table 3-5, whereas its mesh parameters are summarised in Table 3-4. Figure 3-7 shows the CFD model adopted for HETRA for its hydraulic characterization.

Table 3-3: HETRA: assumptions, models and BCs.

Parameter	Value
Analysis type	Steady-state
Material library	Helium
Flow temperature	293.15 K
Turbulence model	SST
Boundary layer modelling	Blended Near Wall Treatment
Wall absolute roughness	Smooth (~2μm)
Inlet BC	Mass flow rate
Outlet BC	Average static pressure

Table 3-4: Mesh parameters adopted for the pin discretization.

Parameter	Value
Nodes	$1.19 \cdot 10^{7}$
Elements	$6.25 \cdot 10^{6}$
Node density [m³]	$2.76 \cdot 10^{8}$
Defeature size [m]	$1.57 \cdot 10^{-4}$
Body sizing [m]	$5.00 \cdot 10^{-4}$
First layer height [μm]	10.00
Layers number	17.00
Grow rate	1.20

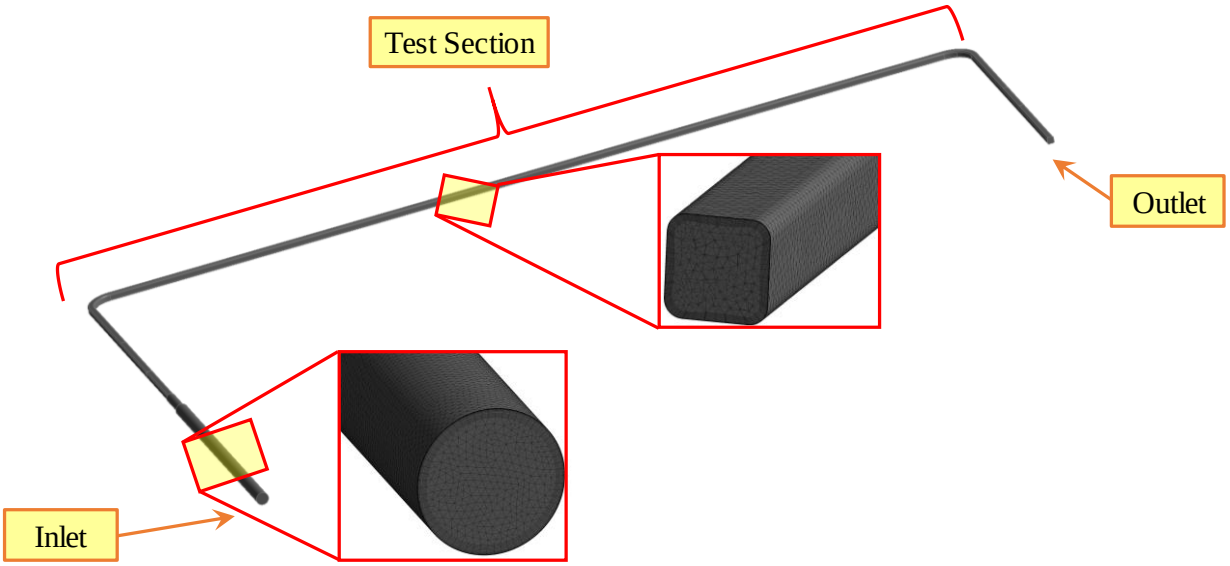

Figure 3-7: HETRA CFD model with details of mesh for the hydraulic characterization.

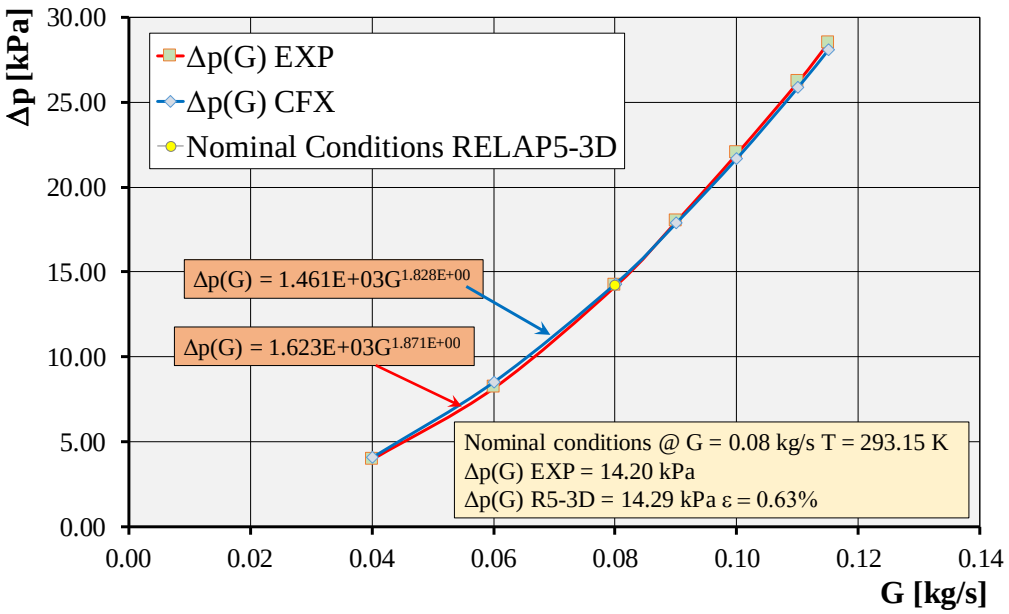

Figure 3-8: Experimental and computed hydraulic characteristic Δp(G) of HETRA.

As already disclosed, for the considered experiment the heat losses cannot be neglected in qualifying the prediction capability of the developed model, thus it has been decided to run two different calculations

by varying the power provided to the heated section model. Indeed, it has been simulated:

- a case in which the power provided to the structural material has been equal to that measured for the electrical heaters (P_Heaters);
- the case in which the adopted power input has been obtained from the following energy balance equation (P_Fluid):

$$P\_Fluid = Gc_p(T_{He,o} - T_{He,i}) \tag{3.1}$$

In particular, it has been simulated for both the two identified cases the power ramp-up phase as reported in Figure 3-9.

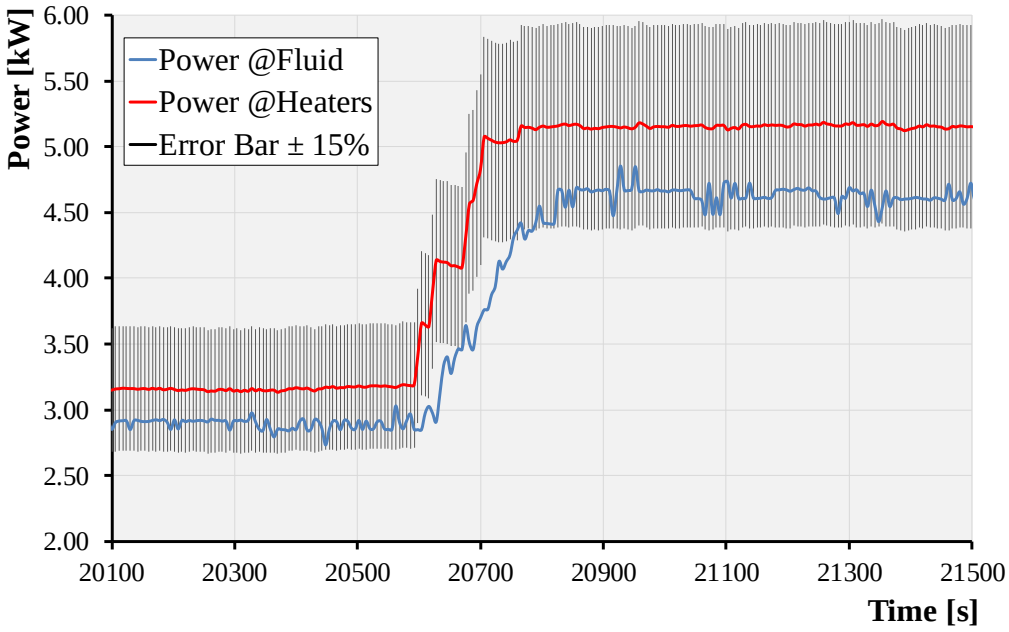

Figure 3-9: Power trend for the performed calculations.

As concerns the thermal modelling, the heat transfer phenomena have been reproduced implementing the thermo-physical properties of all the structural materials involved and by adopting the Gnielinski heat transfer model, in order to predict the heat transfer coefficient between helium and the structural material, which is reported in Equation 3.1:

$$Nu = \frac{(f/8)\cdot(Re-1000)\cdot Pr}{1+12.7\cdot\left(\sqrt{f/8}\right)\left(Pr^{2/3}-1\right)}\cdot\left[1+\left(\frac{D}{L}\right)^{2/3}\right]\cdot F \tag{3.1}$$

where Nu, Re and Pr are the adimensional Nusselt, Reynolds and Prandtl numbers, respectively; while f is the drag coefficient, L the entrance length, D the hydraulic diameter and F is a correction factor that accounts for heated wall effects. The drag coefficient, namely the Darcy factor, is calculated as reported in Equation 3.2:

$$f = \left(1.82\cdot\log_{10} Re - 1.64\right)^{-2} \tag{3.2}$$

while F, whether the bulk fluid is gas/vapour, is evaluated as: $F = \left(T/T_W\right)^{0.45}$, where T and T_W are the fluid and wall temperatures, respectively. Since, the Gnielinski correlation is valid for $2300<Re<10^6$, $0.6<Pr<10^5$ and $0.5<T/T_W<1.5$, it can be applied for the analyses experimental test.

Moreover, since 4 different HEAT STRUCTUREs have been adopted (see detail in Figure 3-6) to better reproduce the geometrical characteristics of the heated section, the so-called 'conduction enclosure model' has been activated in RELAP5-3D. This function allows to simulate multi-dimensional heat conduction in

a lumped parameter fashion [46], thus the capability to transfer heat via physical contact between different heat structure surfaces.

3.2.3 Comparison between Experimental Data and Computational Results

The main goal of the activity has been to verify the prediction capability of the computational model developed for RELAP5-3D by applying the proposed methodology in reproducing qualitatively and quantitatively the experimental data. With regards to

Figure 3-10, the outlet helium temperature obtained for the case identified as 'P_Fluid' lies on the experimental curve, as expected; while the one assessed for the case 'P_Heaters' is 0.23% greater, due to the already mentioned insulation problems which do not allowed to transfer completely the thermal power.

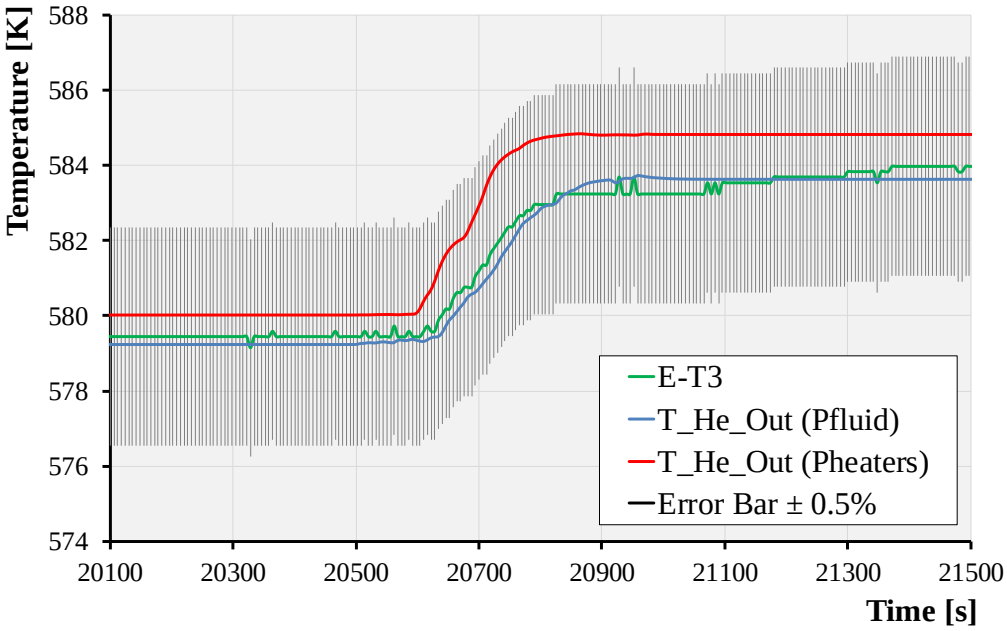

Figure 3-10: Outlet helium temperature.

As concerns the pressure drop prediction, it has been possible to reproduce the experimental data with a high confidence level, as shown in Figure 3-11, by implementing the resistance loss coefficient derived from the CFD characterization performed at an average temperature of 579.63 K, suggesting the suitability to adopt such a strategy for the further simulations.

Moreover, since the average helium temperature for both the cases considered are relatively small as well as the thermo-physical properties variations, the pressure drop trend evaluated in both the calculations performed practically reproduces the experimental one.

More precisely, the main goals of the activity described in this paragraph have been to assess the capability of the developed methodology to predict the temperature distribution in the structural material along with deriving precious indication to be taken into account for the DEMO simulation, such as the adoption of the conduction enclosure model. Indeed, its application has been crucial to better reproduce the experimental conditions since the 4 HEAT STRUCTUREs adopted to mimic the geometry of the heated section were physically de-coupled.

As a matter of fact, preliminary calculations have shown errors in the prediction of the temperature distribution of about ± 20÷25% without using it, especially for the Eurofer temperatures in the rear side (HS1032 in Figure 3-6) which were drastically underestimated.

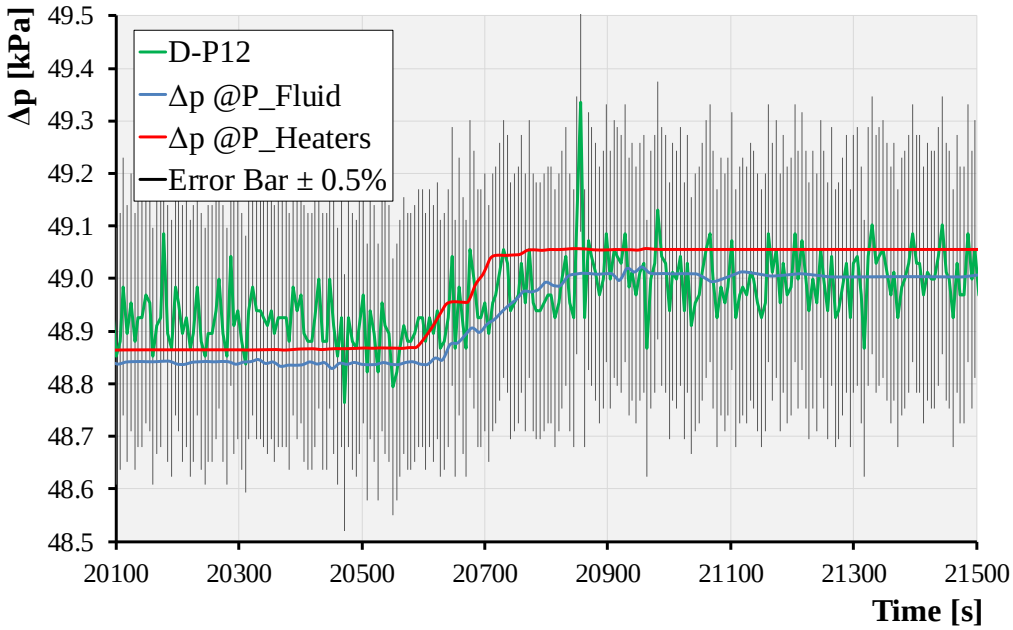

Figure 3-11: Pressure drop along the HETRA test section.

As previously said, 60 different temperature measuring point have been installed along the heated section equally distributed in 6 ‘measuring planes’ as depicted in Figure 3-5. In the following, Figure 3-12 to Figure 3-21 are comparing the measured temperature with those obtained with RELAP5-3D. In particular, the comparison has involved the thermocouples placed in the centreline, e.g. T_{i2}, T_{i3}, T_{i1}, T_{i7} and T_{i8} for the representative measuring planes, namely plane I and VI. In order to facilitate their detection, in each figure two legends have been included, showing the reference plane (in the top) and the thermocouple considered (bottom right corner). As it can be derived from such graphs, the temperatures predicted by the developed models reproduce qualitatively the experimental trend. Moreover, as expected when defining the two case, the experimental temperature falls into the range determined by the two calculated temperatures within a good degree of accuracy. Indeed, all the calculated values lie on the ±0.5% error bar of the experimental temperature. With special regard to the temperatures evaluated for the plasma side (T_{i2}, T_{i3}, and T_{i1} for the HS1031), it is possible to observe that for the plane I the experimental values are closer to those obtained with P_Fluid, while near the outlet, e.g. for the plane VI, the experimental ones are near those evaluated with P_Heaters.

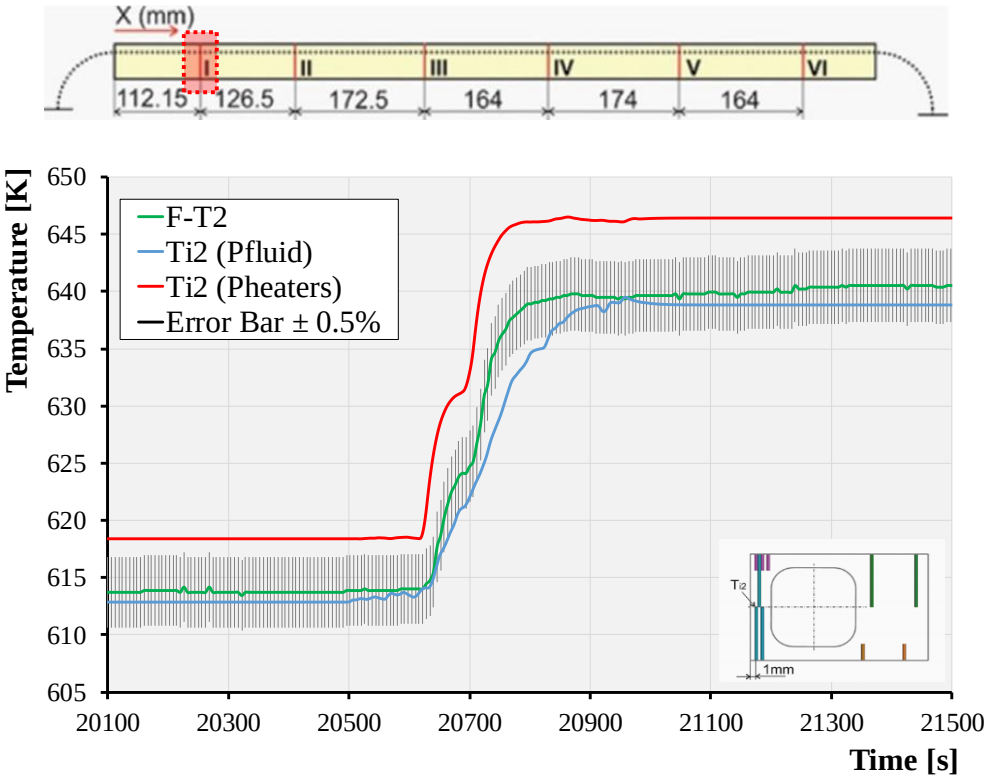

Figure 3-12: Temperature T_{i2} at Plane I.

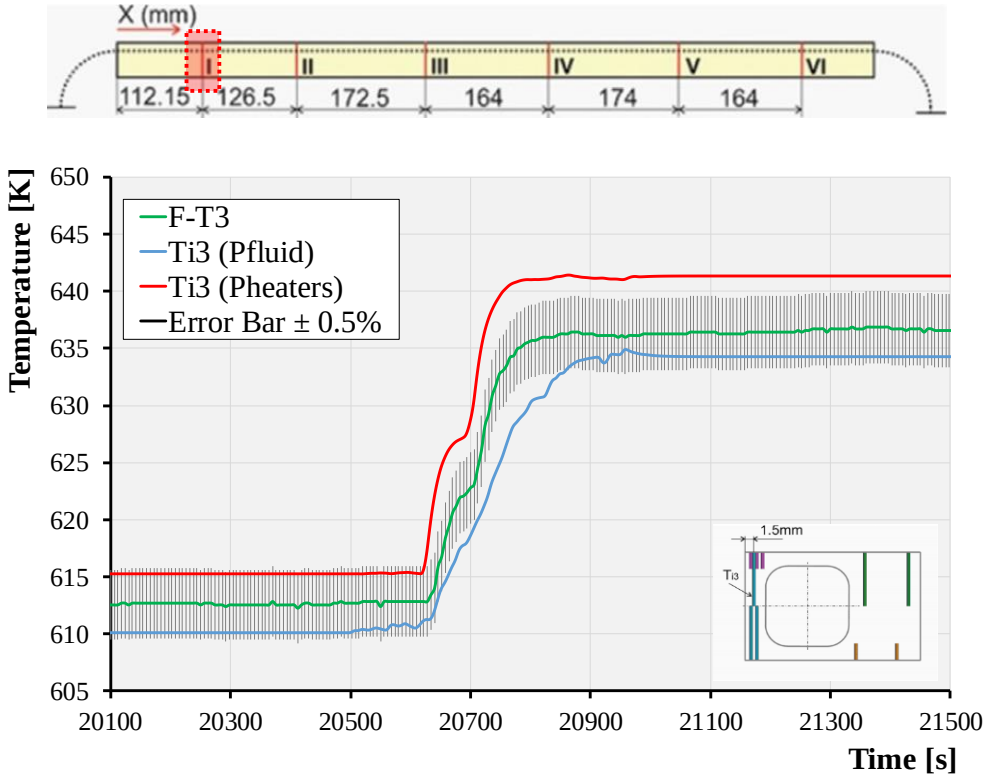

Figure 3-13: Temperature T_{i3} at Plane I.

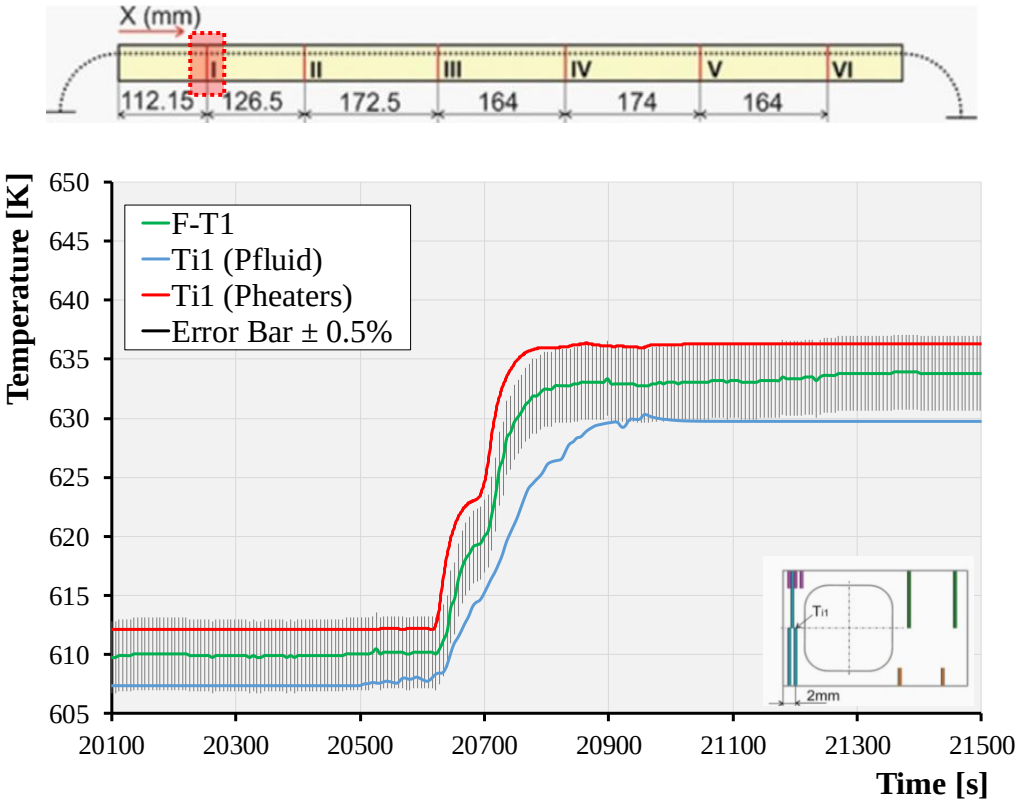

Figure 3-14: Temperature T_{i1} at Plane I.

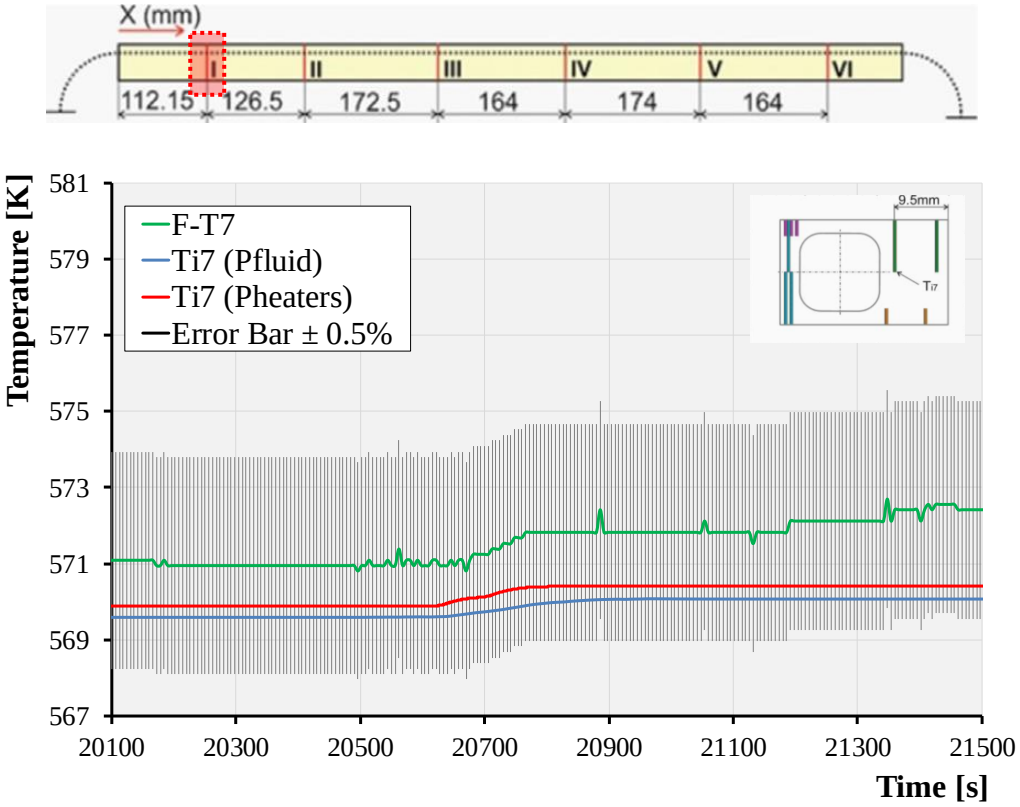

Figure 3-15: Temperature T_{i7} at Plane I.

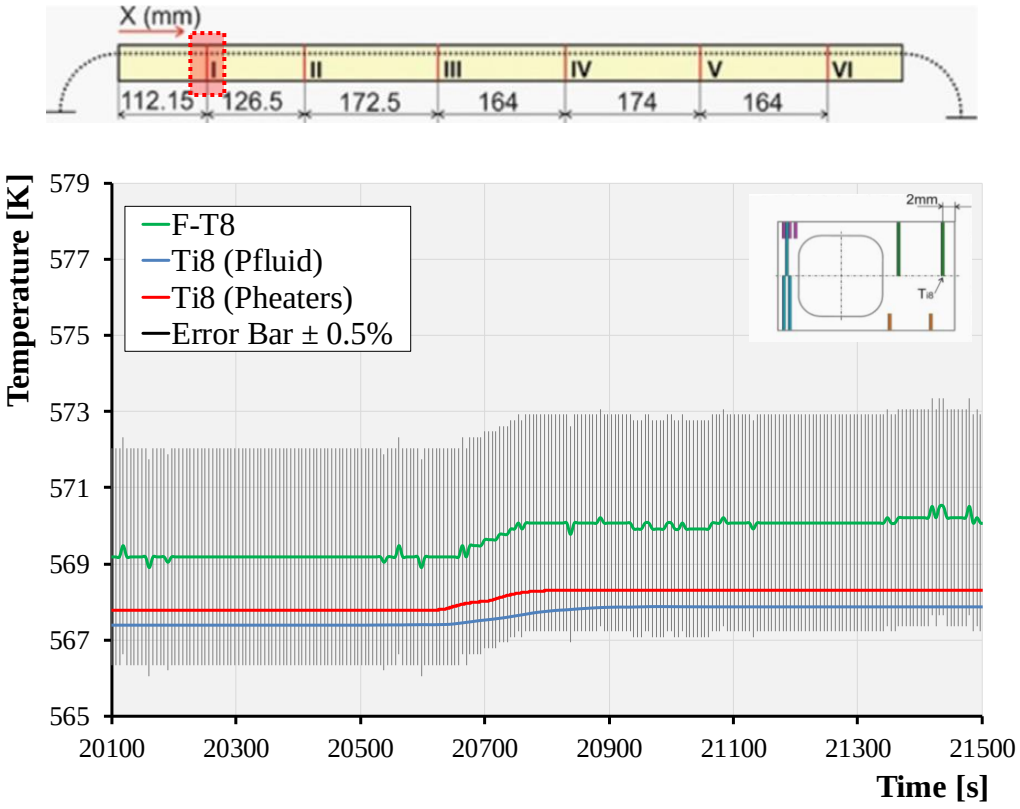

Figure 3-16: Temperature T_{i8} at Plane I.

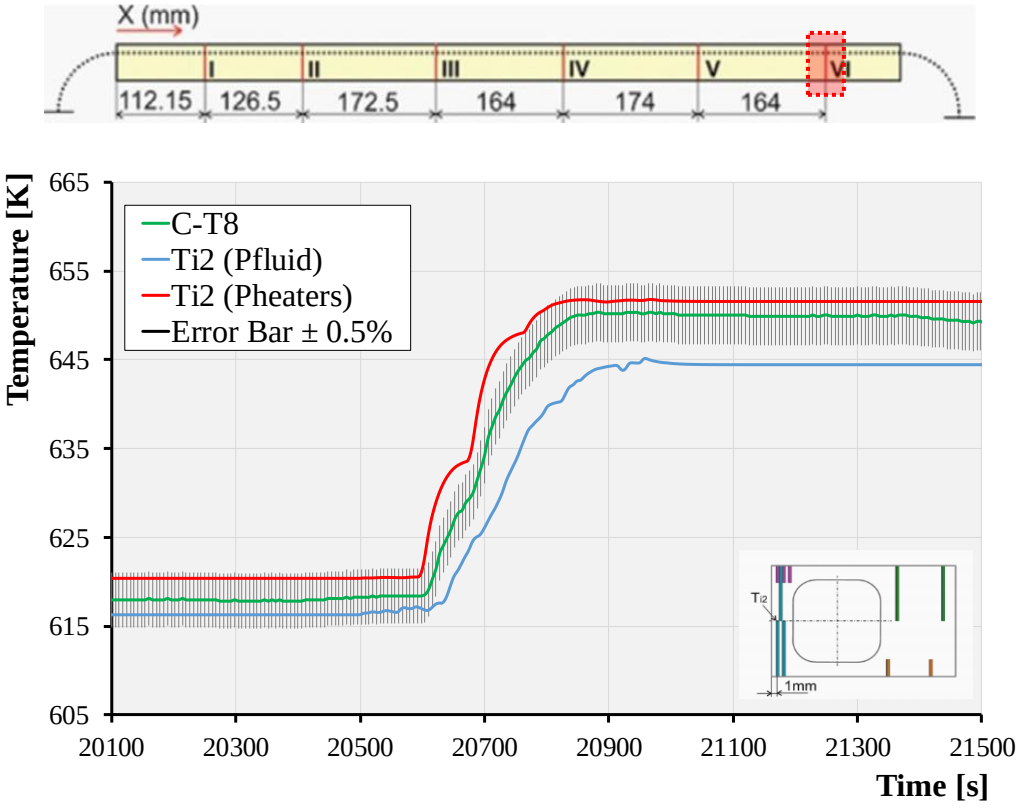

Figure 3-17: Temperature T_{i2} at Plane VI.

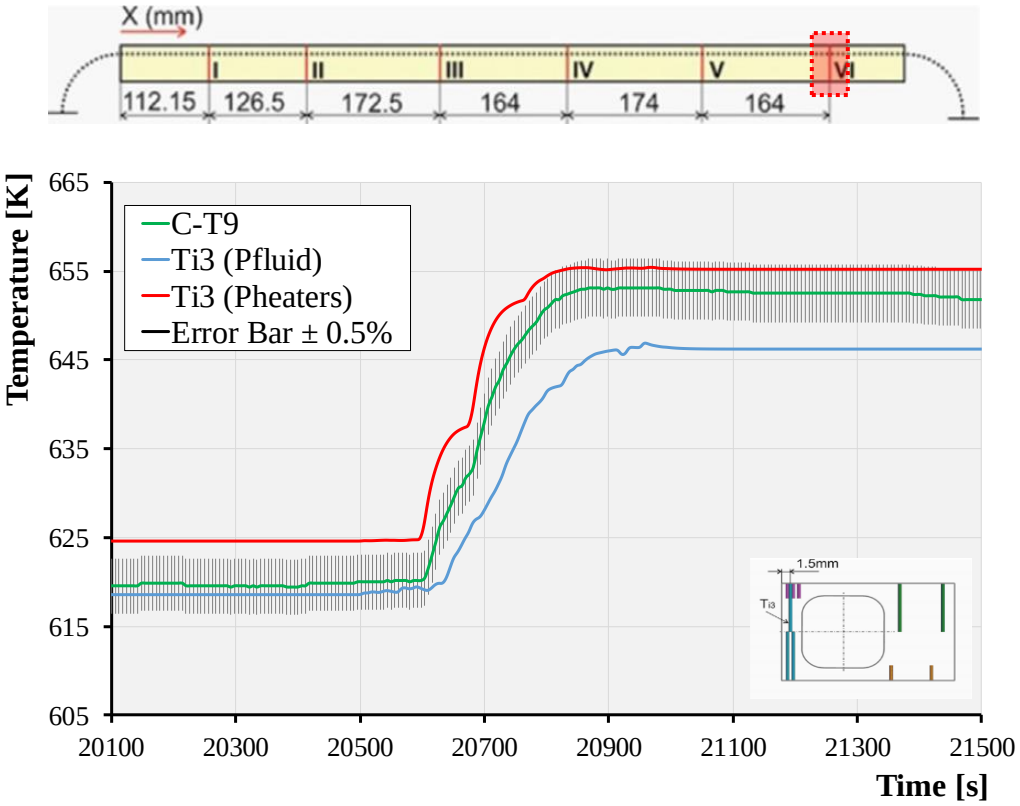

Figure 3-18: Temperature T_{i3} at Plane VI.

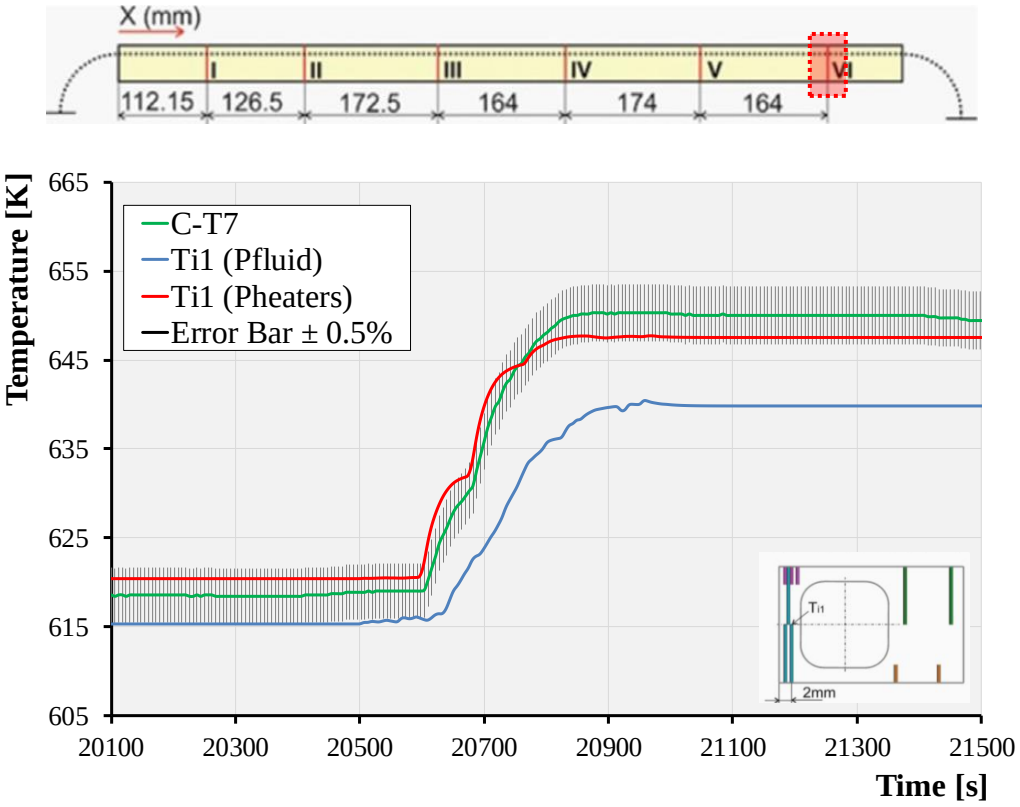

Figure 3-19: Temperature T_{i1} at Plane VI.

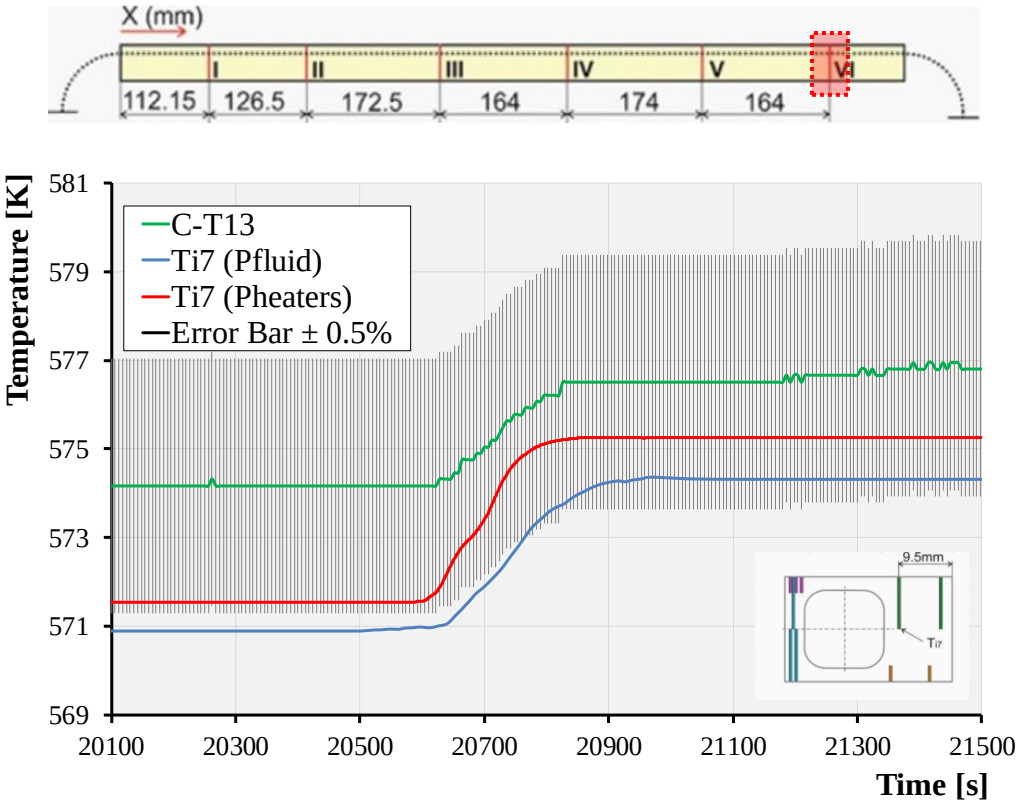

Figure 3-20: Temperature T_{i7} at Plane VI.

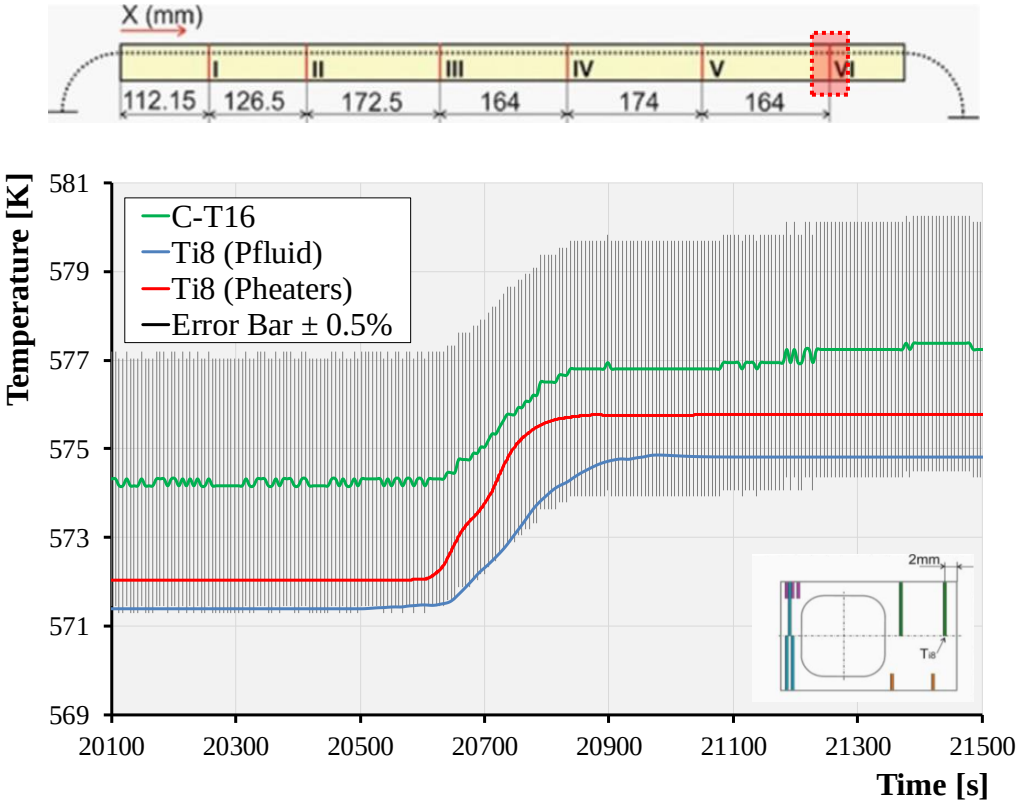

Figure 3-21: Temperature T_{i8} at Plane VI.

3.3 A Code-to-Code benchmark by using the RELAP5-3D and CATHARE system codes

The numerical benchmark involving the RELAP5-3D and CATHARE system codes in simulating the normal operational scenario of the relevant BB-PHTS loop of the HCPB DEMO baseline 2015 is described in this paragraph.

The main goal has been to compare the results obtained with the RELAP5-3D model, developed applying the proposed integral procedure, with those of an equivalent model for a thermal-hydraulic system code (i.e. CATHARE) widely adopted to simulate the GCR behaviour, highlighting features and assumptions. Indeed, the CATHARE2 system code is a reference thermal-hydraulic and safety code developed and validated in collaboration among CEA, Electricité de France (EDF), Institut de Radioprotection et de Sûreté Nucléaire (IRSN) and AREVANP for the French Pressurized Water Reactors (PWR) and adapted to deal also with GCR applications.

The code has a flexible modular structure for the thermal-hydraulic modelling in applications ranging from simple experimental test facilities to large and complex installations as Nuclear Power Plants (NPP). The main hydraulic components or elements are pipes (1-D), volumes (0-D), 3-D vessel and boundary conditions, connected to each other by junctions. Other sub-modules simulate pumps, turbo-machines, control valves, T-junctions, sinks and sources, breaks and many other ones. All these CATHARE modules are based on the six-equation two-fluid model described in §2.2.2. However, an additional option has been added to improve CATHARE numerical efficiency when the flow is a single-phase gas. The modifications are based on the hypothesis that the residual liquid phase is present with concentration low enough to have a negligible impact on the gas phase and the surrounding walls. Even if the residual phase is still computed in the calculation, the treatment of the associated source terms and closure laws can be drastically simplified. The results of the calculation are unchanged compared to the corresponding full two-phase calculation, but the computational overhead involved in carrying equations and variables for the residual phase is drastically reduced, and the convergence is significantly improved.

The CATHARE system code is currently used to study a large number of rather different GCR concepts and component designs. The ‘standard’ correlations are consistent with the PWR applications and dedicated correlations have been implemented for the specific GCR components designs.

In order to simplify the modelling it is now possible selecting special correlations (with relevant parameters) for wall friction and heat transfer from an extensible correlation library. The selection is done for individual hydraulic elements, directly in the input deck. This feature is particularly useful for heat exchangers of different designs: tube-and-shell heat exchangers, tubes with or without fins, etc.

The GCR concepts studied by the CEA usually involve turbines, compressors and/or blowers, possibly linked on one or more common shafts. A turbo-machine module has therefore been developed for the CATHARE code. The turbo-machine specifications are either given directly in the input deck, or implemented in a user library from which different turbo-machines can be selected by their name in the input deck. The data of the turbo-machine performance maps can be entered either as fitted polynomial functions, or as tables of performance data.

The code has been also validated against HE-FUS 3 experimental data increasing the confidence to use CATHARE 2 for GCR calculations [77].

3.3.1 Base Case Scenario Adopted for the Benchmark

As already disclosed, the base case adopted for the numerical benchmark has been the simulation of normal operational conditions for the relevant BB-PHTS loop designed for the HCPB DEMO baseline 2015 [86]. The DEMO baseline 2015 consists of 18 identical sectors of 20° along the toroidal direction, subdivided according to the number of coils. In each sector, there are 5 BB segments, 2 IBs and 3 OBs.

Considering such a baseline and with reference to Figure 3-22, each HCPB BB segment (IB and OB) is divided into 7 modules. The BZ is housed behind a U-shape FW, conceived along a radial-toroidal-radial path, with the two remaining poloidal sides closed by caps, forming a structural box/module that is attached to the back supporting structure (BSS). Within the BZ the pebble beds of Li_4SiO_4 and Be are alternating with the cooling plates (CPs). Within the CP, 32 cooling channels are routed along the toroidal direction for cooling down the structure using a counter-current flow scheme. In-between these 'functional' cooling channels, the so-called 'dummy' channels are implemented so as to minimize the steel volume fraction in the BZ, thus reducing the parasitic neutron absorption in the BZ and maximizing the T breeding. The half of the pebbles beds and one cooling plate form the elementary cell that is repeated along the poloidal direction. Hereafter, the term "slice" will be used to indicate this elementary unit.

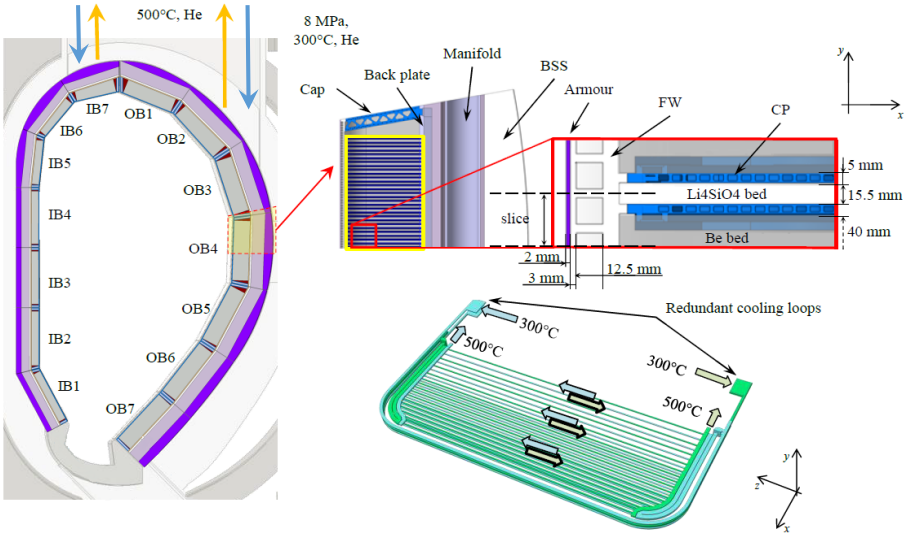

Figure 3-22: HCPB BB concept segmentation and module details in the EU DEMO baseline 2015.

The FW is covered with a W-armour layer and it shall tolerate the high heat flux coming from the plasma ensuring sufficient neutron transport to fulfil tritium breeding function.

The BSS shall ensure a structural function along the poloidal direction to support all the blanket modules at the right position. Within the BSS, the manifolds for coolant and purge gas are routed to distribute and collect He in the various blanket modules. The coolant pressure and inlet temperature are assumed to be 8 MPa and 573.15 K, respectively. The coolant outlet temperature is set to 773.15 K, as the Eurofer creep strength is greatly reduced at temperatures above ~823.15 K, as already mentioned. The cooling scheme, within the modules, is articulated in two parallel circuits that take the half of coolant and are used for ensuring a counter-current flow in the FW and BZ. Beginning from the BSS at 573.15 K, the first cooling loop (namely, loop1) cools the 50% of the FW and then of the CPs, exiting the BZ and entering again the BSS, where the flow at about 773.15 K is routed out of the VV. At the same time, the second cooling loop (namely, loop2) covers the other 50% in the opposite direction ensuring a fully counter-flow of FW and CPs. The purge gas is helium with an addition of 0.1%wt. H_2. Its pressure is set to 0.2 MPa and it exits the BSS at about ~723.15 K. Both the inlet and outlet coolant manifolds enter from are routed at the upper part of the segment.

As concerns the BB PHTS architecture, it relies on the adoption of 9 cooling loops, completely independent from both mechanical and functional point of view in order to limit some common mode failures. The IB is cooled by means of 3 loops whereas the remaining 6 circuits are employed to remove the thermal power from the OB portion of the tokamak. An IB loop is responsible for providing helium to 6 blanket sectors while an OB loop cools the segments of 3 sectors. Figure 3-23 shows the 3D-CAD model of the HCPB BB PHTS simulated, while Table 3-5 reports its main data.

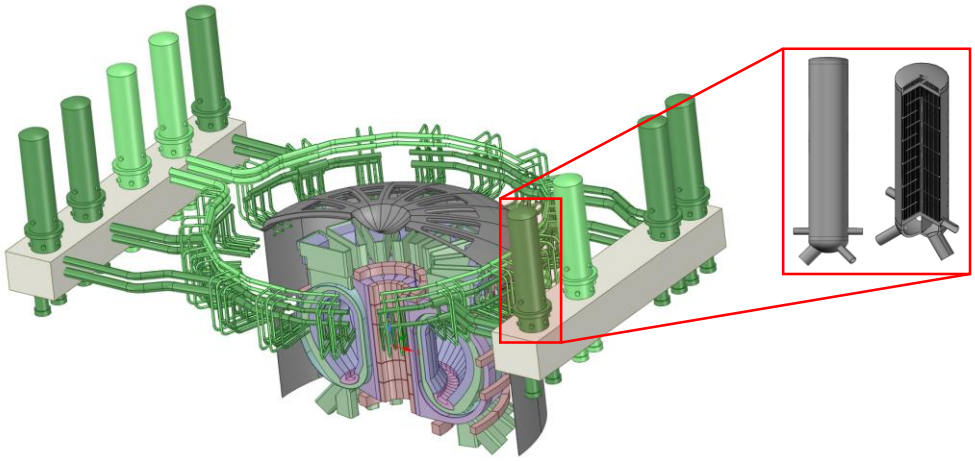

Figure 3-23: 3D view of the HCPB BB-PHTS cooling loops.

Table 3-5: HCPB BB-PHTS main data

Parameter	Value
Thermal power [MW]	2101.7
Circulator power [MW]	130.4
Total He volume [m³]	1976.4
Total piping length [m]	4002.8
IB/OB cooling loop [-]	3/6
IB/OB FW&BZ ΔP [kPa]	194.0/154.0
IB/OB Ex-VV piping ΔP [kPa]	62.0/56.6

As already shown in Figure 1-9, the Intermediate Heat eXchanger (IHX) represents the interface between the DEMO PHTS and the IHTS. In particular, the IHX has similar features to existing model widely adopted in nuclear and conventional industrial applications. Indeed, its availability on the market has been one of the main drivers for the component selection. As concerns its design, a two-pass tubes, two-pass shell configuration (TEMA BFM type [37, 38]) has been adopted. In this configuration, helium flows within tubes whereas the HITEC salt crosses the shell side. Such choice has been made mainly due to the helium higher pressure and to mitigate the effects of loss-of-coolant accident. The tube side thermal-hydraulic conditions have been selected to be compliant with the blanket requirements. In particular, the helium temperature at the IHX outlet decreases until 558.15 K before helium is compressed by the circulators (2 per loop) reporting its temperature at the BB target value of 573.15 K. On the other hand, the secondary cycle temperatures have been set to 543.15 K – 738.15 K (T_{in} and T_{out} respectively). Table 3-6 is summarising the main parameters related to the IHX for both IB and OB segments [37, 38].

Table 3-6: IHXs main data

Parameter	IB	OB
Thermal power [MW]	208.1	267.8
T_{in}/T_{out} He [K]	773.15/560.85	773.15/562.45
T_{in}/T_{out} HITEC [K]	543.15/738.15	543.15/738.15
Tube length (per pass) [m]	12.2	11.6
Tube number (per pass) [-]	5801	7426
Tube ext. diameter [mm]	19.05	19.05
Tube int. diameter [mm]	15.75	15.75
IHX ΔP [kPa]	87.9	85.1
Total He volume [m³]	49.5	61.5

Concerning the compressors design, the HElium LOop KArlsruhe (HELOKA) experimental facility has been considered [87]. The HELOKA facility was built at KIT-INR to test helium cooled components for fusion applications, especially those related to the HCPB TBM programme. Since only a few parameters for the working point (pulse phase) of the compressor, namely head, efficiencies, and then power, have been defined so far for DEMO in order to model its dynamic behaviour, the performance maps of the HELOKA-like centrifugal compressor have been adopted. Such performance maps have been properly scaled-up to fit the HCPB PHTS specifications. Figure 3-24 and Figure 3-25 are showing the pressure ratio and the efficiency maps for the considered compressor.

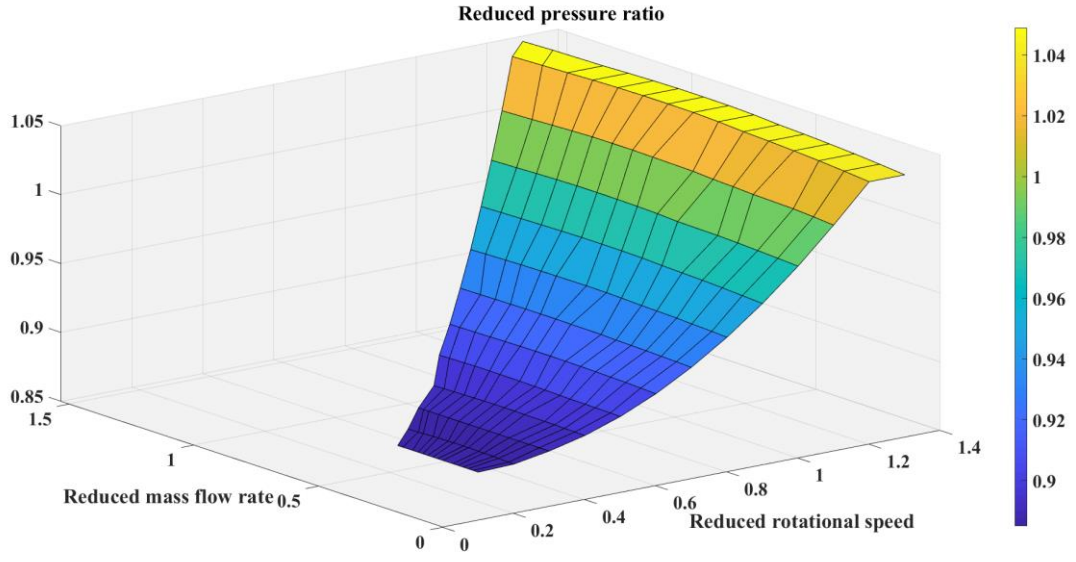

Figure 3-24: Reduced pressure ratio.

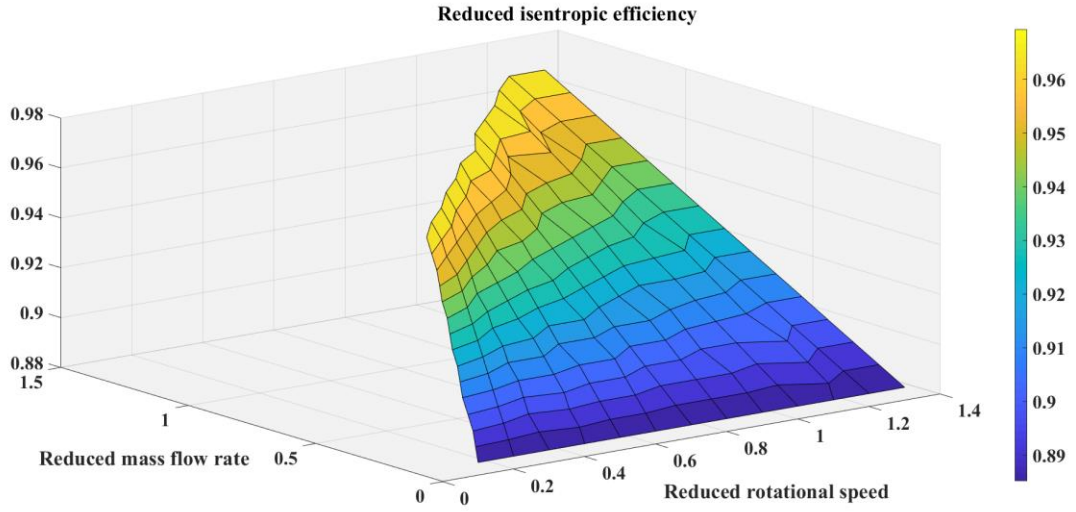

Figure 3-25: Reduced isentropic efficiency.

With regards to the thermal loads to be considered, as already said before, the simulated scenario consists in the normal operational conditions of the HCPB DEMO reactor. It foresees a continuous succession of 2 main phases joined by 2 transitional phases: (i) the plasma ramps-up within 100 seconds bringing its power from zero to the maximum value, (ii) when the full power level is reached this condition is sustained for 2 hours, then (iii) a ramp-down of 100 seconds brings the system into (iv) the dwell phase which lasts 10

minutes and where almost no power is generated, as the decay heat 1 second later the shut-down is around 1.7% of the nominal power. Figure 3-26 depicts the DEMO fusion power trend highlighting the 4 phases mentioned before. Whilst Table 3-7: OB Segment Thermal Loads reports the thermal loads of each OB Segment module, distinguishing between the FW and BZ heat loads.

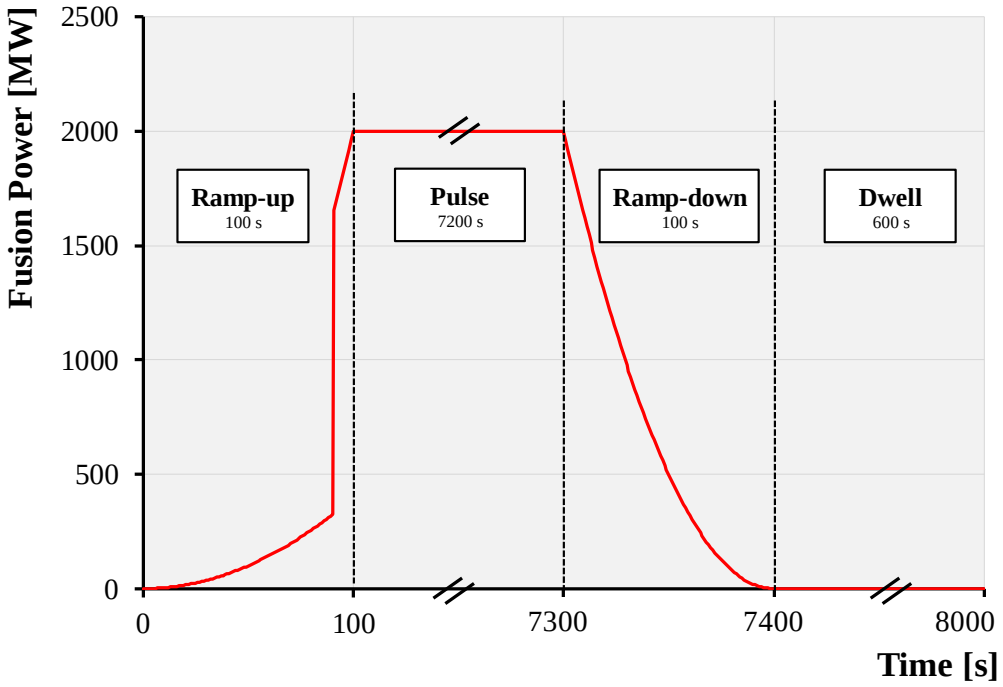

Figure 3-27: Fusion power.

Table 3-7: OB Segment Thermal Loads

OB Module	FW radiative power [MW]	FW neutron heat load [MW]	FW radiative power from BZ [MW]	BZ total power [MW]
#1	4.183E-01	3.505E-01	1.880E-01	2.119E+00
#2	5.352E-01	4.484E-01	2.405E-01	2.711E+00
#3	5.852E-01	4.903E-01	2.629E-01	2.964E+00
#4	6.348E-01	5.319E-01	2.852E-01	3.216E+00
#5	6.067E-01	5.084E-01	2.726E-01	3.074E+00
#6	5.462E-01	4.576E-01	2.454E-01	2.767E+00
#7	4.712E-01	3.948E-01	2.117E-01	2.387E+00

3.3.2 Computational Models Developed for the Benchmark Assessment

In order to perform the numerical benchmark between RELAP5-3D and CATHARE codes, suitable models of the relevant BB PHTS loop have been developed paying particular attention in removing possible inconsistencies in the nodalization scheme, initial conditions and model's options. Moreover, the models nodalization has been carried out to realistically simulate the thermal-hydraulic behaviour of the selected loop under the foreseen operating conditions. In particular, the primary side of the considered loop has been modelled, while the secondary side of the IHX has been considered by applying a proper thermal boundary condition able to remove the thermal power and to control both pressure and temperature at the BB inlet. In fact, both the two system codes were not equipped with the proper libraries specifying the thermo-physical properties of the HITEC molten salt.

In both the two models four main sub-models can be identified, namely (i) the flow domain model, reproducing the geometric features of the cooling circuit; (ii) the constitutive models implemented into the

system codes, describing the thermo-dynamic behaviour of the coolant; (iii) the hydraulic model simulating the fluid flow inside the cooling loop and (iv) the thermal model reproducing the heat transfer phenomena which take place along the considered system.

As concerns the geometrical sub models, both the model nodalizations have been developed to reproduce the main features of the systems briefly described in the previous paragraph and detailed in [37, 84] by adopting the convenient components available in the two system codes in accordance with what is reported in §2.2.3.

More specifically, since each OB BB-PHTS remove the thermal power of 3 different sectors, each one housing 3 OB segments with 7 BB modules per segment, it has been decided to model just 1 sector in a more 'detailed' fashion, e. g. preserving the segments; while for the 2 remaining sectors the segments have been collapsed together. This has proved necessary in order to adopt an admissible components number and to allow the simulations running in a reasonable calculation time. Moreover, in the RELAP5-3D model, 1 segment has been detailed simulating each modules to provide useful information about the mass flow rate distribution to the BB design team. In particular the RELAP5-3D model, shown in Figure 3-27, consists of 345 thermal-hydraulic components, being 67 PIPEs, 2 MULTIPLE JUNCTIONs, 5 BRANCHs, 1 COMPRESSOR and 270 HEAT STRUCTUREs. In addition, 35 CONTROL BLOCKs, 36 SIGNAL VARIABLEs and 49 TABLEs complete the model. Figure 3-28 illustrates the nodalization adopted for the detailed segment model and the one adopted for both segment and sector.

The CATHARE model includes 110 hydraulic 'modules', which are 60 AXIALs, 30 BCONDITs (boundary conditions) and 20 VOLUMEs. Additionally, there are 105 'sub-modules': 1 TCOMCHAR (compressor), 29 TEEs, 60 WALLs and 15 EXCHANGER which complete the nodalization depicted in Figure 3-29.

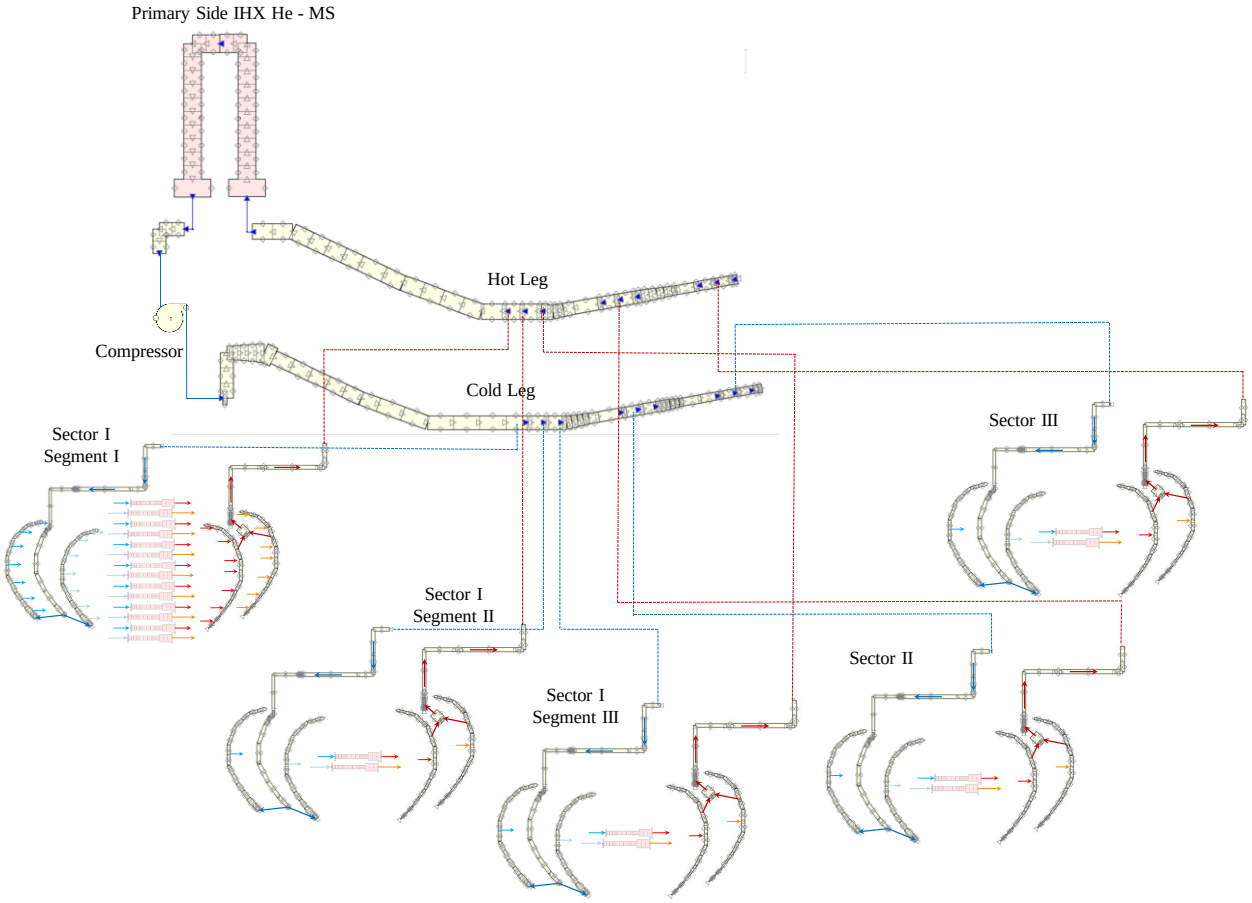

Figure 3-27: RELAP5-3D nodalization scheme.

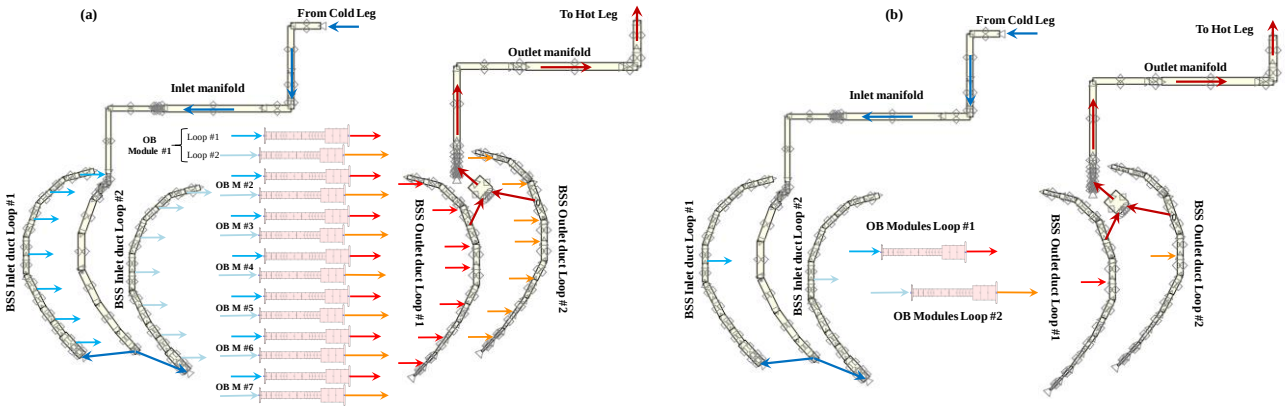

Figure 3-28: View of the nodalization adopted for the (a) detailed segment and (b) the other segments/sectors.

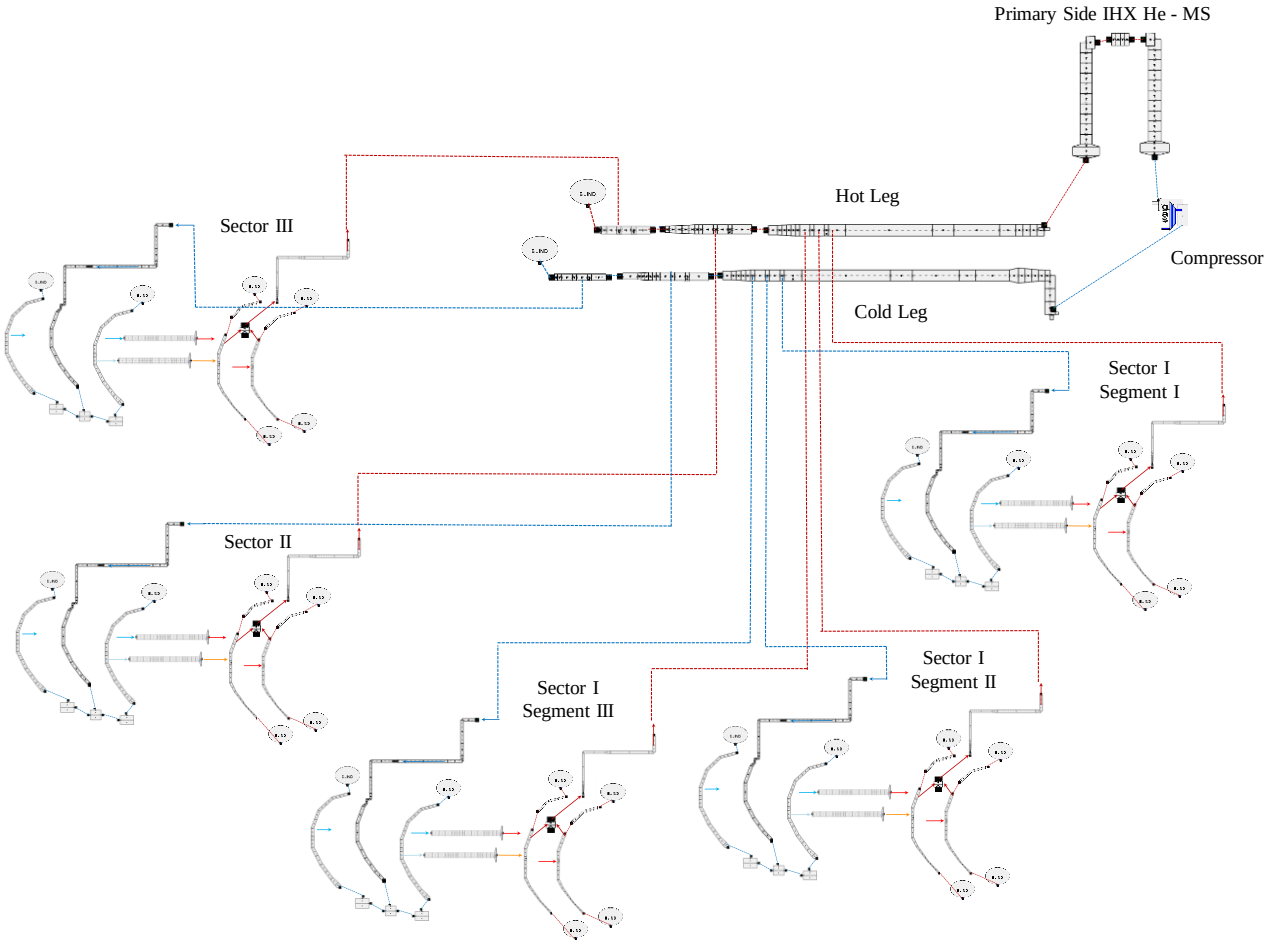

Figure 3-29: CATHARE nodalization scheme.

With regards to the hydraulic sub-model, as anticipated in §2.3, a detailed parametric analyses has been performed by means of ANSYS CFX evaluating the hydraulic characteristic function needed to input the effective hydraulic loss coefficient in both the two system codes.

In particular, such a characterization has been carried out for the so-called slice, since there deeply 3-D phenomena taking place. While for the other components the concentrated hydraulic loss coefficients have been evaluated by using [88]. To this end, a dedicated model of the slice cooling circuit has been set up (Figure 3-30). Tetrahedral elements are adopted taking into account the geometrical features of the domains to be meshed and the required optimization of the nodes number and mesh quality. The mesh is composed of ~17.1E+06 nodes linked in ~7.5E+06 elements with an orthogonal quality average of 0.643 and skewness

average of 0.356. A number of 10 inflation layers has been used with first layer height of 5.5E-05 m and a growth rate of 1.2. For the calculation of hydraulic characteristic, an average temperature of 673.15 K has been assumed and the mass flow rate has been ranged from 0.01 kg/s to 0.1 kg/s subdivided in 10 bins (the nominal mass flow rate for each HCPB slice loop is 0.046072 kg/s [84]). The planes on which the pressure drops have been calculated are illustrated in Figure 3-30, while the characteristic functions Δp(G) and K(u) are reported in Figure 3-31 and Figure 3-32, respectively.

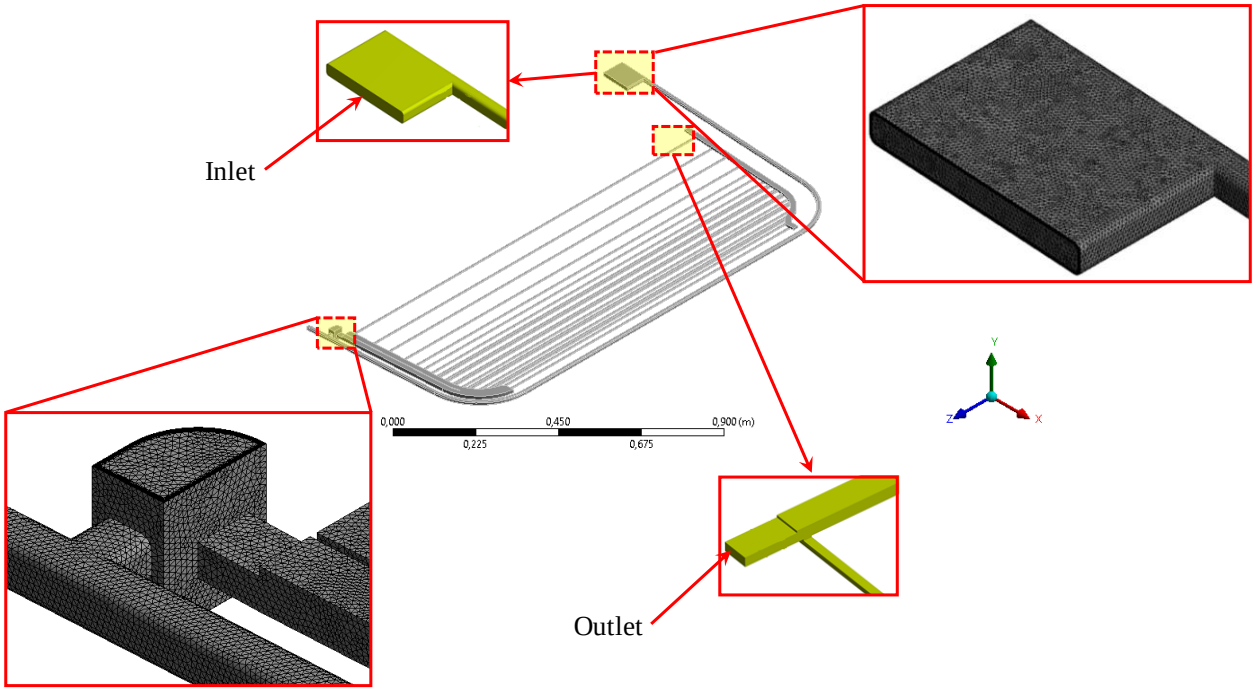

Figure 3-30: Slice cooling circuit with detail of mesh and planes for the determination of pressure drops.

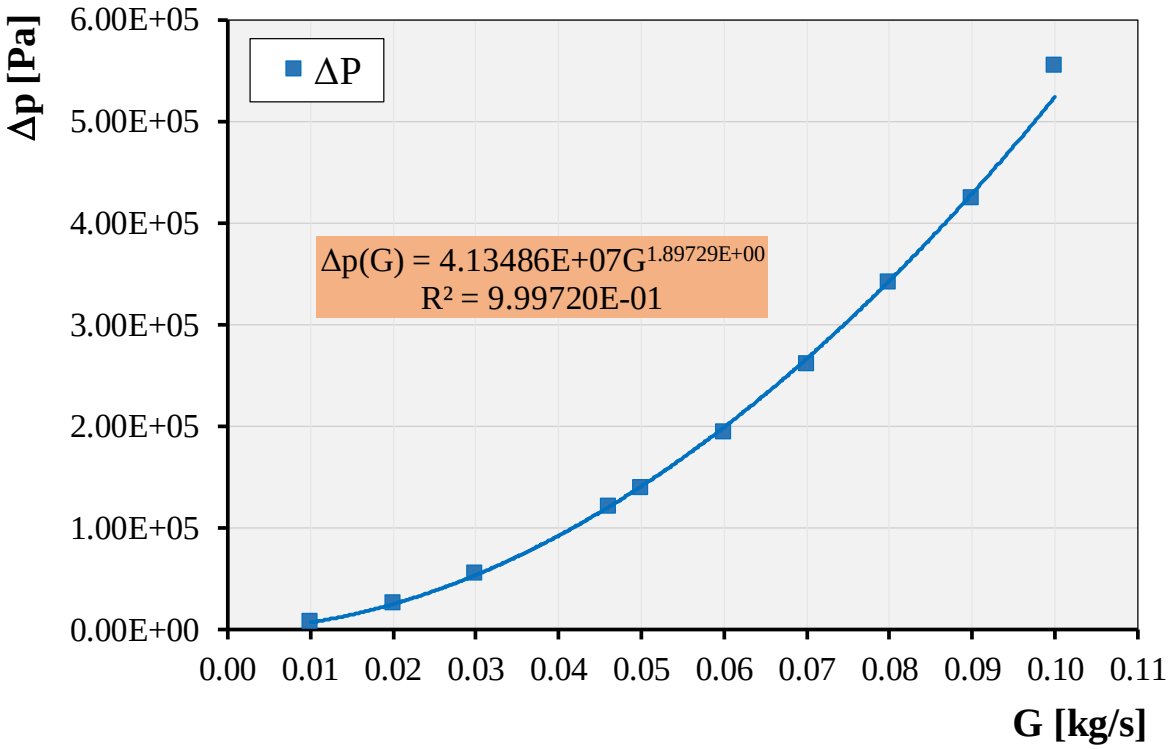

Figure 3-31: Δp(G) characteristic function and interpolation equation.

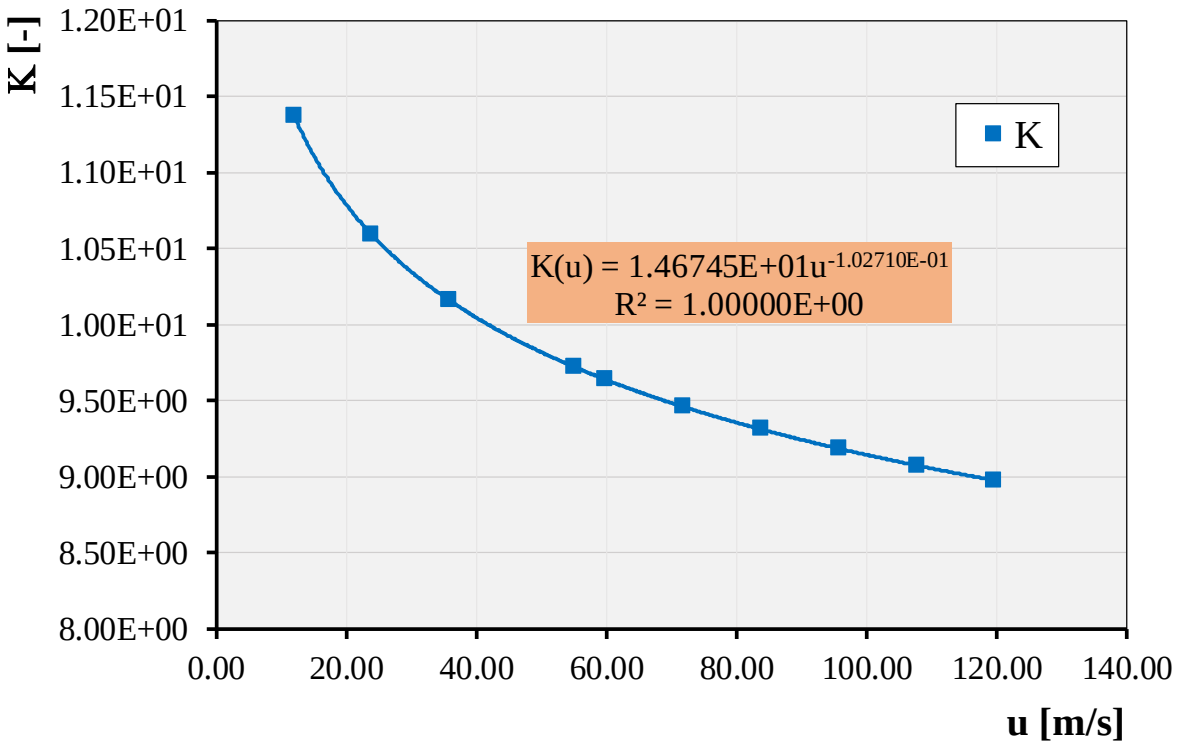

Figure 3-32: K(u) characteristic function and interpolation equation.

Moreover, still as regards the hydraulic model, it should be pointed out that the CATHARE code calculates distributed pressure losses for smooth tubes by the Blasius equation. Since the models developed are simulating components where the absolute roughness varies between ~ 12 and 50 μm, the FRICLAW keyword has been used to reproduce this aspect. In particular, for each hydraulic component - apart those simulating the slices -, the coefficients of FRICLAW have been calculated trough the Zygrang and Sylvester formulation of the Colebrook-White equation [47, 89]. The only drawback of this adopted procedure is that, as input of the FRICLAW keyword, a single value of hydraulic diameter is required for each of the axial component largely adopted. For this reason, aiming for preserving the pipe overall pressure drop, in case of pipes with variable cross-section, an equivalent hydraulic diameter has been iteratively calculated minimising the difference between the overall pressure drop of the real pipe and that of an equivalent pipe with constant cross-section. However, such discrepancies, although very small, affect the helium mass flow rate distribution among the simulated segments and sectors, as shown in the following paragraph.

As concerns the thermal modelling, the heat transfer phenomena have been reproduced implementing the thermo-physical properties of all the structural materials involved [37, 84] and by adopting the properly selected heat transfer models, namely the largely adopted Gnielinski correlation, already implemented in the RELAP5-3D models package and purposely assigned in CATHARE by means of the EXCHLAW keyword. While, on the shell side of the IHX, a proper boundary condition has been adopted, in order to evaluate the heat flux to be removed as function of the thermal power generated. Moreover, the heat flux to be removed is also function of two other contributions driven by the need to maintain the BB inlet helium temperature and pressure to the required values of 573.15 K and 8 MPa, respectively. These two terms, added in order to avoid strong temperature and pressure variations during the dwell phase, are obtained by means of two Proportional-Integral (PI) controllers. However, since the control loop mechanism are implemented in a different way in the two system codes and considering also the different time discretization method adopted (see §2.2.1) [47, 48, 71], some slight differences have been expected especially during the dwell phase.

3.3.1 Significant Benchmark Results

As concerns the simulation of the normal operational conditions, it has been mainly intended to preliminarily investigate the capability of the two developed models to predict the main thermal-hydraulic phenomena occurring into the system. In particular, the rationale of this activity has been to highlight the differences in reproducing such scenario taking advantage of the already proved applicability of the CATHARE code in simulating GCRs [76, 77, 90].

The thermal power adopted for simulating the normal operational scenario, including the ramp-up /down as depicted in Figure 3-27, takes into account both the FW heat flux and the nuclear heating as reported in Table 3-7. The thermal power trend for the investigated loop is shown in Figure 3-33.

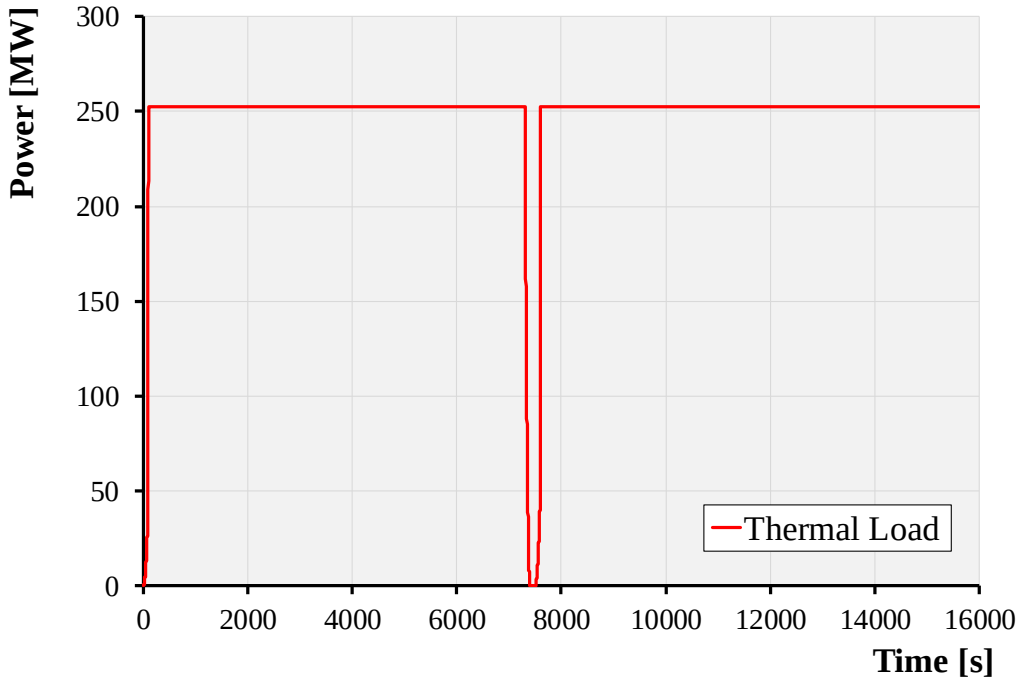

Figure 3-33: Thermal power trend.

The comparison of the main results of both the RELAP5-3D and CATHARE models, obtained during the pulse phase, with the design values is reported in Table 3-8. As it can be observed in the table, both the numerical results show a good agreement with the design reference values. Moreover, at a first glance, a very good agreement is predicted between CATHARE and RELAP5-3D too.

Table 3-8: OB BB-PHTS Loop main results.

Value	Unit	Design Values	RELAP5-3D	Deviation [%]	CATHARE	Deviation [%]
BB Power	[MW]	2.5231E+02	2.5231E+02	-	2.5231E+02	-
He mass flow rate	[kg/s]	2.4318E+02	2.4237E+02	-0.3342%	2.4344E+02	0.1068%
BB inlet temperature	[K]	5.7315E+02	5.7863E+02	0.9471%	5.8046E+02	1.2593%
BB outlet temperature	[K]	7.7315E+02	7.7930E+02	0.7892%	7.8004E+02	0.8835%
Compressor inlet temperature	[K]	5.6261E+02	5.6777E+02	0.9095%	5.6990E+02	1.2793%
BB inlet pressure	[MPa]	8.0000E+00	7.8941E+00	-1.3415%	8.0348E+00	0.4325%
Slice pressure drop	[MPa]	1.5400E-01	1.5370E-01	-0.1932%	1.5367E-01	-0.2144%
BSS manifolds pressure drop	[MPa]	~1.2500E-01	1.2820E-01	2.4961%	1.2890E-01	3.0256%
Piping pressure drop	[MPa]	5.6600E-02	5.6342E-02	-0.4571%	5.6233E-02	-0.6519%
IHX pressure drop	[MPa]	8.5100E-02	8.4746E-02	-0.4179%	8.4927E-02	-0.2041%

With regard to the BB inlet pressure, shown in Figure 3-34, the mismatch between the two calculated results is less than 2%. Hence, from this standpoint, one can state that a very good agreement has been found between the two codes. However, the obtained discrepancies can be mainly attributed to the difference in the initialization procedure followed by CATHARE and RELAP5-3D. Indeed, while in RELAP5-3D each component allows to define a proper set of initial conditions at which the code evaluates a compatible steady state condition, in CATHARE a special procedure must be followed. In fact, the initialisation order for each hydraulic circuit is defined with the PERMINIT directive. Then, the imposed thermal hydraulic state has to be defined. To perform this operation, the code needs to know the values of the main variables for, at least, one junction in each fluid zone of the circuit from which the initialisation will be propagated to the entire zone.

The initialisation procedure is then performed in two steps. The first step, following the initialisation order given by PERMINIT, calculates within each element the variable values which satisfy the stationary condition. Then, the inlet conditions are propagated along the element taking into account a hydrostatic pressure correction. Knowledge of the thermal-hydraulic variables for all the inlet junctions is thus required. This implies that if the inlet junction conditions are not given by elements that have already been calculated, then additional real constraint points have to be defined.

Another easily predictable consequence is that all the imposed conditions may not be obtained by the code (either if they are not coherent or if the code finds another solution than the one expected).

The second step allows the user to reach an overall coherent state. This is the stabilised solution of the standard transient calculation of ten time steps for the entire reactor, the so-called steady-state transient (i.e. a calculation with time set to zero). As to the regulation step, its purpose is to obtain a system at equilibrium with the desired initial conditions (p at pressuriser, flowrate at secondary side, compressor rotation speed, etc.). Then, depending on the difference between the state at the beginning of the transient (reference state) and the initial (PERMINIT) state obtained, the user may need to make adjustments in order to reach the transient starting point. This step is also called stabilised transient.

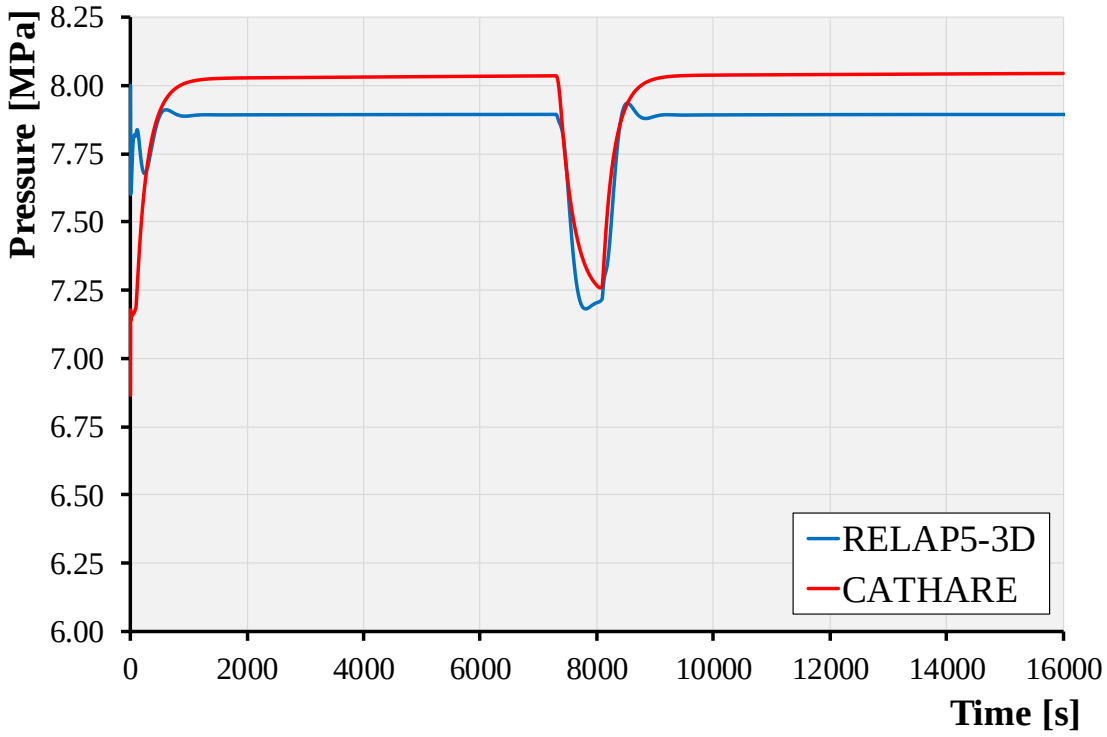

Figure 3-34: BB Inlet pressure.

Moreover, also the small discrepancies in the loop mass flow rate evaluations, recognized in Table 3-8

and displayed in Figure 3-35, give another confirmation of the good agreement between the two codes. In particular, the small mass flow rate discrepancies can be ascribed to minor difference in the two models. The differences become more remarkable during the dwell phase, that is when are changing the thermal-hydraulic conditions at the compressor intake. Indeed, the compressor model has been implemented in CATHARE paying attention to better reproduce the effective performance maps reported in Figure 3 24 and Figure 3 25 and to avoid possible interpolation errors [48] noticed during preliminary calculations.

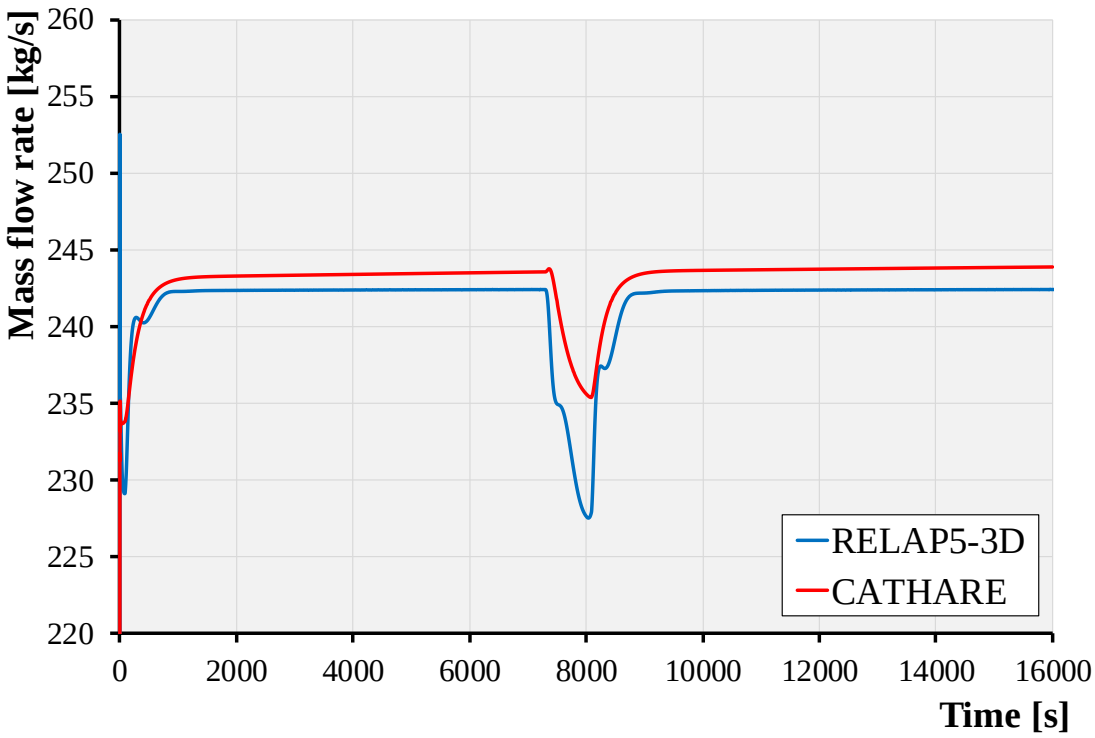

Figure 3-35: Loop mass flow rate.

Also the calculated pressure drops are well reproduced by the models, with small discrepancies arising because of the different procedure adopted by the system codes in evaluating the distributed pressure losses, as earlier disclosed.

These small discrepancies in pressure drop distribution, especially along the piping, are the main reason of those observed in the helium mass flow rate distribution along the sectors and the segment, depicted in Table 3-9, where the sectors are numbered starting from compressor outlet. However, it should also be noted that the piping design was not optimised to properly distribute the helium coolant among the segments (by installing valves or orifices), thus small differences between design values and calculated results have been expected. As it can be seen, a good agreement between the two codes is found under this aspect too.

Table 3-9: OB BB-PHTS Loop mass flow rate distribution.

Component	Design Value	RELAP5-3D	Deviation [%]	CATHARE	Deviation [%]
OB Seg. #1 @Sector #1 [kg/s]	2.702E+01	2.645E+01	-2.155%	2.678E+01	-0.896%
OB Seg. #2 @Sector #1 [kg/s]	2.702E+01	2.646E+01	-2.101%	2.708E+01	0.211%
OB Seg. #3 @Sector #1 [kg/s]	2.702E+01	2.705E+01	0.111%	2.692E+01	-0.371%
OB Sector #2 [kg/s]	8.106E+01	8.053E+01	-0.664%	8.178E+01	0.880%
OB Sector #3[kg/s]	8.106E+01	8.189E+01	1.016%	8.086E+01	-0.247%

As concerns the BB inlet temperature, depicted in Figure 3-36, the small differences observed in the calculation results are affected by the mass flow rate behaviour and to which is strongly coupled by the compressor model [47, 48]. In fact, such discrepancies are emphasized precisely during the dwell phase

simulation. Moreover, the boundary condition adopted for simulating the shell-side of the IHX acts slight different between the two models during the dwell phase (e. g. when the PI controller contributions become relevant) further accentuating the noticed mismatch. The heat flux transferred from the IHX and evaluated by means of the selected boundary condition is shown in Figure 3-37.

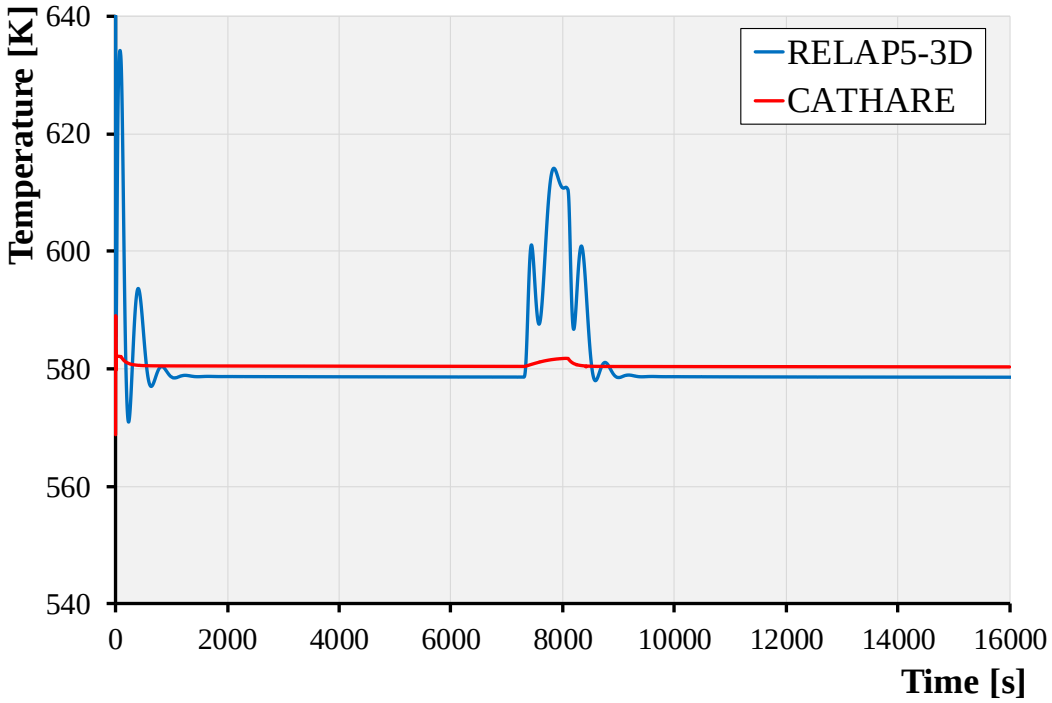

Figure 3-36: BB Inlet temperature.

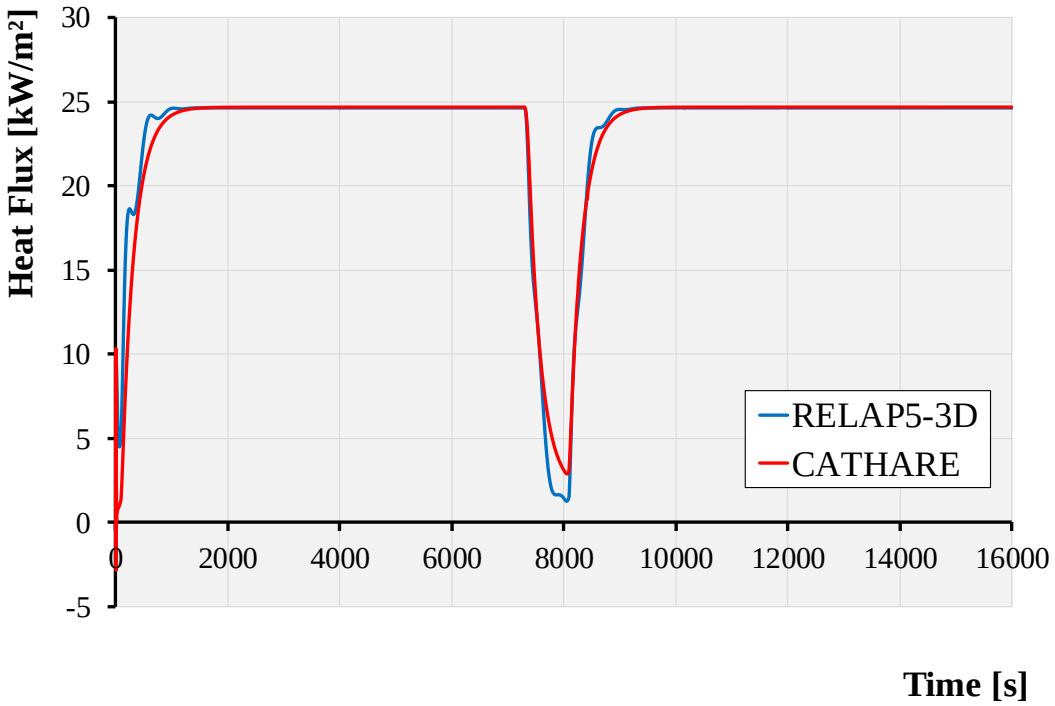

Figure 3-37: Heat flux reproducing the shell side of the IHX.

The BB outlet temperature trend, illustrated in Figure 3-38, is similarly predicted by the two developed models. The differences, assessed in Table 3-8, are practically maintained also during the dwell phase confirming the overall good agreement between CATAHRE and REAP5-3D approaches.

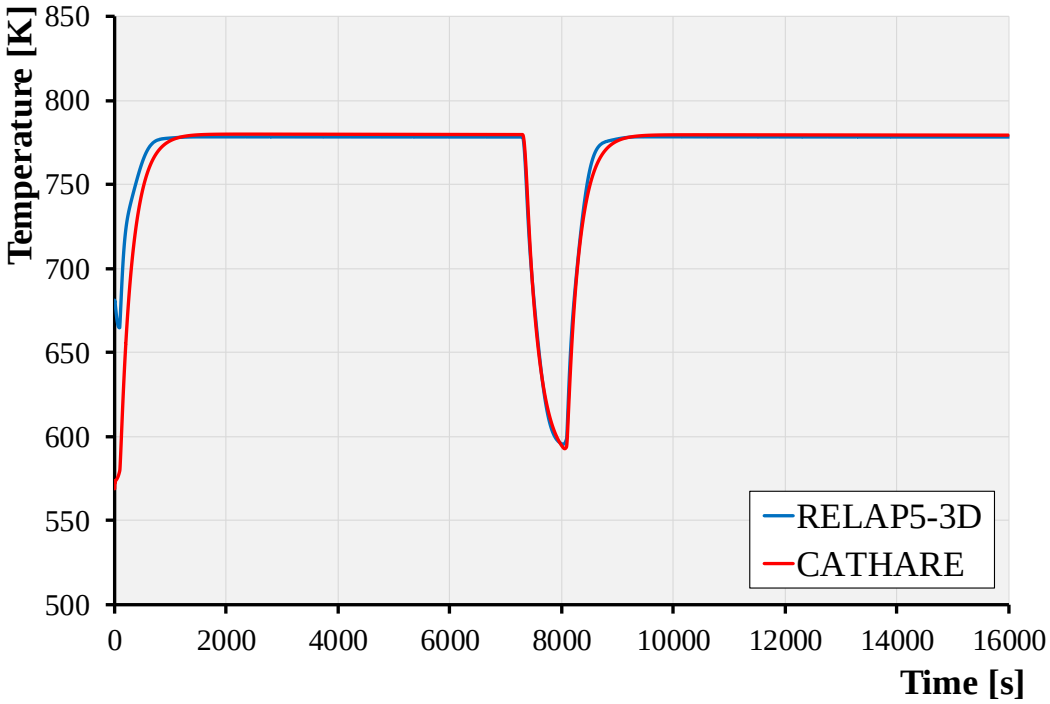

Figure 3-38: BB Outlet temperature.

For the sake of completeness, looking at Table 3-8, it should be noticed that the pressure drops along the BSS manifolds here reported are referring to the new configuration, in which both inlet and outlet to the segments are routed through the upper port. As reported in Figure 3-22 and Figure 3-28, this new configuration was just a very preliminary design when this activity has been done.

In fact, even if the helium coolant enters from the top, it was assumed that its distribution among the FW channels took place according to a bottom-top scheme, as it was in the previous configuration to homogenize the mass flow rate distribution [84]. Conversely, such a manifolds layout involves greater distributed and concentrated pressure drops, which should be minimized to keep the compressor size near the current state-of-the-art for these components. Indeed, for DEMO baseline 2017 the HCPB BB design has been modified simplifying considerably the manifolds routing inside the BSS [34].

In order to highlight the improvements due to the adoption of the integrated procedure, Table 3-10 reports the comparison between the pressure drops evaluated with the integral procedure proposed and those evaluated relying on to the fitting law reported by Idelchik in [88] with regards to the design values. As it can be observed in the table, the integral numerical results show a better agreement with the design reference values.

Table 3-10: OB BB-PHTS Loop pressure drop comparison.

Value	Unit	Design Values	RELAP5-3D Integrated	Deviation [%]	RELAP5-3D Standalone	Deviation [%]
BB inlet pressure	[MW]	8.0000E+00	7.8941E+00	-1.3415%	8.12E+00	1.54%
FW inlet pressure	[MPa]	6.30E-02	6.28E-02	-0.29%	5.20E-02	-17.51%
BZ pressure drop	[MPa]	9.10E-02	9.09E-02	-0.13%	1.20E-01	32.21%
BSS manifolds pressure drop	[MPa]	~1.2500E-01	1.2820E-01	2.4961%	1.10E+00	-12.34%
Piping pressure drop	[MPa]	5.6600E-02	5.6342E-02	-0.4571%	5.96E-02	5.23%
IHX pressure drop	[MPa]	8.5100E-02	8.4746E-02	-0.4179%	9.07E-02	6.57%

In conclusion, one can state that both the models predict similarly the thermal-hydraulic behaviour of the loop analyses reproducing all the main phenomena. As concerns the discrepancies encountered in simulating the dwell phase, they can be easily addressed by further improvement in the models.

Indeed, it has been envisaged to align the RELAP5-3D compressor model to the same degree of accuracy used in CATHARE, and to conform the initial conditions state obtained by the two computational models.

However, the capability of RELAP5-3D to investigate gas cooled systems, preliminary assessed in [91], has been proven by the performed benchmark activity, the finding of which have been carefully taken into account for the research activity described in chapter §4.

3.4 Recommendations

The research activities described in this chapter have been mainly intended to prove the capability of the integral approach proposed to realistically simulate the DEMO HCPB relevant systems. Indeed, as a proof-of-concept, the methodology has been applied to simulate an experimental test carried out on the HETRA facility, which has exposed its suitability in reproducing the experimental data. As highlighted in §3.2, this activity has also suggested the need to adopt the 'conduction enclosure model' to simulate the multi-dimensional heat conduction in order to correctly predict the temperature distribution, especially when modelling the FW channels for the DEMO HCPB BB.

As concerns the code-to-code benchmark, it has been useful to compare the RELAP5-3D modelling procedure with that adopted for the validated CATHARE code in GCRs applications [76, 77, 90]. In particular, some worthy recommendations have been derived for the compressor modelling which, for the activities described in chapter §4, have been completely followed revising its description to better fit the performance maps.

Moreover, consequently to the numerical benchmark and with the purpose of better reproduce the thermal-hydraulic performances of the PHTS without resorting to special boundary conditions, a proper tool has been developed, in cooperation with the RELAP5-3D developers, to implement the HITEC molten salt thermo-physical properties [39] in a proper binary file readable by the code [73].

4 Thermal Hydraulic Analysis of the EU-DEMO HCPB Reactor under normal operational conditions

4.1 Introduction

The integral approach methodology to the safety design of the EU-DEMO HCPB reactor, already depicted in paragraph §2.3 and validated in the previous chapter §3, is applied to assess the thermal-hydraulic performances of the representative and safety relevant cooling loop of the BB-PHTS DEMO HCPB. To this purpose, the currently adopted design baseline 2017 has been taken into account. The model developed and the obtained results are reported and critically discussed in the present chapter, paying attention to the application aspects of the proposed integral analysis methodology.

The aim of the study reported in this chapter is to assess the BB-PHTS DEMO HCPB thermal-hydraulic behaviour during normal operational conditions, including pulse, dwell and the transition phases (ramp-up and ramp-down). In particular, the main objective is to identify a possible regulation strategy able to comply with the prescribed requirements, especially keeping the coolant's BB inlet temperature at 573.15 K when switching from pulse to dwell and vice versa.

For the sake of brevity and clearness, the assessment has been carried out on the representative loop, but it can be easily extended to investigate the thermal-hydraulic behaviour of the 'heat transfer chain' main systems, inclusive of the whole IHTS and PCS. To this end, it has to be noted that the geometric features of the assessed system have been already introduced in paragraph §1.3 but, when more detailed information is needed, it is reported within the text.

4.2 Thermal-hydraulic modeling of the EU-DEMO HCBP main systems

The computational model developed for RELAP5-3D, explaining in details all the steps prescribed by the adopted methodology, is reported and critically described in this paragraph. The overall model consists of four main sub-models:

- the flow domain model, reproducing in a quasi-2D approximation the lay-out of the cooling circuit by using the nodalization modelling method explained in paragraph § 2.2.3;
- the constitutive models, provided by the system code to describe the thermo-dynamic behaviour of the helium circulating inside the cooling system, based on the considerations stated in paragraph §2.2.2;
- the hydraulic model, intended to simulate the fluid flow along the cooling system;
- the thermal model articulated in different sub-patterns aimed at realistically reproducing the heat transfer phenomena taking place along the cooling system.

In the following of this paragraph, a particular attention will be focused on the description of the latter two sub-models since they are playing a crucial role in predicting the thermal-hydraulic behaviour we set out to investigate.

4.2.1 The RELAP5-3D computational model

In order to better reproduce the thermal-hydraulic performances of the analysed systems, the proposed integral methodology has been applied with special regards to the IVCs. Indeed, they are forming newly and deeply 3D circuits so that the application of empirical formulas, like those reported in [88], could determine miscalculation which could heavily affect the prediction capability of the model. Therefore, the proposed integral methodology finds its whole application with the investigation of the IVCs thermal-hydraulic behaviour, showing for them its full prediction power.

Whilst, regarding the Ex-Vessel Components (EVCs), as they geometries involve features (e.g. bends,

restrictions/expansions and distributors) which have been extensively characterized on an experimental basis, the resort to the well-known fitting law reported by Idelchik in [88] has been considered trustworthy. Indeed, their own design widely rely on such empirical formulas [35].

Instead, as to IVCs, the proposed integral methodology has been adopted. Thus, as prescribed by the procedure summary reported in paragraph §2.3, the hydraulic characteristic function of the IVCs has been first evaluated by means of a dedicated campaign of CFD parametric analysis performed using the ANSYS CFX software. Then, it has been possible to subsequently derive the resistance loss coefficient (Eq. (2.62)) to be given as input for RELAP5-3D calculations.

In this regard, since the geometric peculiarities of each segment does not allow to identify an elementary unit which can be properly studied in ANSYS CFX by applying usual boundary conditions (e.g. symmetry or periodic boundaries), it has been necessary to investigate the whole BB segment thermal-hydraulic behaviour in order to get the desired characteristic functions. In particular, the performed CFD analyses have been focussed on the COB segment due to its regular poloidal extension which has facilitated the construction of the flow domain starting from the designed 'slice', as depicted in Figure 4-1. To this purpose, the elementary slice has been manually replicated following the COB poloidal development in order to attain the geometric model of the flow domain. Once derived the characteristic functions for the analysed segment, they have been scaled to obtain those of the remaining segments modelled in RELAP5-3D as well.

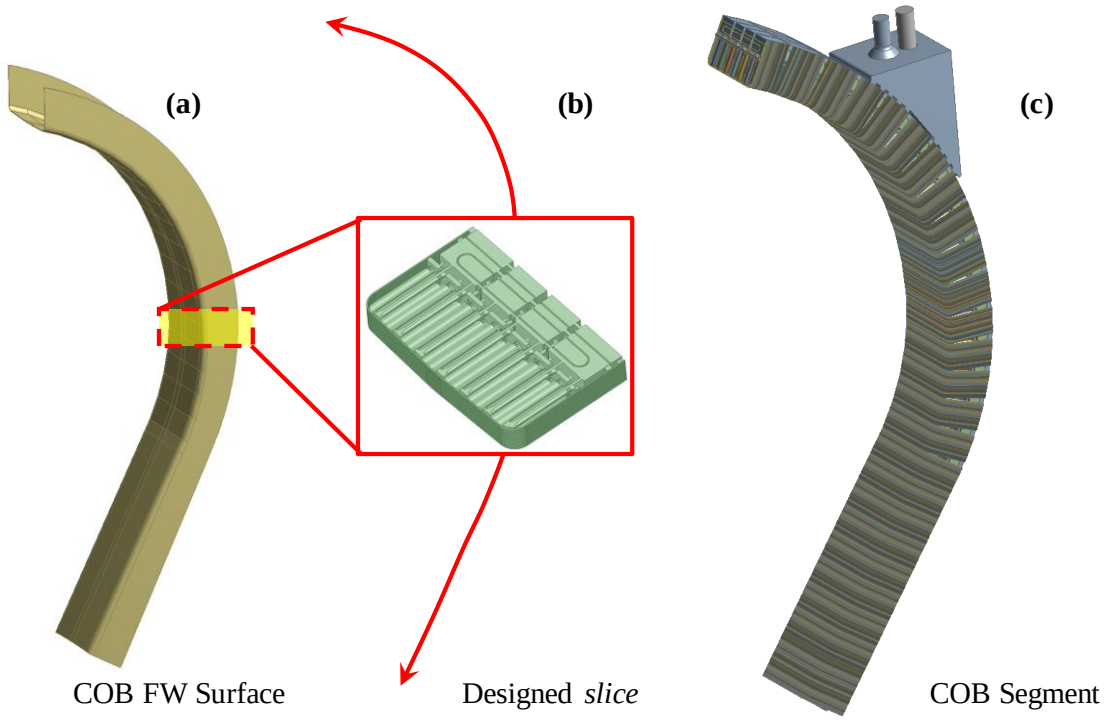

Figure 4-1: COB Segment flow domain: starting from the FW surface (a) the designed slice (b) has been poloidally replicated to obtain the whole segment flow domain (c).

In order to properly assess so a huge flow domain, billions of elements would have been required for the needed computational mesh. Hence, taking into account the constraint of reasonable computing time and resources, the methodology described in paragraph §2.3 (porous media model method) has been applied in order to reduce the mesh size without significantly decreasing the accuracy of the obtained results. Indeed, one of the core aspects of the proposed integral approach is the possibility to gather in a reliable way the thermal-hydraulic behaviour of a complex system by analysing a simplified one, adopting a proper set of assumptions briefly recalled in the following.

As mentioned before, the simplification has been performed resorting to the porous media method where the geometric effects are taken into account through the surface and volume porosities.

In general, a porous medium is a material consisting of a solid matrix containing pores (voids). It is most often characterized by two main parameters, which are porosity and permeability [92]. For porous media, the porosity is defined as the ratio of the volume occupied by voids to the total volume:

$$\gamma = \frac{V_f}{V} \tag{4.1}$$

where, V_f refers to the fluid volume and V refers to the total volume. The functional relationship among the volumetric flow rate, the pressure gradient and the permeability in a porous media is provided by the Darcy's law:

$$Q = -k\frac{S}{\mu}\frac{dp}{dl} \tag{4.2}$$

where, Q is the volumetric flow rate, S the cross-section area, $\frac{dp}{dl}$ is the pressure gradient, μ the dynamic viscosity and k the permeability.

The effect of porous media on pressure drops and turbulence intensity in a CFD analysis could be considered by adding extra momentum loss term into the Navier-Stokes (Equations (2.10)). In ANSYS CFX the momentum loss through an isotropic porous region could be formulated using permeability and loss coefficients as follows:

$$S_{m,i} = -\frac{\mu}{k}u_i - K_{loss}\frac{\rho}{2}|u_i|u_i \tag{4.3}$$

where, K_{loos} is the quadratic loss coefficient. The linear component of this source represents viscous losses and the quadratic term represents the inertial losses. When the flow through an anisotropic porous region is considered, the source term could be modelled using the directional loss model. Considering a streamwise-oriented coordinate system (x', y', z') where the z'-axis is aligned with the stream wise direction and the x', y'-axes are lied on the transversal plane, the momentum losses in these directions are:

$$S_{m,x'} = -\frac{\mu}{k^T}u_{x'} - K_{loss}^T\frac{\rho}{2}|u_{x'}|u_{x'} \tag{4.4}$$

$$S_{m,y'} = -\frac{\mu}{k^T}u_{y'} - K_{loss}^T\frac{\rho}{2}|u_{y'}|u_{y'} \tag{4.5}$$

$$S_{m,z'} = -\frac{\mu}{k^S}u_{z'} - K_{loss}^S\frac{\rho}{2}|u_{z'}|u_{z'} \tag{4.6}$$

where, k_S and k_T are the stream wise and transversal permeability, respectively. K_{loss}^S and K_{loss}^T are the streamwise and transversal quadratic loss coefficients, respectively.

Assessing these quantities is at the heart of the adopted procedure. In fact, the simplified model reproducing the real complex one, is obtained by replacing its sub-components with others likewise behaving, as shown in Figure 4-2. Practically, pins and FW channels have been replaced with simpler and smaller components which leads to a consistent flow domain simplification and a worthy reduction (~30%) in the model size, see Figure 4-3. Consequently, this modelling approach has allowed reducing the size of the adopted spatial discretization grid.

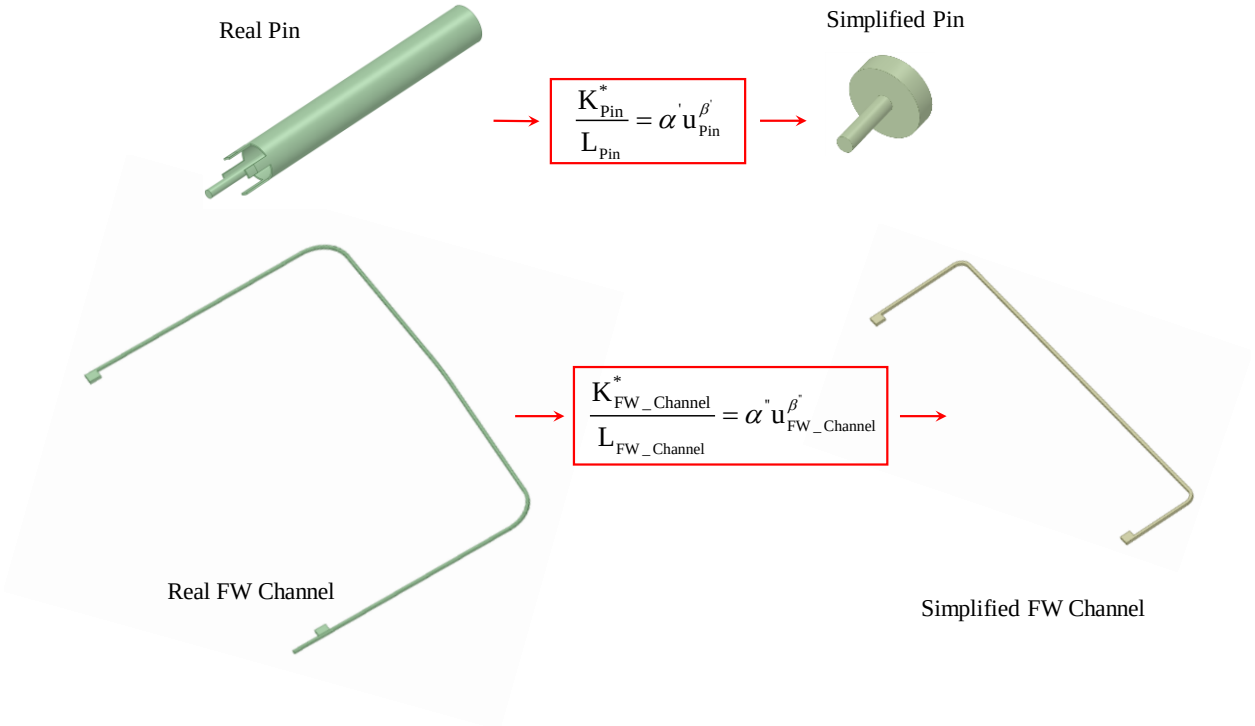

Figure 4-2: Pin and FW channel simplification by means of porous media models.

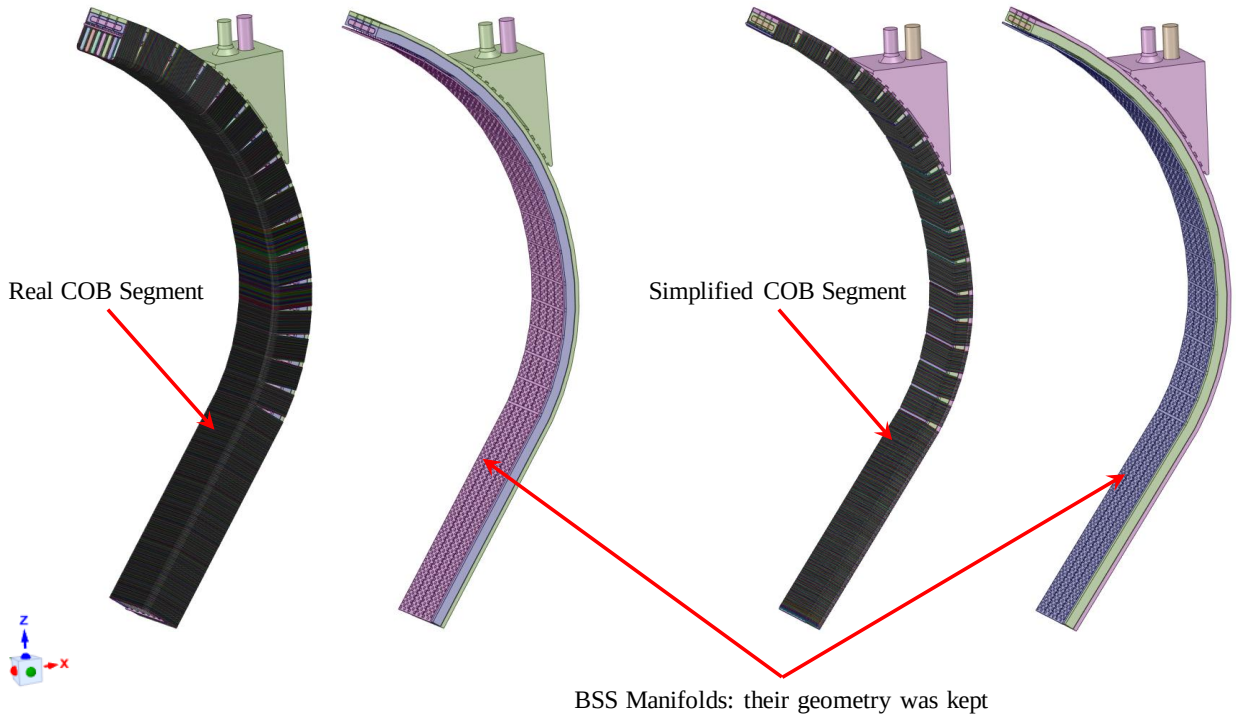

Figure 4-3: COB segment simplification.

In order to perform the first step for the determination of the thermal-hydraulic characteristics reported in Equation (2.60) and Equation (2.62), dedicated models of pin and FW channel have been set up. Tetrahedral elements have been mainly adopted for their meshes to better take into account the geometrical features of the domains to be discretized and the required optimization of the node number and mesh quality.

The main assumptions and boundary conditions adopted for the pin model (Figure 4-4) are reported in Table 4-1, whereas its mesh parameters are summarised in Table 4-2.

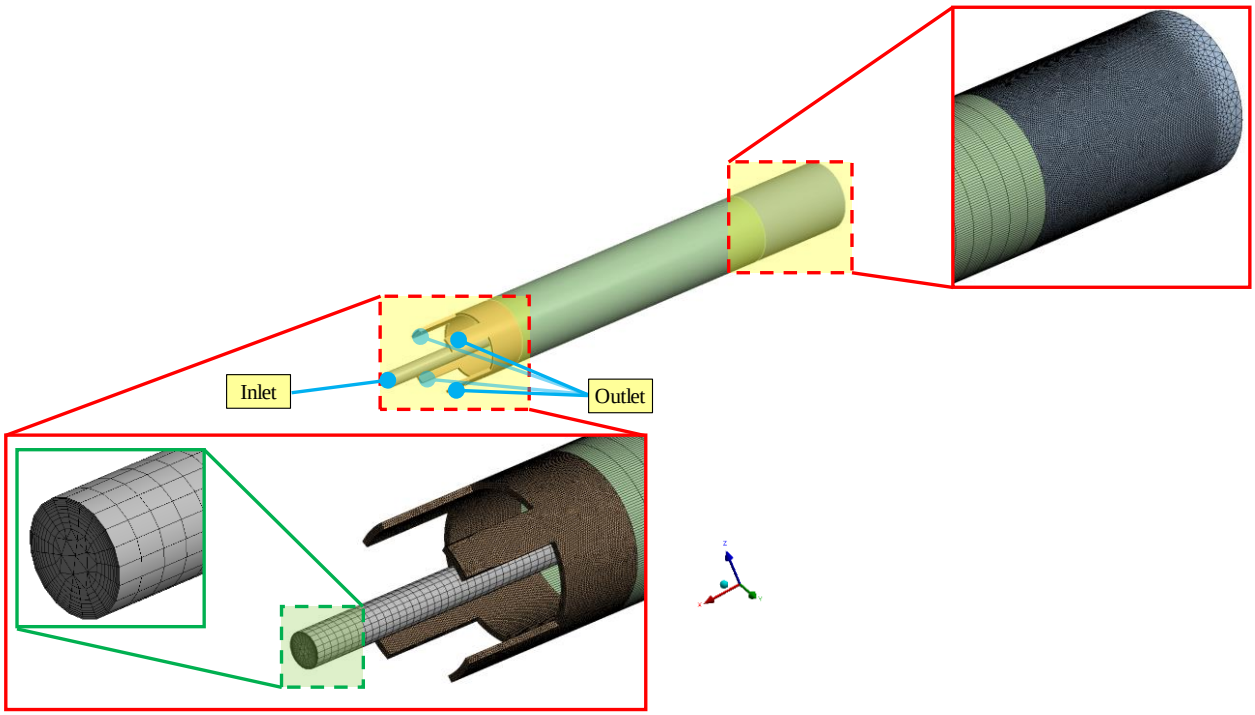

Figure 4-4: Pin model with details of mesh.

Table 4-1: Pin analysis: assumptions, models and BCs.

Parameter	Value
Analysis type	Steady-state
Material library	Helium
Flow temperature	683.15 K
Turbulence model	SST
Boundary layer modelling	Blended Near Wall Treatment
Wall absolute roughness	300 μm @ ~90% SW & 10 μm @ ~10% SW
Inlet BC	Mass flow rate
Outlet BC	Average static pressure

Table 4-2: Mesh parameters adopted for the pin discretization.

Parameter	Value
Nodes	$1.07 \cdot 10^{6}$
Elements	$2.18 \cdot 10^{6}$
Node density [m³]	$2.13 \cdot 10^{9}$
Defeature size [m]	$1.57 \cdot 10^{-4}$
Body sizing [m]	$1.00 \cdot 10^{-2}$
First layer height [μm]	20.00
Layers number	10.00
Grow rate	1.60

As concerns the main assumptions and boundary conditions adopted for the FW channel model (Figure 4-5), they are reported in Table 4-3, whereas their mesh parameters are summarised in Table 4-4.

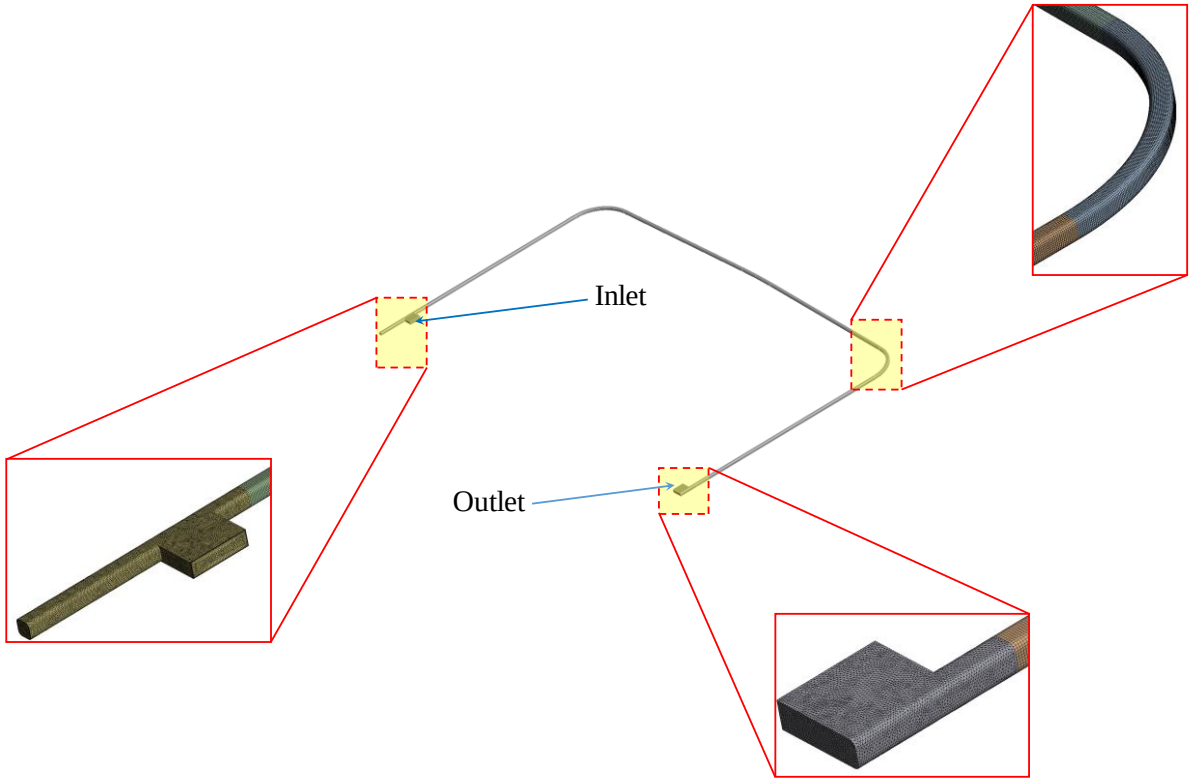

Figure 4-5: FW channel model with details of mesh.

Table 4-3: FW channel analysis: assumptions, models and BCs.

Parameter	Value
Analysis type	Steady-state
Material library	Helium
Flow temperature	683.15 K
Turbulence model	SST
Boundary layer modelling	Blended Near Wall Treatment
Wall absolute roughness	300 μm @ ~13% SW & 10 μm @ ~87% SW
Inlet BC	Mass flow rate
Outlet BC	Average static pressure

Table 4-4: Mesh parameters adopted for the pin discretization.

Parameter	Value
Nodes	$1.59 \cdot 10^{6}$
Elements	$1.95 \cdot 10^{6}$
Node density [m³]	$4.04 \cdot 10^{9}$
Defeature size [m]	$4.95 \cdot 10^{-4}$
Body sizing [m]	$1.00 \cdot 10^{-3}$
First layer height [μm]	20.00
Layers number	10.00
Grow rate	1.60

The obtained characteristic functions Δp(G) for both pin and FW channel are shown in Figure 4-6, while their K(u) functions are reported in Figure 4-7 and Figure 4-8, respectively.

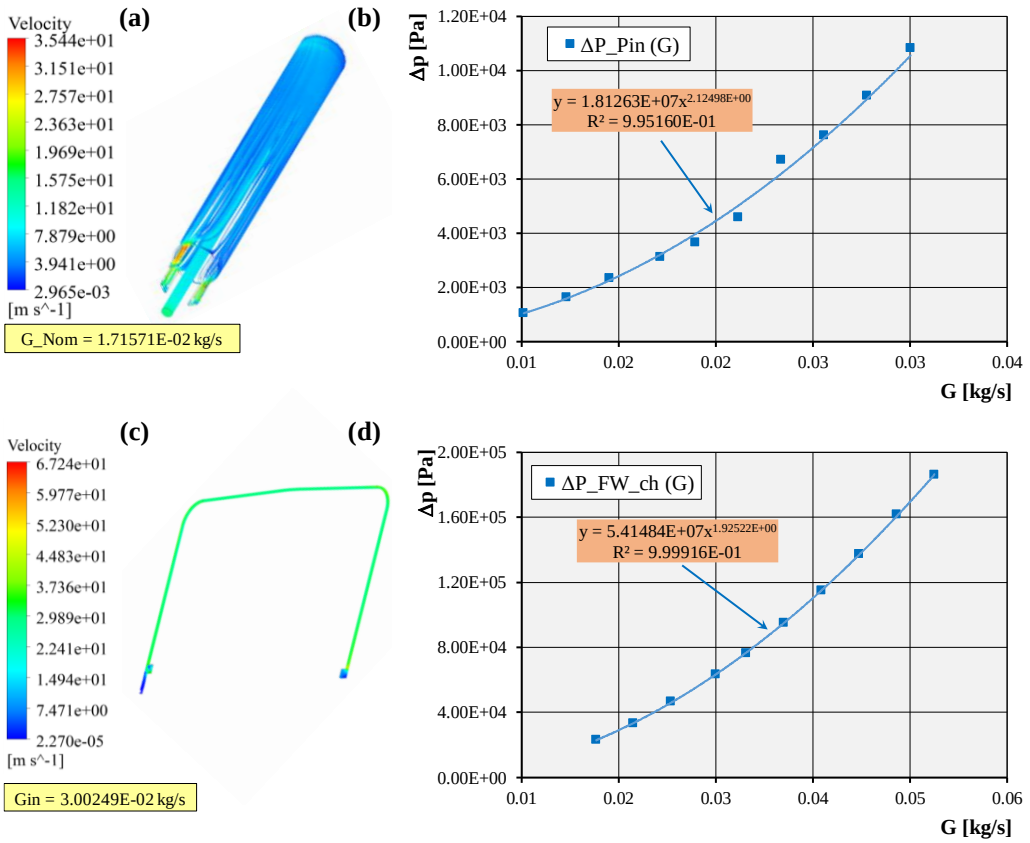

Figure 4-6: Pin (b) and FW channel (d) characteristic functions Δp(G) and interpolation equations.

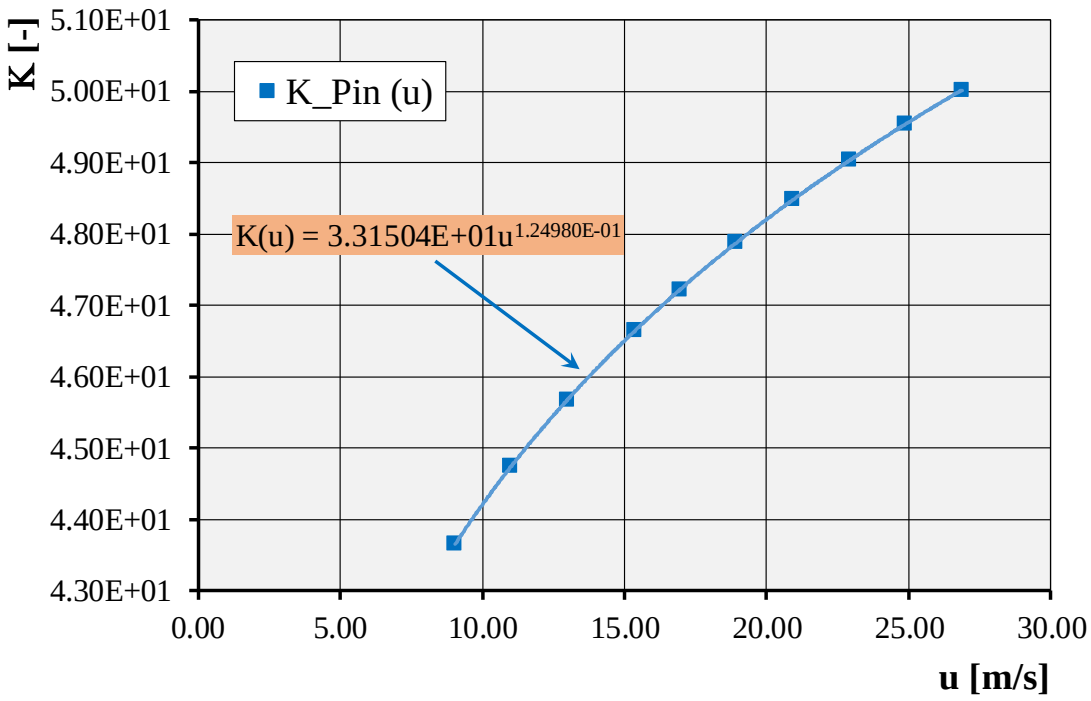

Figure 4-7: Pin characteristic function K(u) and interpolation equation.

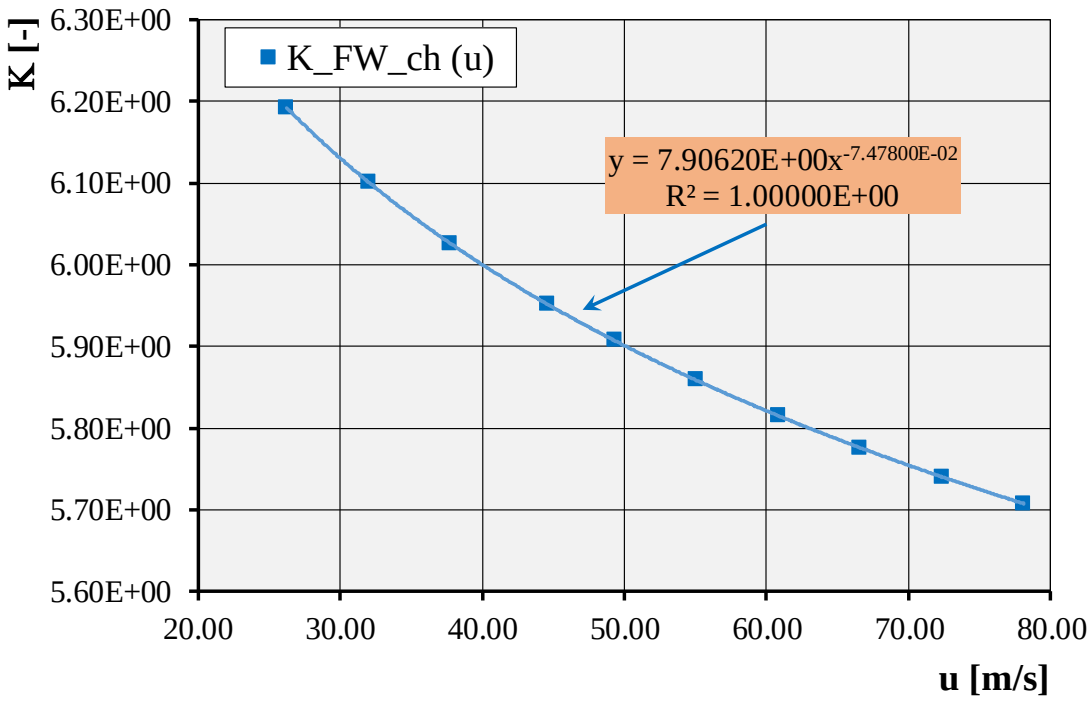

Figure 4-8: FW channel characteristic function K(u) and interpolation equation.

The latter characteristic functions K(u) have been used to set up the porous domains simulating the two sub-components pins and FW channels into the simplified segment according to the step 2 of the adopted procedure. Indeed, a dedicated finite volume model for the whole COB simplified model has been developed, see Figure 4-9. Table 4-5 summarised the main assumption, models and boundary conditions adopted for this analysis, whilst the mesh parameters are reported in Table 4-6.

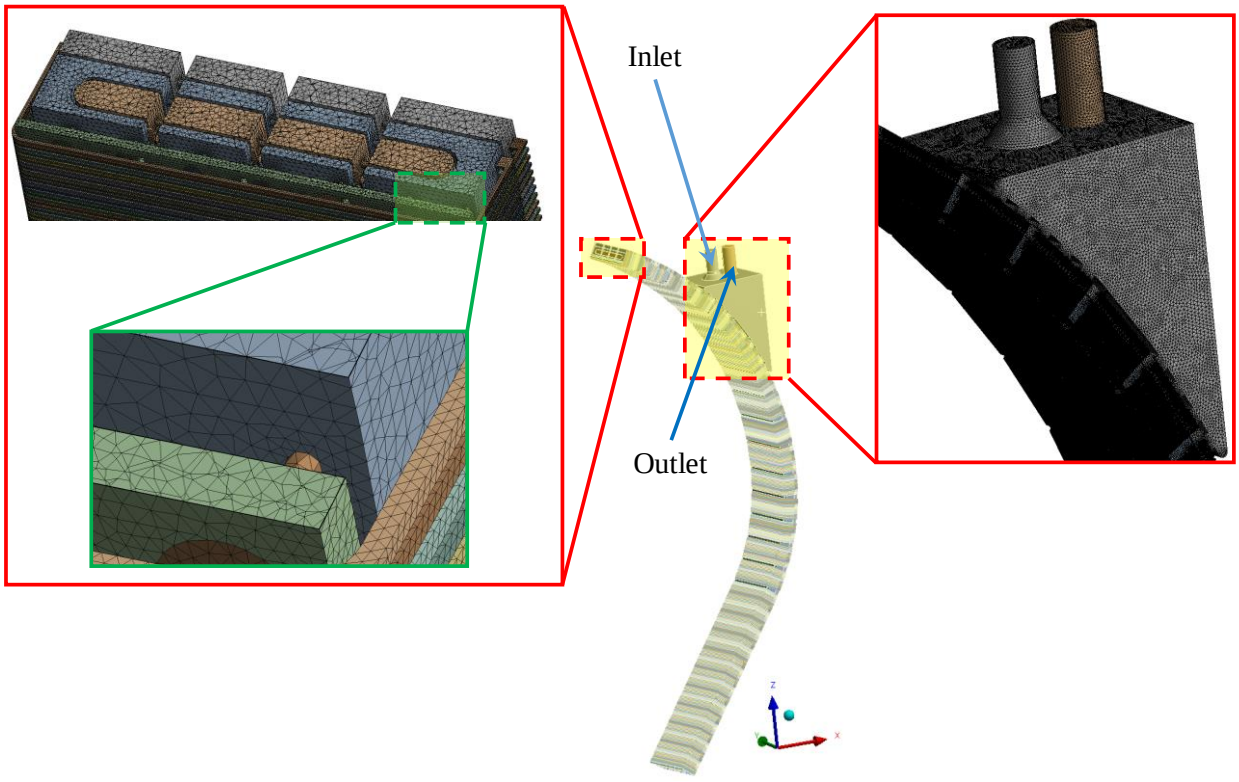

Figure 4-9: Simplified segment model with details of mesh.

Table 4-5: Simplified segment analysis: assumptions, models and BCs.

Parameter	Value
Analysis type	Steady-state
Material library	Helium
Flow temperature	683.15 K
Turbulence model	SST
Boundary layer modelling	Blended Near Wall Treatment
Wall absolute roughness	smooth @ porous domain & 10 μm @ elsewhere
Inlet BC	Mass flow rate
Outlet BC	Average static pressure

Table 4-6: Mesh parameters adopted for the simplified segment discretization.

Parameter	Value
Nodes	$30.41 \cdot 10^{6}$
Elements	$75.38 \cdot 10^{6}$
Node density [m³]	$3.36 \cdot 10^{6}$
Defeature size [m]	$3.54 \cdot 10^{-3}$
Body sizing [m] @BSS_Manifolds	$2.50 \cdot 10^{-2}$
Body sizing [m] @Pins&FW_Channels	$2.00 \cdot 10^{-2}$
First layer height [μm]	20.00
Layers number	5.00
Grow rate	1.60
Average Skewness	0.37
Average Orthogonality Quality	0.67

The obtained Δp(G) characteristic function for the COB segment is reported in Figure 4-10, while the K(u) is showed in Figure 4-11. The latter has been inputted in the RELAP5-3D model according to the step 3 in paragraph §2.3. As concerns the other segments (both R/LOB and IB) it has been assumed, in agreement with the HCPB BB design team, to preliminary assume the same thermal-hydraulic behaviour acquired for the COB one.

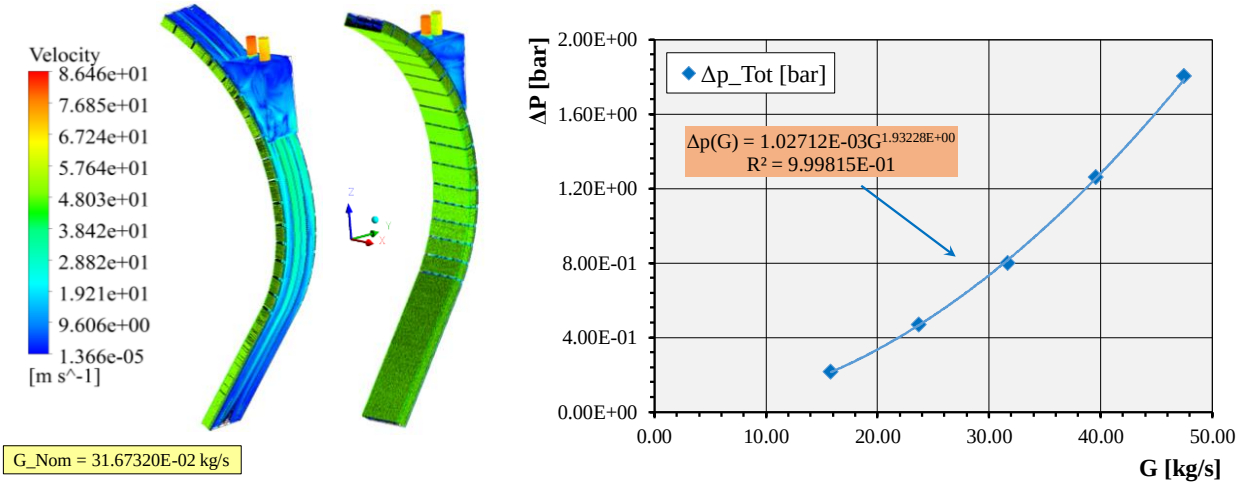

Figure 4-10: Simplified segment characteristic functions Δp(G) and interpolation equations.

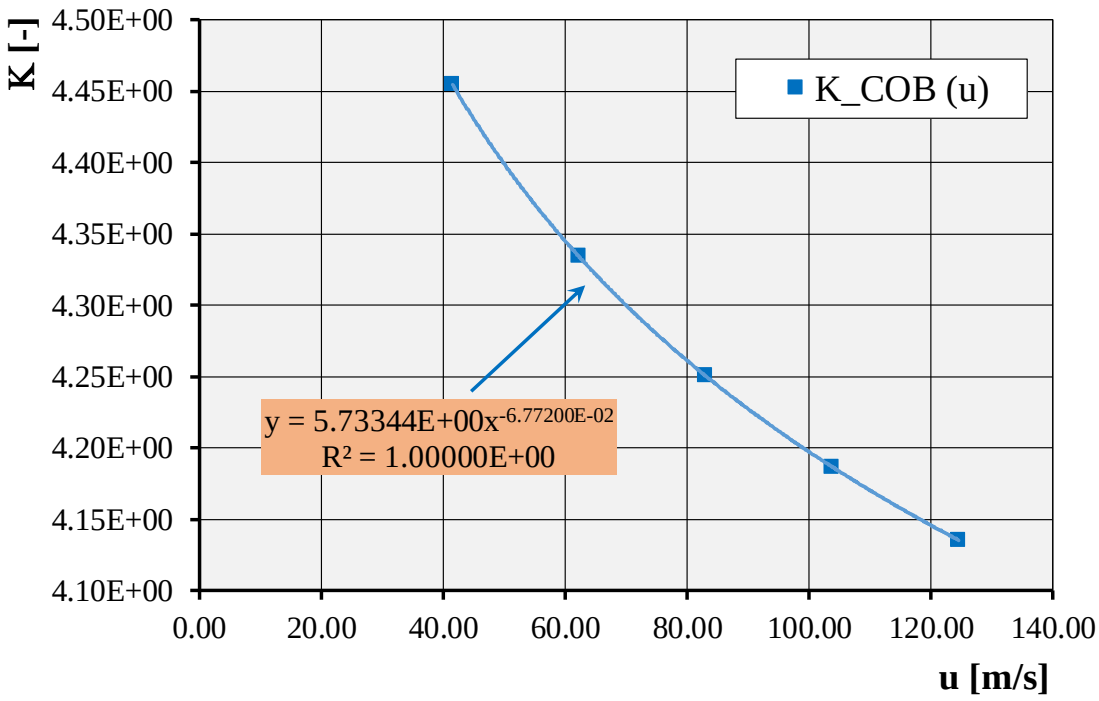

Figure 4-11: Simplified segment characteristic function K(u) and interpolation equation.

Once assessed the IVCs hydraulic models, that of the EVCs has been addressed. The attention has been focussed on one of the longest loop of the PHTS, reported in Figure 4-12. The current BB-PHTS architecture relies on the adoption of 8 homogeneous and completely independent cooling loops, from both mechanical and functional point of view, in order to limit some common mode failures. Each loop, feeding both IB and OB segments of 2 sectors, is equipped with a helium-molten salt IHX and 2 helium circulators [37]. The main data of the HCPB BB PHTS and the IHX are reported in Table 4-7 and Table 4-8 , respectively.

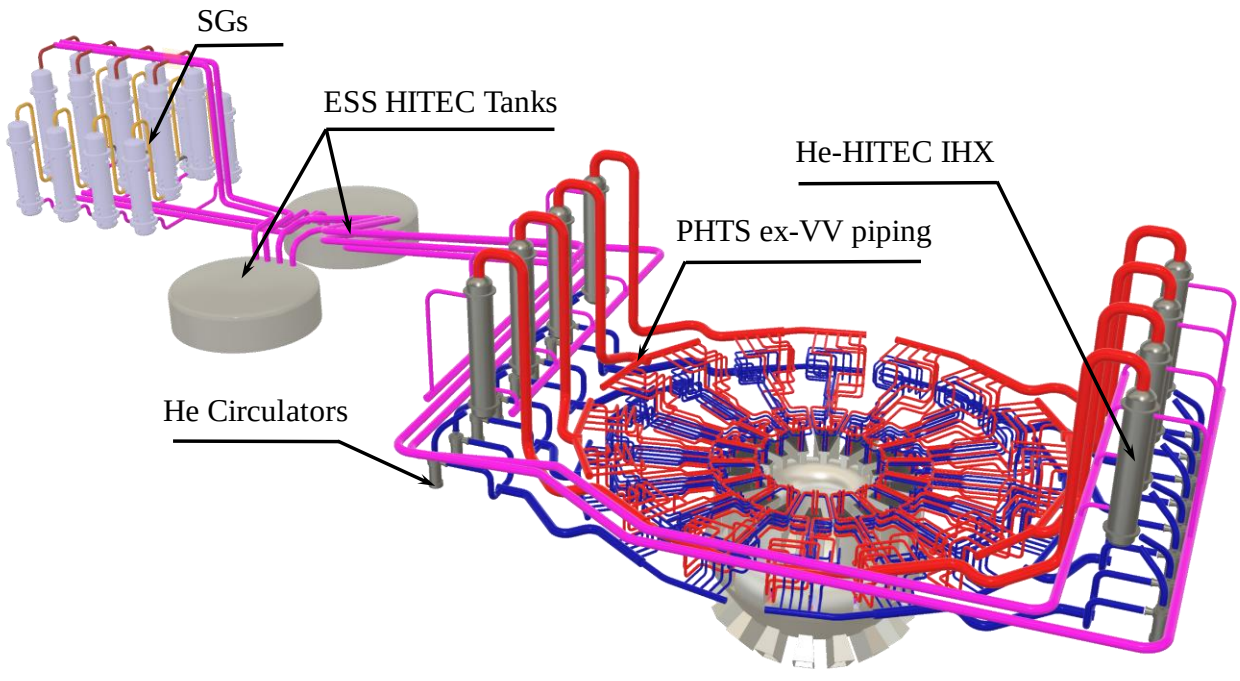

Figure 4-12: A 3D view of the EU DEMO HCPB BB PHTS cooling loops.

Table 4-7: HCPB BB-PHTS main data

Parameter	Value
Thermal power [MW]	2101.7
Circulator power [MW]	130.4
Total He volume [m³]	1976.4
Total piping length [m]	4002.8
Total ΔP [kPa]	270.0

Table 4-8: IHXs main data

Parameter	Value	Unit
Thermal Power	264.10	[MW]
T_{in}/T_{out} helium	793.15/564.05	[K]
T_{in}/T_{out} HITEC	543.15/738.15	[K]
Tubes active length	13.70	[m]
Tube number	9812	[-]
Tube d_{ext}	15.875	[mm]
Tube thickness	1.245	[mm]
Helium pressure drop	60.70	[kPa]
Helium volume	30.20	[m^3]

As mentioned before, the EVCs thermal-hydraulic behaviour has been reproduced paying attention to reproduce their geometrical features inputting the designed pressure loss coefficients evaluated as recommended in [88] and reported in [93].

Moreover, as concerns the compressor model, the more suitable performance maps developed for the German Thorium High Temperature Reactor (THTR-300) have been adapted and implemented in the model as recommended in paragraph §3.4 (see Figure 4-13 and Figure 4-14).

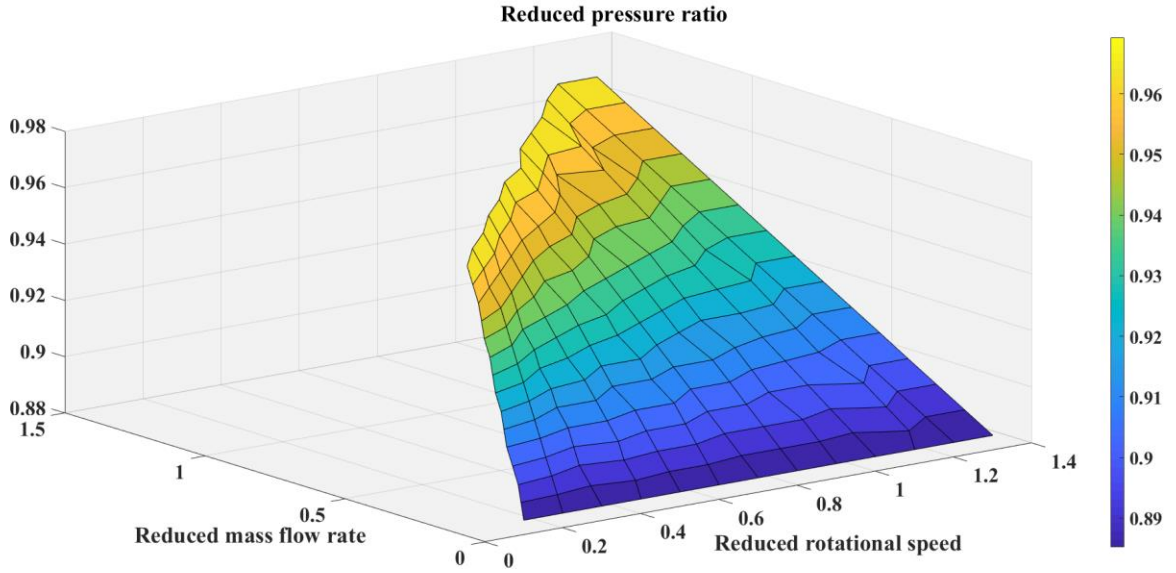

Figure 4-13: THTR-300-like pressure ratio map.

In fact, the compressor performance maps are read in RELAP5-3D in a series of tables, one for each value of the angular velocity. Each table consists of number triplets of mass flow rate, pressure ratio, and efficiency. Both angular velocity and mass flow rate are entered as relative values, corrected to rated

stagnation sound speed and density, as described in [94].

These tables are read using simple linear interpolation, using the angular velocity and mass flow parameters as independent variables. Thus, in order to reduce the potential interpolation errors when reading them, 30 triplets corresponding to so many values of angular velocities have been inputted.

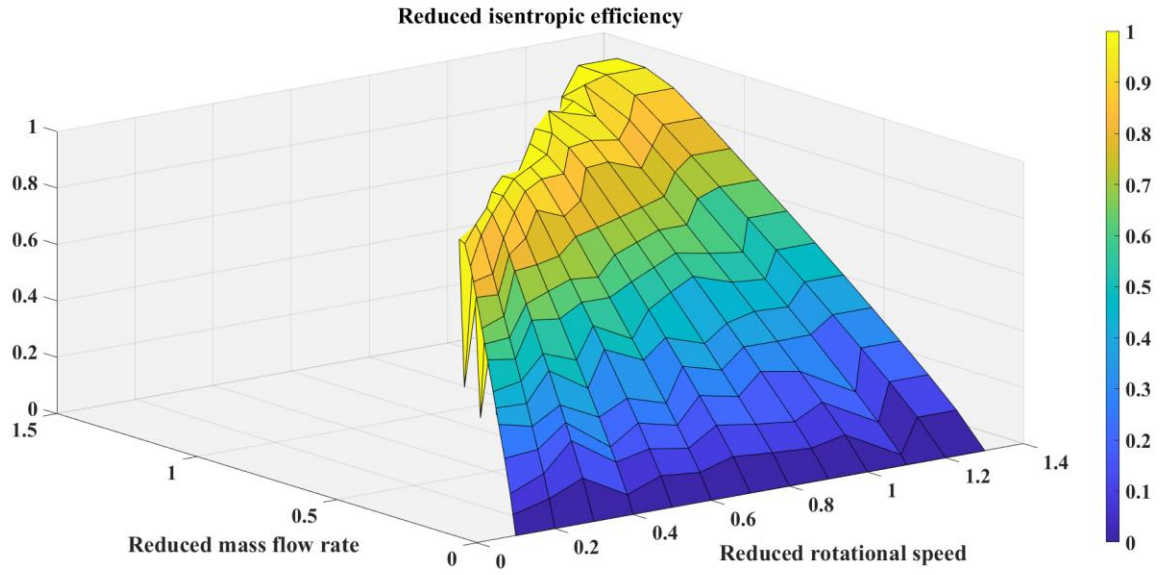

Figure 4-14: THTR-300-like isentropic efficiency map.

As concerns the thermal modelling, the heat transfer phenomena have been reproduced implementing the thermo-physical properties of all the structural materials involved [93] [34]. Properly selected heat transfer models, namely the Gnielinski correlation as validated in paragraph §3.2, and the Bell-Delaware procedure, have been adopted for evaluating the heat transfer coefficient on the shell side of the IHX, as already done for its design [35]. The considered Bell-Delaware procedure evaluates the heat transfer coefficient as following [95]:

$$h_{ideal} = jC_p G' Pr^{-\frac{2}{3}} \left(\frac{\mu_b}{\mu_w} \right)^{0.14} \tag{4.7}$$

$$h_{real} = h_{ideal} J_C J_l J_b J_S J_R \tag{4.8}$$

where:

$$j = a_1 \left(\frac{1.33}{L_T / D_e} \right)^{\frac{a_3}{1+0.14 Re^{a_4}}} Re^{a_2} \tag{4.9}$$

with a_1, a_2, a_3, a_4 depending on Re and lattice, while J_C, J_l, J_b, J_S, J_R depending just on the selected geometry. These coefficients have been implemented as reported in [93].

Since such a correlation is not directly available into the system code models package, it has been implemented by using proper CONTROL FUNCTIONs which allow to evaluate the heat flux as boundary conditions for the HEAT STRUCTUREs simulating the IHX shell side.

Moreover, as concerns the FW channels thermal model and as recommended in paragraph §3.4, the 'conduction enclosure model' has been adopted in order to simulate the multi-dimensional heat conduction.

Concerning the IHX and its model, since the solar molten salt HITEC has been foreseen as working fluid for the IHTS of the HCPB EU-DEMO, as anticipated in paragraph §3.4, a dedicated tool has been set

up, together with the RELAP5-3D developers, reproducing that adopted in [96] in order to generate a binary file implementing the HITEC thermo-physical properties readable by the code.

The model nodalization has been developed to realistically reproduce all the geometric features of the involved systems demanding admissible computing time. To that end, 211 thermal-hydraulic RELAP5-3D components have been used. They are: 110 PIPEs, 4 MULTIPLE JUNCTIONs, 90 SINGLE JUNCTIONs, 2 SINGLE VOLUMEs, 1 COMPRESSOR, 2 TIME DEPENDENT VOLUMEs, 2 TIME DEPENDENT JUNCTIONs and 93 HEAT STRUCTUREs. In addition, 1031 CONTROL BLOCKs, 167 SIGNAL VARIABLEs and 125 TABLEs complete the model.

In Figure 4-15 the nodalization scheme adopted for the cold legs is shown. Their modelling has been done by using 23 PIPEs subdivided in 283 volumes. Similarly, the discretization of the hot legs has required 21 PIPEs with 279 volumes, as depicted in Figure 4-16. In both the latter figures the discretization adopted for the IHX is shown as well. It has been made by using 6 PIPEs, 2 SINGLE VOLUMEs reproducing accurately the shell side of the heat exchanger, while the inlet and outlet boundary conditions have been simulated by adopting 2 TIME DEPENDENT VOLUMEs and 1 TIME DEPENDENT JUNCTION for setting the HITEC mass flow rate.

As said before, each loop of the BB-PHTS feeds 2 different sectors, thus 10 segments have been modelled.

Figure 4-17 shows the nodalization adopted to simulate both IB and OB segments. Indeed, they are sharing the same topology and cooling scheme, as can be seen in Figure 1-8 . Indeed, the components adopted for modelling both FW channels and pins, but also the manifolds located inside the BSS, have been chosen to reproduce such scheme. Consequently, 60 PIPEs subdivided in 740 control volumes have been required for their simulation.

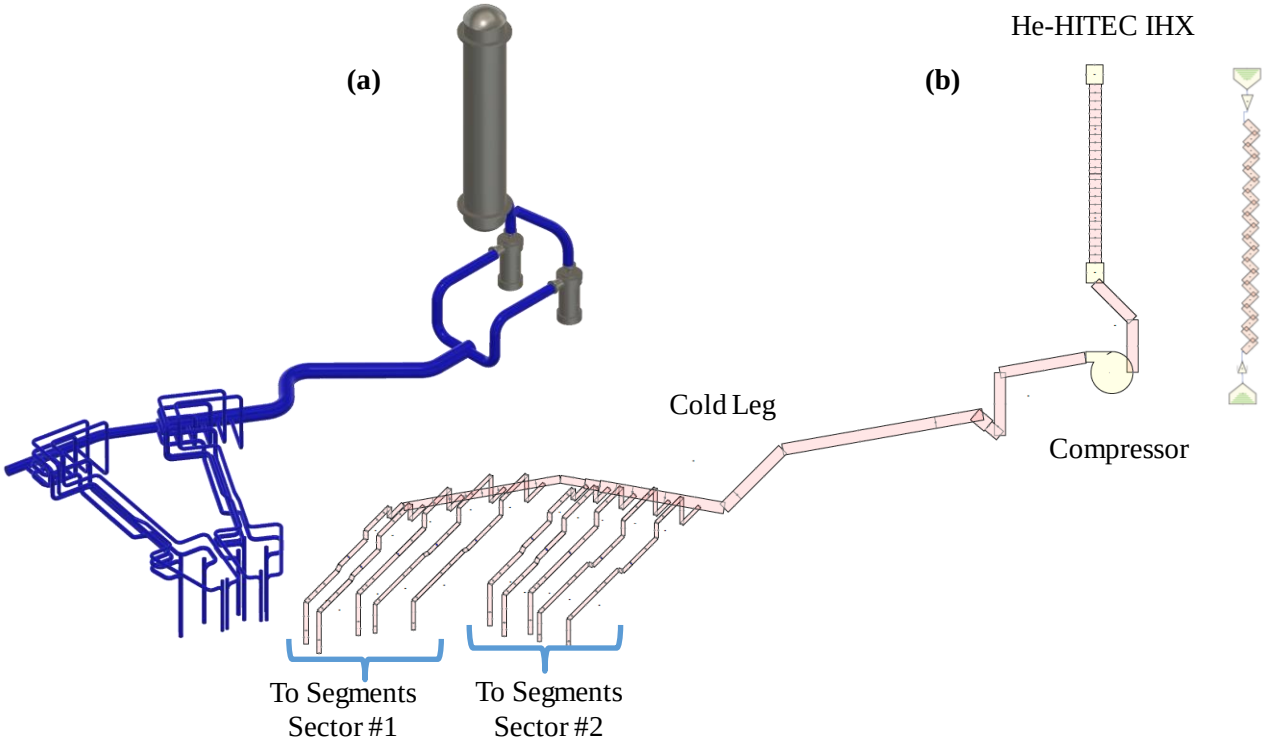

Figure 4-15: Cold legs CAD model (a) and nodalization scheme (b).

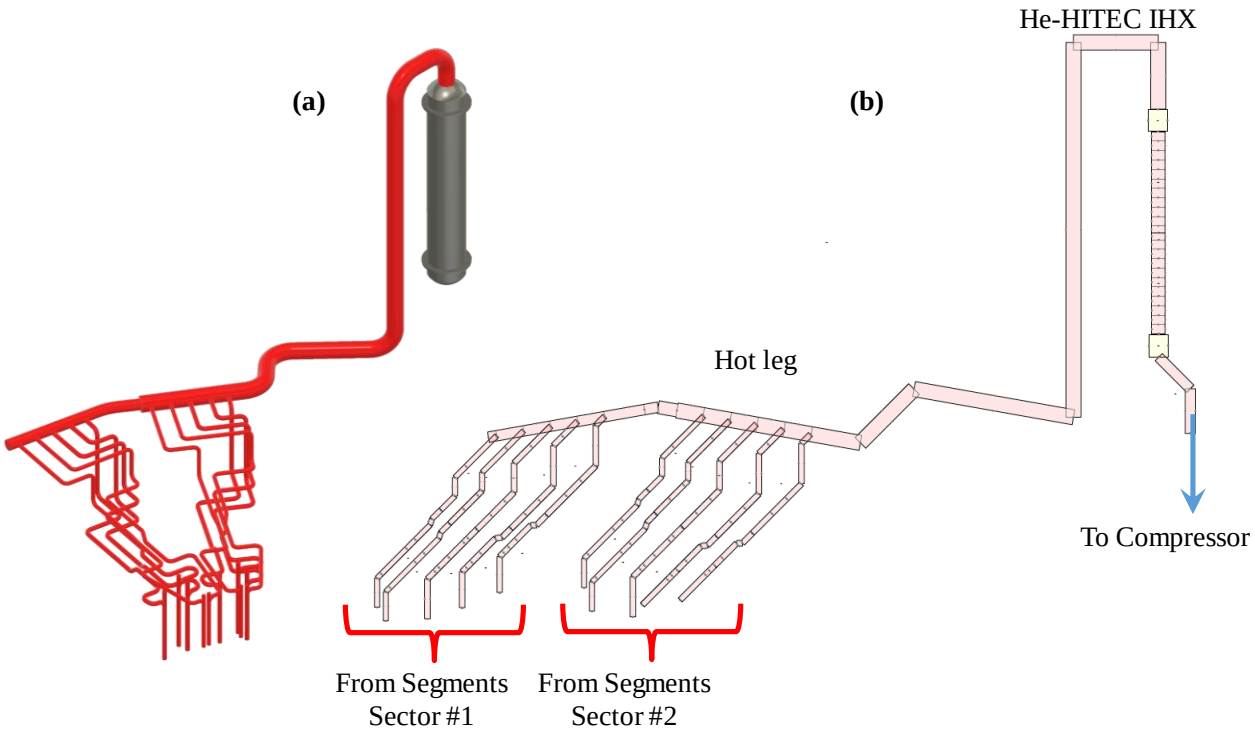

Figure 4-16: Hot legs CAD model (a) and nodalization scheme (b).

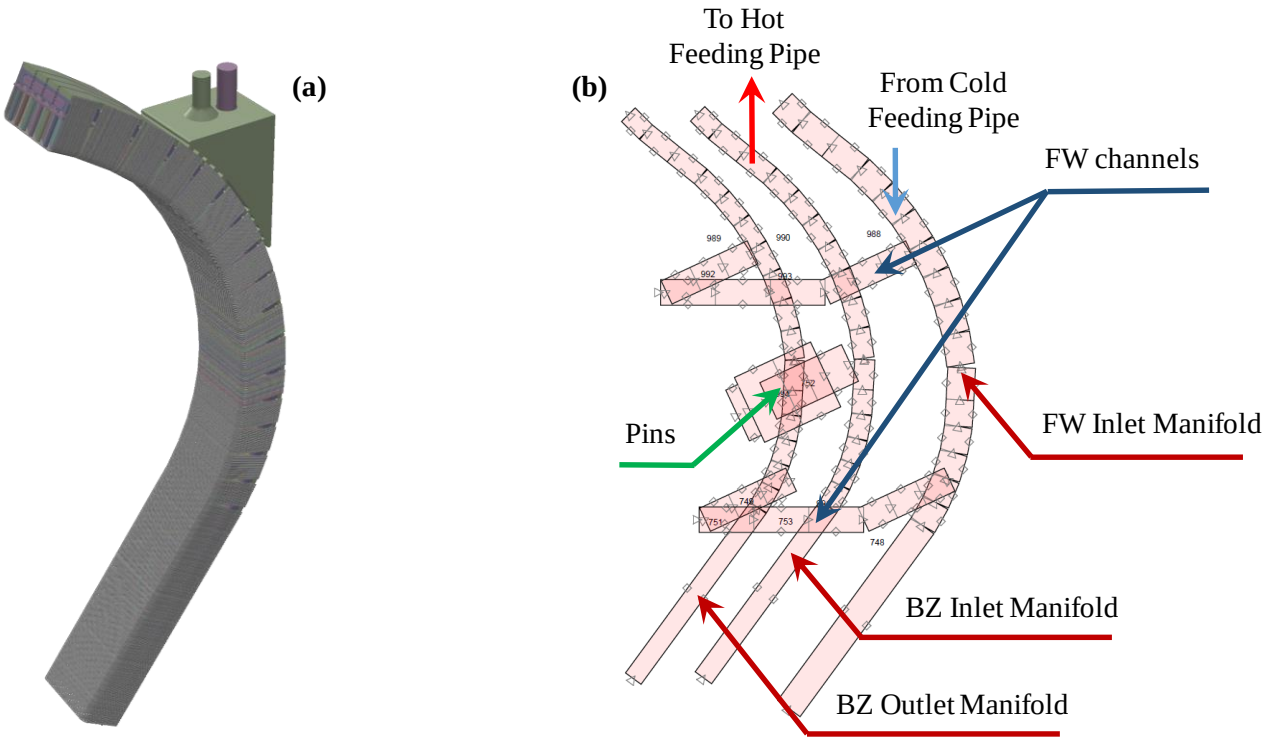

Figure 4-17: Segment model CAD model (a) and nodalization scheme (b).

4.2.2 Thermo-Physical Properties of Materials

As far as the thermo-physical properties of the materials are concerned, temperature-dependent values have been adopted for the performed analysis.

In particular, since in DEMO the reduced activation ferritic-martensitic steel EUROFER has been

adopted as structural material, the proper thermo-physical properties to simulate the EUROFER in RELAP5-3D code (namely density, specific heat and thermal conductivity) are reported in Table 4-9 [34] against temperature from 293.15 to 973.15 K.

Table 4-9: Thermo-physical properties of EUROFER97

T [K]	ρ [kg/m³]	c_p [kJ/(kg·K)]	λ [W/(m·K)]
293.15	7750	448	31.5
373.15	7753	460	32.2
423.15		477	
473.15	7713	494	32.7
523.15		510	
573.15	7685	527	33.2
623.15		544	
673.15	7655	565	33.3
723.15		586	
773.15	7625	611	32.8
823.15		644	
873.15	7594	682	32.3
923.15		728	
973.15		866	44.8

Moreover, the 2 mm-thick FW tungsten armour has been modelled as well. Its thermo-physical properties (thermal conductivity, specific heat and density) are in the following reported as functions depending uniquely on temperature expressed in degrees Celsius.

Indeed, for the thermal conductivity is:

$$\lambda(T) = 174.9274 - 0.1067 \cdot T + 5.0067 \cdot 10^{-5} \cdot T^2 - 7.8349 \cdot 10^{-9} \cdot T^3 \quad [W/(m\cdot°C)] \quad (4.10)$$

the specific heat functional dependence is:

$$c_p(T) = 128.308 + 93.2797 \cdot 10^{-2} \cdot T - 3.4097 \cdot 10^{-6} \cdot T^2 \quad [kJ/(kg\cdot°C)] \quad (4.11)$$

while the density can be expressed as:

$$\rho(T) = 19302.7 - 2.3786 \cdot 10^{-1} \cdot T - 2.2448 \cdot 10^{-5} \cdot T^2 \quad [kg/m^3] \quad (4.12)$$

It has to be noted that, in Equation 4.10, Equation 4.11 and Equation 4.12, the temperature values must be expressed in [°C].

As concerns the functional materials, namely KALOS and $Be_{12}Ti$, their thermo-physical properties are reported in Table 4-10 and in Table 4-11, respectively [33].

Regarding KALOS, values of property as density, specific heat and thermal conductivity are reported against temperature from 293.15 to 1273.15 K. It has to be noted that density can be considered uniform in this range of temperatures.

Instead, as far as $Be_{12}Ti$ thermo-physical properties are concerned, it has to be observed that, in Table 4-11, values for both unirradiated and irradiated (up to 37.1 dpa @923.15 K) material are reported in the temperature range 308.15-923.15 K.

Table 4-10: Thermo-physical properties of KALOS

T [K]	ρ [kg/m³]	c_p [kJ/(kg·K)]	λ [W/(m·K)]
293.15	1646	1240.4	0.919
373.15			0.946
423.15			0.964
473.15			0.979
523.15			0.985
573.15		1641.3	1.013
623.15			1.030
673.15			1.047
723.15			1.064
773.15		1823.44	1.081
823.15			1.097
873.15			1.114
923.15			1.131
973.15		2324.6	1.148
1273.15			1.249

Table 4-11: Thermo-physical properties of $Be_{12}Ti$

T [K]	ρ [kg/m³]	c_p [kJ/(kg·K)]	λ [W/(m K)]
uniraddiated			
623.15	2250.0	2640.0	52.9
723.15	2250.0	2780.0	55.7
873.15	2250.0	2920.0	58.4
923.15	2250.0	2970.0	62.2
irradiated up to 37.1 dpa @923.15 K			
623.15	2211.0	2630.0	37.2
723.15	2198.0	2760.0	44.3
873.15	2203.0	2950.0	43.5
923.15	2156.0	2970.0	45.4

4.2.3 Thermal Loads and Boundary Conditions

The thermal power adopted for simulating the normal operational scenario, including the ramp-up and ramp-down, takes into account both the heat flux acting on FW and the nuclear heating due to thermal power deposited by neutron interactions, as reported in [97, 98].

In this regard, Figure 4-18 shows the DEMO fusion power highlighting the two transition phases between pulse and dwell. In this picture, the duration of each single phase is indicated as well. Instead, Figure 4-19 reports the duty cycle adopted for the analysed loop.

As a consequence, in Table 4-12 and Table 4-13 the thermal loads for both OB and IB segments are reported, according to the classification given in Figure 4-20. In these tables, the FW and BZ heat loads are properly distinguished.

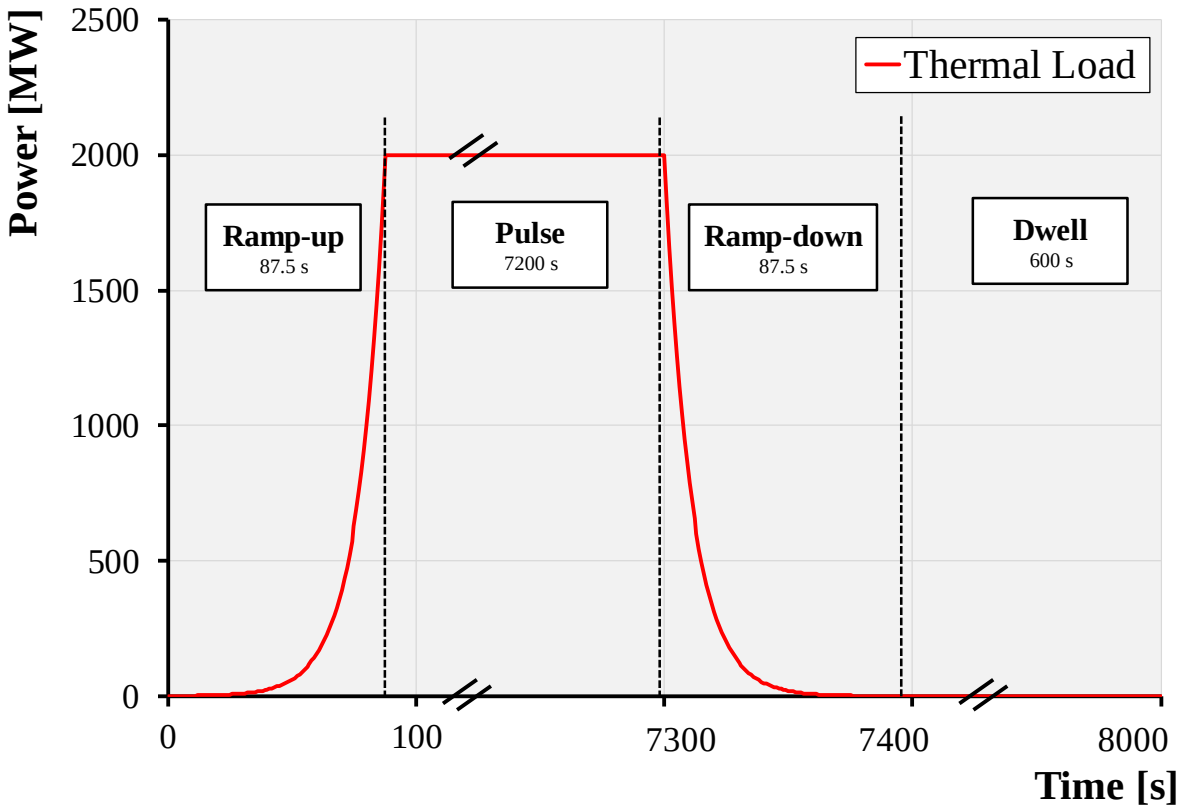

Figure 4-18: DEMO fusion power.

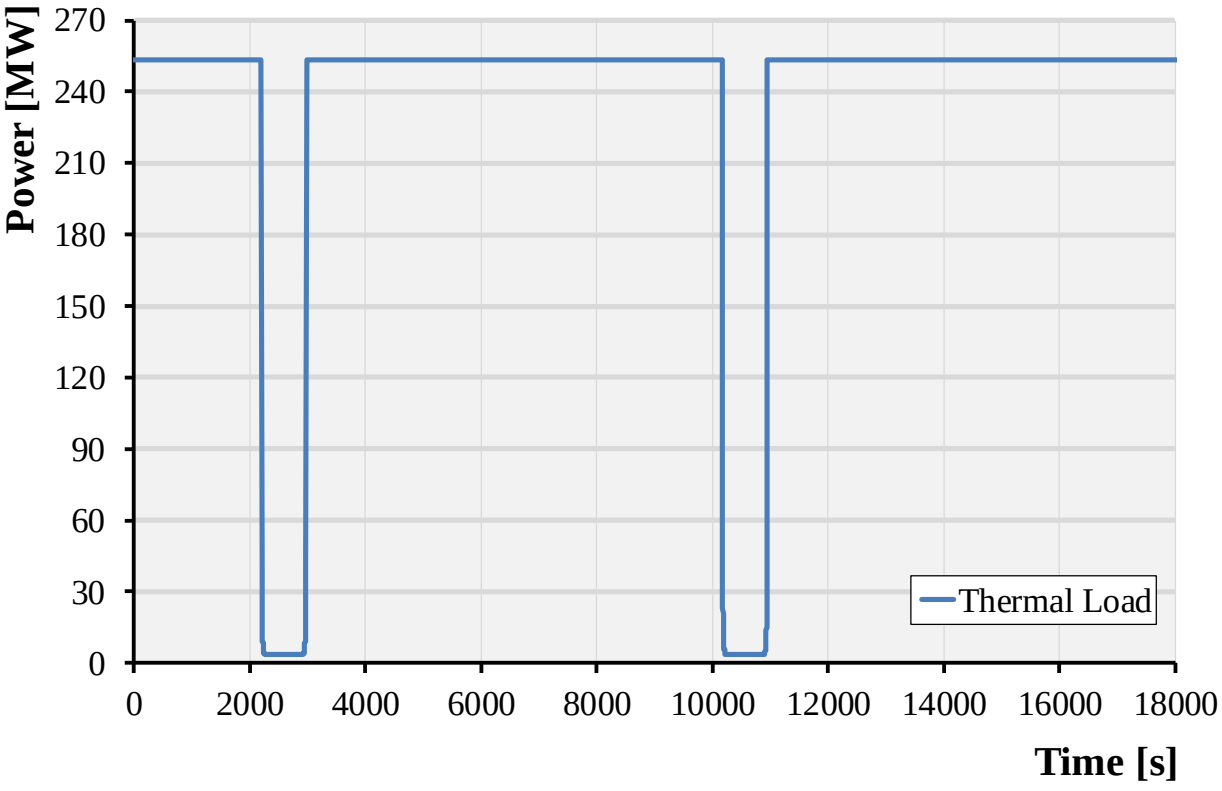

Figure 4-19: Loop thermal power profile.

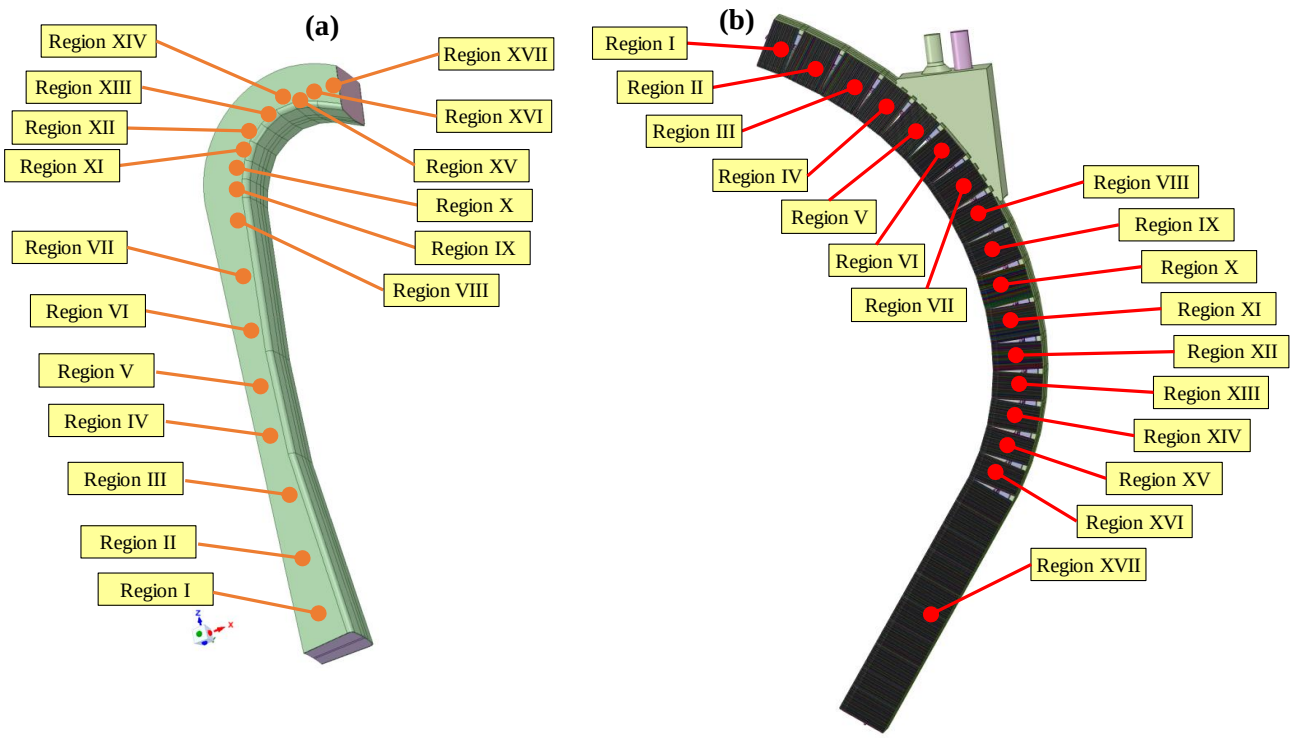

Figure 4-20: Classification of (a) IB and (b) OB segment's regions.

Table 4-12: OB segments thermal loads [97]

COB Region No.	FW Power [MW]	BZ Power [MW]	L/ROB Region No.	FW Power [MW]	BZ Power [MW]
#1	1.629E-01	7.286E-01	#1	1.042E-01	4.671E-01
#2	2.401E-01	1.222E+00	#2	1.662E-01	8.828E-01
#3	2.401E-01	1.296E+00	#3	1.898E-01	1.035E+00
#4	2.001E-01	1.144E+00	#4	1.717E-01	9.898E-01
#5	2.084E-01	1.185E+00	#5	1.870E-01	1.094E+00
#6	2.084E-01	1.223E+00	#6	1.874E-01	1.186E+00
#7	2.084E-01	1.255E+00	#7	2.104E-01	1.273E+00
#8	2.084E-01	1.286E+00	#8	2.178E-01	1.344E+00
#9	2.084E-01	1.307E+00	#9	2.232E-01	1.399E+00
#10	2.084E-01	1.325E+00	#10	2.269E-01	1.439E+00
#11	2.168E-01	1.327E+00	#11	2.333E-01	1.456E+00
#12	1.667E-01	1.066E+00	#12	1.830E-01	1.166E+00
#13	1.734E-01	1.063E+00	#13	1.852E-01	1.158E+00
#14	1.667E-01	1.065E+00	#14	1.849E-01	1.138E+00
#15	1.734E-01	1.057E+00	#15	1.818E-01	1.112E+00
#16	1.734E-01	1.051E+00	#16	1.732E-01	1.073E+00
#17	2.066E+00	7.856E+00	#17	1.649E+00	6.699E+00

Table 4-13: IB segments thermal loads [97]

IB Region No.	FW Power [MW]	BZ Power [MW]
#1	3.322E-01	1.097E+00
#2	3.322E-01	1.461E+00
#3	3.322E-01	1.722E+00
#4	2.158E-01	1.584E+00
#5	2.158E-01	1.453E+00
#6	2.152E-01	1.423E+00
#7	2.152E-01	1.257E+00
#8	2.152E-01	9.986E-01
#9	5.830E-02	3.450E-01
#10	5.941E-02	3.525E-01
#11	6.339E-02	4.046E-01
#12	7.257E-02	4.731E-01
#13	8.121E-02	5.270E-01
#14	9.319E-02	5.724E-01
#15	6.647E-02	4.044E-01
#16	6.922E-02	4.098E-01
#17	1.699E-01	6.871E-01

4.3 Thermal-hydraulic Parametric Campaign of Analysis

The investigation of the BB-PHTS DEMO HCPB thermal-hydraulic behaviour under normal operational conditions has been mainly intended to preliminarily investigate the thermal-hydraulic phenomena occurring into the system.

The main aim of this assessment has been the study of a possible strategy to control both the helium and HITEC mass flow rate in order to maintain the inlet temperature to the BB equal to 573.15 K, as required in [43]. The obtained results are presented and commented in this paragraph, giving some hints for the follow up of this activity.

4.3.1 Normal Operational Scenario Results

The comparison between the main results obtained and the design values is reported in Table 4-14. From a general standpoint, a very god agreement can be observed as deviations lower than 1 % have been calculated for He mass flow rate, BB inlet/outlet temperatures and pressure drops.

Table 4-14: Loop main results.

Value	Unit	Design Values	RELAP5-3D	Deviation [%]
BB Power	[MW]	253.64	253.64	-
He mass flow rate	[kg/s]	222.24	222.24	0.001%
BB inlet temperature	[K]	573.15	573.15	-0.002%
BB outlet temperature	[K]	793.15	793.64	0.061%
BB pressure drop	[kPa]	79.90	79.69	-0.264%
IHX pressure drop	[kPa]	60.70	60.37	-0.542%
Total pressure drop	[MPa]	270.00	271.00	0.369%

Moreover, in order to qualify the developed nodalization, the pressure drops calculated by the code along a relevant path have been compared to the theoretical ones, see Figure 4-21. The results show a very

good accordance between theoretical values and the RELAP5-3D ones. In fact, as show in Table 4-14, the total pressure drop predicted by the code is 271 kPa with respect to the 270 kPa theoretically evaluated. The calculated deviation is about 0.369 %.

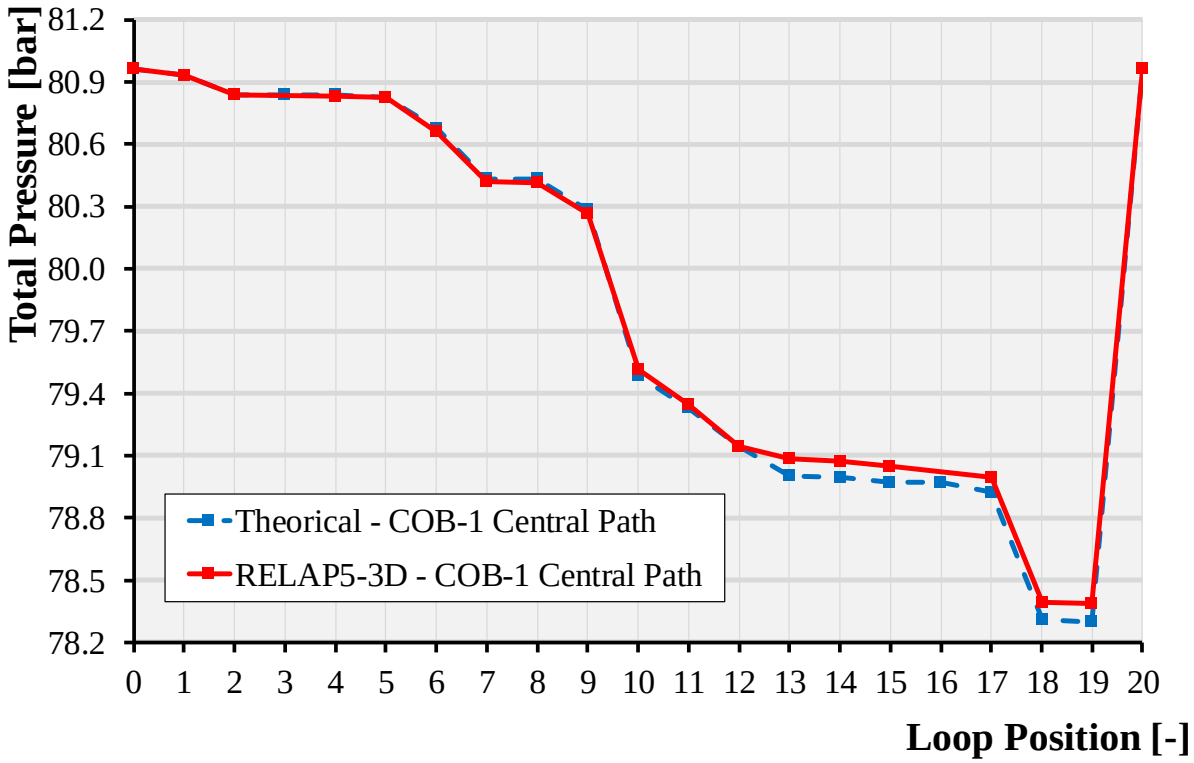

Figure 4-21: Pressure drops along the COB-1 central path.

Furthermore, Figure 4-22 compares the calculated temperature profiles of helium, wall and HITEC along the IHX extension with the design values. Even in this case a very good agreement has been found, especially for both the fluid temperatures where the maximum deviation observed for molten salt is about the 1.78%. As it can be seen, just the wall temperature results are slightly underestimated. Anyway, the maximum deviation observed is equal to 3.79% and therefore results can be considered reliable. This deviation in the wall temperature can be mainly ascribed to the way in which the fouling has been accounted for with respect to the design approach. Indeed it has been simulated in the model by adding a layer of an equivalent material (t=50 μm; λ= 0.568 W/mK and $\rho \cdot c_p$=5.0E5 J/m³K) compared to the so-called fouling factor adopted in [93].

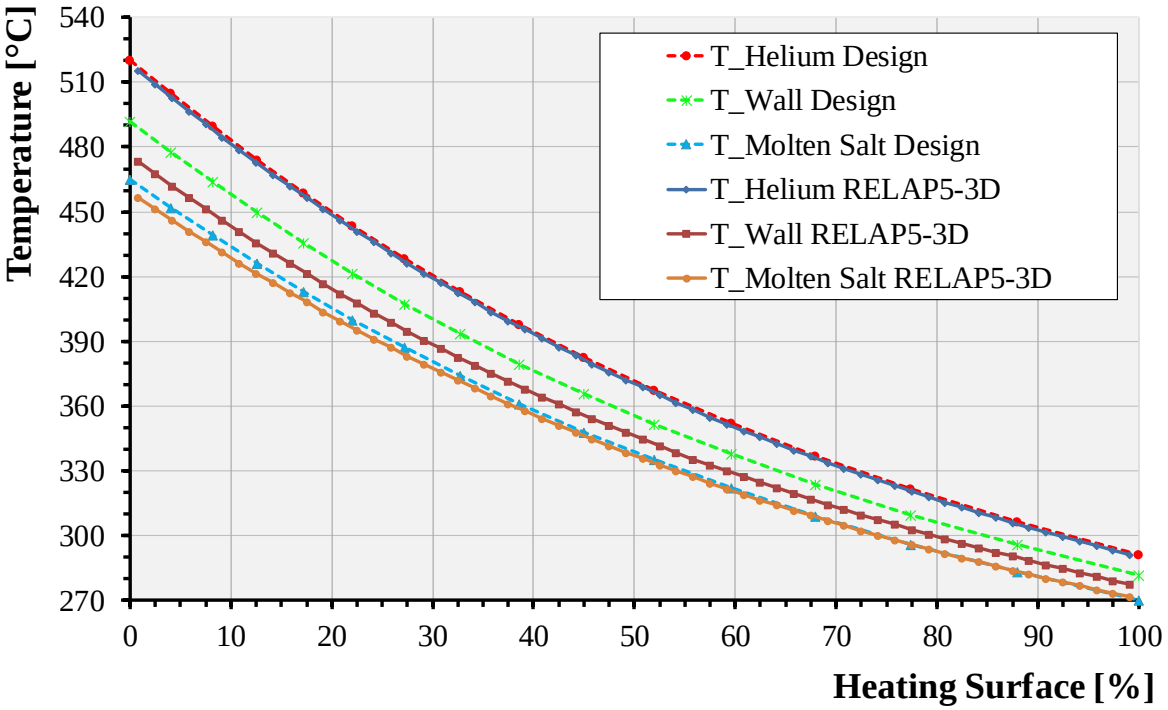

Figure 4-22: IHX temperature profile.

Once performed so a kind of evaluation, a parametric study has been thereafter performed analysing the normal operational conditions. The main objective of this study has been to assess the dynamic response of the system when it switches from pulse to dwell and vice versa. In particular, 4 cases involving a combination of different mass flow rates on both helium and HITEC sides has been set-up with the aim of understanding the potential maximum variations that relevant quantities such as pressure and temperatures can experience for a given Balance of Plant control. The 4 identified cases are:

I. both the helium and the HITEC mass flow rate are kept constant at the nominal pulse value during the entire period;
II. the helium flow rate is the same that in (I), while the HITEC one follows the same functional shape of the BB thermal power;
III. it consists in changing the helium mass flow rate according to the same functional shape of the BB thermal power, while the molten salt mass flow does not change;
IV. both the helium and the HITEC mass flow rates evolve like the power functional shape.

The Helium and HITEC mass flow rates in the four assessed cases are depicted in Figure 4-23 and Figure 4-24, respectively.

As to the obtained results, the trend of the temperatures in cold and hot legs is shown in Figure 4-25 and Figure 4-26, respectively; whilst in Figure 4-27 the cold leg pressure is displayed.

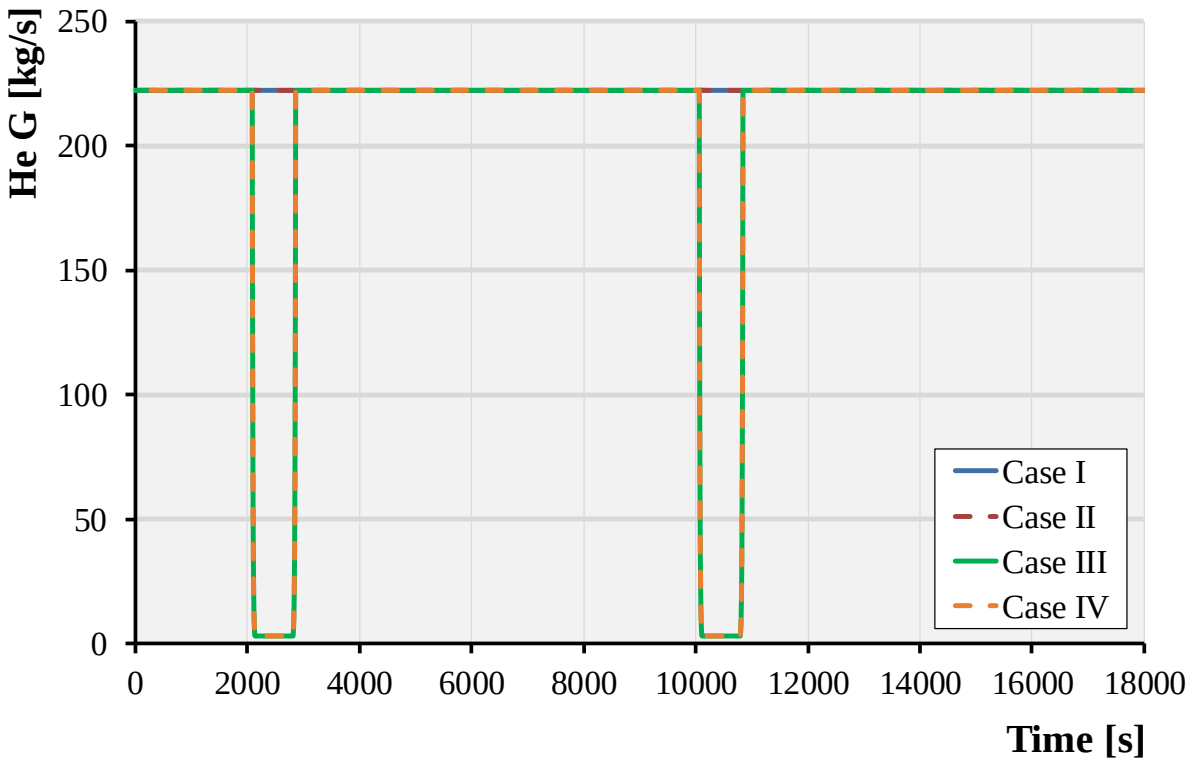

Figure 4-23: Helium mass flow rate.

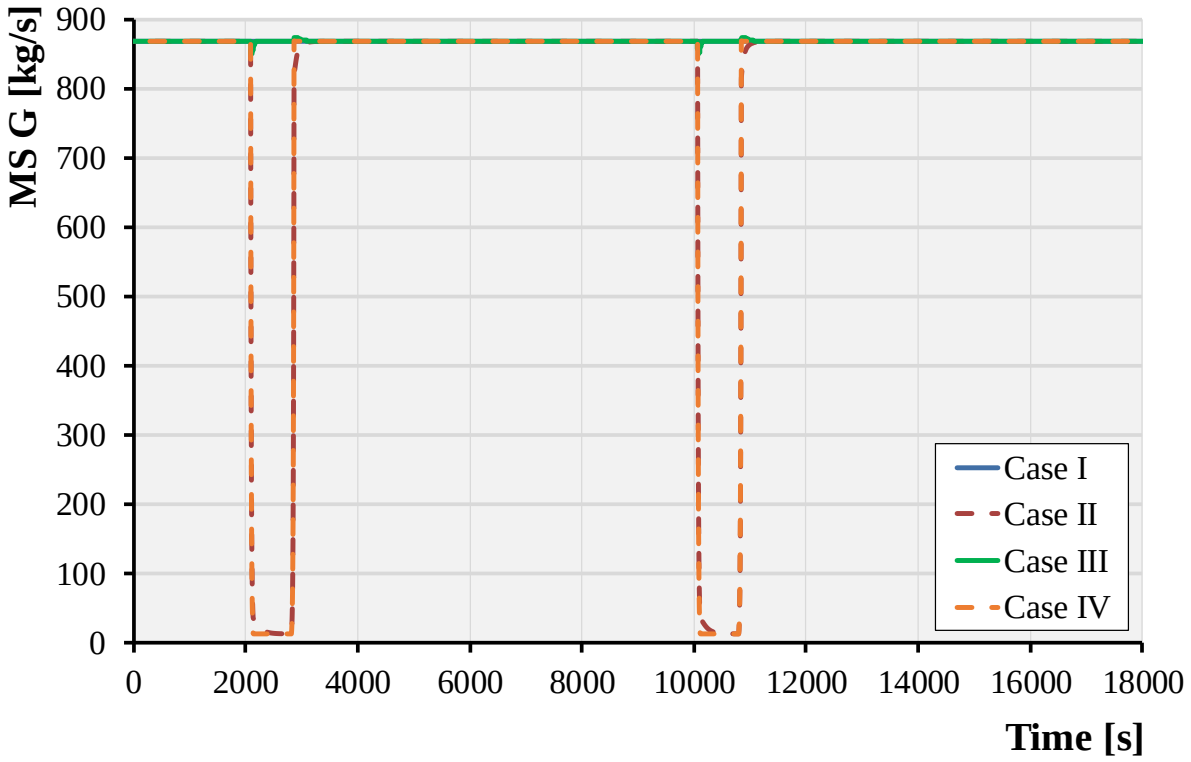

Figure 4-24: HITEC mass flow rate.

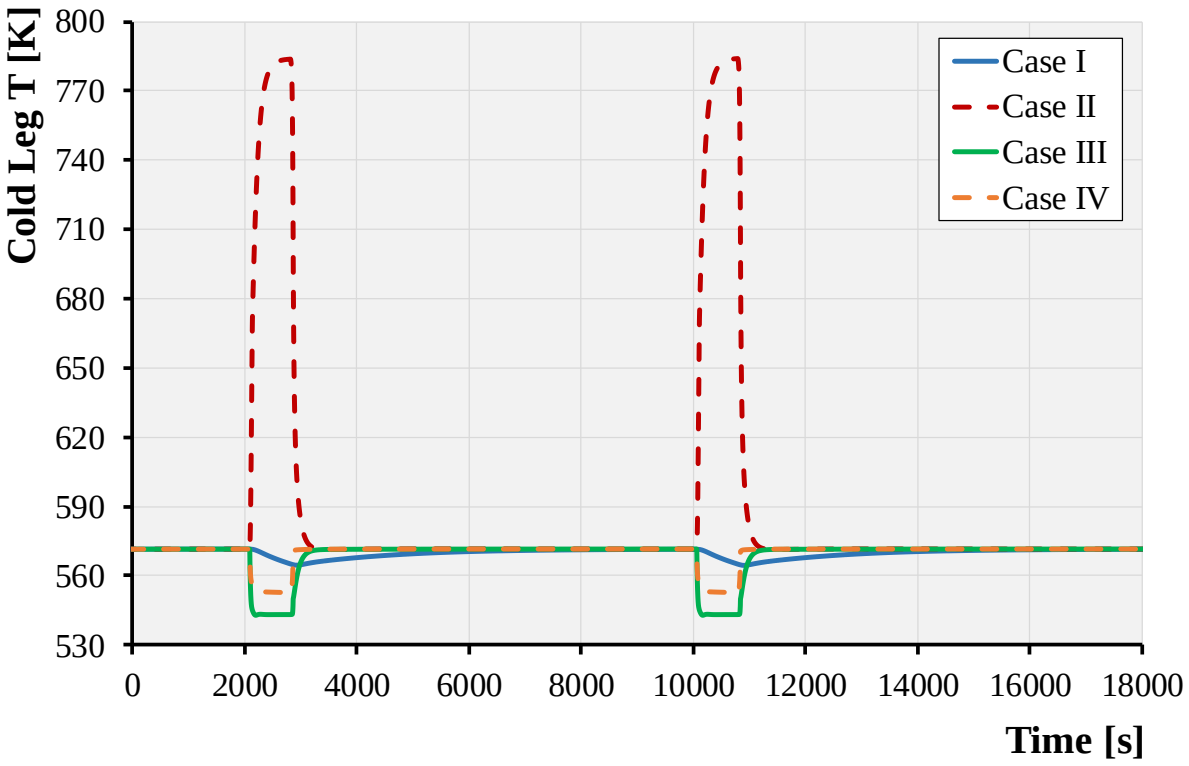

Figure 4-25: Cold leg temperature.

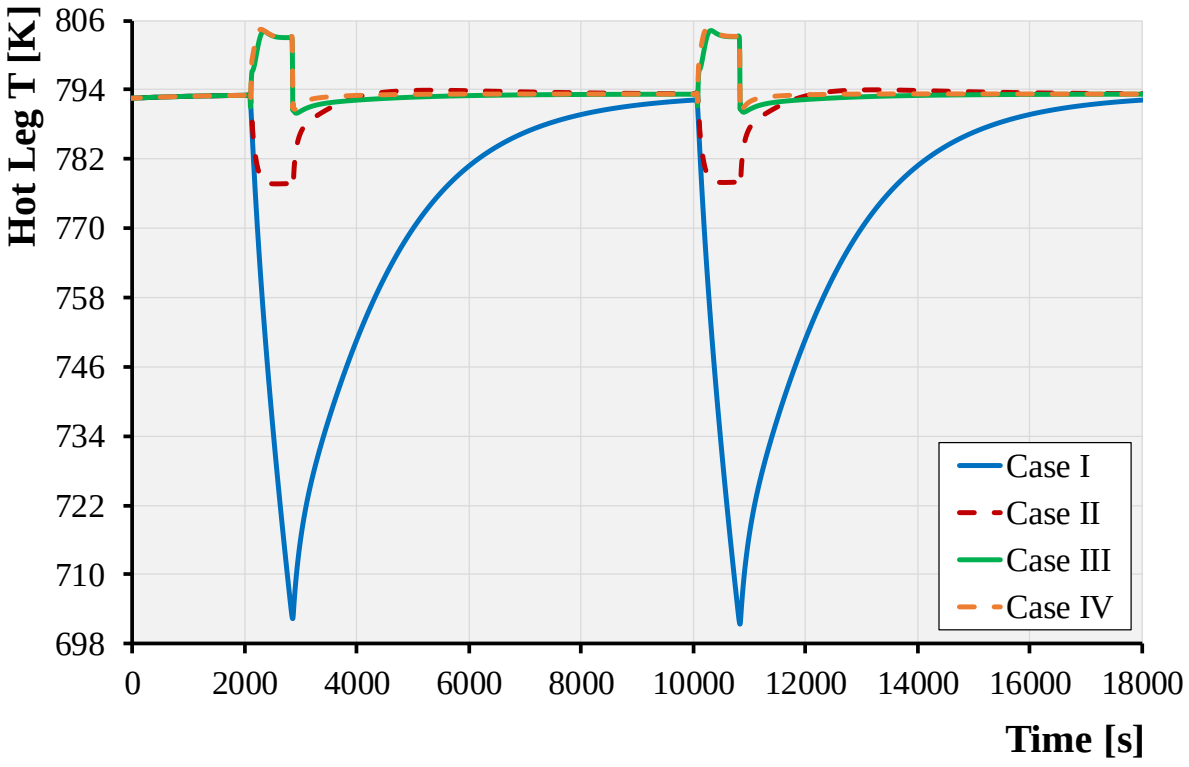

Figure 4-26: Hot leg temperature.

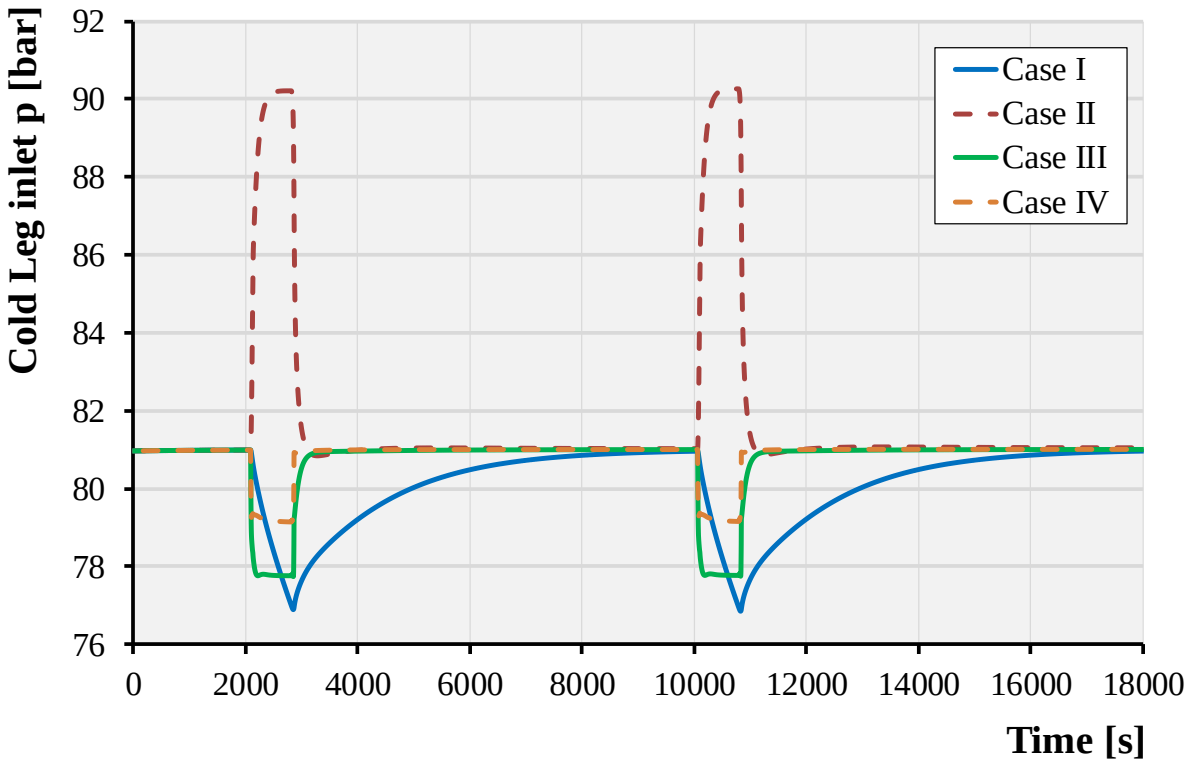

Figure 4-27: Cold leg inlet pressure.

Starting from these outcomes, which have allowed to explore the 'extreme' regulation scenarios, a more viable case has been envisaged. In this further case, the helium mass flow rate evolves assuming a practicable [99, 100] rate of change of 12.5 % per minute compared to the power law analysed before. This assumed rate has enabled the helium mass flow rate to reach the minimum value of 83.34 kg/s during the dwell (Figure 4-28), whilst the molten salt mass flow rate has been evaluated by the system code with a dedicated proportional-integral controller aimed at maintain the required coolant's BB inlet temperature at 573.15 K. The new PHTS system control modelled for this case allows to reduce the main quantities excursion when switching between the two operational phases. Indeed, this can be observed for both the hot and cold temperatures depicted in Figure 4-29 and Figure 4-30, respectively. But also for the cold leg inlet pressure which is shown in Figure 4-31.

However, further studies would be needed in the future to better understand the feasibility of such PHTS control system. Indeed, even if the BB inlet temperature slightly sways around the required value of 573.15 K and also the pressure changes may be tolerate by the system (~3% in ~8 minutes), the hot leg outlet temperature behaviour suggests the need to investigate other regulation solutions (bypass or pressure relief and throttled inlet compressor), in order to further reduce the helium mass flow rate during the dwell avoiding to submit the components to the observed temperature variations which may determine their damaging due to the thermal fatigue.

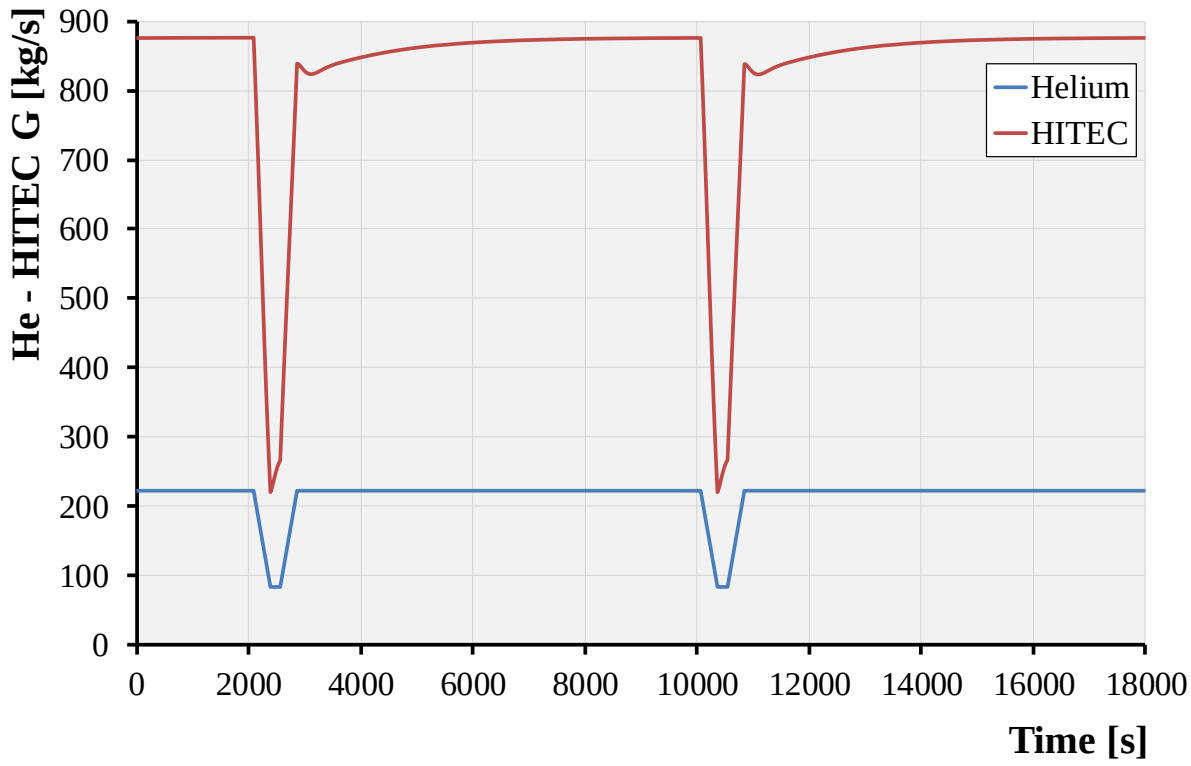

Figure 4-28: Helium and HITEC mass flow rate.

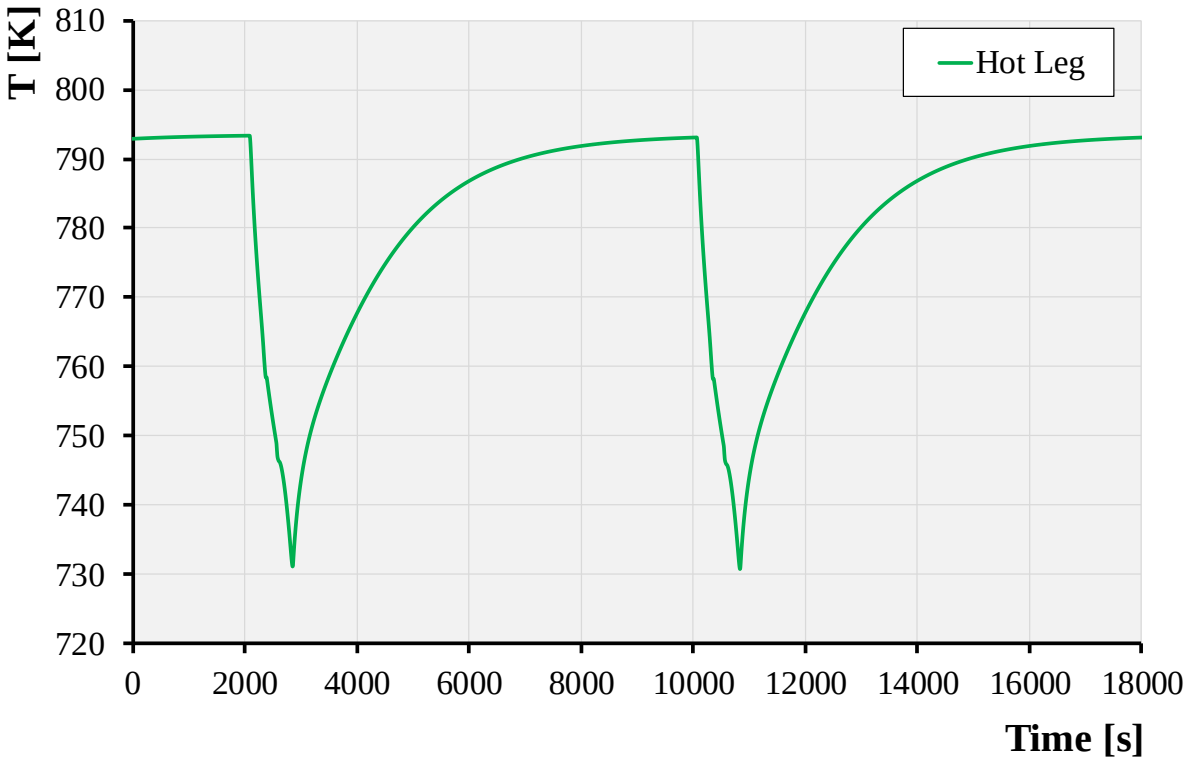

Figure 4-29: Hot leg temperature.

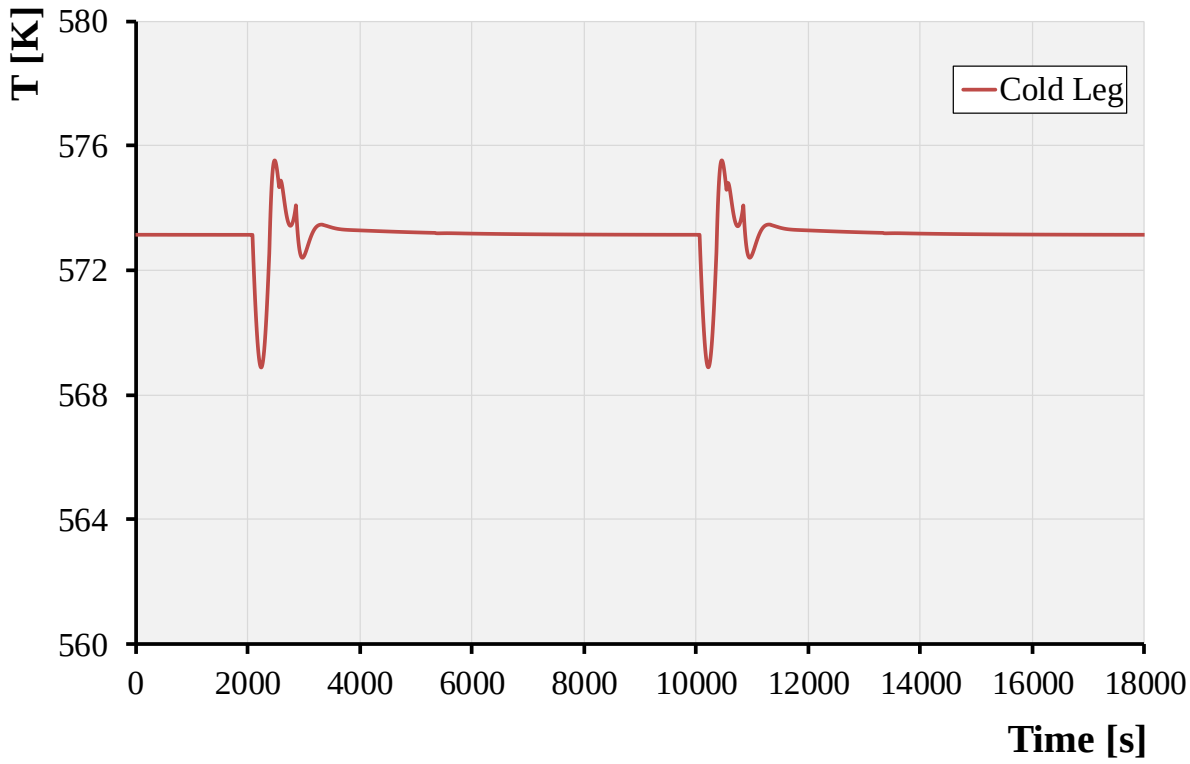

Figure 4-30: Cold leg temperature.

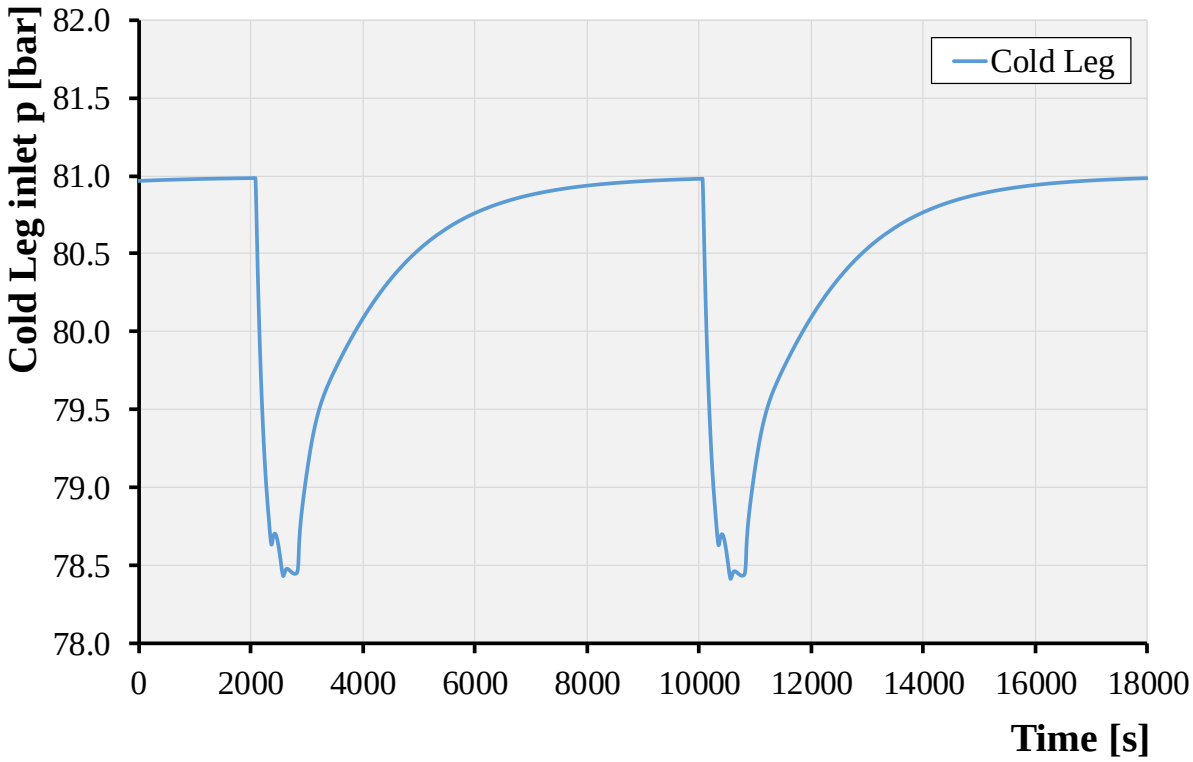

Figure 4-31: Cold leg inlet pressure.

5 Thermal Hydraulic Analysis of the EU-DEMO HCPB Reactor during Accidental Scenarios

5.1 Introduction

The integral approach methodology depicted in §2.3, validated in chapter 3 and already adopted to assess the thermal-hydraulic behaviour of the selected loop under normal operational conditions in the previous chapter 4 has been used to analyse the consequences of some representative accidental scenarios. The obtained results are reported and critically discussed in this chapter.

5.2 Loss of Coolant Accident Scenarios

In the current pre-conceptual design stage of the DEMO reactor, several studies have been performed in the frame of the EUROfusion safety project to support design activities, ensuring that the evolving system design will satisfy safety requirements and that it is optimized for the safety of personnel, public and environment [101].

Within this framework, a Functional Failure Modes and Effects Analysis (FFMEA) has been completed for all DEMO key systems. Indeed, FFMEA is applied to define an exhaustive set of accident initiators when the project level is still in a pre-conceptual status. According to this procedure, firstly each system is subdivided in different subsystem following the structure of simplified Process Flow Diagrams (PFDs). For each subsystem, i.e. for each specific component, different functions are identified and listed. Hence for each function the failure associated to its loss is postulated and the possible causes analysed and listed. The individuation of the causes is carefully treated. Usually, this refers to the failure of components (e.g. piping, valves, I&C, etc.) of a subsystem (e.g. cold leg between steam generator and pump, hot leg, feeding pipes, etc.) that can induce the loss of the specific function [45, 102]. Each important initiator is then discussed in order to define the accident sequences that could stem from the initiator and the deterministic assessment that could be required. If the design detail level does not allow individuating in the diagrams all the components of a system, engineering judgement is applied, also using reference from similar systems with higher level of design detail. Thus, the consequences associated to the loss of function from a component are analysed for the whole system. Such consequences can be distinguished in immediately occurring after the loss of the function and aggravating sequences. A set of mitigating actions is also proposed to limit the failure consequences.

Hence, despite the possible lack of information for some system's designs, through this approach it is possible to identify elementary initiators, possible causes and safety consequences. In fact, by the FFMEA, it is possible to provide a complete list of potential accident initiating events (IEs) and to give suggestions in order to improve the machine overall safety. From the complete list of IEs, a set of Postulated Initiating Events (PIEs) has been identified as the most representative in terms of challenging conditions for the safety of the plant. Each elementary accident initiator is associated to the related PIE. In such a way, it is possible to concentrate safety studies on the most relevant accident sequences, avoiding studies related to the other minor and almost equivalent sequences [45, 103].

As reported in [103], the application of the FFMEA analysis has led to the selection of 21 PIEs that envelope all the identified failures. In particular, among them some ex-vessel and in-vessel Loss Of Coolant Accidents (LOCAs) scenarios have been classified among the most representative events in terms of challenging conditions for plant safety.

5.2.1 Ex-Vessel Loss of Coolant Accident Analysis

As already disclosed, one of the most challenging accidental scenarios identified by the FFMEA are the

ex-vessel LOCAs due to the possible consequences in terms of radiological releases to the environment. Clearly, because of the relative small radiological inventory and to the lower decay heat density, the risk associated with a break of the primary cooling loop in a fusion reactor is lower than the risk of the same event in a fission reactor. Nevertheless the consequent pressure peak in the Tokamak Cooling Room (TCR) could severely impact the confinement function of the tokamak building, hence the overall safety of the plant. In particular, three different PIEs encompass the possibility to loss the coolant from the DEMO PHTSs, one of which is right the BB-PHTS as a result of a large rupture in the coolant manifold feeder.

The adopted integral approach has been applied in analysing an ex-vessel LOCA scenario due to a Double-Ended Guillotine (DEG) in the largest hot feeding pipe. The models set-up and the obtained outcomes are reported in this paragraph.

5.2.1.1 Models and Asssumptions

In order to simulate the selected scenario, the computational model described in chapter §4 has been extended to include the TCRs modelled as expansion volumes. In particular, they include both lower and upper chase, 7 vertical shaft and the BB-PHTS building levels, namely L3, L4 and L5 as shown in Figure 5-1 (a). The total ex-vessel volume available for the helium expansion is ~$1.36 \cdot 10^5$ m³. This value has been evaluated from the CAD file subtracting the equipment volumes.

The expansion volumes have been simulated by using 12 PIPEs, 6 SINGLE JUNCTIONs and 1 MULTIPLE JUNCTION, as depicted in Figure 5-1 (b). As concerns the air conditions, its temperature has been set to 323.15 K, while the initial pressure has been considered equal to 95 kPa. The break occurring in that portion of the hot feeding pipe where the cross section is the greatest, namely $8.07 \cdot 10^{-2}$ m², has been simulated by means of a VALVE component.

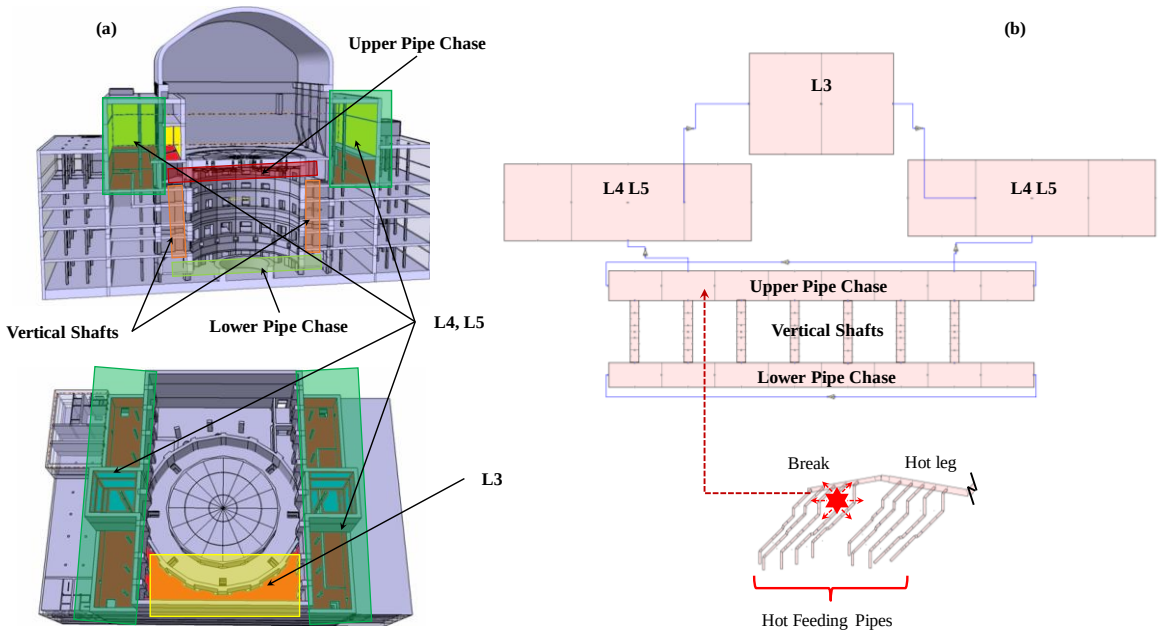

Figure 5-1: HCPB DEMO Tokamak building (a) CAD model and (b) TCR nodalization scheme.

5.2.1.2 Results

The ex-vessel LOCA begins at t=0 s nearly the end of the pulse phase, which has been assumed the reference condition to start the transient analysis. It is simulated a time delay, t_{res}, in detecting the break equal to 3 s according to [104], after which both the practically immediate plasma shutdown and the decay heat are simulated. The latter has been implemented into the model distinguishing between the involved materials in order to reproduce as close as possible the heat load reported in Figure 5-2 according to the

nomenclature shown in Figure 5-3. Practically, at t= t_{res} the total thermal power is about the 1.3% of the nominal one and in almost 1 hour it is halved.

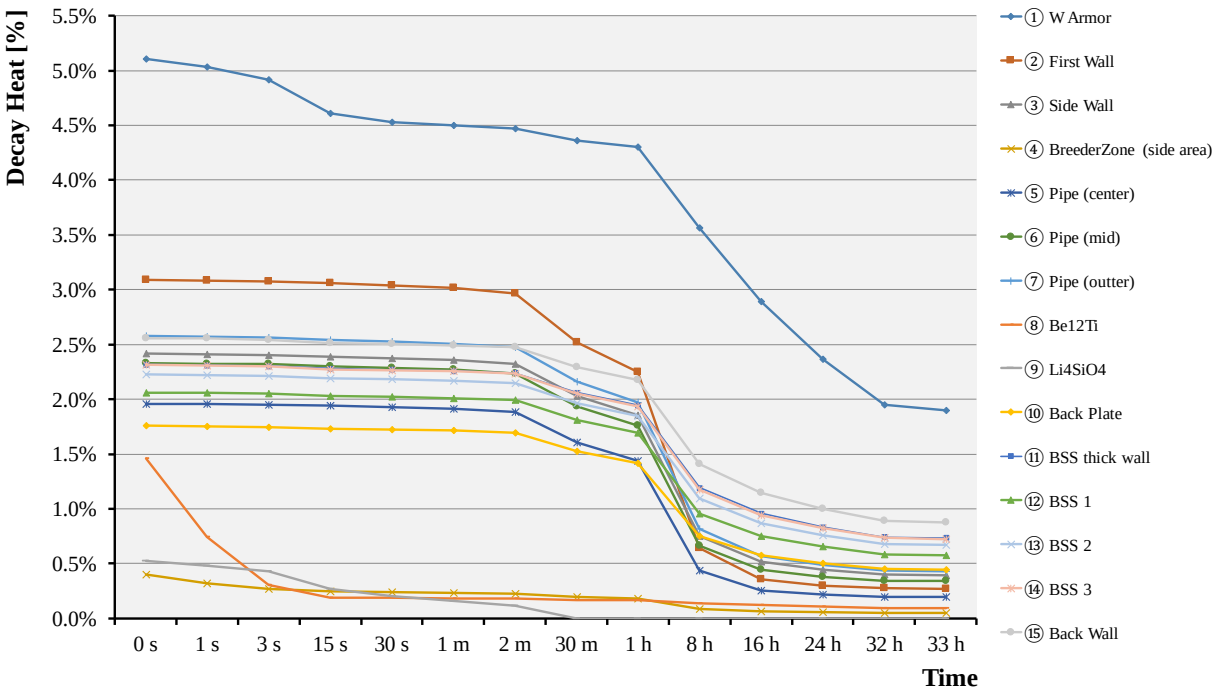

Figure 5-2: Decay heat time-evolution.

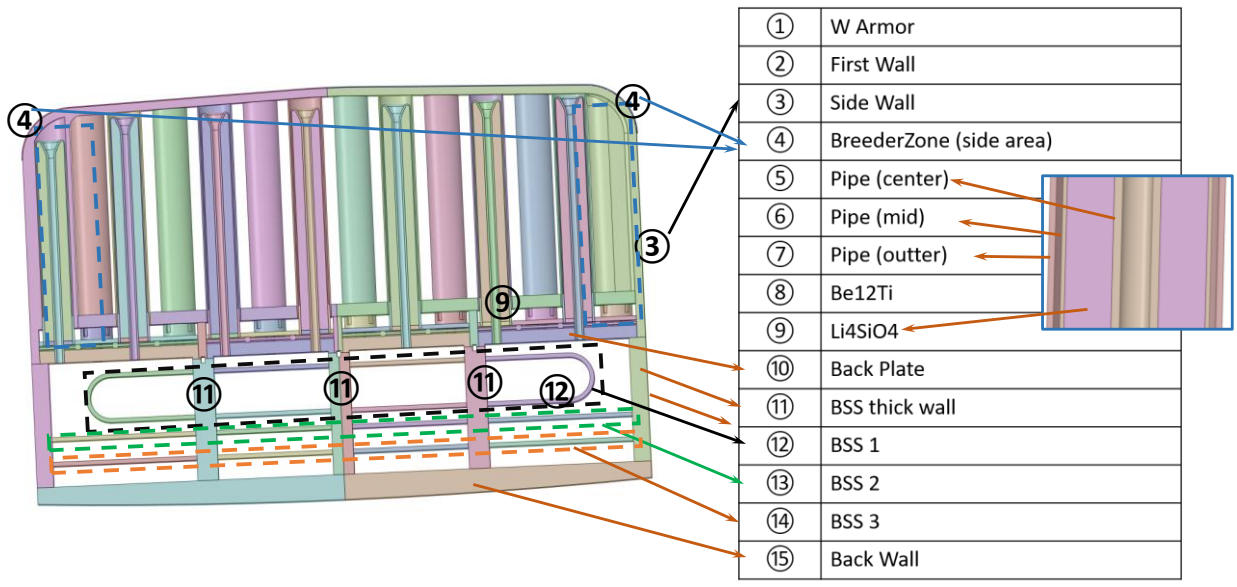

Figure 5-3: Material identification for the decay heat calculation.

As can be deduced from the evolution of the break mass flow rate depicted in Figure 5-4, the equilibrium conditions are reached after about 30 s from the rupture occurrence, that is when the loop is practically empty being with a residual mass of approximately 35 kg, see Figure 5-5.

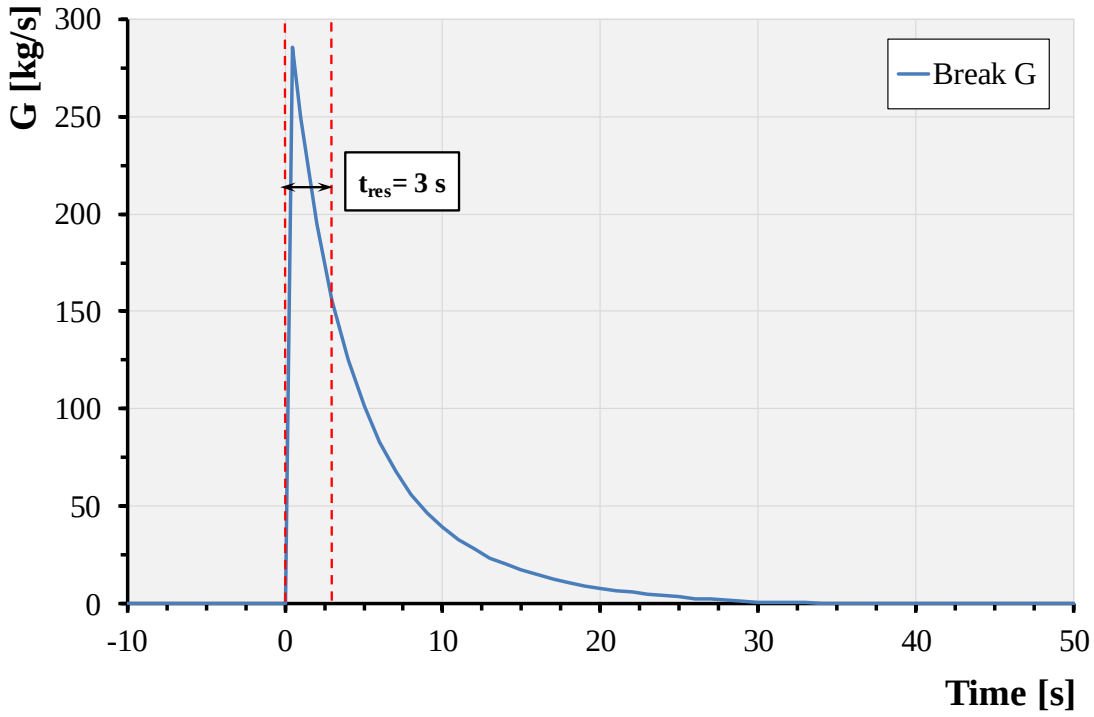

Figure 5-4: Break mass flow rate.

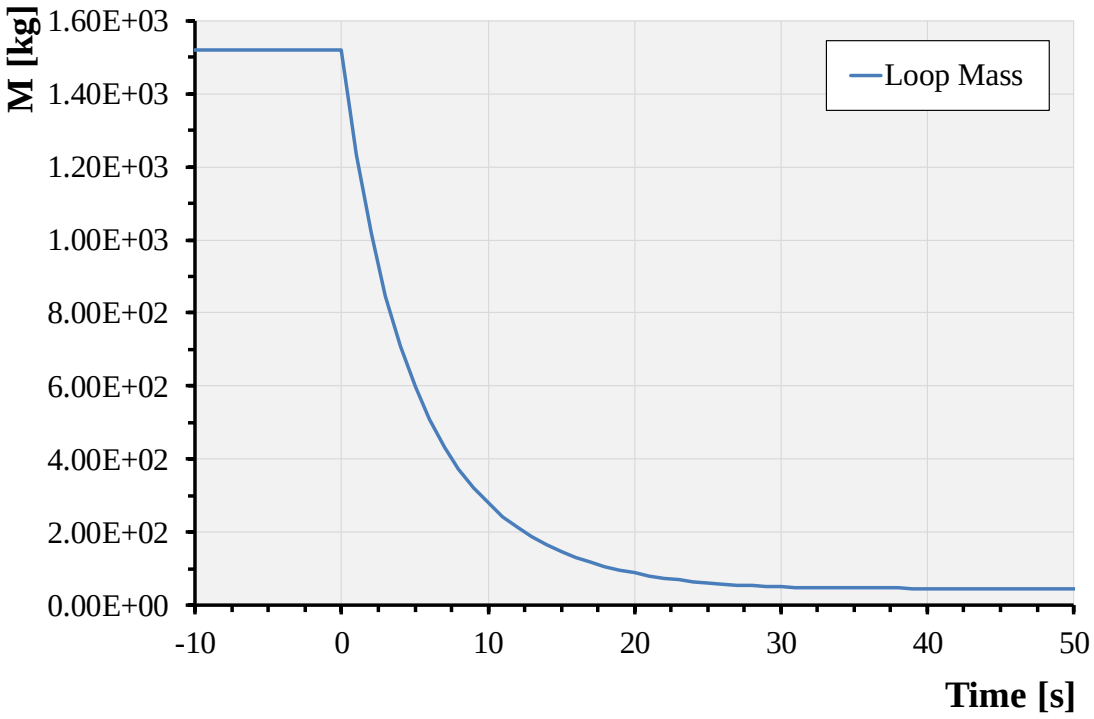

Figure 5-5: Loop mass time-evolution.

The pressure reaches, at the equilibrium, the maximum value of 116 kPa, as reported in Figure 5-6, which is safely below the prescribed limit of 200 kPa [24]. Whilst, the equilibrium temperature inside the tokamak cooling rooms is about 362 K, as shown in Figure 5-7.

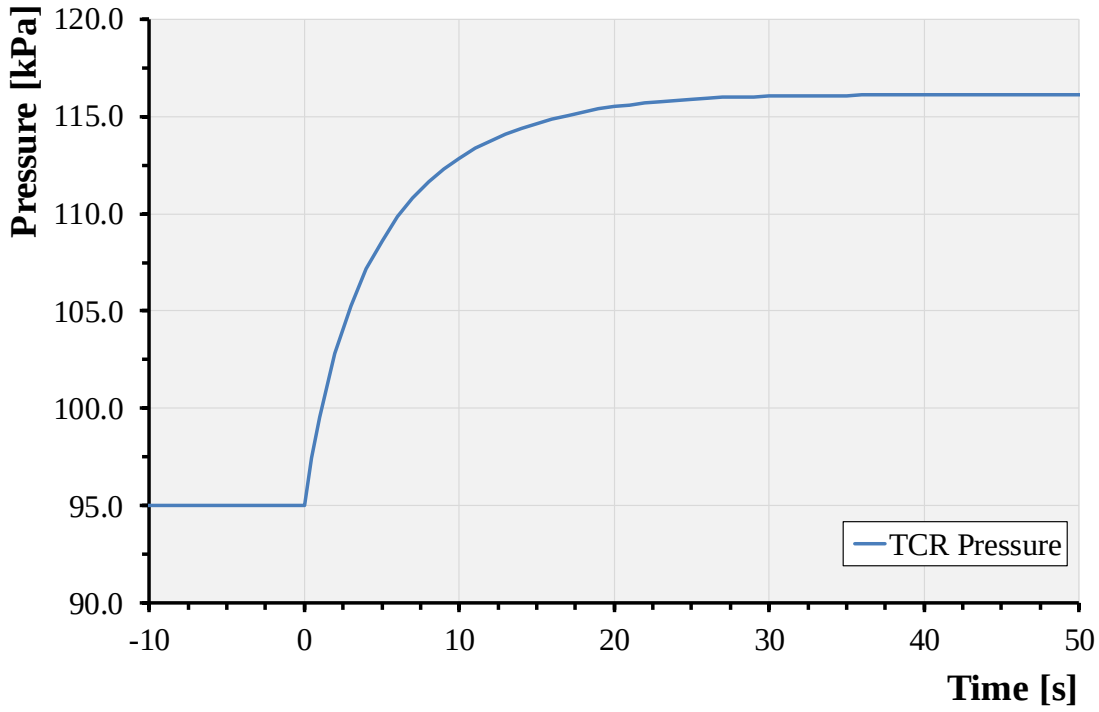

Figure 5-6: TCR pressure time-evolution.

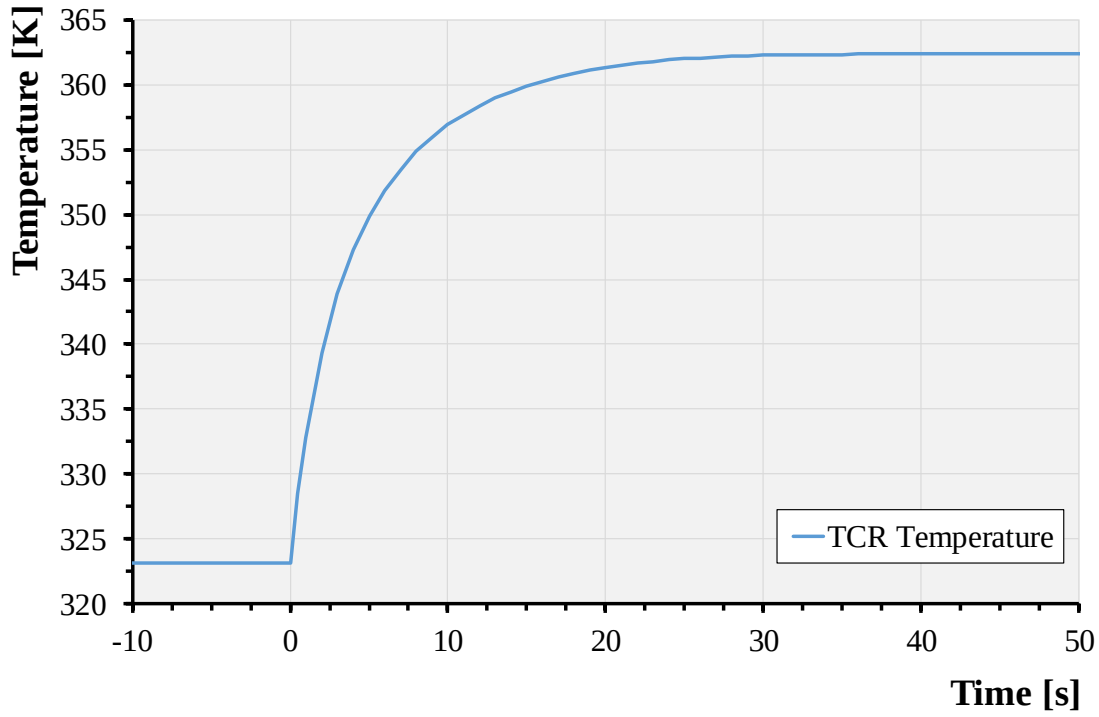

Figure 5-7: TCR temperature time-evolution.

Due to the size of the rupture, the transient timing would allow to investigate the possibility to adopt isolation valves in order to reduce the helium inventory released into the TCR, whereas the transient time scale of an equivalent break in the hot leg will be a serious cause for concern relating to such a possibility. Indeed, after a DEG break in hot leg the maximum pressure value is reached at about 2.5 s (Figure 5-8)

from the opening. At the same time, the helium inventory inside the loop reaches is equilibrium value as shown in Figure 5-9.

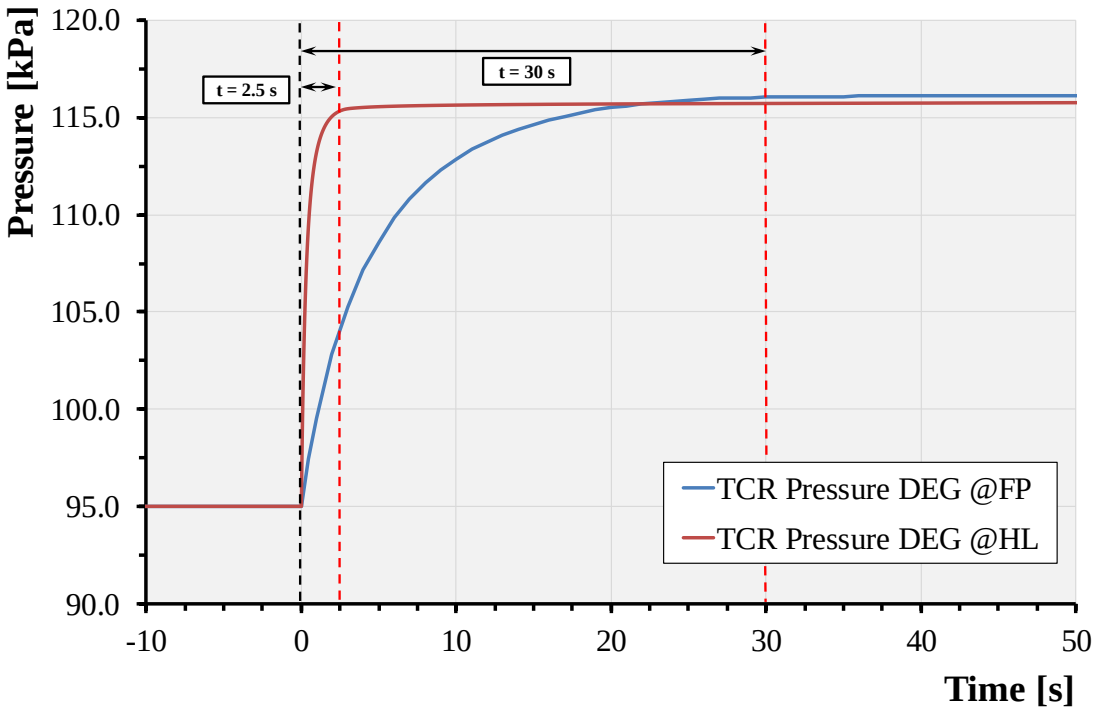

Figure 5-8: TCR pressure evolution for both hot leg (HL) and feeding pipe (FP) DEG scenarios.

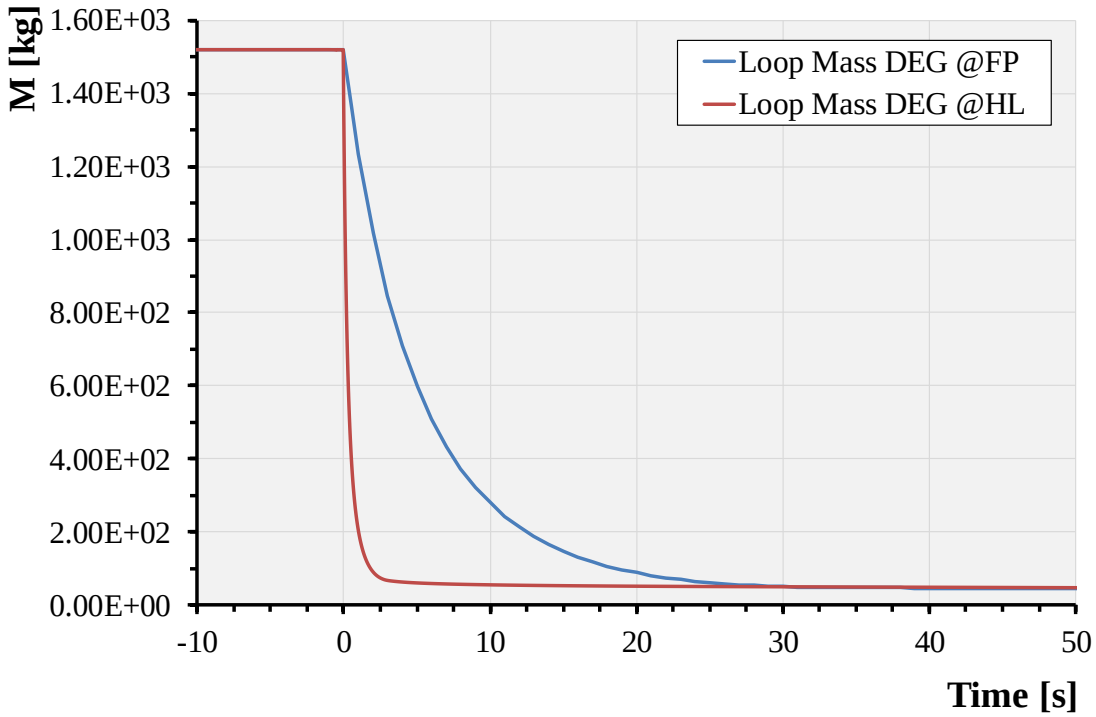

Figure 5-9: Loop mass for both hot leg (HL) and feeding pipe (FP) DEG scenarios.

5.2.2 In-Vessel Loss of Coolant Accident Analysis

As stated in [103], the in-vessel LOCA scenario consists in one of the most representative PIEs in terms

of challenging conditions for plant safety, since it could cause considerable damage to the components within the VV. In this paragraph, the consequences of a DEG rupture of one OB segment hot feeding pipe on the vacuum side will be investigated, see Figure 5-10. In particular, two scenarios have been envisaged: the first foresees a dry expansion volume while for the second one the VVPSS is equipped with an in-pool heat exchanger emulating the Isolation Condenser (IC) installed in some advanced BWR designs. The main goal is to assess the pressure behaviour in the VV considering the design limit value of 200 kPa.

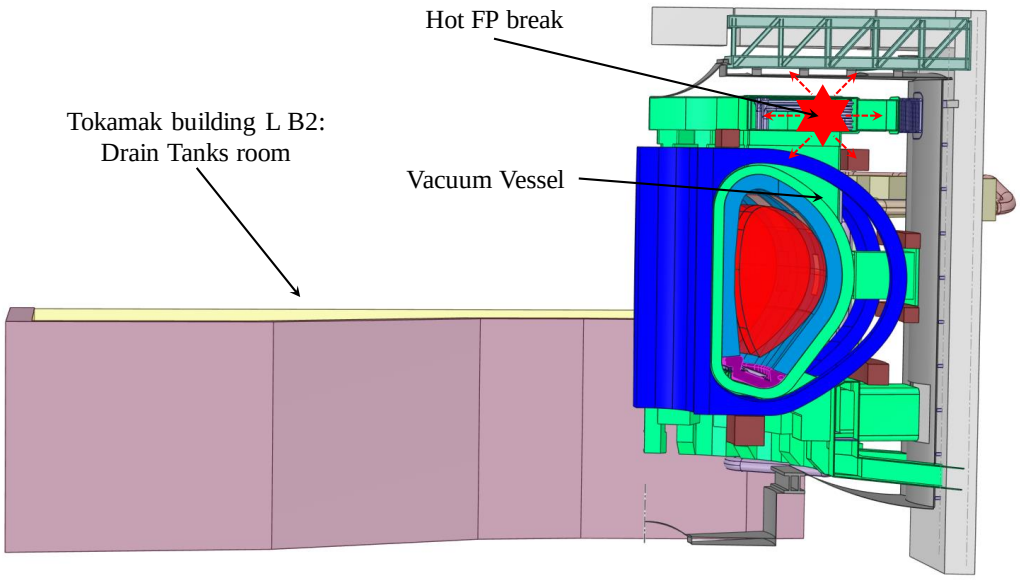

Figure 5-10: Hot feeding pipe DEG break location.

5.2.2.1 Models and Asssumptions

The developed model has been extended to include both the VV and the VVPSS components, namely the 5 Suppression Tanks (STs) depicted in Figure 1-10 and both the relief and bleed lines equipped with burst disks (BDs) and bleed valves (BVs) as described in §1.3. In particular, it has been considered to have 5 identical STs of ~980 m³ connected to the VV by means of 5 relief lines with a discharge area of 1 m² and an equal number of bleed lines which section is 0.05m² [104].

The VV has been modelled with 5 SINGLE VOLUMEs to more realistically reproduce the helium flow path to the VVPSS. Indeed, as shown in Figure 5-11, they represent the plasma chamber, the upper and lower port regions, the interspace between VV and divertor and the volume between VV and the BB segments. The STs have been collapsed together and discretized with 1 SINGLE VOLUME; similarly the connection lines have been simulated with 2 PIPEs, one for each type. While for BDs and BVs have been adopted 2 VALVE components. With regards to the connection junctions (Figure 5-11) between the different VV subdivisions, they have been assumed as reported in Table 5-1 [105]:

Table 5-1: HCPB BB-PHTS main data

Junction	Area [m²]
J-1	5.77E-01
J-2	2.35E+00
J-3	1.79E+00
J-4	6.30E+00
J-5	1.07E-01
J-6	6.33E+00

As concerns the thermal model, 8 HEAT STRUCTUREs have been used to model the component's structural materials and the main heat transferring phenomena. In particular, the attention has been focussed in modelling the radiation from the BSS to the inner side of the VV and from the VV to the external environment. To that end, a boundary condition evaluating the heat flux on the basis of an equivalent Heat Transfer Coefficient (HTC) has been applied. The HTC has been evaluated as follows:

$$h_{rad} = \varepsilon\sigma\left(T_s + T_{sur}\right)\left(T_s^2 + T_{sur}^2\right) \qquad (5.1)$$

where ε is the emissivity (assumed to be equal to 0.3) σ the Stefan–Boltzmann constant ($5.67 \cdot 10^{-8} W/m^2 \cdot K^4$), while T_s and T_{sur} are the surface and surroundings absolute temperatures properly averaged by means of dedicated CONTROL FUNCTIONs.
With regards to the VV initial conditions, it has been assumed to have hydrogen at 1 Pa and 573.15 K.

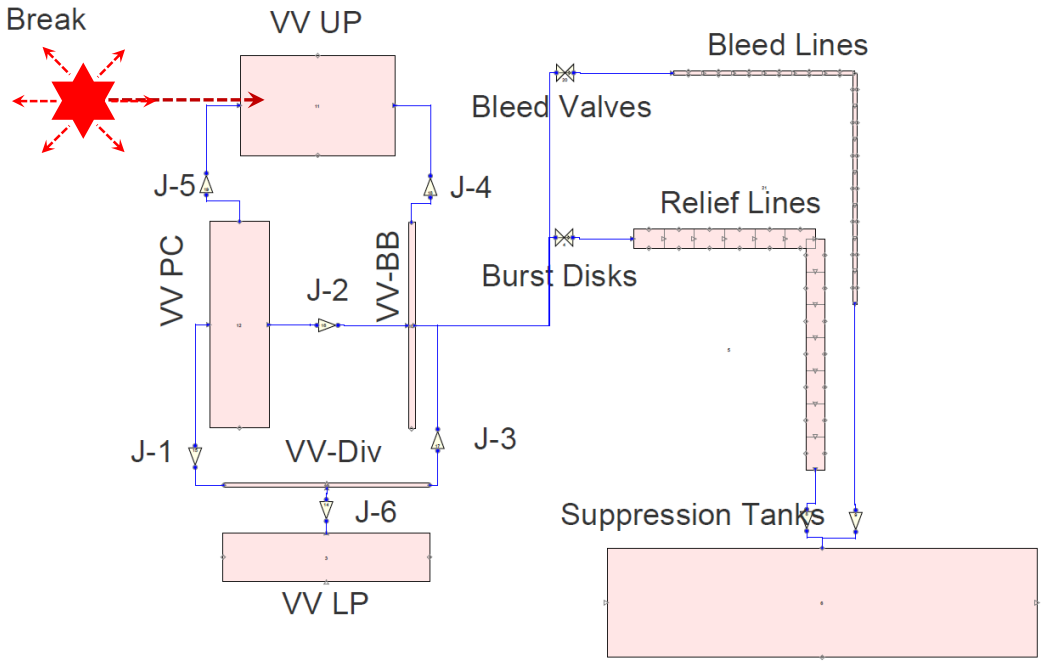

Figure 5-11: Vacuum vessel and VVPSS nodalization scheme.

5.2.2.2 Results

The pressure time-evolution for both the considered BB-PHTS loop and the VV is shown in Figure 5-12. The break occurrence is assumed at t = 0 s and, as already done for the assessment of the ex-vessel LOCA, a time delay of 3 s is assumed to shut-down the plasma and starting with the decay heat simulation.

The BVs open at 0.9 s, since the differential pressure of 90 kPa is reached, while the BDs opening occurs at around 1.5 s when the 150 kPa setpoint is achieved.

As it can be seen, for the simulated conditions the VV exceeds the design limit of 200 kPa. Indeed, the pressure reaches the maximum value of 260.3 kPa at around 15 s from the break opening, then it goes down at the equilibrium value of ~231.2 kPa.

The VV temperature trend is shown in Figure 5-13. Here, the initial peak is mainly due to the fluid compression caused by the flow discharged from the loop. Lastly the helium inventory in the loop, which at the equilibrium (around 30 s) becomes equal to ~85 kg, is reported in Figure 5-14.

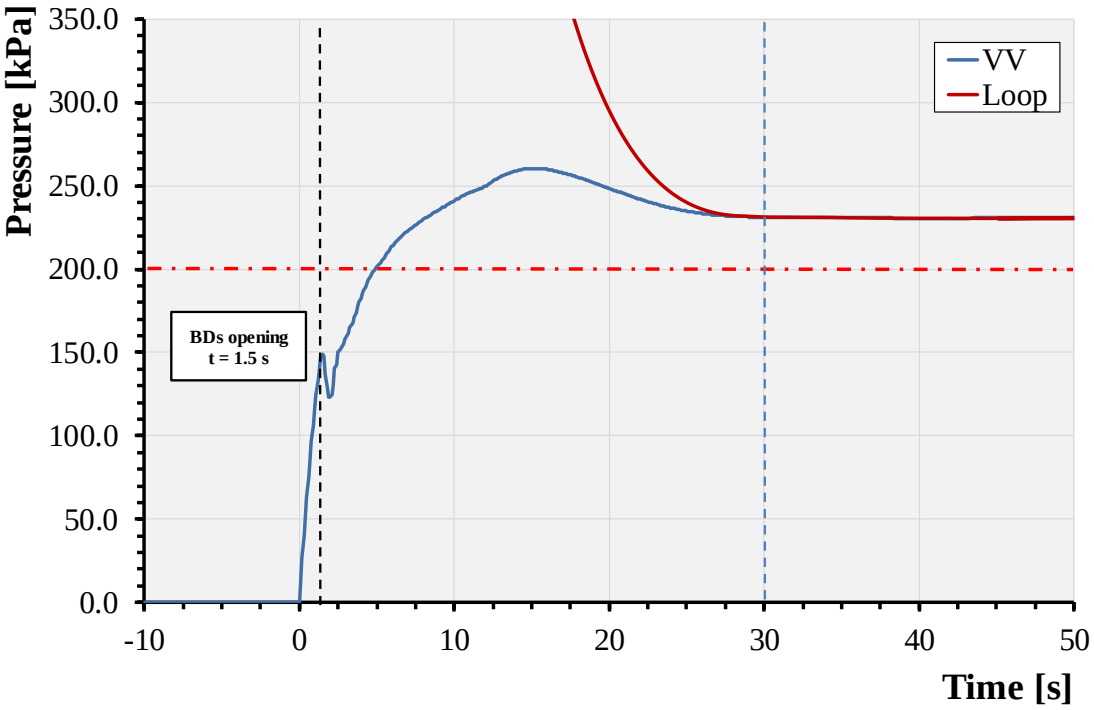

Figure 5-12: Pressure time-evolution in the VV.

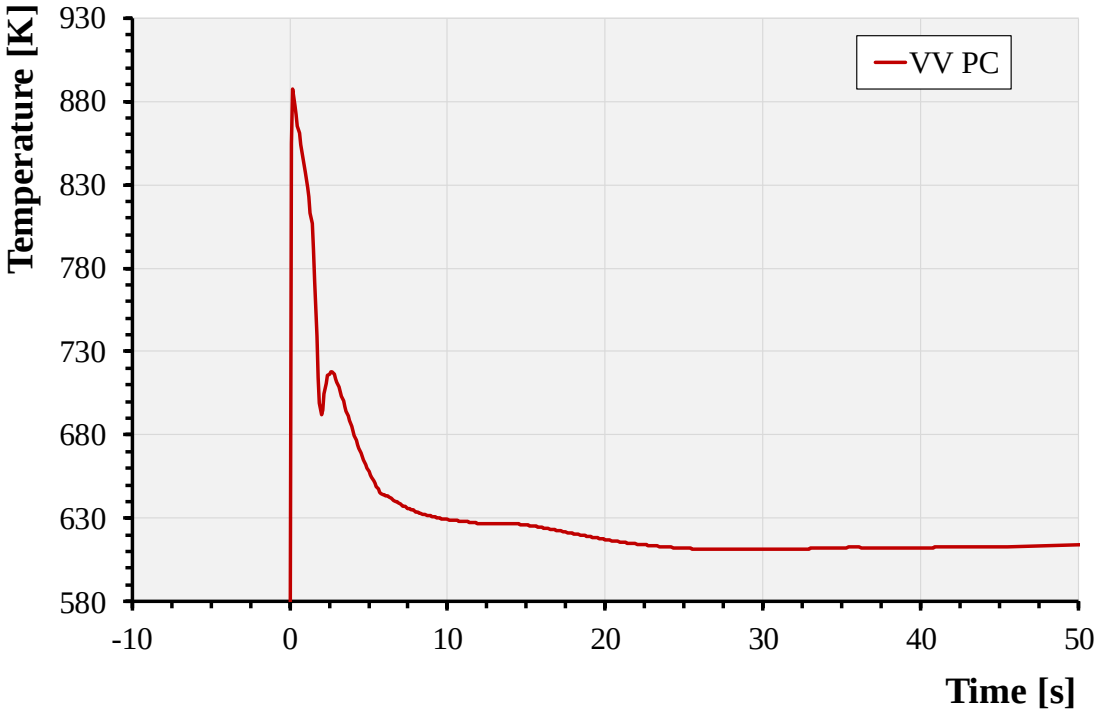

Figure 5-13: Temperature time-evolution in the VV.

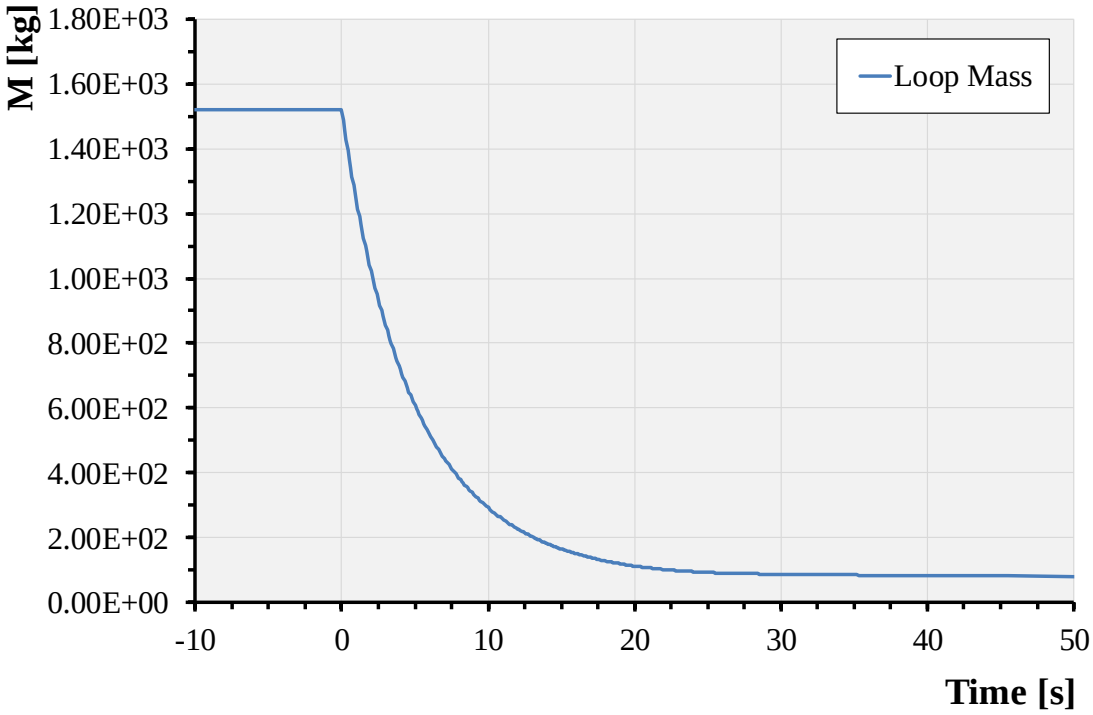

Figure 5-14: Loop mass trend.

5.3 Possible Design Modification for the VVPSS

In order to comply with the pressure design limit of 200 kPa, the possibility to cool down the helium before coming to the STs has been preliminary investigated. In this way the needed volume for its expansion can be reduced to an acceptable pressure. To that end, an IC-like [106] solution has been considered instead of mixing directly helium with cold water to avoid the contamination (with tritium, activated corrosion products and dust) of the latter, since the limited capability of a potential detritiation system would require long period of time to process it [107, 108].

5.3.1 Description of the new VVPSS configuration

At the base of the analysed configuration, sketched in Figure 5-15, there is a Heat eXchanger (HX) immersed in a pool containing water at room temperature. The HX inlet is directly connected to the VV by means of both relief and bleed lines, while the outlet is attached to the STs. Practically, two of the previously considered tank are now used as water reservoir (Pool) which host the HX connected to the remaining tanks acting as expansion volume. The nodalization adopted for the considered VVPSS configuration is depicted in Figure 5-16.

As concerns the HX design, the computational procedure has been based on the methodology reported in [95]. Starting from preliminary RELAP5-3D calculations the thermal power (W) to be exchanged has been assessed to ~150 MW, then both the internal (h_i) and external (h_e) side heat transfer coefficient have been calculated. The first one, h_i, by using the Bell-Delaware procedure (see Equation (4.7)), whereas the latter h_e, by means of the Gnielinski correlation shown in Equation (3.1). Once all the thermal resistance involved have been estimated, the overall heat transfer coefficient has been calculated as follows (referring to the internal surface):

$$U_i = \left[\frac{1}{h_i} + f_i + \frac{D_i}{2\lambda_{tube}} \ln\left(\frac{De}{D_i}\right) + f_e \frac{D_i}{De} + \frac{1}{h_e}\frac{D_i}{De} \right]^{-1} \qquad (5.1)$$

where f_i and f_e are the internal and external fouling factors, respectively; D_i and D_e the inner and outer diameter of the chosen tubes with thermal conductivity λ_{tube}. Then, the heat transfer surface has been evaluated as [109]:

$$S_i = \frac{W}{U_i \Delta T_{LM}} \tag{5.2}$$

where ΔT_{LM} is the logarithmic mean temperature, which in this case is defined as:

$$\Delta T_{LM} = \frac{T_i^{HX} - T_o^{HX}}{\ln\left(\frac{T_i^{HX} - T^{Tank}}{T_o^{HX} - T^{Tank}}\right)} \tag{5.3}$$

where T_i^{HX} and T_o^{HX} refer to inlet and outlet temperature in the immersed HX and T^{Tank} is the average pool temperature. The HX assessment has been done assuming the pool water temperature at 303.15 K, while the helium inlet and outlet temperatures have been iteratively obtained from RELAP5-3D calculations. The main HX information are summarized in Table 5-2.

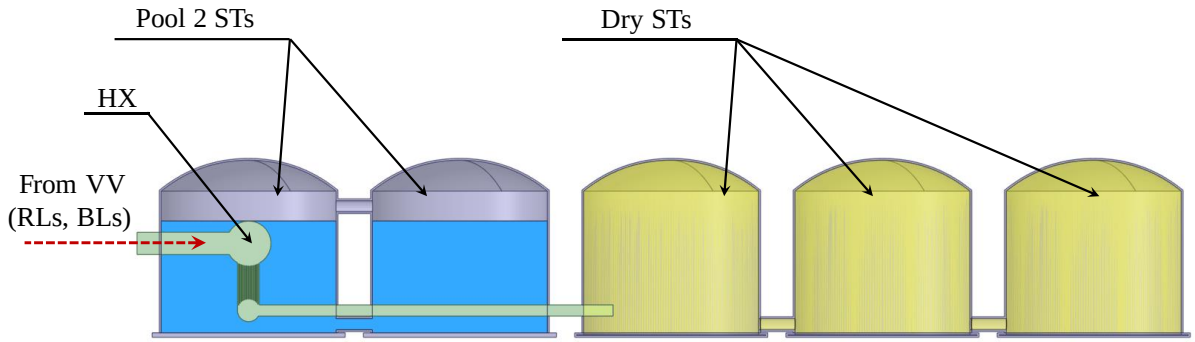

Figure 5-15: VVPSS configuration with an immersed HX.

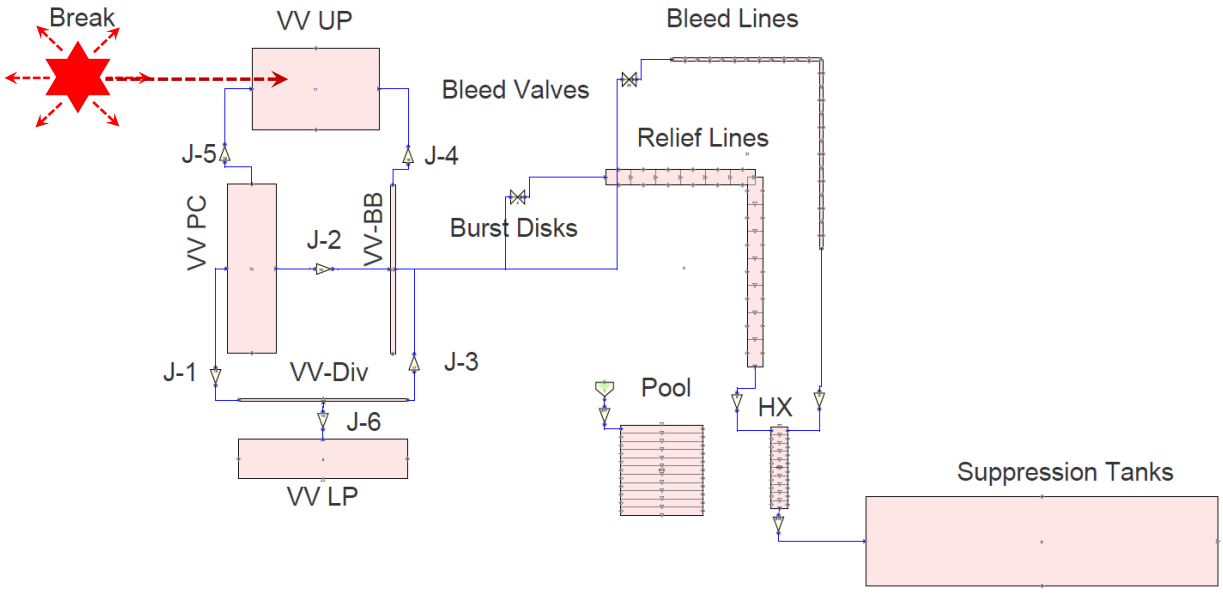

Figure 5-16: New VVPSS nodalization.

Table 5-2: HX main data

Parameter	Value
Tube outer diameter [mm]	50.80
Tube inner diameter [mm]	48.80
Tube thickness [mm]	1.00
Design pressure [kPa]	250.00
Thermal conductivity [W/m·K]	20.34
Thermal power [MW]	150.00
Tubes length [m]	6.04
Number of tubes [-]	7821

5.3.2 Evaluation of the Safety Performances

The HX, when triggered by the BDs opening, allows to cool down the helium up to ~250 K thanks to the heat transferred to the pool water as depicted in Figure 5-17. This effect works positively to reduce both the peak and equilibrium pressure values.

The VV pressure obtained for the analysed configuration is reported, in Figure 5-18, in comparison with that previously calculated. As it can be deduced, the adopted solution is really promising as it allows to reach a peak pressure slightly below the prescribed 200 kPa. However, the VV equilibrium pressure, being 198 kPa, basically lies on the design limit suggesting the need of further enhancement in order to safely stay underneath the limit. Some possible solutions may be the adoption of a greater expansion volume or to adopt a different HX configuration, but both require additional feasibility studies which will be assessed in future work.

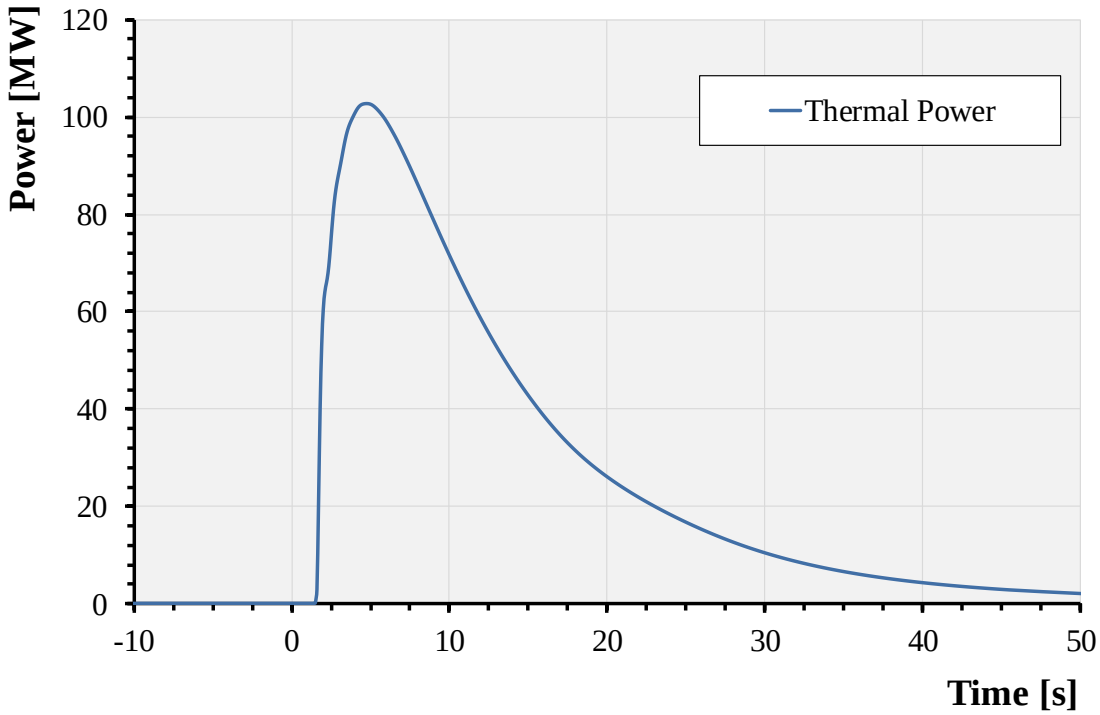

Figure 5-17: Thermal power transferred to the pool water.

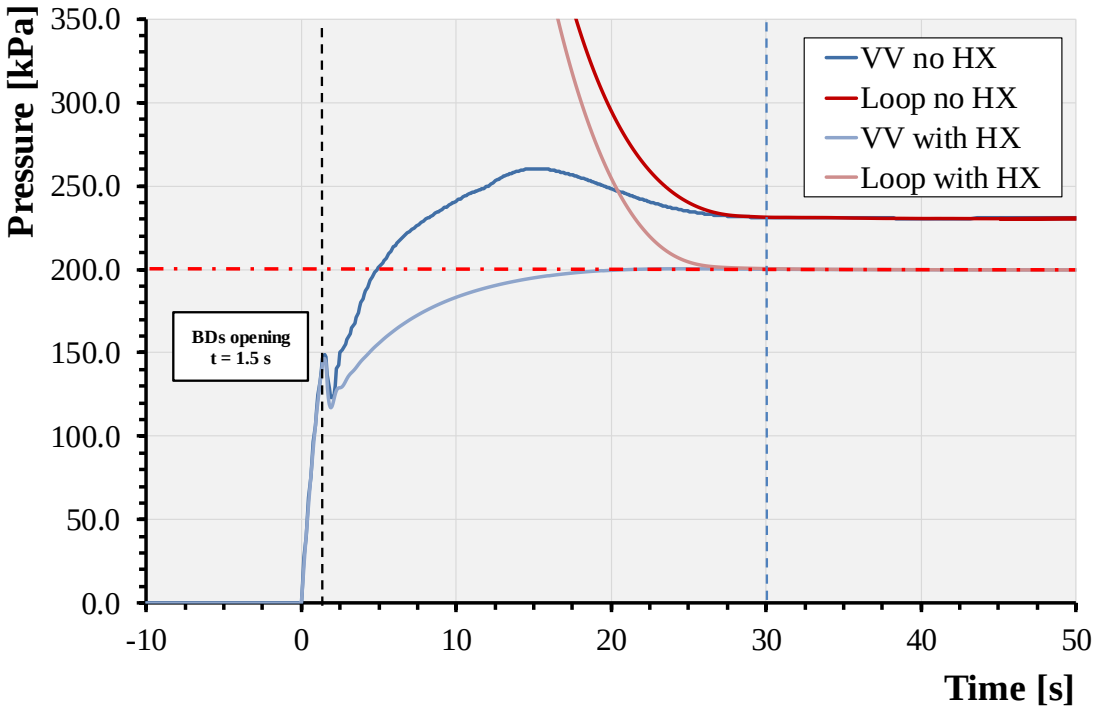

Figure 5-18: VV pressure comparison.

6 Conclusion

This thesis has covered the main research activities carried out during the Ph.D. course of the XXXII Cycle on “Energia e Tecnologie dell’Informazione - curriculum Fisica Tecnica e Ingegneria Nucleare” (Energy and Information Technologies - Applied Physics and Nuclear Engineering curriculum), held at the University of Palermo, in the time frame going from the end of 2016 to the end of 2019.

In particular, the PhD research project finds its place within the framework of the Work Package Safety and Environment (WPSAE) of the EUROfusion action and it has been mainly focussed on the investigation of the thermal-hydraulic and safety performances of the HCPB DEMO reactor system under steady state, operational and accidental transient conditions.

To that end, due to the extreme complexity of the HCPB DEMO reactor systems that definitely excludes any possibility of adopting a theoretical-analytical methodology, the research activity has been carried out following a theoretical-computational approach based on the finite volume method and adopting suitable releases of both the RELAP5-3D system code and the ANSYS CFX CFD code. These two tools have been properly integrated in order to achieve a more detailed and realistic simulation of the HCPB DEMO plant thermal-hydraulics with respect to the state of the art.

This integral approach has allowed taking advantage of the best characteristics of both the computational tools. Indeed, in this way, the integration of the system code aptitude to synthetically simulate the thermal-hydraulic performances of wide and complex energy transfer systems with the highly realistic predictive potential guaranteed by the 3-D CFD code in the thermo-fluid dynamic assessment of fluids flowing through deeply 3-D circuits has been performed.

More specifically, with reference to those components where deeply 3-D thermo-fluid-dynamic phenomena take place (e.g. HCPB DEMO BB), detailed parametric analyses have been performed by means of ANSYS CFX aiming at assessing the hydraulic characteristic function of the component, giving the functional dependence of its total pressure drop on the corresponding mass flow rate under steady state conditions. Once obtained, this function has been adopted to derive the dependence on mass flow rate of the effective concentrated hydraulic loss coefficients of each sub-component (e.g. FW channels, pins, etc.) which have been given in input to RELAP5-3D in order to let it simulate realistically the whole circuit with a lumped parameter approach.

As a proof-of-concept, the adopted integral procedure has been validated in applying it to reproduce an experimental test carried out on the HETRA facility. The performed activity has in fact demonstrated the suitability in reproducing the Eurofer temperature distribution in FW-like components, i.e. where the thermal loads are strongly asymmetrical. Indeed, in view of satisfying the requirement on the Eurofer maximum allowable temperature, its correct prediction has been considered pivotal for a proper investigation of the DEMO behaviour. Furthermore, a numerical benchmark has been fruitfully built up with the extensively validated CATHARE system code allowing testing the adopted procedure prediction capability in reproducing the main thermal-hydraulic phenomena occurring in DEMO HCPB-relevant applications.

Hence, once widely validated, the proposed integral modelling approach has been applied to the safety design of the EU-DEMO HCPB reactor.

First, the modelling approach has been applied to investigate the thermal-hydraulic behaviour of the relevant BB-PHTS loop conceived for the DEMO HCPB baseline 2017. The main goal has been to explore possible strategies controlling both the helium and HITEC molten salt mass flow rates in order to maintain the BB inlet temperature very close to the required value of 573.15 K during all the phases of the normal operational duty cycle. For this purpose, a parametric study has been performed analysing the dynamic response of the system when it switches from pulse to dwell and vice versa. In particular, 4 cases involving

a combination of different mass flow rates on both helium and HITEC sides has been set-up with the aim of understanding the potential maximum variations that relevant quantities such as pressure and temperatures can experience for a given Balance of Plant control. Indeed, such a parametric study has enabled to identify a potential scenario where the helium mass flow rate evolves assuming a turbo-machine viable rate of change of 12.5 % per minute, reaching the minimum value of 83.34 kg/s during the dwell. The proposed control system allows to reduce the main quantities excursion when switching between the two operational phases respect those envisaged for the parametric study. However, even if the BB inlet temperature can be considered satisfactorily controlled, the hot leg temperature fluctuations seems still too large to let the system operate in a very reliable and safe mode. Thermo-mechanical analysis using the obtained results to assess their damaging due to the thermal fatigue are indeed strongly suggested. Hence, further investigations on the most suitable system control strategy (bypass or pressure relief and throttled inlet compressor) seems needed with the support of the Balance of Plant experts.

Second, the modelling procedure has been finally been applied to analyse two DEMO relevant accidental scenarios, namely ex-vessel and in-vessel LOCAs. For the first scenario, a DEG break occurring in an OB segment hot feeding pipe has been postulated, on the basis of the previously identified PIEs. The main purposes have been to assess both the robustness of the developed computational model and the dynamic pressure loads on the civil structures of the tokamak building assuring it does not exceed the imposed design limit. In this case, considering the available expansion volume in TCR, the evaluated maximum pressure is safely below the limit of 200 kPa. In order to further reduce the accidental scenario consequences, the feasibility to install isolation valves to limit the coolant inventory released to the TCR and therefore the release of radioactive materials can be addressed in future work. Then, the consequences of an in-vessel LOCA due to a vacuum side DEG rupture in the largest feeding pipe have been investigated. In particular, two variants have been envisaged for such a scenario. Firstly, it has been assumed to have the VVPSS equipped with a dry expansion volume composed of 5 identical tanks of ~980 m^3 each, whereas in the second case the possibility to adopt a HX to cool down the helium coming from the VV has been preliminarily explored. For the latter variant, it has been assumed to use 2 tanks as water reservoir where the HX is immersed while the remaining tanks serve as expansion volume. By doing so, the same space reservation has been considered. As concerns the first variant, both the peak and equilibrium pressure are much higher than the design limit value of 200 kPa, whereas for the VVPSS configuration equipped with the immersed HX the pressure reach the maximum value of 198 kPa. This latter solution is promising, but since the obtained pressure peak is lying on the design limit, it requires thus the recourse to possible modifications. Some potential solutions might be the adoption of a greater expansion volume or a different HX configuration, but both require additional feasibility studies. However, an alternative solution could be the adoption of a wet expansion volume where the heat sink may be provided by discharging the helium directly in cold water or spraying water in the expansion volume atmosphere during the discharge to better ensure the thermal mixing. In this case, the consequences of treating huge water inventory with radioactive materials (tritium, ACPs and dust) should be considered since the limited capability of a potential detritiation system would require long period of time to process it, so before the reactor restart its operation. It is planned to investigate the listed solutions in future work.

In perspective, the extension of the modelling procedure to all the remaining components needed to simulate the intermediate system as well as power conversion system is programmed and already ongoing. In such a way, the computational model, taking advantage of the validated integral procedure adopted, will allow to broaden the scope of the possible PIEs to be analysed providing a high fidelity tool to evaluate the system dynamic under accidental conditions.

References

[1] United Nations Department of Economic and Social Affairs Population Division, World Population Prospects 2019, Working Paper No. ST/ESA/SER.A/424., 2019, Available: https://population.un.org/wpp/, Accessed on: 15.07.2019.

[2] U S Energy Information Administration, Annual Energy Outlook 2019 with projections to 2050, 2019, Available: https://www.eia.gov/outlooks/aeo/, Accessed on: 15.07.2019.

[3] International Energy Agency, Global Energy and CO_2 Status Report 2018, 2019, Available: https://webstore.iea.org/global-energy-co2-status-report-2018, Accessed on: 15.07.2019.

[4] UN Climate Change, Report of the Conference of the Parties on its twenty-first session held in Paris from 30 November to 13 December 2015, 2016, vol. FCCC/CP/2015/10/Add.1 Available: https://unfccc.int/process-and-meetings/conferences/past-conferences/paris-climate-change-conference-november-2015/cop-21/cop-21-reports, Accessed on: 15.07.2019.

[5] International Renewable Energy Agency, Global energy transformation: A roadmap to 2050 2019, Available: https://www.irena.org/publications/2019/Apr/Global-energy-transformation-A-roadmap-to-2050-2019Edition, Accessed on: 15.07.2019.

[6] European Commissioner for Energy, Energy Roadmap 2050, 2012, Available: https://ec.europa.eu/energy/en/topics/energy-strategy-and-energy-union/2050-energy-strategy, Accessed on: 15.07.2019.

[7] P. H. Rebut *et al.*, The Joint European Torus: installation, first results and prospects, *Nuclear Fusion*, vol. 25, no. 9, pp. 1011-1022, 1985.

[8] ASDEX Upgrade Design Team and Tokamak Theory Group, ASDEX-Upgrade. Definition of a tokamak experiment with a reactor compatible poloidal divertor, Max-Planck-Institut für Plasmaphysik, Garching (DE), Technical Report IPP 1/197, 1982.

[9] R. Aymar *et al.*, The ITER design, *Plasma Physics and Controlled Fusion*, vol. 44, no. 5, pp. 519-565, 2002.

[10] EUROfusion Programme Manager, European Research Roadmap to the Realisation of Fusion Energy, EUROfusion, 978-3-00-061152-0, 2018, Available: https://www.euro-fusion.org/fileadmin/user_upload/EUROfusion/Documents/2018_Research_roadmap_long_version_01.pdf.

[11] A A Harms *et al.*, *Principles of Fusion Energy: An Introduction to Fusion Energy for Students of Science and Engineering*. World Scientific, 2000.

[12] W M Stacey, *Fusion Plasma Physics*. WILEY-Verlag, 2012.

[13] J A Bittencourt, *Fundamentals of Plasma Physics*. Springer, 2004.

[14] National Physical Laboratory, Tables of Physical & Chemical Constant, Available: https://www.npl.co.uk/resources, Accessed on: 15.07.2019.

[15] W. M. Stacey, *Fusion: An Introduction to the Physics and Technology of Magnetic Confinement Fusion*. WILEY-Verlag, 2010.

[16] H. Zohm, On the Minimum Size of DEMO, *Fusion Science and Technology*, vol. 58, no. 2, pp. 613-624, 2017.

[17] J. D. Lawson, Some Criteria for a Power Producing Thermonuclear Reactor, *Proceedings of the Physical Society. Section B*, vol. 70, no. 1, pp. 6-10, 1957.

[18] R. Stieglitz, Introduction to fusion technology, Karlsruhe Institute of Technology, 2009.

[19] The National Academies, Interim Report - Status of the Study "An assessment of the prospects for inertial fusion energy", Washington DC, 2011.

[20] E. A. Azizov, Tokamaks: from A D Sakharov to the present (the 60-year history of tokamaks), *Physics-Uspekhi*, vol. 55, no. 2, pp. 190-203, 2012.

[21] L. Jr. Spitzer, The Stellarator Concept, *The Physics of Fluids*, vol. 1, no. 4, pp. 253-264, 1958.

[22] G. Federici *et al.*, European DEMO design strategy and consequences for materials, *Nuclear Fusion*, vol. 57, no. 9, 2017.

[23] G. Federici *et al.*, An overview of the EU breeding blanket design strategy as an integral part of the DEMO design effort, *Fusion Engineering and Design*, vol. 141, pp. 30-42, 2019.

[24] C. Bachmann, DEMO Plant Description Document, EUROfusion, Techinacal Report: EFDA_D_2KVWQZ, 2015, Available: https://idm.euro-fusion.org/?uid=2KVWQZ.

[25] M. Abdou *et al.*, Blanket/first wall challenges and required R&D on the pathway to DEMO, *Fusion*

Engineering and Design, vol. 100, pp. 2-43, 2015.
[26] R. Wenninger, DEMO1 Reference Design - 2017 March ("EU DEMO1 2017") - PROCESS Two Page Output, 2017, Available: https://idm.euro-fusion.org/?uid=2NE9JA.
[27] C. Bachmann *et al.*, Overview over DEMO design integration challenges and their impact on component design concepts, *Fusion Engineering and Design*, vol. 136, pp. 87-95, 2018.
[28] G. Federici *et al.*, Overview of the DEMO staged design approach in Europe, *Nuclear Fusion*, vol. 59, no. 6, 2019.
[29] J. E. Vetter, Breeding blanket development for NET, *Fusion Engineering and Design*, vol. 11, no. 1-2, pp. 101-114, 1989.
[30] D. Maisonnier *et al.*, Power plant conceptual studies in Europe, *Nuclear Fusion*, vol. 47, no. 11, pp. 1524-1532, 2007.
[31] F. A. Hernández *et al.*, An enhanced, near-term HCPB design as driver blanket for the EU DEMO, *Fusion Engineering and Design*, vol. 146, pp. 1186-1191, 2019.
[32] F. A. Hernández *et al.*, Advancements in the Helium-Cooled Pebble Bed Breeding Blanket for the EU DEMO: Holistic Design Approach and Lessons Learned, *Fusion Science and Technology*, vol. 75, no. 5, pp. 352-364, 2019.
[33] F. A. Hernández and P. Pereslavtsev, First principles review of options for tritium breeder and neutron multiplier materials for breeding blankets in fusion reactors, *Fusion Engineering and Design*, vol. 137, pp. 243-256, 2018.
[34] G. F. Hernandez, HCPB Design Report 2018, 2018, Available: https://idm.euro-fusion.org/?uid=2NUTXK.
[35] I. Moscato *et al.*, Preliminary design of EU DEMO helium-cooled breeding blanket primary heat transfer system, *Fusion Engineering and Design*, vol. 136, pp. 1567-1571, 2018.
[36] E. Bubelis *et al.*, Conceptual designs of PHTS, ESS and PCS for DEMO BoP with helium cooled BB concept, *Fusion Engineering and Design*, vol. 136, pp. 367-371, 2018.
[37] I. Moscato *et al.*, Progress in the design development of EU DEMO helium-cooled pebble bed primary heat transfer system, *Fusion Engineering and Design*, vol. 146, pp. 2416-2420, 2019.
[38] I. Moscato *et al.*, On the thermal dynamic behaviour of the helium-cooled DEMO fusion reactor, *Journal of Physics: Conference Series*, vol. 1224, 2019.
[39] L. L. C. Coastal Chemical Co., HITEC Heat Transfer Salt
[40] W. Hering, DEMO HCPB PHTS&BOP with IHTS+ESS, Design Review Report, 2019, Available: https://idm.euro-fusion.org/?uid=2MG7NW.
[41] L. Barucca *et al.*, Status of EU DEMO heat transport and power conversion systems, *Fusion Engineering and Design*, vol. 136, pp. 1557-1566, 2018.
[42] E. Bubelis, Conceptual designs and sizing of PHTS, IHTS, ESS and PCS components, 2019, Available: https://idm.euro-fusion.org/?uid=2MH7AQ.
[43] C. Bachmann, Design Description Document of the DEMO Vacuum Vessel 2019, Available: https://idm.euro-fusion.org/?uid=2NSJCC.
[44] T. Haertl *et al.*, Rationale for the selection of the operating temperature of the DEMO vacuum vessel, *Fusion Engineering and Design*, vol. 146, pp. 1096-1099, 2019.
[45] Tonio Pinna, Selection of reference accident scenarios for the DEMO plant, 2016, Available: https://idm.euro-fusion.org/?uid=2MA6TU.
[46] F. D'Auria, *Thermal-Hydraulics of Water Cooled Nuclear Reactors*. Woodhead Publishing, 2017.
[47] Idaho National Laboratory, *Models and Correlations* (RELAP5-3D Code Manuals). 2018.
[48] CEA-Grenoble, CATHARE2: General description, in "CATHARE Code Manuals," Institut de Radioprotection et de Sûreté Nucléaire 2015.
[49] US Nuclear Regulatory Commission, Field Equations, Solution Methods, and Physical Models, in "TRACE Manual," 2015.
[50] J. Mahaffy, Best Practice Guidelines for the Use of CFD in Nuclear Reactor Safety Application, 2015.
[51] M. Böttcher and R. Krüßmann, Primary loop study of a VVER-1000 reactor with special focus on coolant mixing, *Nuclear Engineering and Design*, vol. 240, no. 9, pp. 2244-2253, 2010.
[52] M. H. Rahimi and G. Jahanfarnia, Thermal-hydraulic core analysis of the VVER-1000 reactor using a porous media approach, *Journal of Fluids and Structures*, vol. 51, pp. 85-96, 2014.
[53] Z. V. Stosic and V. D. Stevanovic, Advanced Three-Dimensional Two-Fluid Porous Media Method for Transient Two-Phase Flow Thermal-Hydraulics in Complex Geometries, *Numerical Heat*

Transfer, Part B: Fundamentals, vol. 41, no. 3-4, pp. 263-289, 2002.
[54] T. Cong *et al.*, Three-dimensional study on steady thermohydraulics characteristics in secondary side of steam generator, *Progress in Nuclear Energy*, vol. 70, pp. 188-198, 2014.
[55] R. Chen *et al.*, Three dimensional thermal hydraulic characteristic analysis of reactor core based on porous media method, *Annals of Nuclear Energy*, vol. 104, pp. 178-190, 2017.
[56] P. Martinez and J. Galpin, CFD modeling of the EPR primary circuit, *Nuclear Engineering and Design*, vol. 278, pp. 529-541, 2014.
[57] C. E. W. James R. Welty, Robert E. Wilson, Gregory L. Rorrer,, *Fundamentals of Momentum, Heat, and Mass Transfer*. John Wiley & Sons, Inc., 2000.
[58] Robert Greenkorn, *Momentum, Heat, and Mass Transfer Fundamentals*. CRC Press, 1999.
[59] D. C. Wilcox, Reassessment of the scale-determining equation for advanced turbulence models, *AIAA Journal*, vol. 26, no. 11, pp. 1299-1310, 1988.
[60] B. Aupoix, Roughness Corrections for the k–ω Shear Stress Transport Model: Status and Proposals, *Journal of Fluids Engineering*, vol. 137, no. 2, 2015.
[61] Veres Gabor, Thermo-hydraulic analysis support of HCPB DDD– Activities in 2018, 2019, Available: https://idm.euro-fusion.org/?uid=2P3AQ7.
[62] F. R. Menter, Two-equation eddy-viscosity turbulence models for engineering applications, *AIAA Journal*, vol. 32, no. 8, pp. 1598-1605, 1994.
[63] J. E. Bardina *et al.*, Turbolence Modeling Validation, Testing, and Development, NASA, 1997.
[64] J. C. F. Florian Menter, Thomas Esch, Brad Konno,, The SST Turbulence Model with ImprovedWall Treatment for Heat Transfer Predictions in Gas Turbines, *Proceedings of the International Gas Turbine Congress 2003 Tokyo*, 2003.
[65] V. I. Gryn, Exact solutions of the navier-stokes equations, *Journal of Applied Mathematics and Mechanics*, vol. 55, no. 3, pp. 301-309, 1991.
[66] J. H. Ferziger *et al.*, *Computational Methods for Fluid Dynamics*. Springer, 2020.
[67] I. ANSYS, *ANSYS CFX-Solver Theory Guide*. 2018.
[68] European Research Community on Flow Turbulence and Combustion, Industrial Computational Fluid Dynamics of Single-Phase Flows in "ERCOFTAC Best Practice Guidelines," 2000.
[69] G. L. Mesina, A History of RELAP Computer Codes, *Nuclear Science and Engineering*, vol. 182, no. 1, pp. v-ix, 2017.
[70] W. J. Garland, *The Essential CANDU*. UNENE Department of Engineering Physics, McMaster University, Hamilton, Ontario, CANADA, 2014.
[71] Idaho National Laboratory, *Code Structure, System Models and Solution Methods* (RELAP5-3D Code Manuals). 2018.
[72] G. A. Roth and F. Aydogan, Theory and implementation of nuclear safety system codes – Part II: System code closure relations, validation, and limitations, *Progress in Nuclear Energy*, vol. 76, pp. 55-72, 2014.
[73] S. D'Amico *et al.*, Preliminary thermal-hydraulic analysis of the EU-DEMO Helium-Cooled Pebble Bed fusion reactor by using the RELAP5-3D system code, *Proceedings of the ISFNT-14*, 2019.
[74] S. Patankar and D. Spalding, McGraw-Hill, Ed. *A calculation procedure for transient and steady state behaviour of shell-and-tube heat exchangers*. New York, USA, 1974.
[75] G. M. M. Ilić, K. Zinn, V. Szabo , B. Kiss, S. Kecskes, Manufacturing and testing of a FW channel mock-up for experimental investigation of heat transfer with He at 80 bars and reference cooling conditions. Comparison with numerical modelling, EFDA Technology Programme, 2011.
[76] F. Bentivoglio *et al.*, Validation of the CATHARE2 code against experimental data from Brayton-cycle plants, *Nuclear Engineering and Design*, vol. 238, no. 11, pp. 3145-3159, 2008.
[77] G. Geffraye *et al.*, CATHARE 2 code validation on HE-FUS3 loop, *Nuclear Engineering and Design*, vol. 249, pp. 237-247, 2012.
[78] M. Ilić *et al.*, Experimental investigations of flow distribution in coolant system of Helium-Cooled-Pebble-Bed Test Blanket Module, *Fusion Engineering and Design*, vol. 103, pp. 53-68, 2016.
[79] T. K. M. Ilić, O. Albrecht, G. Schlindwein, K. Zinn, O. Bitz, R. Schmidt,, Manufacturing and testing of mock-ups for investigation of coolant distribution in the manifold system of HCPB TBM (GRICAMAN experiments), 2013.
[80] Francisco Alberto Hernández González, "Simulation of Volumetrically Heated Pebble Beds in Solid Breeding Blankets for Fusion Reactors: Modelling, Experimental Validation and Sensitivity Studies," PhD Thesis, Karlsruher Institut für Technologie (KIT), 2016.

[81] M. Ilic *et al.*, HETRA experiment for investigation of heat removal from the first wall of helium-cooled-pebble-bed test blanket module, *Fusion Engineering and Design*, vol. 86, no. 9-11, pp. 2250-2253, 2011.
[82] M. Ilić *et al.*, Experimental and numerical investigations of heat transfer in the first wall of Helium-Cooled-Pebble-Bed Test Blanket Module – Part 1: Presentation of test section and 3D CFD model, *Fusion Engineering and Design*, vol. 90, pp. 29-36, 2015.
[83] P. Norajitra *et al.*, The first HEBLO experiments based on the EU HCPB blanket concept, *Fusion Engineering and Design*, vol. 58-59, pp. 623-627, 2001.
[84] G. F. Hernandez, HCPB Design Report 2015, 2016.
[85] T. L. Bergman A. S. Lavine, *Fundamentals of Heat and Mass Transfer*. 2017.
[86] R. Wenninger, Reference Design - 2015 April (EU DEMO1 2015) PROCESS Full Output, EUROfusion, 2015.
[87] B. Ghidersa, HCLL HCS preliminary engineering design and analyses, 2010.
[88] I. E. Idelchik, *Handbook of Hydraulic Resistance*. 2005.
[89] D. J. Zigrang and N. D. Sylvester, Explicit approximations to the solution of Colebrook's friction factor equation, *AIChE Journal*, vol. 28, no. 3, pp. 514-515, 1982.
[90] N. Tauveron, *Overview of Gas Cooled Reactor applications with CATHARE*. 2005.
[91] B. D. Cliff *et al.*, Assessment of RELAP5-3D for Analysis of Very High Temperature Gas-Cooled Reactors, Idaho National Laboratory, 2005.
[92] D. A. Nield and A. Bejan, *Convection in Porous Media*. Springer, 2013.
[93] Ivo Moscato, HCPB - Relevant data of BB PHTS and IHTS - 2019, 2019, Available: https://idm.euro-fusion.org/?uid=2NDGNW.
[94] James E. Fisher and Cliff B. Davis, RELAP5-3D Compressor Model, Idaho National Laboratory, 2005.
[95] E U Schlunder, *Heat exchanger design handbook*. Hemisphere Pub. Corp, 1983.
[96] Cliff B. Davis, Implementation of Molten Salt Properties into RELAP5-3D/ATHENA, Idaho National Engineering and Environmental Laboratory, Idaho Falls, Idaho 83415, 2005.
[97] G. Zhou, Definition of elementary load cases and load cases combination, EUROfusion, 2019, Available: https://idm.euro-fusion.org/?uid=2NUETW.
[98] A. Spagnuolo, Breeding Blanket Load Specifications Document, EUROfusion, 2019, Available: https://idm.euro-fusion.org/?uid=2NLL6N.
[99] Kurt Kugeler and Zuoyi Zhang, *Modular High-temperature Gas-cooled Reactor Power Plant*. Springer, 2019.
[100] S. L. Dixon and C. A. Hall, *Fluid Mechanics and Thermodynamics of Turbomachinery*. Elsevier Inc., 2014.
[101] N. Taylor *et al.*, Safety and environment studies for a European DEMO design concept, *Fusion Engineering and Design*, vol. 146, pp. 111-114, 2019.
[102] T. Pinna *et al.*, Failure mode and effect analysis on ITER heat transfer systems, *Fusion Engineering and Design*, vol. 42, no. 1-4, pp. 431-436, 1998.
[103] T. Pinna *et al.*, Identification of accident sequences for the DEMO plant, *Fusion Engineering and Design*, vol. 124, pp. 1277-1280, 2017.
[104] M T Porfiri *et al.*, DEMO BB Safety Data List (SDL), 2018, Available: https://idm.euro-fusion.org/?uid=2MF8KU.
[105] Matteo D'Onorio *et al.*, Preliminary Safety Analysis of an in-vessel LOCA for the EU-DEMO WCLL Blanket Concept, *Proceedings of the ISFNT-14*, 2019.
[106] A. Schaffrath *et al.*, Operation conditions of the emergency condenser of the SWR1000, *Nuclear Engineering and Design*, vol. 188, no. 3, pp. 303-318, 1999.
[107] Y. Iwai *et al.*, The Water Detritiation System of the ITER Tritium Plant, *Fusion Science and Technology*, vol. 41, no. 3P2, pp. 1126-1130, 2017.
[108] I. Cristescu, Enhanced configuration of a water detritiation system; impact on ITER Isotope Separation System based cryogenic distillation, *Fusion Engineering and Design*, vol. 109-111, pp. 1404-1407, 2016.
[109] J. Cadafalch *et al.*, Modelling of storage tanks with immersed heat exchangers, *Solar Energy*, vol. 112, pp. 154-162, 2015.